

# The Quantum Electron Dynamics of Materials Subjected to Extreme Environments

by

Patrick Lauren Theofanis

In Partial Fulfillment of the Requirements

for the Degree of

Doctor of Philosophy



California Institute of Technology

Pasadena, California

2012

(Defended March 8, 2012)

© 2012

Patrick Lauren Theofanis

All Rights Reserved

To my wife and family

# Acknowledgements

This thesis is the culmination of many years of intellectual preparation, nurturing and support, and I firmly believe that one does not survive a Ph.D. program without a strong network of advisors, friends and family. I would like to acknowledge the people who have filled those roles for me.

Research with Professor Bill Goddard has been a whirlwind experience. Professor Goddard's interests are broad to say the least, and the number of research fields explored in his lab and the volume of research is astonishing. To succeed as one of Professor Goddard's students you must be ready to tackle any problem in any field. Fortunately Professor Goddard is enthusiastic, open-minded, and eager to help his students. I also appreciate the freedom Dr. Goddard afforded me to work on projects at my own pace and in my own way. If I needed his advice, he was always available to help.

Other members of the Goddard lab deserve special mention for their support: Andres Jaramillo-Botero mentored me on my hypervelocity impact, eFF, shock and fracture projects. Andres is the kind of man I aspire to become: a polymath scientist, a sportsman, and a devoted father and husband. Robert (Smith) Nielsen and Jonas Oxgaard have been excellent mentors on catalysis projects and good friends. Without them I doubt I could have finished the projects that I did. Todd Pascal, Will Ford, Hai Xiao, and Qi An offered advice, code, or support on research projects. Mu-Jeng Cheng has been a good friend in the Goddard group, and I enjoyed our talks about research, travel, and graduate student life.

Of course, in an atmosphere as stressful and intense as Caltech, one needs diversions. I can credit my friends at Caltech for providing me with a wide variety of them. I have fond memories of teaching introductory chemistry lab courses with Chithra Krishnamurthy, who is always willing to

take a coffee break to chat. Vivian Ferry and David Valley were excellent study buddies during our first year, and good friends later in the program. I enjoyed earning my pilot's license through the Caltech flying club, AACIT, and serving on the board as a student representative. I am proud of two intramural football championship titles with Playmakers and playing football with Ryan Zeidan, Jeff Krimmel, Habib Ahmad, Michael Krout, Justin Mohr, Jonathan Young, Chiraj Dalal, Chris Gilmore, Pat Donovan, Ken Lin, Matt Corrigan, Jon Eilbes, and Steven Becker was a blast. My old lab mates from the Zewail group hosted some of the most fun diversions. Early morning and weekend surfing trips to El Porto, C-street in Ventura, and San Onofre with Peter Baum, Jonas Weissenrieder, and Andreas Gahlmann were much needed breaks from the rigors of research. Andreas Gahlmann is a great friend, and a good surfing, swimming, cycling, and gym partner. I was proud to have him as a groomsman at my wedding.

During my years at Caltech, my group of Pasadena family and friends has grown. In my first year I lived in a house in South Pasadena with Siobhan Donovan, Shari Sakamoto, Harry Plotkin, and, later Mary Cholko. Through Siobhan and Shari's soccer team I met my wife, Kelly. Siobhan's brother, Patrick, and his girlfriend Heather Lander, are great friends and were roommates during my third and fourth years of graduate school. Patrick was also one of my groomsmen. T. Boyle's Trivia nights with Kelly and her cousins Charlie and Kevin O'Connor and our friends Pat, Heather, Erin Donovan, Crystal Crockett, Shari and Brendan Grubbs, are always the best way to start the week. Kathleen McCarthy's pastries helped keep me fat and happy, and lounging by her pool with Kelly, and Kathleen's daughters Meg, Molly and Claire was always a nice get-away.

Writing a thesis and research propositions involves lots of late-night writing sessions, and I am thankful to have had a furry nocturnal friend to keep me company. My cat Lil' Thunder always let me know which literature reference was the most pertinent because he inevitably fell asleep on it when I needed it most.

There's no exaggerating the important role my family has played in my life. My Mom, Celina, and Dad, George, nurtured my intellectual curiosity from a young age. They tolerated my chemistry set messes, my experiments with combustion, and my preoccupation with disassembling and

reassembling household electronics. They even supplemented this research with visits to just about every museum in Los Angeles and New York, and to archaeological sites in the Southwest. My Grandparents, John and Beatriz Theofanis, encouraged me to question what I had been taught in school, and encouraged me to think freely. My Abuelita Carmen to this day impresses upon me that none of the world around us has meaning without faith. My brothers Robert and Eric, and my beautiful little sister Raquel, were fun to grow up with, and I appreciate their support. The level of their support is evident in this holiday misadventure: during Christmas break in 2009, at a particularly gloomy moment in my graduate career, I admitted to my family that I was considering dropping out of Caltech. Eric responded by saying he never thought of me as a quitter, and he suggested that I was too stubborn to give up. He said, "It's like being in a choke hold. I'll bet you would fight it and pass out instead of tapping out." For some reason we decided to actually test this analogy and Eric proceeded to put me in a full-on choke hold. I recall pulling one of his arms off, but my next memory is waking up on the kitchen floor with Robert slapping my face back to consciousness and mom screaming my name frantically. Eric was right; I was too stubborn to give up and now I've accomplished what I set out to do. I've finally earned my Ph.D. My in-laws John and Maureen Heintz, and my new siblings in-law, Molly, Jack and Wil have been welcoming and supportive.

Lastly, and most importantly, I want to thank my beautiful wife, Kelly. Kelly and I started dating during my second year of graduate school. Between then and now, we have endured living at opposite ends of Los Angeles, two three-month separations during my internships in New Mexico and Michigan, her stint in business school at USC, and the ups and downs of my time at Caltech. We enjoyed vacations to Portugal, Spain, and Thailand, along with weekend trips to Monterrey, Santa Barbara, Las Vegas, San Diego, Albuquerque, Santa Fe, Midland, and countless dinners and outings with our families and friends. We celebrated our marriage with an incredible reception on October 23, 2010, at the beginning of my 5th year. Kelly's support and encouragement helped me find the fortitude to continue working hard when research was difficult or when progress was slow. She always has the right input when I am a loss for ideas, and her (unsolicited) advice is quite good,

too. I am glad I met my partner in life during graduate school. It tested our mettle, and Kelly and I are stronger for it. Kelly, love of my life, I look forward for the adventures that lie ahead of us.

*Thank you.*

# Abstract

Quantum wavepacket molecular dynamics simulations are used to study the effects of extreme environments on materials. The electron forcefield (eFF) method provides energies and forces from which wavepackets can be propagated in time under conditions ranging from standard temperature and pressure to tens of thousands of Kelvin and hundreds of GPa of pressure with strain rates as high as 1 km per second. Using this technique nanometer scale systems with hundreds of thousands of particles can be simulated for up to hundreds of picoseconds.

High strain rate fracture in solids is accompanied by the emission of electrons and photons, though atomistic simulations have thus far been unable to capture such processes. The eFF method for nonadiabatic dynamics accounts for electron emission and large potential differences consistent with the experiments, providing the first atomistic description of the origin of these effects. The effects that we explain are (1) loading of a crack leads to a sudden onset of crack propagation at 7 GPa followed by uniform velocity of the crack at 2500 km/sec after initiation, and (2) voltage fluctuations in the 10–400 mV range, charge creation (up to  $10^{11}$  carriers/cm<sup>2</sup>), and current production (up to 1.3 mA). The development of an effective core potential for eFF enabled this large scale study.

Using the eFF wavepacket molecular dynamics method, simulations of the single shock Hugoniot are reported for crystalline polyethylene (PE). The eFF results are in good agreement with previous DFT theories and experimental data which is available up to 80 GPa. We predict shock Hugoniot for PE up to 350 GPa. In addition, we analyze the phase transformations that occur due to heating. Our analysis includes ionization fraction, molecular decomposition, and electrical conductivity during isotropic compression. We find that above a compression of 2.4 g/cm<sup>3</sup> the PE structure transforms into a Lennard-Jones fluid, leading to a sharp increase in electron ionization and a significant increase

in system conductivity. eFF accurately reproduces shock pressures and temperatures for PE along the single shock Hugoniot.

# Contents

<b>Acknowledgements</b>	<b>iv</b>
<b>Abstract</b>	<b>viii</b>
<b>List of Figures</b>	<b>xiv</b>
<b>List of Tables</b>	<b>xix</b>
<b>1 Matter in Extreme Environments</b>	<b>1</b>
1.1 Extreme Chemistry . . . . .	1
1.2 This Thesis . . . . .	4
<b>2 The Electron Forcefield Method</b>	<b>6</b>
2.1 Simulating Excited State Dynamics . . . . .	6
2.1.1 Modeling Excited States is Challenging for Theorists . . . . .	6
2.1.2 Traditional Molecular Dynamics Techniques . . . . .	8
2.1.3 Precursors to eFF . . . . .	10
2.2 The eFF Wavefunction and Forcefield . . . . .	12
2.3 Wave Packet Molecular Dynamics . . . . .	16
2.4 Temperature, Pressure, and Heat Capacity . . . . .	17
2.5 eFF Successes . . . . .	19
<b>References</b>	<b>21</b>

<b>3</b>	<b>Nonadiabatic Electron Dynamics During Brittle Fracture in Silicon</b>	<b>25</b>
3.1	Abstract . . . . .	25
3.2	Brittle Fracture in Silicon . . . . .	26
3.3	Silicon Models and Methods . . . . .	28
3.4	Electron Dynamics During Brittle Fracture . . . . .	29
3.4.1	Fracture Mechanics . . . . .	29
3.4.2	Atomistic Mechanisms of Fracture . . . . .	30
3.4.3	Fracture-Induced Electron Excitation . . . . .	31
3.5	Conclusions . . . . .	37
	<b>References</b>	<b>39</b>
<b>4</b>	<b>The Electron Dynamics of Shocked Polyethylene Crystal</b>	<b>42</b>
4.1	Abstract . . . . .	42
4.2	Shocked Polyethylene . . . . .	42
4.3	Crystalline Polyethylene Model and Computational Methods . . . . .	43
4.4	Results and Discussion . . . . .	46
4.4.1	The Principal Hugoniot . . . . .	46
4.4.2	Structural Decomposition . . . . .	48
4.4.3	Conductivity . . . . .	51
4.5	Conclusions . . . . .	52
	<b>References</b>	<b>53</b>
<b>5</b>	<b>Core Pseudoparticles as an Effective Core Approximation</b>	<b>55</b>
5.1	Motivation . . . . .	55
5.2	Theoretical Development of Core Pseudoparticles . . . . .	55
5.2.1	Core Pseudoparticle Pauli Potential . . . . .	58
5.2.2	Core Pseudoparticle Electrostatic Potentials . . . . .	59

5.3	Fitting Technique . . . . .	60
5.4	Computational Performance . . . . .	62
5.5	Validation of the Fit Parameters . . . . .	64
5.5.1	Silicon . . . . .	64
5.5.2	Si(111)-7×7 Reconstruction . . . . .	70
5.5.3	Aluminum . . . . .	74
5.6	Future Directions . . . . .	76
	<b>References</b>	<b>78</b>
	<b>A Ligand Effects in Rhodium Catalyzed Methane Activation</b>	<b>80</b>
A.1	Introduction . . . . .	80
A.2	Computational Methods . . . . .	82
A.3	Results and Discussion . . . . .	84
A.3.1	Two Pathways to C-H Activation . . . . .	84
A.3.2	Rh(III) in Water . . . . .	85
A.3.3	Rh(I) in Water . . . . .	88
A.3.4	Rh(III) in TFA . . . . .	89
A.3.5	Rh(I) in TFA . . . . .	90
A.3.6	Decreasing the Reductive Functionalization Barrier with Bulky Ancillary Ligands . . . . .	91
A.4	Conclusions . . . . .	94
	<b>References</b>	<b>95</b>
	<b>B Estimating Phosphorescence Lifetimes in Cyclometalated Platinum Phosphors</b>	<b>98</b>
B.1	Phosphorescent Cyclometalated Platinum Complexes . . . . .	98
B.2	Computational Methodology . . . . .	101
B.3	Computing Radiative and Non-Radiative Decay Rates . . . . .	103

B.3.1	Radiative Transitions . . . . .	103
B.3.2	Non-Radiative Transitions . . . . .	103
B.4	Results and Discussion . . . . .	106
B.4.1	Excitation Energies . . . . .	106
B.4.2	Radiative Decay Rates . . . . .	109
B.4.3	Intersystem Crossing . . . . .	111
B.5	Conclusions . . . . .	114
	<b>References</b>	<b>115</b>
	<b>C Supplemental Material</b>	<b>118</b>
	<b>D Published Research</b>	<b>127</b>
	<b>E Final Thoughts</b>	<b>148</b>

# List of Figures

1.1	Domains of practical use for various theories. eFF is able to model systems within the dashed box. The scope of the conditions for the two major studies presented in this thesis are plotted for reference. . . . .	3
2.1	A gallery of snapshots from toy calculations to demonstrate eFF capabilities. Top: a vibrationally excited “walker” on the $\text{H}_3\text{Si}-\text{SiH}_3 \cdots \text{SiH}_3$ $\text{S}_{\text{N}}2$ potential energy surface. The transition states are marked with red ‡ symbols and the surface minima is marked with a green dot. Middle: A silicon particle colliding with and rebounding from a silicon {111} surface at 5 km/s. Bottom: The same silicon particle colliding with and penetrating the surface at 20 km/s. Ionized electrons are colored red. . . . .	7
3.1	A snapshot of a crack propagating in a silicon single crystal with mode I loading in the x-direction producing a {100}⟨011⟩ edge crack. The transparent spheres are paired electrons. Unpaired spin up electrons are colored red, and unpaired spin down electrons are colored blue. . . . .	26
3.2	(a) Crack tip velocity versus reduced load for {111} fracture with experimental data from [17], ReaxFF-Tersoff and SW data from [31], environmental dependent interatomic potential (EDIP) and the results of a multiscale method that couples empirical potentials and quantum mechanical tight-binding approaches (DCET) from [26]. (b) The crack tip velocity versus reduced load for the eFF {100} model. The gray lines are visual guides. . . . .	29

3.3	{100}<011> fracture is produced by stepwise “zig-zag” bond breaking in lower energy {111} planes. . . . .	30
3.4	Snapshots of {111}<112> fracture at 6.5, 7, and 15.3 ps after the initiation of crack propagation. At 15.3 ps a dislocation (boxed in red) is visible. The dislocation is emitted due to the shear stresses caused by the crack tip crossing into the neighboring left bilayer. In the upper panes electrons are depicted as transparent spheres. The lower panes show silicon nuclei. . . . .	32
3.5	(a) The absolute distance between the crack tip and electrons that will ionize. (b) The radii of ionized electrons (in color), ground state surface electrons (black dotted lines), and bulk electrons (solid black lines). . . . .	33
3.6	The stages of fracture leading to electron emission and Si(111)-2×1 surface reconstruction: (a) a tensile load is applied, (b) shuffle plane $\sigma$ -bonds break, usually homolytically, but heterolytic cleavage is energetically possible, (c) the new surface relaxes, (d) a surface electron attempts to pair with an adjacent anion, (e) the resulting spin clash causes an electron to ionize and detach from the surface. (e) a {111} surface showing a 1×1 unit cell (shaded in gray) and a 2×1 surface dimer (shaded in pink with a dashed line representing the surface dimer bond). . . . .	34
3.7	(a) The total energy of the same group of electrons as Figure 3.5. (b) The kinetic energy of said group of electrons. . . . .	35
3.8	The evolution of electrostatic potential calculated on a grid is given at (a) 0 ps, (b) 9 ps, and (c) 15 ps. Warm colors denote positive potential and cool colors signify negative potential. The crack edges are given by solid black lines and the midline of the crack is provided in red. . . . .	35
3.9	(a) The electric current velocity correlation functions for the {111} system at equilibrium (red) and after a crack has occurred (blue). (b) The ionized electron yield along the crack trajectory for the {111} and {100} models. . . . .	37
4.1	Three views of orthorhombic polyethylene with electrons. . . . .	44

4.2	(a) The principal Rankine-Hugoniot for PE. Experimental data from the LASL shock compression handbook [17] and Nellis [18] is provided along with data for the classical MD potentials, OPLS [4], and AIREBO [4], a reactive force field, ReaxFF [4], and quantum mechanical approaches, DFT/AM05 and tight binding [19], for comparison. (b) An expansion of the low compression region of the Hugoniot. . . . .	47
4.3	(a) The pressure-temperature locus of the Hugoniot curve for the eFF, DFT/AM05, OPLS, AIREBO, and ReaxFF methods. (b) The pressure-temperature seam at greater pressures. . . . .	47
4.4	The temperature-density plane of the principal Hugoniot for the eFF (black circles) and DFT/AM05 (open green diamonds) methods. . . . .	48
4.5	Radial distribution functions for (a) C-C atom pairs, (b) C-H pairs, and (c) H-H pairs. The corresponding coordination number functions for (d) C-C pairs, (e) C-H pairs, and (f) H-H pairs. . . . .	49
4.6	Structural decomposition along the PE Hugoniot. The open black circles and open green diamonds correspond to the % intact C-C backbone for the eFF and DFT/AM05 simulations, respectively. The red circles are the average % ionization along the Hugoniot calculated from the eFF simulations. . . . .	50
4.7	(a) The direct current electrical conductivity plotted against temperature and (b) plotted along the eFF Hugoniot curve (black circles). The blue diamonds are finite temperature DFT data points for PE in the warm dense matter regime [1]. . . . .	51
5.1	The construction of core pseudoparticles from all-electron atoms: aluminum (left) and silicon (right). The $2sp^3$ core electrons are visible as tan nested tetrahedra. . . . .	56
5.2	Single processor performance for bulk silicon: (a) The cpu time (in seconds) per timestep. (b) The cpu time per timestep per particle (includes nuclei and electrons). Run on a Linux CentOS 4.5/RHEL 4 system with 2.33 GHz Dual Quad Core Intel Xeon processors. . . . .	62
5.3	Conservation of energy during NVE dynamics. . . . .	63

5.4	Comparisons of (a) internuclear distances and (b) angles between eFF1, eFFcore, and B3LYP/6-31g** reference values for a variety of silicon hydrides and saturated silylhydrocarbons. . . . .	64
5.5	A galley of primary, secondary, tertiary, and quaternary substituted silicon hydrides. Structures from effcore (red) are overlaid with those from B3LYP/6-31g** (blue). . .	66
5.6	(a) Cohesive energy curves for silicon diamond (A4). (b) The energy of $\beta$ -Sn silicon (A5) relative to the A4-silicon with QM values from [11]. . . . .	67
5.7	eFF homolytic bond dissociation energies versus reference QM or experimental data (values closer to the line are better). See Table 5.5 for the bonds and references. . . .	68
5.8	The energies (eV) of reactive SiH <sub>3</sub> species. B3LYP/6-311g**++ values are in parenthesis. 70	70
5.9	Si(111)-7 $\times$ 7 reconstruction intermediates. The das3 $\times$ 3 and das7 $\times$ 7 structures are actually rectangular 2 $\times$ 1 projections extracted from 2 $\times$ 2 supercells of the reconstruction models. T <sub>4</sub> adatoms are colored blue, fourth-layer dangling bond atoms are colored orange, dimer atoms are green, and second layer dangling bond atoms are colored magenta. In the das3 $\times$ 3 structure the 12 member ring hole is highlighted with red circles. . . . .	72
5.10	The bond energies of Al <sub>n</sub> H <sub>3n</sub> clusters [eV]. QM from [28] . . . . .	75
5.11	fcc-Al bulk cohesive energy curves. DFT/LDA from [29] . . . . .	76
A.1	Pathways for methane C-H activation using Rh(I) (red) and Rh(III) (blue) in solvent, X. 84	84
A.2	Methane activation catalytic cycles from Rh(III) in water at pH = 0. . . . .	86
A.3	C-H activation <i>via</i> Rh(I) in pH = 0 water. . . . .	88
A.4	The Rh(III) C-H activation catalytic cycle in pH = -7 TFAH. . . . .	89
A.5	The Rh(I) C-H activation catalytic cycle in pH = -7 TFAH. . . . .	91
A.6	Three derivatives of PNP (from left to right): PNP, PNP <sup>CF<sub>3</sub></sup> , and PNP <sup>C<sub>6</sub>H<sub>5</sub>6</sup> , and the Rh(I) and Rh(III) C-H activation pathway. . . . .	92
A.7	Derivatives of the CNC ligand and the Rh(III) C-H activation pathway. . . . .	93

B.1	The experimental absorption spectra (left) and combined absorption-emission spectra (right) of 1NpPt and 2NpPt. . . . .	100
B.2	The subjects of this study: (C <sup>∧</sup> N)Pt(II)(acac). C <sup>∧</sup> N = 1Np, 2Np, bzq, and ppy. . . .	101
B.3	A conceptualization of two intersecting excited state manifolds and the seam, <i>s</i> (green curve), orthogonal to the crossing coordinate, <i>h</i> . . . . .	104
B.4	The highest occupied and lowest unoccupied orbitals of the S0 optimized geometries for 1NpPt, 2NpPt, bzqPt, and ppyPt. . . . .	109
B.5	Overlays of groundstate S0 stationary points (blue) and the S1-T1 minimum energy crossing point geometries (red) for 1NpPt, 2NpPt, bzqPt, and ppyPt. . . . .	112

# List of Tables

1.1	Extreme conditions . . . . .	1
3.1	Comparison of experimental and computed mechanical values: Young's modulus, $E$ , yield strength, Griffith critical load, $G_c$ , and the stress intensity factor, $K_{Ic}$ . References are in square brackets. . . . .	28
5.1	Parameter fits . . . . .	62
5.2	Small molecule bond lengths . . . . .	65
5.3	Small molecule angles . . . . .	65
5.4	Emergent material properties. *Calculated from the linear elastic relationship $G = 9B_0E/9B_0 - E$ . † from reference [13]. . . . .	67
5.5	Calculated bond dissociation energies (kcal/mol) . . . . .	69
5.6	Ring strain of various $\text{Si}_6\text{H}_{12}$ conformers (kcal/mol) . . . . .	70
5.7	The energies of $\text{Si}(111)$ - $7\times 7$ reconstruction intermediates relative to the unrelaxed surface energy [eV] . . . . .	73
5.8	Aluminum hydride geometric values ( $\text{\AA}$ and degrees) . . . . .	75
A.1	Gibbs free energies (kcal/mol) along the reaction coordinate defined in figure A.6. . .	92
A.2	Gibbs free energies (kcal/mol) along the reaction coordinate defined in Figure A.7. . .	93
B.1	The experimental and computed absorption spectra and oscillator strengths, $f$ , of $1\text{NpPt}$ , $2\text{NpPt}$ , $\text{ppyPt}$ , and $\text{bzqPt}$ . . . . .	107
B.2	Transition dipole moments (Debye) from the TD-DFT calculations . . . . .	108

B.3	CASSCF(18,12) vertical excitation energies (nm) . . . . .	108
B.4	CASSCF state energies (eV) relative to the T1 state at the T1 minima . . . . .	110
B.5	CASSCF spin orbit coupling constants $\hat{H}_{so}$ ( $\text{cm}^{-1}$ ) and transition moments $\mu_{el}$ (Debye) for states at the T1 minima and S1-T1 minimum energy crossing point . . . . .	110
B.6	The calculated rates and lifetimes for fluorescence and phosphorescence and the exper- imental phosphorescence rates and lifetimes . . . . .	111
B.7	Landau-Zener hopping probabilities, intersystem crossing rates ( $\text{s}^{-1}$ ), and lifetimes (s)	113
C.1	Experimental crack tip velocities versus reduced critical energy release rates for $\{111\}\langle 112 \rangle$ fracture. The references for this data are provided in Chapter 3 . . . . .	118
C.2	Computed eFF crack tip velocities versus reduced critical energy release rates . . . . .	119
C.3	Computed ReaxFF crack tip velocities versus reduced critical energy release rates . . . . .	120
C.4	Computed Stillinger-Weber crack tip velocities versus reduced critical energy release rates . . . . .	120
C.5	Computed multi scale-method crack tip velocities versus reduced critical energy release rates . . . . .	121
C.6	eFF Hugoniot equation of state data for polyethylene . . . . .	121

# Chapter 1

## Matter in Extreme Environments

### 1.1 Extreme Chemistry

The mid-twentieth century was host to a flurry of technological advancements that thrust humans from an age of low-energy-density chemistry, classical electromagnetic physics, and subsonic transportation into the age of high-energy materials, nuclear physics, amplified light, hypersonic travel, space exploration, and advanced microdevices. These advancements either produce extreme conditions or the technologies are exposed to these conditions in their operating environments. Consequently, characterizing extreme conditions and understanding their effects on materials is critical to enabling the next generation of technologies.

Property	Range
Temperature	> 1000 K
Pressure	> 30 MPa
Strain Rate	> 1 km/s
Radiative flux	> 100 dpa
EM field	> 15 T

Table 1.1: Extreme conditions

Table 1.1 contains our definitions of extreme conditions. Practical examples of extreme conditions can be found readily. For example, the fourth generation of nuclear reactors includes supercritical-water-cooled reactors that operate near the thermodynamic critical point of water. Conditions within the reactor will reach 1000 °C with neutron fluxes being increased by an order of magnitude.<sup>1</sup> At this temperature water itself is corrosive, and the pressure of the steam imparts a high mechanical load

<sup>1</sup>Office of Science, U.S. Department of Energy: Basic research needs for materials under extreme conditions. 2008.

on the reactor piping. The neutron flux causes material damage at the atomistic scale through heat transfer, momentum transfer, and nuclear activation. Supercritical steam technology can also be found in modern coal-fired power plants. Using supercritical steam raises the operating temperature from 540 °C to 760 °C and more than doubles the pressure to 37.9 MPa. These conditions improve the thermal efficiency of the plant to 60% from the typical 35% of current plants.<sup>2</sup> The transportation sector is also affected by extreme operating environments. The NASA X-43A scramjet aircraft is capable of airspeeds in excess of 3 km/s.<sup>3</sup> At these speeds the mechanical loads on the airframe, skin, and wing spars are high, and the structural materials must withstand these high stresses over the aircraft's operational lifetime. In outer space, the Cassini-Huygens space probe was briefly clocked at 44 km/s.<sup>4</sup> Small molecule impacts from space debris above 10 km/s can cause chemical changes at the atomistic scale like pitting, melting, and fracture. Above 15 km/s the energy imparted by the impact can cause complete material failure, ionization, plasma formation, and spallation. As aircraft and spaceships continue to increase their cruising speeds, they will need improved material shielding to protect passengers, avionics, and power plants from particulate impacts and convective and radiative gas flow conditions during hypervelocity flight.

The common thread among these examples is that the result of being exposed to extreme conditions is premature material aging. High temperatures, either due to external heating, or in response to a shock pressure, increase the rates of chemical reactions and this can lead to undesirable chemical transformations and bond breaking. Mechanical loading can initiate or propagate material defects which can also lead to failure. High radiative or particle fluxes embrittle materials. There are numerous examples of current applications that require materials to withstand extreme conditions, and the number is certain to grow with time. The demands on these materials require that we study and understand material properties under extreme conditions.

Studying the response of materials in extreme conditions is complicated because in these high

---

<sup>2</sup>Idaho National Laboratory: Current research in nuclear energy. <http://inlportal.inl.gov/portal/server.pt/community/nuclearenergy/277>. 2010.

<sup>3</sup>National Aeronautics and Space Administration: X-43A Research Aircraft. <http://www.nasa.gov/missions/research/x43-main.html>. 2010.

<sup>4</sup>Jet Propulsion Laboratory, California Institute of Technology: Cassini Equinox Mission. <http://saturn.jpl.nasa.gov/faq/FAQgeneral/>. 2010.

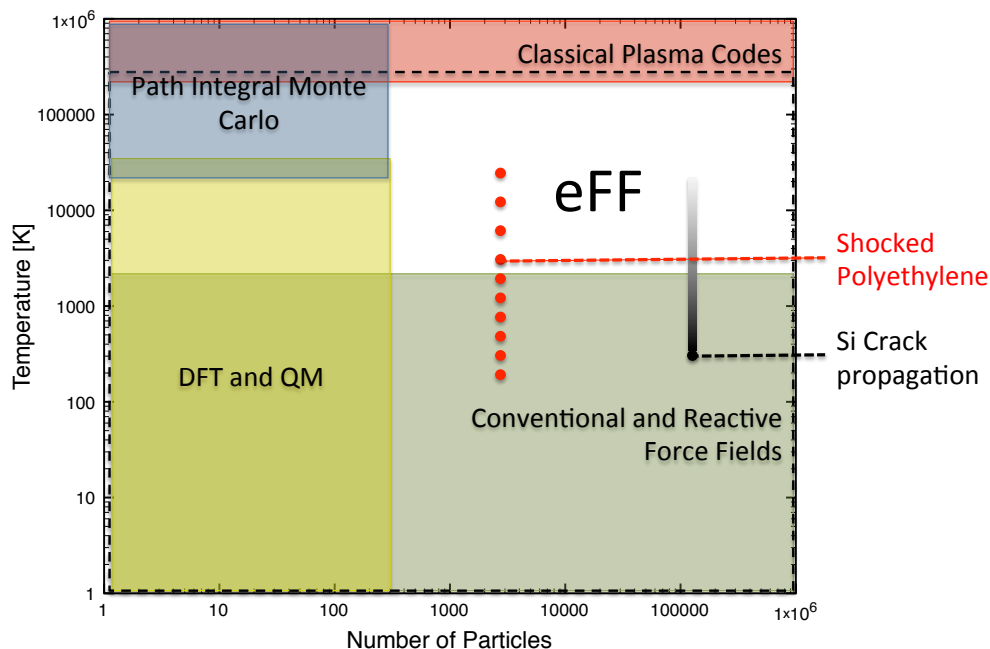


Figure 1.1: Domains of practical use for various theories. eFF is able to model systems within the dashed box. The scope of the conditions for the two major studies presented in this thesis are plotted for reference.

energy regimes chemicals and materials are excited out of their ground state. Density functional theory and other *ab initio* quantum mechanical techniques provide excellent descriptions of matter at low temperature and pressure, but these methods are limited to hundred of particles. Forcefield-based methods are capable of modeling a wide variety systems and forcefields can treat systems with millions of atoms, but because they are parameterized based on Born-Oppenheimer QM potential energy surfaces, they are also limited to low temperature and pressure. Classical plasma theories provide good descriptions of matter at high temperatures and, like forcefields, they can treat millions of particles. There exists a “computational no-man’s land” between these thermodynamic regimes that remains a challenge to theorists. The electron force field (eFF) was developed to bridge this gap and provide good descriptions of matter near its ground state *and* in highly excited states. The body of this thesis contains a compilation of eFF electron dynamics studies of materials being subjected to extreme environments.

## 1.2 This Thesis

The research presented in this thesis was performed in support of the California Institute of Technology's Predictive Science Academic Alliance Project (PSAAP). PSAAP is a National Nuclear Security Administration applied research collaboration between several groups at Caltech. The overarching objective is to understand the multi-scale physics that accompany the hypervelocity impact of metallic and polymer-based impactors and targets. Melting, vaporization, dissociation, ionization, plasma formation, luminescence, radiative transport, high-strain-rate deformation, fracture, fragmentation, spall and ejecta, shear banding, and hydrodynamic instabilities are all expected to complicate the application of modeling and theory. Atomistic studies of these phenomenon are intended to provide material equation of state data and other material properties to larger-scale constitutive engineering models. Ultimately the combined experimental and theoretical data inputs are used to drive uncertainty quantification and verification and validation calculations so that failure probabilities can be provided.

The body of this thesis contains eFF studies of important materials like crystalline silicon and polyethylene being subjected to extreme conditions. Chapter 2 provides a detailed description of the eFF method and clarifications for the way in which properties like temperature and pressure are computed from eFF simulations. The electronic response of silicon to high-strain rate fracture is examined in Chapter 3. In Chapter 4, the material and electronic responses of polyethylene to shock-induced pressure and heating are examined. In both of these studies eFF's ability to model the ground and excited state dynamics of electrons is advantageously used to characterize the material response to extreme conditions in ways that no other method can. Chapter 5 introduces a unique core-approximation for eFF and provides validations for silicon and aluminum; this core-approximation enabled the nanometer scale investigation of silicon fracture in Chapter 3.

The appendices contain published and unpublished but complete research projects involving *ab initio* and density functional theory studies of organometallic complexes. Appendix A is a study of rhodium-catalyzed methane C-H bond activation chemistry. Appendix B is a study of cyclometalated platinum phosphorescing complexes wherein the excited state manifolds of several complexes are

explored. The spin-orbit coupling between states and their potential energy surface topologies are used to compute the rates for fluorescence, phosphorescence, and intersystem crossing. Appendix C contains tables of raw data and the xyz coordinates of important molecular geometries. Appendix D is a compendium of published works containing a fundamental study of the  $\beta$ -hydride elimination mechanism for Wacker cycle-like substrates, and the publications corresponding to Chapters 3 and 4.

## Chapter 2

# The Electron Force Field Method

### 2.1 Simulating Excited State Dynamics

The electron forcefield was developed by Su and Goddard and officially released in 2007 [1]. eFF is a reactive forcefield method, though it has been described by the terms wave packet molecular dynamics, approximate quantum dynamics, quantum electron dynamics, semiclassical molecular dynamics, electron molecular dynamics, and electron dynamics. If these descriptions are ambiguous, then understand that at the very least eFF is unique. This is because eFF was developed with modeling matter under extreme conditions in mind. Figure 2.1 demonstrates eFF's ability to model systems in their ground state and in increasingly energetic states. Since eFF is the method used in Chapters 3, 4, and 5, the physics behind eFF will be described in detail in the following sections.

#### 2.1.1 Modeling Excited States is Challenging for Theorists

Quantum mechanics allows theoretical chemists to understand the details of chemical transformations in the gas, liquid, and solid phases for systems in their ground states or lowly excited states. Unfortunately these methods, while accurate, are inefficient for studying the dynamics of materials under extreme conditions because propagating the Schrödinger equation for large systems when many electronic states are present or for many time steps is computationally expensive. eFF allows us to parametrize the electron wavefunction so that we may quickly evaluate system energies and forces. When used with wave packet molecular dynamics, eFF allows for practical simulations of

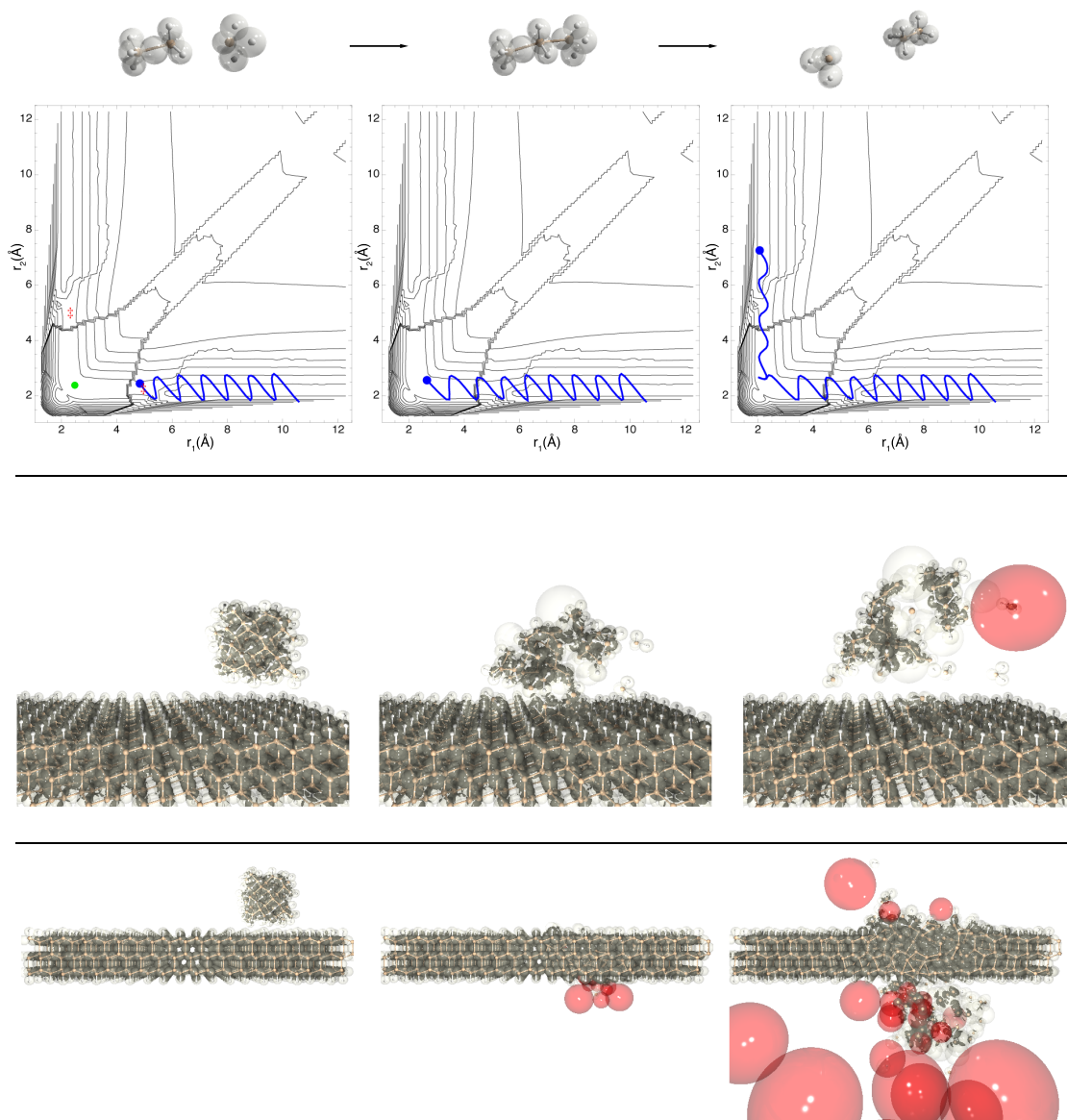


Figure 2.1: A gallery of snapshots from toy calculations to demonstrate eFF capabilities. Top: a vibrationally excited “walker” on the  $\text{H}_3\text{Si}-\text{SiH}_3 \cdots \text{SiH}_3^-$   $S_{\text{N}}2$  potential energy surface. The transition states are marked with red ‡ symbols and the surface minima is marked with a green dot. Middle: A silicon particle colliding with and rebounding from a silicon {111} surface at 5 km/s. Bottom: The same silicon particle colliding with and penetrating the surface at 20 km/s. Ionized electrons are colored red.

large systems in their excited states.

What makes modeling high energy condensed matter so difficult is the breakdown of the Born-Oppenheimer approximation. When the system energy is high, the kinetic energy of electrons is on the order of individual Coulomb interactions with nuclei. In such excited systems the density of states and number of curve crossings are high, so a wavefunction based on the superposition of stationary states is poor. In this phase space electronic motions are decoupled from nuclear motions and we can consider electron motions to be nonadiabatic. In other words, the system does not satisfy the assumptions of the Born-Oppenheimer approximation because small variations of the geometry cause electronic state switching. When the density of states is sufficiently high we can model nuclear motions classically as moving through a “mean field” of electronic states [2]. The trick then is to treat nonadiabaticity and the electronic structure which must necessarily involve a superposition of adiabatic states. The goal of eFF is to provide nonadiabatic couplings and gradients for excited electronic states.

### 2.1.2 Traditional Molecular Dynamics Techniques

eFF is the latest development in a series of approximate quantum dynamics methods. Following the establishment of molecular quantum theory [2–4], researchers shifted their efforts to simulating the motions of systems of molecules. In truth, molecular dynamics methods evolved in concert with *ab initio* techniques for static systems in their ground state. Ground state systems are well behaved, and their nuclei lie on adiabatic potential energy surfaces. Small nuclear motions produce small changes in energy. Because electrons are so much lighter than nuclei, we can assume that for systems near their ground state, electrons instantaneously react to nuclear motions [5]. This assumption is called the Born-Oppenheimer approximation and for the majority of earthly chemical systems it holds true. The Born-Oppenheimer approximation allows theorists to propagate systems forward in time using the time-independent Schrödinger equation [2]. The energy of the system is

evaluated based on the nuclear coordinates,  $\mathbf{R}$ :

$$\hat{H}(\mathbf{R})\psi(\mathbf{r}) = E(\mathbf{R})\psi(\mathbf{r}). \quad (2.1)$$

The forces on each nuclei are computed using the Hellman-Feynman theorem [6–8], and integration of these forces provides new positions and velocities. The procedure is repeated to propagate a system forward in time. This procedure, called Born-Oppenheimer quantum molecular dynamics (BOQMD) [9], is accurate but slow, and it’s only valid for purely adiabatic systems. Other *ab initio* molecular dynamics techniques enjoy substantial speed-ups by only partially converging the wavefunction [10], or by using fast density functionals [11]. Despite these advances, *ab initio* MD methods are still limited to hundreds of atoms over few picoseconds.

In order to extend the scope of molecular dynamics methods to larger systems and timescales, classical forcefields were developed. Theorists fit the coefficients of standard energy expressions to the results of static quantum calculations. These expressions, and their gradients, are called forcefields. The energy expressions used in forcefields are physically motivated and a typical total energy expression includes pairwise bonding terms, electrostatic terms, van der Waals interactions, and multi-center angle and dihedral terms, all of which are functions of nuclear coordinates,  $\mathbf{R}$ :

$$E_{total}(\mathbf{R}) = \sum_{i<j} E_{bond}(R_{ij}) + \sum_{ijk} E_{angle}(\theta_{ijk}) + \sum_{ijkl} E_{dihedral}(\phi_{ijkl}) + \sum_{i<j} \frac{q_i q_j}{R_{ij}} + \sum_{ij} E_{vdW}(R_{ij}). \quad (2.2)$$

Bonds are fit to bonding potentials like the Lennard-Jones or exp-6 potentials, angles are fit to harmonic potentials, and dihedral angles are fit to periodic potentials. More sophisticated components of (2.2), like the van de Waals expression, and other terms, like hydrogen bonding and polarizable atomic charges, can be included, and these expressions are fit to QM data. Forcefields have become popular methods for studying proteins [12–14], bulk liquids and solids [15, 16], and polymers [17]. While these methods offer orders of magnitude improvement in computational efficiency and scale over BOQMD methods, they require that the system stay close to its initial bonding configuration.

So what happens if a chemical system is sufficiently excited to cause bonds to break? What

if chemistry happens? The next generation of forcefields addresses this issue by eschewing fixed bonds in favor of bond orders [18–20], or by considering only the most important valence bond configurations and parametrizing energy expressions based on those [21]. These so-called reactive forcefields allow theorists to study systems in flux, and they are gaining traction in the chemical, materials, and solid-state physics communities.

The quantum, classical, and reactive forcefield techniques described here share their reliance on the Born-Oppenheimer approximation. The evolution of classical and reactive forcefields increased the variety and size of the systems that could be studied with molecular dynamics, however the issues raised in Sections 2.1 and 2.1.1 still remain. What happens when a chemical system is excited by a photon, heated to thousands of degrees, shock compressed, exposed to a strong electrical potential, or bombarded by other chemicals at high velocities? In these environments the Born-Oppenheimer approximation may not be valid and to study these systems Fermion molecular dynamics techniques have been developed.

### 2.1.3 Precursors to eFF

The inspiration for the eFF wavefunction came from early floating spherical Gaussian orbital (FSGO) methods [1]. FSGO methods, developed by Frost in the 1960s, are *ab initio* methods wherein each electron is described by a single floating spherical Gaussian orbital, rather than a basis of nuclei-centered linear combination of Gaussian orbitals or nuclei-centered Slater functions [22]. Frost’s FSGO wavefunctions are Slater determinants of FSGOs and he evaluates the electronic energy by a version of the Roothaan equations generalized to nonorthogonal orbitals [22, 23]. Because the method involves two-electron integral transformations it scales like Hartree-Fock methods,  $\mathcal{O}(N^4)$  [24]. The FSGO method gave reasonably good geometries for first-row hydrides and small iso-electronic species [25, 26], though early versions failed to produce stable triplet species or good geometries for higher valence species like  $\text{BeH}_2$ ,  $\text{CH}_4$ ,  $\text{H}_2\text{O}$ , and others [22, 26]. By employing linear combinations of concentric FSGOs, the method was able to capture most of the Hartree-Fock energy [27, 28]. Later versions corrected earlier issues and achieved particularly good geometries

for saturated hydrocarbons [29]. Eventually pseudopotential methods were added and this enabled faster and more accurate calculations on hydrocarbons and heavy group IV atoms like silicon and germanium [30–33]. FSGO methods evidently gained traction and were applied to polymers [34], and the prediction of photoelectron spectra of hydrocarbons [35], though this was during a time when computational power was low, and presumably Hartree-Fock methods were too expensive to treat these systems. Most recently, the approach was coupled to diffusion Monte-Carlo simulations of lithium hydride [36]. These techniques demonstrate that one function per electron basis sets, if implemented correctly, can provide reasonably good structures and energies for simple molecules.

Recognizing that the computational bottleneck in FSGO calculations is the computation of the antisymmetrization energy, researchers devised a means to estimate it by developing so-called Pauli potentials. By devising a pairwise function that mimics the antisymmetrization energy they could reduce the scaling to  $\mathcal{O}(N^2)$  and still adhere to the Pauli principle. These potentials limit same-spin electrons to regions of phase-space so that the electrons cannot occupy the same position or momentum, thereby mimicking orbital orthogonality [37–40]. Kirschbaum’s potential successfully reproduced the shell structure of atoms up to  $Z = 94$  [41], but none of the potentials cited in the previous line produce stable bonds for  $Z > 3$ . Other groups used a wavefunction orthogonality approach to derive their Pauli potentials. In these approaches an analytic form for the kinetic energy difference between a fully antisymmetrized wavefunction and a non-orthogonalized wavefunction is derived [42, 43]. The latter approach is the basis for the eFF Pauli potential.

The origin of the dynamics engine behind eFF can be traced back to the wave packet molecular dynamics (WPMD) techniques developed in the 1970s [1]. Heller and coworkers proved that wavefunctions of heavy particles may be decomposed into time-dependent wave packets which then follow nearly classical trajectories [44–46]. The details of Heller’s WPMD method will be discussed in Section 2.3. Using WPMD, several groups devised methods to propagate quantum wave packets in time. In these methods nuclei are treated classically and electrons are treated quantum-mechanically. Electrons are typically treated as Gaussian functions with variable positions and width [43, 47], fully antisymmetrized Slater sums of periodic Gaussian wave packets [48, 49], or antisymmetric products

of localized Gaussian functions [40]. The trade-off in these methods is in managing electron correlation. The fully antisymmetric approaches capture the indistinguishability of electrons at the cost of computational efficiency. As you shall see, abandoning rigorous antisymmetrization in favor of a pairwise spin-dependent repulsion potential captures most of the exchange correlation energy while enabling a substantially faster calculation [50, 51]. Though these methods are *ab initio*, the emphasis is on qualitatively describing the dynamics of the system rather than obtaining quantitatively correct values for bond energies or the electronic structure of the matter in question. WPMD techniques have proven particularly useful for modeling the dynamics of systems in extreme environments like plasmas [43, 52], laser-shocked deuterium [48] and hydrogen in the warm dense matter regime [49, 50] because in these techniques the electrons can evolve independently of the nuclei.

## 2.2 The eFF Wavefunction and Forcefield

eFF overcomes the difficulties of modeling potentially nonadiabatic systems by evaluating the energy of the system as a function of the nuclear coordinates *and* electron coordinates with a small set of universal electron parameters. This ensures that energy may be partitioned separately into nuclear and electronic degrees of freedom. Consequently electrons may hop between states without concomitant nuclear motion. In eFF nuclei are described with classical point particles and electrons are described by a wavefunction of floating spherical Gaussian orbitals. The N-electron wavefunction is actually a Hartree product of floating spherical Gaussian wave packets whose size and positions are dynamical variables:

$$\Psi \propto \prod_j \exp\left[-\left(\frac{1}{s^2} - \frac{2p_s}{s}i\right)(\mathbf{r} - \mathbf{x})^2\right] \cdot \exp[i\mathbf{p}_\mathbf{x} \cdot \mathbf{x}] \quad (2.3)$$

with positions  $\mathbf{x}$ , translational momenta  $\mathbf{p}_\mathbf{x}$ , radial size  $s$ , and radial momental  $p_s$ .

The full potential energy expression is the sum of standard electrostatic interactions between nuclei ( $E_{NN}$ ), electrons ( $E_{ee}$ ), and nuclei and electrons ( $E_{Ne}$ ). Also included in this sum are two quantum mechanical terms: the total electronic kinetic energy ( $E_{ke}$ ), and the two-electron spin-

dependent Pauli repulsion energy ( $E_{Pauli}$ ):

$$U(R, r, S, s) = E_{NN}(R) + E_{Ne}(R, r, s) + E_{ee}(r, s) + E_{ke}(s) + E_{Pauli}(\uparrow\downarrow, S). \quad (2.4)$$

$R$  and  $r$  are the nuclear and electron positions,  $s$  is the electron Gaussian radius,  $\uparrow\downarrow$  is the spin state of the electrons, and  $S$  is the overlap integral of the electrons. Energy evaluations using the Hartree product only require  $\mathcal{O}(N^2)$  operations, a significant advantage over a fully antisymmetrized wavefunction. This scaling advantage is achieved by avoiding the costly calculation of four-center exchange integrals. However, using a Hartree product wavefunction violates the antisymmetry principle for Fermions. In order to satisfy the Pauli principle, and to account for the missing orthogonality that the antisymmetrizer would impose, a spin-dependent correction term,  $E_{Pauli}$  is added. The derivation of the Pauli potential will be given shortly.

The electrostatic interaction energies are defined by Coulomb interactions between point charges and Gaussian charge distributions. Of course nuclei-nuclei interactions are purely classical. They are defined as follows:

$$E_{nuc-nuc} = \frac{1}{4\pi\epsilon_0} \sum_{i<j} \frac{Z_i Z_j}{R_{ij}} \quad (2.5)$$

$$E_{nuc-elec} = -\frac{1}{4\pi\epsilon_0} \sum_{i,j} \frac{Z_j}{R_{ij}} \text{Erf} \left[ \frac{\sqrt{2}R_{ij}}{s_i} \right] \quad (2.6)$$

$$E_{elec-elec} = \frac{1}{4\pi\epsilon_0} \sum_{i<j} \frac{1}{x_{ij}} \text{Erf} \left[ \frac{\sqrt{2}x_{ij}}{\sqrt{s_i^2 + s_j^2}} \right] \quad (2.7)$$

where  $i$  and  $j$  are particle indices,  $Z$  are the particle charges,  $R_{ij}$  are internuclear distances,  $r_{ij}$  are interelectron distances, and  $s$  are the electron radii. The error functions in (2.6) and (2.7) arise from the fact that the electron charges are ‘‘smeared’’ over the volume of the Gaussian sphere. Recall that an error function is defined as the integral over a Gaussian and its argument is the upper limit of the integral. This formulation of the Coulomb interactions ensures that the finite sized spherical Gaussians act like point charges at large distances from the other interacting particle.

The full Hamiltonian in equation (2.4) includes two quantum mechanical terms: the electronic

kinetic energy and the Pauli repulsion energy.

$$E_{ke} = \frac{\hbar^2}{2m_e} \sum_i \int_{-\infty}^{\infty} |\nabla\psi_i|^2 dV = \frac{\hbar^2}{m_e} \sum_i \frac{3}{2} \frac{1}{s_i^2}. \quad (2.8)$$

Equation (2.8) describes the electronic kinetic energy, which should not be confused with the translational kinetic energy of the electron. (2.8) can be better understood in terms of the Heisenberg uncertainty principle. Consider a highly localized electron:  $\Delta x$  is small, and according to the uncertainty principle  $\Delta p$  must be large to compensate. This higher momentum spread corresponds to higher kinetic energy and this is reflected in the form of (2.8). The second quantum mechanical term is the Pauli repulsion energy for same spin and opposite spin electrons, respectively:

$$E_{Pauli} = \sum_{\sigma_i=\sigma_j} E(\uparrow\uparrow)_{ij} + \sum_{\sigma_i\neq\sigma_j} E(\uparrow\downarrow)_{ij}. \quad (2.9)$$

Here  $\sigma_{i,j}$  refers to the spin state of the electrons being evaluated. The same spin Pauli energy function is defined as

$$E(\uparrow\uparrow)_{ij} = \left( \frac{S_{ij}^2}{1 - S_{ij}^2} + (1 - \rho) \frac{S_{ij}^2}{1 + S_{ij}^2} \right) \Delta T_{ij}, \quad (2.10)$$

and the opposite spin Pauli energy is

$$E(\uparrow\downarrow)_{ij} = \left( \frac{(1 - \rho)S_{ij}^2}{1 + S_{ij}^2} \right) \Delta T_{ij}. \quad (2.11)$$

In (2.10) and (2.11),  $\Delta T$  is the kinetic energy change upon antisymmetrization and  $S$  is the overlap of the wavepackets. We can further define these two terms:

$$\Delta T_{ij} = \frac{3}{2} \left( \frac{1}{\bar{s}_i^2} + \frac{1}{\bar{s}_j^2} \right) - \frac{2(3(\bar{s}_i^2 + \bar{s}_j^2) - 2\bar{x}_{ij}^2)}{(\bar{s}_i^2 + \bar{s}_j^2)^2} \quad (2.12)$$

$$S_{ij} = \left( \frac{2}{\bar{s}_i^2/\bar{s}_j^2 + \bar{s}_i^2/\bar{s}_i^2} \right)^{3/2} \exp(-\bar{x}_{ij}^2/(\bar{s}_i^2 + \bar{s}_j^2)). \quad (2.13)$$

The last two equations contain the only empirical parameterizations in eFF:  $\rho = -0.2$ ,  $\bar{x}_{ij} =$

$x_{ij} \cdot 1.125$ , and  $\bar{s}_i = s_i \cdot 0.9$ . These parameters were fit using a small set of hydrocarbons and light metal hydrides [1].  $\rho$  can be thought of as an orthogonalization parameter while  $\bar{x}$  and  $\bar{s}$  are distance and size scaling parameters, respectively.

The Pauli energy functions in (2.10) and (2.11) are derived by taking the kinetic energy differences of orthogonalized and non-orthogonalized wavefunctions. The full derivation of (2.10) and (2.11) makes it easy to understand why eFF improves on bond energies and structures for more complicated molecules, so a brief derivation will be provided here. Consider a proper fully antisymmetrized wavefunction,  $\Psi_{\text{Slater}}$ , and a Hartree product wavefunction,  $\Psi_{\text{Hartree}}$ , for two same-spin electrons:

$$\Psi_{\text{Slater}} = \frac{1}{\sqrt{2 - S^2}} (\phi_1(r_1)\phi_2(r_2) - \phi_2(r_1)\phi_1(r_2)) \quad (2.14)$$

$$\Psi_{\text{Hartree}} = \phi_1(r_1)\phi_2(r_2). \quad (2.15)$$

$S = \int \phi_i \phi_j dV$  is simply the normalization coefficient. The Pauli energy is estimated to be the *ungerade* energy difference between the Slater and Hartree wavefunction kinetic energies:

$$E_u = \langle \Psi_{\text{Slater}} | -\frac{1}{2} \nabla^2 | \Psi_{\text{Slater}} \rangle - \langle \Psi_{\text{Hartree}} | -\frac{1}{2} \nabla^2 | \Psi_{\text{Hartree}} \rangle = \frac{S^2}{1 - S^2} \left( t_{11} + t_{22} - \frac{2t_{12}}{S} \right) \quad (2.16)$$

where  $t_{ij} = \langle \psi_i | -\frac{1}{2} \nabla^2 | \psi_j \rangle$ . Klakow assumed that  $E(\uparrow\uparrow) = E_u$  and  $E(\uparrow\downarrow) = 0$ , and the result is a Pauli potential that fails to produce stable structures or correct bond energies for anything larger than lithium. eFF uses the more chemically relevant valence bond wavefunction in place of the Slater determinant to obtain  $E(\uparrow\downarrow)$ :

$$\Psi_{\text{VB}} = \frac{1}{\sqrt{2 + 2S^2}} (\phi_1(r_1)\phi_2(r_2) + \phi_2(r_1)\phi_1(r_2)). \quad (2.17)$$

The *gerade* energy expression is computed from the VB wavefunction:

$$E_g = \langle \Psi_{\text{VB}} | -\frac{1}{2} \nabla^2 | \Psi_{\text{VB}} \rangle - \langle \Psi_{\text{Hartree}} | -\frac{1}{2} \nabla^2 | \Psi_{\text{Hartree}} \rangle = \frac{S^2}{1 + S^2} \left( t_{11} + t_{22} - \frac{2t_{12}}{S} \right). \quad (2.18)$$

The final same-spin and opposite-spin Pauli energy terms in (2.9) are obtained by mixing the *gerade* and *ungerade* expressions together:

$$E(\uparrow\uparrow) = E_u - (1 - \rho)E_g \quad (2.19)$$

$$E(\uparrow\downarrow) = -\rho E_g. \quad (2.20)$$

From these two equations it is evident that the purpose of the *gerade* energy expression is to make the same-spin and opposite-spin Pauli potentials more repulsive. Ironically, greater repulsion between electrons improves eFF's ability to describe bonds, compared to earlier methods where the tendency of electrons to coalesce was high. The expressions in equations (2.10) and (2.11) can be obtained by substituting a general FSGO into (2.19) and (2.20). The purpose and action of the Pauli potential can be more easily understood in terms of orthogonal orbitals. When two same-spin electrons approach one another, their wavefunctions increase in slope to decrease their overlap (they compress in width). This increase in slope increases their gradient and kinetic energy is increased. Wilson and Goddard interpret this change in energy as the Pauli repulsion energy [53]. (2.9) recovers this energy and ensures that eFF electrons satisfy the Pauli exclusion principle.

## 2.3 Wave Packet Molecular Dynamics

In 1975 Heller demonstrated wavepacket molecular dynamics (WPMD) as a method for simulating systems in a semi-classical manner [44]. Rather than making a WKB approximation, wherein one assumes that  $\hbar$  is very small [54, 55], he approximated that the wavepacket exists in a local harmonic potential. By substituting a wavefunction of the type in (2.3) into the time-dependent Schrödinger equation with a harmonic potential, Heller derived the Hamilton equations of motion:

$$\mathbf{p}_x = m\dot{\mathbf{x}} \quad \dot{\mathbf{p}}_x = -\nabla V. \quad (2.21)$$

These equations are consistent with Ehrenfest’s theorem, which states that the average position of a wavepacket follows a classical trajectory [2]. Following the same procedure for the first exponential in (2.3), and making the assumption that no external potential exists, we can derive the equations of motion for the radial degree of freedom:

$$p_s = \frac{3}{4}m_{elec}s \quad \dot{p}_s = -\frac{\partial E}{\partial r}. \quad (2.22)$$

The factor of 3/4 in (2.22) arises because the radial coordinate varies in three dimensions. These equations are exact for harmonic potentials, and it was shown that they performed well for simple anharmonic potentials like the double well potential [1]. Because we do not express our wavepackets as superpositions of multiple basis functions, there is no possibility for quantum interference. Consequently our wavepacket will oscillate indefinitely without deconstructive interference “damping it out”. It is reasonable to expect that our radial degree of freedom may become too energetic relative to exact WPMD calculations under some circumstances. We can use the energies and forces from the electron force field in conjunction with this WPMD scheme as a fully functioning molecular dynamics method.

## 2.4 Temperature, Pressure, and Heat Capacity

Because eFF simulations include electrons as discrete particles, a discussion of how macroscopic system properties like temperature, pressure, heat capacity, and stress are computed is warranted. Carefully defining these properties is particularly important to this thesis since extreme conditions are defined by extremes in temperature, pressure, strain rate, and others.

The kinetic energy of the particles in an eFF simulation is defined classically for nuclei, and semiclassically for electrons:

$$E_{ke} = \sum_i \frac{1}{2}m_i\dot{x}_i^2 + \sum_i \frac{1}{2}\frac{3}{4}m_e\dot{s}_i^2 \quad (2.23)$$

where  $\dot{x}$  is the translational velocity and  $\dot{s}$  is the electron radial velocity. The second term on the

right side of equation (2.23) is null for nuclei.  $m_i$  corresponds to the nuclear mass or the dynamic electron mass.  $m_e$  is the true electron mass (0.000548579867 amu). In eFF the electron mass is defined in three places: 1) in the electronic kinetic energy, (2.8), 2) in the Pauli potential, (2.9), and 3) in the kinetic energy of motion, (2.23). In the electronic kinetic energy and the Pauli potential the electron mass is the true electron mass and it is fixed, since altering this value would change energies, bond lengths, and other static properties of atoms and molecules. The user may adjust the dynamic electron mass in equation (2.23). Changing the electron mass in the equations of motion varies the overall time scale of excited electron motions, with the time scale of excitations, relaxations, and energy transfer proportional to  $\sqrt{m_e}$ . This is what we refer to as changing the dynamic masses. This does not affect the net partitioning of energy in the system nor the magnitude of the thermodynamic parameters we are interested in measuring. This does not alter the system's chemistry, just its evolution in time.

Temperature is defined from the classical viral expression with a twist:

$$\langle E_{ke} \rangle = \frac{3}{2} N k_B T \quad (2.24)$$

and rearranging this term provides the macroscopic temperature:

$$T = \frac{2}{3} \frac{1}{k_B N_{nuc}} \langle E_{ke} \rangle. \quad (2.25)$$

Notice that the kinetic energy  $\langle E_{ke} \rangle$  is summed over all the particles but divided by the number of nuclei only,  $N_{nuc}$ . This adjustment is valid for temperatures well below the Fermi temperature. At intermediate temperatures the kinetic contribution to the pressure from the electrons is recovered indirectly through the Pauli potential. Thus as temperature increases, the electrons are excited, which causes their average size to increase, in turn raising the pressure through the Pauli potential. At temperatures in the vicinity of and above the Fermi temperature a separate ideal gas electron pressure correction is required.

This eFF temperature expression, (2.25), sets the heat capacity of the system to the classical heat

capacity  $C_v = \frac{3}{2}k_B N_{nuc}$ . If one measures the actual specific heat capacity of their system through eFF simulations, one finds that it is elevated due to the presence of the electrons. The measured specific heat capacity would equal  $C_v = \frac{3}{2}N_{nuc}k_B + 2N_{elec}k_B$ , since electrons obtain  $\frac{1}{2}k_B$  from each of 4 degrees of freedom. This unphysical high heat capacity would be reflected in the classical temperature definition (i.e., if you calculate  $T = 2/(3k_B N_{nuc+elec})\langle E_{ke} \rangle$  it is by definition always lower than the eFF temperature definition). This is why it is imperative to use the temperature definition in (2.25) when comparing eFF simulations to the results from other MD techniques.

The pressure is extracted from simulations using the virial expression [56]:

$$P = \frac{1}{V} \left[ N_{nuc}k_B T + \frac{1}{d} \sum_{i<j} \mathbf{r}_{ij} \cdot \mathbf{f}_{ij} \right] \quad (2.26)$$

where  $V$  is the volume,  $T$  the eFF temperature from (2.25), and  $d$  the dimensionality of the system.  $\mathbf{r}_{ij}$  are the interparticle positions and  $\mathbf{f}_{ij}$  the interparticle force vectors.

Another significant difference between eFF and true quantum methods is in the distribution of electrons in eigenstates. In eFF electrons are simulated like classical particles interacting through effective potentials. eFF electrons avoid one another if they are same-spin, and the Pauli potential penalizes same-spin electrons when they approach one another. However, eFF does not produce discrete eigenstates or eigenenergies. eFF electrons are not distributed through a rigorous Fermi-Dirac distribution. As a result, eFF electrons match classical statistics, not quantum Fermion statistics. eFF electrons are excited uniformly as temperature increases, unlike true electrons which are only excited near the Fermi level. Despite this limitation, eFF has proven that it accurately models the electron dynamics of systems near their ground state and in excited states.

## 2.5 eFF Successes

The beauty of eFF is in its simplicity. With only three empirical parameters it can reproduce a variety of physical quantities like electronic shell structure, molecular structure, bond energies, ionization potentials, and bulk properties. The simple nature of the energy and gradient expressions

makes eFF perform much faster than quantum mechanics [1, 57]. eFF has been used to simulate the behavior of hydrogen in the warm dense matter regime [58], the mechanisms of Auger-induced chemistry, [59], the high-temperature, high-pressure phases of lithium [60], the emission of exoelectrons, current bursts, and voltage generation during brittle fracture (see Chapter 3) [61], and the electron dynamics of shock in polyethylene (see Chapter 4) [62]. eFF has been incorporated into the popular molecular dynamics software suite, LAMMPS, and this has extended the functionality and scope of computational simulations that can be carried out with eFF [57, 63]. The remainder of this thesis will detail eFF studies of matter subjected to extreme environments.

# References

- [1] J. T. Su, *An electron force field for simulating large scale excited electron dynamics*. PhD thesis, California Institute of Technology, Pasadena, CA, 2007.
- [2] B. Dui, C. Cohen-Tannoudji, and F. Laloe, *Quantum Mechanics Volumes 1 and 2*. New York, NY: Wiley-Interscience, 1978.
- [3] P. Atkins and R. Friedman, *Molecular Quantum Mechanics*. Oxford, United Kingdom: Oxford University Press, fourth ed., 2005.
- [4] P. A. M. Dirac, “Quantum mechanics of many-electron systems,” *Proc. Royal Soc. A*, vol. 123, no. 792, pp. 714–733, 1929.
- [5] M. Born and R. Oppenheimer, “Zur quantentheorie der molekeln,” *Annalen der Physik*, vol. 389, no. 20, pp. 457–484, 1927.
- [6] R. P. Feynman, “Forces in molecules,” *Phys. Rev.*, vol. 56, no. 4, p. 340, 1939.
- [7] P. Pulay, “Ab initio calculation of force constants and equilibrium geometries in polyatomic molecules,” *Molecular Phys.*, vol. 17, no. 2, pp. 197–204, 1969.
- [8] W. A. Goddard, III, “Improved quantum theory of many-electron systems. iii. the gf method,” *J. Chem. Phys.*, vol. 48, no. 1, p. 450, 1968.
- [9] R. N. Barnett and U. Landman, “Born-oppenheimer molecular-dynamics simulations of finite systems: Structure and dynamics of H<sub>2</sub>O<sub>2</sub>,” *Phys. Rev. B*, vol. 48, no. 4, p. 2081, 1993.
- [10] R. Car and M. Parrinello, “Unified approach for molecular dynamics and density-functional theory,” *Phys. Rev. Lett.*, vol. 55, no. 22, pp. 2471–2474, 1985.
- [11] S. Goedecker, “Linear scaling electronic structure methods,” *Rev. Mod. Phys.*, vol. 71, no. 4, p. 1085, 1999.
- [12] J. Wang, R. M. Wolf, J. W. Caldwell, P. A. Kollman, and D. A. Case, “Development and testing of a general AMBER force field,” *J. Comp. Chem.*, vol. 25, no. 9, pp. 1157–1174, 2004.
- [13] A. D. MacKerell, Jr, N. Banavali, and N. Foloppe, “Development and current status of the CHARMM force field for nucleic acids,” *Biopolymers*, vol. 56, no. 4, pp. 257–265, 2000.
- [14] S. L. Mayo, B. D. Olafson, and W. A. Goddard, III, “DREIDING: a generic force field for molecular simulations,” *J. Phys. Chem.*, vol. 94, no. 26, pp. 8897–8909, 1990.
- [15] W. L. Jorgensen, D. S. Maxwell, and J. Tirado-Rives, “Development and testing of the opls all-atom force field on conformational energetics and properties of organic liquids,” *J. Am. Chem. Soc.*, vol. 118, p. 11225, 1996.
- [16] O. Borodin, G. D. Smith, and D. Bedrov, “Development of many-body polarizeable force fields for li-battery components: 1. ether, alkane, and carbonate-based solvents,” *J. Phys. Chem. B.*, vol. 110, p. 6279, 2006.

- [17] J. R. Fried *et al.*, "The COMPASS force field: parameterization and validation for phosphazenes," *Computational and Theoretical Polymer Science*, vol. 8, no. 1–2, pp. 229–246, 1998.
- [18] K. Chenoweth, A. C. T. van Duin, and W. A. Goddard, III, "ReaxFF reactive force field for molecular dynamics simulations of hydrocarbon oxidation," *J. Phys. Chem. A.*, vol. 112, p. 1040, 2008.
- [19] S. J. Stuart, A. B. Tutein, and J. A. Harrison, "A reactive potential for hydrocarbons with intermolecular interactions," *J. Chem. Phys.*, vol. 112, p. 6472, 2000.
- [20] D. W. Brenner, O. A. Shenderova, J. A. Harrison, S. J. Stuart, B. Ni, and S. B. Sinnott, "A second-generation reactive empirical bond order (rebo) potential energy expression for hydrocarbons," *J. Phys.: Condensed Matter*, vol. 14, p. 783, 2002.
- [21] J. Aqvist and A. Warshel, "Simulation of enzyme reactions using valence bond force fields and other hybrid quantum/classical approaches," *Chem. Rev.*, vol. 93, no. 7, pp. 2523–2544, 1993.
- [22] A. A. Frost, "Floating spherical Gaussian orbital model of molecular structure. I. computational procedure. LiH as an example," *J. Chem. Phys.*, vol. 47, p. 3707, 1967.
- [23] C. C. J. Roothaan, "New developments in molecular orbital theory," *Rev. Mod. Phys.*, vol. 23, no. 2, p. 69, 1951.
- [24] A. Szabo and N. S. Ostlund, *Modern quantum chemistry: introduction to advanced electronic structure theory*. Minneola, NY: Dover Publications, 1996.
- [25] A. A. Frost, "Floating spherical Gaussian orbital model of molecular structure. II. one- and two-electron-pair systems," *J. Chem. Phys.*, vol. 47, p. 3714, 1967.
- [26] A. A. Frost, "A floating spherical Gaussian orbital model of molecular structure. III. first-row atom hydrides," *J. Phys. Chem.*, vol. 72, no. 4, pp. 1289–1293, 1968.
- [27] R. A. Rouse and A. A. Frost, "Floating spherical Gaussian orbital model of molecular structure. VI. double-Gaussian modification," *J. Chem. Phys.*, vol. 50, p. 1705, 1969.
- [28] N. K. Ray and J. Switalski, "Floating spherical Gaussian orbital (FSGO) studies with a model potential: Application to two-valence-electron systems," *Theoretical Chemistry Accounts: Theory, Computation, and Modeling (Theoretica Chimica Acta)*, vol. 41, no. 4, pp. 329–333, 1976.
- [29] J. L. Nelson and A. A. Frost, "Floating spherical Gaussian orbital model of molecular structure. x. C3 and C4 saturated hydrocarbons and cyclobutane," *J. Am. Chem. Soc.*, vol. 94, no. 11, pp. 3727–3731, 1972.
- [30] S. Topiol, A. A. Frost, M. A. Ratner, and J. W. Moskowitz, "Use of pseudopotentials within the floating spherical Gaussian orbital method: Calculations on methane," *J. Chem. Phys.*, vol. 65, p. 4467, 1976.
- [31] S. Topiol, A. A. Frost, J. W. Moskowitz, and M. A. Ratner, "A new, simple *ab initio* pseudopotential for use in floating spherical Gaussian orbital calculations. 2. some results for hydrocarbons," *J. Am. Chem. Soc.*, vol. 99, no. 13, pp. 4276–4278, 1977.
- [32] S. Topiol, J. W. Moskowitz, A. A. Frost, and M. A. Ratner, "Pseudopotential floating spherical Gaussian orbital calculations on group IV hydrides," *J. Chem. Soc., Faraday Trans. 2*, vol. 74, pp. 1521–1527, 1978.
- [33] J. J. Toman, A. A. Frost, S. Topiol, S. Jacobson, and M. A. Ratner, "*Ab initio* studies, using the FSGO-pseudopotential method, of the electronic structure in group IV cluster molecules  $M(LH_3)_4$ ; M, L= C, Si, Ge," *Theoretical Chemistry Accounts: Theory, Computation, and Modeling (Theoretica Chimica Acta)*, vol. 58, no. 4, pp. 285–294, 1981.

- [34] J. M. André, J. Delhalle, C. Demanet, and M. E. Lambert-Gerard, “A floating spherical Gaussian orbital model for polymers: I. general formalism and computational procedure,” *Int. J. Quantum Chem.*, vol. 10, no. S10, pp. 99–105, 1976.
- [35] J. M. André, M. E. Lambert-Gérard, and C. Lamotte, “Application of the floating spherical Gaussian orbital (FSGO) model to the determination of photoelectron spectra of alkanes,” *Bulletin des Sociétés Chimiques Belges*, vol. 85, no. 10, pp. 745–753, 1976.
- [36] S. I. Lu, “A diffusion quantum Monte Carlo method based on floating spherical Gaussian orbitals and Gaussian geminals: Dipole moment of lithium hydride molecule,” *J. Chem. Phys.*, vol. 114, p. 3898, 2001.
- [37] C. L. Kirschbaum and L. Wilets, “Classical many-body model for atomic collisions incorporating the Heisenberg and Pauli principles,” *Phys. Rev. A*, vol. 21, no. 3, p. 834, 1980.
- [38] J. P. Hansen and I. R. McDonald, “Microscopic simulation of a strongly coupled hydrogen plasma,” *Phys. Rev. A*, vol. 23, no. 4, p. 2041, 1981.
- [39] C. Dorso and J. Randrup, “Classical simulation of nuclear systems,” *Phys. Lett. B*, vol. 215, no. 4, pp. 611–616, 1988.
- [40] H. Feldmeier and J. Schnack, “Molecular dynamics for Fermions,” *Rev. Mod. Phys.*, vol. 72, pp. 655–688, 2000.
- [41] J. S. Cohen, “Extension of quasiclassical effective Hamiltonian structure of atoms through  $Z = 94$ ,” *Phys. Rev. A*, vol. 57, pp. 4964–4966, 1998.
- [42] D. H. Boal and J. N. Glosli, “Quasiparticle model for nuclear dynamics studies: Ground-state properties,” *Phys. Rev. C*, vol. 38, no. 4, p. 1870, 1988.
- [43] D. Klakow, C. Toepffer, and P. G. Reinhard, “Semiclassical molecular dynamics for strongly coupled Coulomb systems,” *J. of Chem. Phys.*, vol. 101, p. 10766, 1994.
- [44] E. J. Heller, “Time-dependent approach to semiclassical dynamics,” *J. Chem. Phys.*, vol. 62, no. 4, pp. 1544–1555, 1975.
- [45] S. Y. Lee and E. J. Heller, “Exact time-dependent wave packet propagation: Application to the photodissociation of methyl iodide,” *J. Chem. Phys.*, vol. 76, p. 3035, 1982.
- [46] N. E. Henriksen and E. J. Heller, “Quantum dynamics for vibrational and rotational degrees of freedom using Gaussian wave packets: Application to the three-dimensional photodissociation dynamics of icn,” *J. Chem. Phys.*, vol. 91, p. 4700, 1989.
- [47] K. Singer and W. Smith, “Semiclassical many-particle dynamics with Gaussian wave packets,” *Mol. Phys.*, vol. 57, no. 4, pp. 761–775, 1986.
- [48] M. Knaup, P. Reinhard, and C. Toepffer, “Wave packet molecular dynamics simulations of deuterium in the region of laser shock-wave experiments,” *Contributions Plasma Phys.*, vol. 41, no. 2-3, pp. 159–162, 2001.
- [49] M. Knaup, P. G. Reinhard, C. Toepffer, and G. Zwicknagel, “Wave packet molecular dynamics simulations of warm dense hydrogen,” *J. Phys. A: Mathematical and General*, vol. 36, p. 6165, 2003.
- [50] B. Jakob, P. Reinhard, C. Toepffer, and G. Zwicknagel, “Wave packet simulation of dense hydrogen,” *Phys. Rev. E*, vol. 76, no. 3, p. 036406, 2007.
- [51] P. Cordero and E. S. Hernández, “Momentum-dependent potentials: Towards the molecular dynamics of Fermion-like classical particles,” *Phys. Rev. E*, vol. 51, no. 3, p. 2573, 1995.

- [52] J. Ortner, F. Schautz, and W. Ebeling, “Quasiclassical molecular-dynamics simulations of the electron gas: Dynamic properties,” *Phys. Rev. E.*, vol. 56, pp. 4665–4670, 1997.
- [53] C. W. Wilson and W. A. Goddard, III, “Exchange kinetic energy, contragradience, and chemical binding,” *Chem. Phys. Lett.*, vol. 5, no. 1, pp. 45–49, 1970.
- [54] G. Wentzel, “Eine verallgemeinerung der quantenbedingungen für die zwecke der wellenmechanik,” *Zeitschrift für Physik*, vol. 38, pp. 518–529, 1926.
- [55] H. A. Kramers, “Wellenmechanik und halbzahlige quantisierung,” *Zeitschrift für Physik*, vol. 39, pp. 828–840, 1926.
- [56] M. Zhou, “A new look at the atomic level virial stress: On continuum-molecular system equivalence,” *Proc. R. Soc. Lond. A.*, vol. 459, pp. 2347–2392, 2003.
- [57] A. Jaramillo-Botero, J. T. Su, A. Qi, and W. A. Goddard, III, “Large-scale, long-term nonadiabatic electron molecular dynamics for describing material properties and phenomena in extreme environments,” *J. Comp. Chem.*, vol. 32, no. 3, pp. 497–512, 2011.
- [58] J. T. Su and W. A. Goddard, III, “Excited electron dynamics modeling of warm dense matter,” *Phys. Rev. Lett.*, vol. 99, p. 185003, 2007.
- [59] J. Su and W. A. Goddard, III, “Mechanisms of Auger-induced chemistry derived from wave packet dynamics,” *Proc. Nat. Acad. Sci.*, vol. 106, no. 4, pp. 1001–1005, 2009.
- [60] H. Kim, J. T. Su, and W. A. Goddard, III, “High-temperature high-pressure phases of lithium from electron force field (eFF) quantum electron dynamics simulations,” *Proc. Nat. Acad. Sci.*, vol. 108, pp. 15101–15105, 2011.
- [61] P. L. Theofanis, A. Jaramillo-Botero, W. A. Goddard, III, and H. Xiao, “Nonadiabatic study of dynamic electronic effects during brittle fracture of silicon,” *Phys. Rev. Lett.*, vol. 108, p. 045501, 2012.
- [62] P. L. Theofanis, A. Jaramillo-Botero, A. P. Thompson, T. R. Mattsson, and W. A. Goddard, III, “Electron dynamics of shocked polyethylene crystal,” *Phys. Rev. B*, vol. 85, p. 094109, 2012.
- [63] S. J. Plimpton, “Fast parallel algorithms for short-range molecular dynamics,” *J. Comp. Phys.*, vol. 117, pp. 1–19, 1995.

## Chapter 3

# Nonadiabatic Electron Dynamics During Brittle Fracture in Silicon

### 3.1 Abstract

The observation that brittle fracture of materials can lead to the emission of high energy electrons and UV photons is well documented for materials ranging from polymer thermoplastics, glasses, minerals, and semiconductor crystals [1–4]. There has been no previous atomistic description of the origin of such processes. Although fracture in solids involves breaking of chemical bonds, which can be well described with modern quantum mechanics (QM) methods, the observation of exo-electrons and photon emissions indicates that the processes are not purely adiabatic, complicating the application of QM — in particular for model systems that require more than a few hundred atoms. We show here that the eFF method for nonadiabatic dynamics accounts for electron emission and large potential differences consistent with the experiments, providing the first atomistic description of the origin of these effects. In this chapter we consider the  $\{100\}\langle 011\rangle$  and  $\{111\}\langle 112\rangle$ <sup>1</sup> fracture of silicon crystals producing  $\{100\}$  and  $\{111\}$  fracture planes, which have been studied quite thoroughly. The effects that we explain are (1) loading of a crack leads to a sudden onset of crack propagation at 7 GPa followed by uniform velocity of the crack at 2500 km/sec after initiation, and (2) voltage fluctuations in the 10–400 mV range, charge creation (up to  $10^{11}$  carriers/cm<sup>2</sup>), and current production (up to 1.3 mA).

---

<sup>1</sup>In the materials failure community  $\{hkl\}\langle h'k'l'\rangle$  notation refers to fracture that propagates in the  $\langle h'k'l'\rangle$  direction and produces  $\{hkl\}$  crack faces.

### 3.2 Brittle Fracture in Silicon

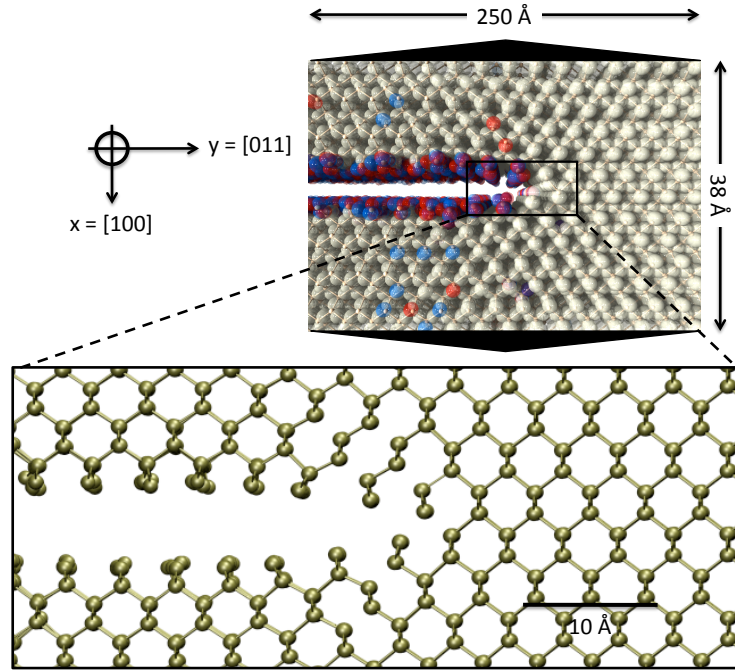


Figure 3.1: A snapshot of a crack propagating in a silicon single crystal with mode I loading in the x-direction producing a  $\{100\}\langle 011\rangle$  edge crack. The transparent spheres are paired electrons. Unpaired spin up electrons are colored red, and unpaired spin down electrons are colored blue.

Historically, brittle fracture has been analyzed using continuum mechanics techniques which predict the macroscopic driving force for crack propagation: the release of elastic energy per unit advancement as the crack progresses. This force is a function of the applied load, the length of the crack and the geometry of the materials [5–7]. The crack is assumed to propagate as long as its energy release rate,  $G$ , is equal to or larger than a material- and geometry-specific factor, the critical energy release rate,  $G_c$ . Griffith, a pioneer in fracture mechanics, equated the critical energy release rate to  $2\gamma$ , the energy needed to create two new surfaces. More recently, experimentalists and theorists have taken to studying more complex issues like the origin of crack path instabilities [5, 8, 9], hyperelasticity [10, 11], the emission of dislocations [12–14], and plastic flow [15, 16]; the latter two contribute to material hardening. Theorists have moved beyond linear elastic fracture mechanics, and they are now studying the atomistic events that precipitate brittle fracture. Some of their approaches will be highlighted in the following paragraphs.

Experimental studies on silicon material defects reveal a rich variety of physics, including electronic excitation. Silicon brittle fracture experiments demonstrate that low crack velocities produce clean surfaces [17] while higher speed cracks that exceed a 2/3 of the Rayleigh wave speed produce uneven and irregular surfaces [5, 18]. Other experiments document fracture mechanics like fracture caused by thermal loading [19], dislocation nucleation [13, 14], and the brittle-to-ductile transition of silicon [9, 20, 21]. There are several experiments that document dynamic electron phenomenon as a result of fracture. Early studies documented the anomalous generation of voltages and currents as a result of fracture [22, 23]. More recent work measured the ejection of electrons [24] and other charged particles [25], in both cases a result of fracture. Despite the abundance of fracture experiments, the effect of fracture nucleation on electrons is not well understood. This gap in the theory of fracture is peculiar because fracture is precipitated by the breaking of covalent bonds. It underscores the inability of established QM or forcefield methods to adequately describe the dynamics of electrons during fracture.

Fracture in solids is nucleated by the breaking of atomic bonds, and quantum mechanical theoretical approaches are capable of describing fracture on the atomistic scale [5, 26, 27]. Some empirical atomistic potentials have failed to reproduce the brittle fracture of silicon and instead they produced plastic flow, or they fail to model the response of the crack velocity to increasing loads [17, 28–30]. Recently “reactive” forcefields have succeeded where classical potentials could not [11, 31, 32]. Because quantum mechanical methods treat electrons like waves, and because classical forcefields account for electronic effects implicitly, a theoretical description of these electronic excitations is missing. No previous attempts were made to model the voltage fluctuations, electron emission, and charge creation phenomena. Current time-dependent QM methods are incapable of describing the dynamics of electron ejection excitation of highly excited states from deformation of the crystal. QM methods are unable to attain the length and time scales ( $> 1,000$  atoms over  $> 1$  ps time scales) required to describe the dynamics of fracture. On the other hand, conventional forcefields in conjunction with molecular dynamics methods can handle the relevant length and time scales, but they do not describe ejected electrons and excited electronics states. eFF is the ideal

tool to model electron dynamics, so in this study we will provide an explanation for the observed voltages, currents, and charge carrier formation.

### 3.3 Silicon Models and Methods

For this study we developed two simulation cells. Figure 3.1 depicts our “{100}” crack model. In this model the x-y-z directions are  $(100)\times(011)\times(01\bar{1})$  direction, creating a  $(100)$  fracture plane with a  $[011]$  fracture direction with dimensions of  $3.8\times 25\times 3.8$  nm<sup>3</sup>. In our “{111}” model, the x-y-z directions are  $(111)\times(\frac{1}{2}\bar{1}\bar{1})\times(\frac{1}{2}\bar{1}0)$  which produces {111} crack surfaces with a  $[112]$  crack propagation direction with dimensions of  $2.7\times 47\times 4.0$  nm<sup>3</sup>. We performed crack simulations on fully periodic replicas and on slabs with hydrogen-passivated surfaces of the previously described geometries. The results presented here correspond to our fully periodic system, though we found negligible differences between the results we obtain in our fully periodic and partially periodic slab models (see Figure 3.2). Both systems were prepared in an isothermal-isobaric ensemble using a Nosé-Hoover thermostat and barostat, at 300 K and 1 atm, respectively. In both samples a seed crack of length  $1/5 L_y$  is created before a load is applied. A continuous uniaxial strain load is applied to the cells in the x-dimension at a rate of 1.2% per ps, and the sample is allowed to crack naturally, which allows us to test the failure modes of the system. No barostat pressure is imposed in the strain direction. The properties of these two models are listed in Table 3.1.

Method	E (GPa)	Yield Strength (GPa)	$G_c$ (J/m <sup>2</sup> )	$K_{ic}$ (MPa)
{111} expt.	163-188 [33]	7 [34]	2.3 [17]	0.76 [35, 36]
{111} eFF	166	15	3.16	0.752
{100} expt.	125-202 [37]	-	-	0.91 [38]
{100} eFF	157	15	2.57	0.96

Table 3.1: Comparison of experimental and computed mechanical values: Young’s modulus, E, yield strength, Griffith critical load,  $G_c$ , and the stress intensity factor,  $K_{ic}$ . References are in square brackets.

Previously eFF treated all electrons of an atom, including the core electrons [39]. Describing the very short time scales of the high energy core orbitals makes simulating picoseconds of fracture computationally intractable on systems large enough to describe crack propagation in Si crystal.

Instead of describing all electrons explicitly, here we replace the core electrons with an effective core pseudo-potential while retaining the accuracy in describing the valence electrons. This allows us to study the dynamics of electronic excitations and ejection simultaneous with nucleation and propagation of crack fracture in silicon. The details of the effective core potential are described in Chapter 5.

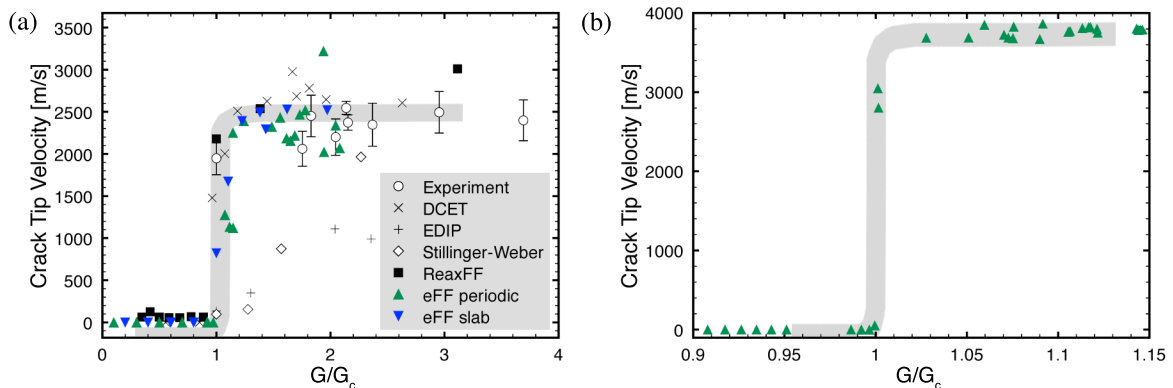


Figure 3.2: (a) Crack tip velocity versus reduced load for  $\{111\}$  fracture with experimental data from [17], ReaxFF-Tersoff and SW data from [31], environmental dependent interatomic potential (EDIP) and the results of a multiscale method that couples empirical potentials and quantum mechanical tight-binding approaches (DCET) from [26]. (b) The crack tip velocity versus reduced load for the eFF  $\{100\}$  model. The gray lines are visual guides.

## 3.4 Electron Dynamics During Brittle Fracture

### 3.4.1 Fracture Mechanics

Figure 3.2 shows the relationship between the crack tip velocity and the energy release rate normalized by the critical energy release rate determined at the onset of fracture. We computed  $G$  from the uniaxial stress ahead of the crack, the crack length, and the Young's modulus that we compute from our model:  $G = 1.12^2 \pi P_{xx}^2 a / E^2$ .  $K_{ic}$  is computed similarly. Both the  $\{100\}$  and  $\{111\}$  models exhibit brittle fracture and both match the experimental observation that upon reaching a critical load, the crack velocity rapidly jumps to 4 km/s and 2 km/s, respectively, and plateaus thereafter. Table 3.1 compares computed mechanical properties to those of experiments. The calculated Griffith critical load for the  $\{111\}$  is 3.16 J/m<sup>2</sup>, which is higher than the experimental value but in agree-

ment with the QM value of  $3.1 \text{ J/m}^2$  [5]. This indicates that our model leads to a small amount of lattice trapping. In general, our simulations of the dynamics of fracture in silicon using the eFF pseudopotential reproduces experimental measurements and results produced with other reactive forcefields [31].

### 3.4.2 Atomistic Mechanisms of Fracture

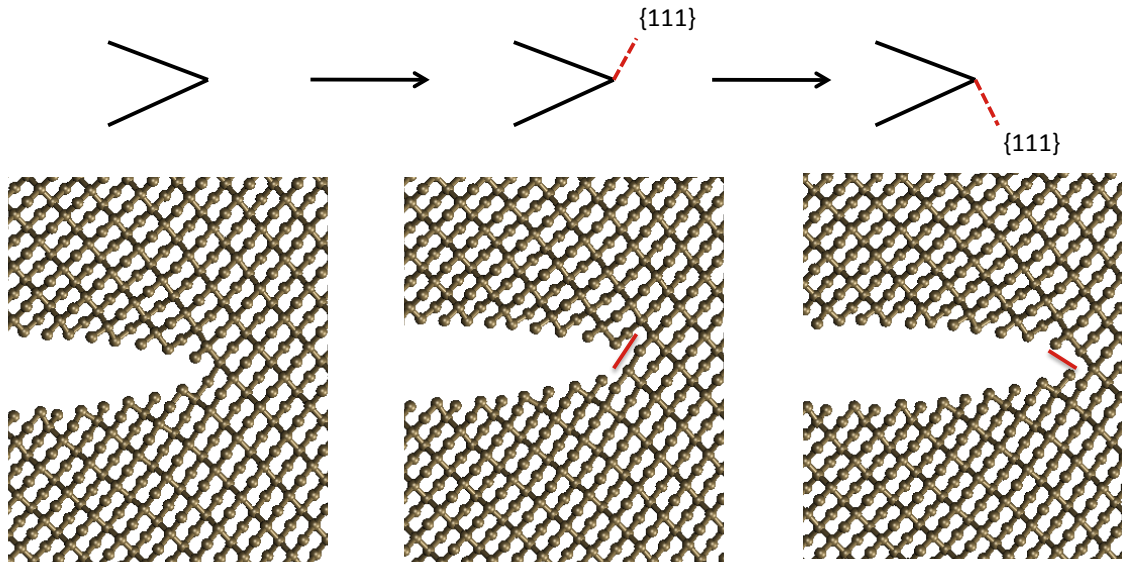


Figure 3.3:  $\{100\}\langle 011\rangle$  fracture is produced by stepwise “zig-zag” bond breaking in lower energy  $\{111\}$  planes.

The use of an atomistic potential allows us to examine the chemical origins of fracture in  $\{100\}\langle 011\rangle$  and  $\{111\}\langle 112\rangle$  cracks. Figure 3.3 shows the stepwise propagation of a crack at the atomic scale for the  $\{100\}$  system. For  $\{100\}\langle 011\rangle$  fracture in the brittle regime, there is competition between bond cleavage in the  $\{100\}$  and  $\{111\}$  planes which intersect at  $54.7^\circ$  angles to the  $\{100\}$  planes. While the tensile load is applied to the  $\langle 100\rangle$  direction, the resulting  $\{100\}$  crack surfaces have higher energies than  $\{111\}$  surfaces. As a result, the crack extends by single bond cleavage into alternating  $\{111\}$  planes that intersect at the crack tip. These zig-zag nanocracks, when they occur in this fashion, lead to crack propagation in the  $\langle 011\rangle$  direction. Local crack propagation along  $\{111\}$  planes for  $\{100\}\langle 011\rangle$  cracks agrees with earlier studies that suggest that  $\{111\}$

is a preferred fracture plane [32, 40]. The behavior near the crack tip has major implications for the behavior of the crack at larger scales. If the crack tip blunts and aligns with a  $\{111\}$  plane it is possible for the resulting local mode II shear to emit a dislocation [32].

Figure 3.4 shows the details of a  $\{111\}\langle 112\rangle$  crack propagating. While we found perfectly brittle fracture in our  $\{100\}$  model, we encountered greater lattice trapping in our  $\{111\}$  model.  $\{111\}\langle 112\rangle$  fracture requires that the shuffle plane  $\sigma$ -bonds be broken simultaneously, unlike  $\{100\}\langle 011\rangle$  fracture, wherein alternating unit cells contain a breaking  $\sigma$ -bond. The strongly bonded bilayers resist fracture and trap elastic energy more effectively than the  $\{100\}$  system. This has the effect of decreasing the crack tip speed (evident in Figure 3.2). Because a greater tensile load is required to break the bonds, and because the lattice trapping is higher, we observed the emission of dislocations and shear banding in many of our simulations. A shear band emission is highlighted in Figure 3.4c. The fracture instabilities also produce rough surfaces, a fact which is experimentally observed [6, 18, 31, 41]. From an atomistic perspective,  $\{111\}$  fracture is less complex than  $\{100\}$  fracture. Cracks propagate by linearly rupturing  $\sigma$ -bonds in the shuffle plane. Shuffle plane cleavage is favored over glide plane cleavage by only 0.17 eV per surface atom [22, 42]. This low energy difference means that it is not difficult for a crack to cross into and through a bilayer, and the high shear stresses near the crack tip ensure that this happens occasionally.

### 3.4.3 Fracture-Induced Electron Excitation

From our simulations we ascertain that there are two prevalent modes of electron ionization: local field-induced ionization and thermal ionization. The simulations show that ionization occurs as a direct result of fracture. Figure 3.5 shows the evolution of a representative group of electrons as the fracture progresses. We find that electron ionization is precipitated by the passing of the crack front. Figure 3.7a shows that ionized electrons are excited by 5 eV, making them sufficiently energetic to escape the Si-surface barrier [24]. The initial excitation promotes the electrons to unbound states (total electron energy  $> 0$ ) but they subsequently relax to 4.1 eV above the ground state, well into the Si conduction band. A close examination of the energy contributions leading to ionization

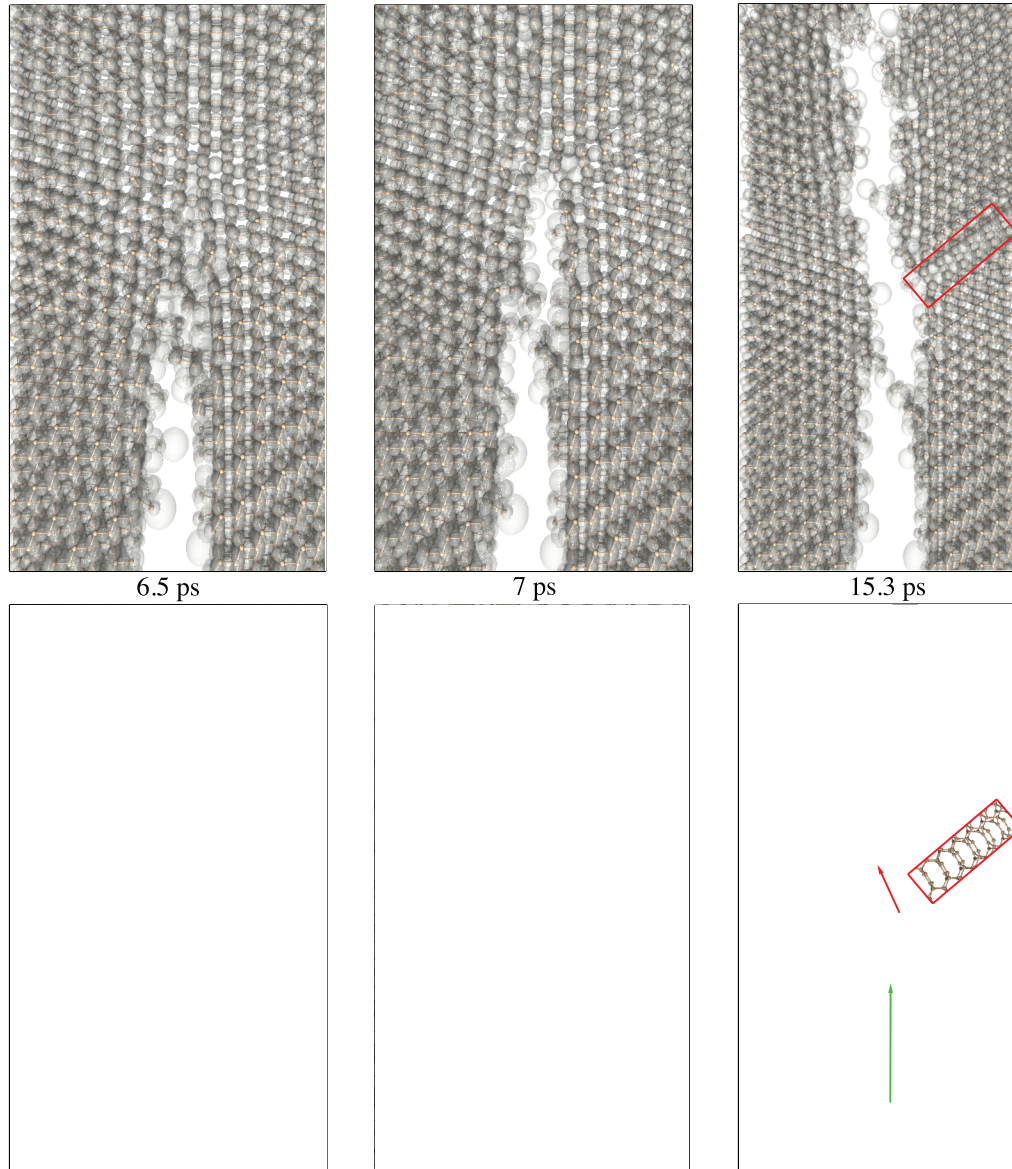


Figure 3.4: Snapshots of  $\{111\}\langle 112\rangle$  fracture at 6.5, 7, and 15.3 ps after the initiation of crack propagation. At 15.3 ps a dislocation (boxed in red) is visible. The dislocation is emitted due to the shear stresses caused by the crack tip crossing into the neighboring left bilayer. In the upper panes electrons are depicted as transparent spheres. The lower panes show silicon nuclei.

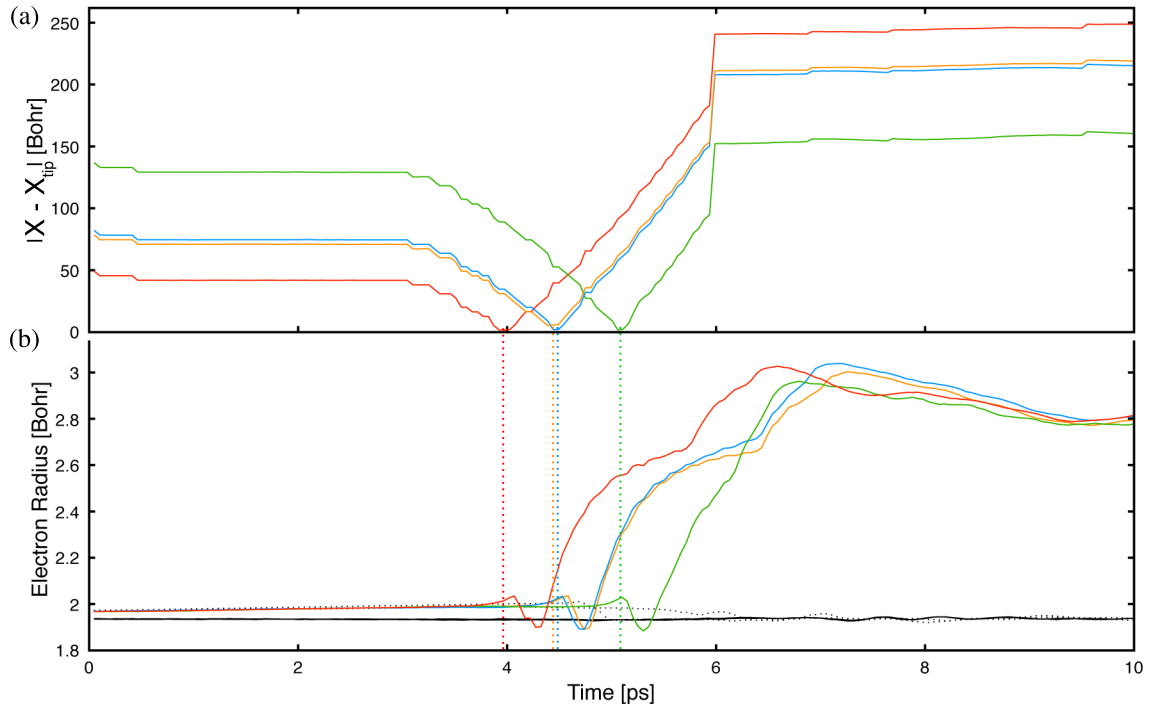


Figure 3.5: (a) The absolute distance between the crack tip and electrons that will ionize. (b) The radii of ionized electrons (in color), ground state surface electrons (black dotted lines), and bulk electrons (solid black lines).

reveals that in most cases an increase in potential energy causes ionization. The cause of this is heterolytic bond cleavage across the crack. In rare instances a heterolytic cleavage creates an anion on one crack face and a cation on the other crack face. As dangling bonds form  $2 \times 1$  valence bond surface dimers, the excess electron causes Pauli exclusion clashes with adjacent surface pairs (see Figure 3.6). As a result, the ionized electron's radius decreases to reduce its overlap with nearby same-spin electrons. The spin clashing forces the electron further from the surface and the electron delocalizes (its radius increases in the eFF description). Ultimately it relaxes and settles into the conduction band.  $80 \pm 10\%$  of ionized electrons are ionized because of local field effects. We do not observe Pandey's Si(111)- $2 \times 1$   $\pi$ -bonded chain surface reconstruction because the timescale of our dynamics is too short [43].

In rare circumstances an increase in an electron's kinetic energy after fracture causes it to ionize. Kinetic excitation is caused by local heating so we conclude that while possible, thermal ionization is not the predominant mechanism. In Figure 3.7 the total energy and kinetic energy of the same

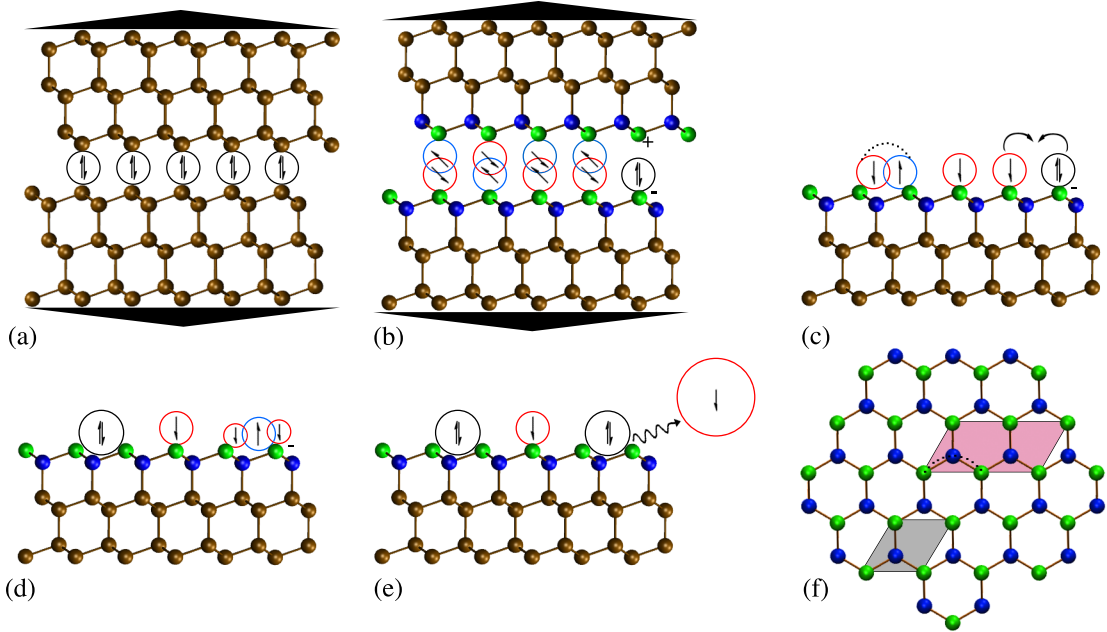


Figure 3.6: The stages of fracture leading to electron emission and Si(111)- $2 \times 1$  surface reconstruction: (a) a tensile load is applied, (b) shuffle plane  $\sigma$ -bonds break, usually homolytically, but heterolytic cleavage is energetically possible, (c) the new surface relaxes, (d) a surface electron attempts to pair with an adjacent anion, (e) the resulting spin clash causes an electron to ionize and detach from the surface. (e) a  $\{111\}$  surface showing a  $1 \times 1$  unit cell (shaded in gray) and a  $2 \times 1$  surface dimer (shaded in pink with a dashed line representing the surface dimer bond).

group of electrons depicted in Figure 3.5 are presented. In Figure 3.7b only one electron is excited thermally — the fingerprint of thermal excitation in increased kinetic energy. We observe that elastic energy in the stress field ahead of the crack is converted to kinetic energy in the recoil of the new surfaces causing local heating. As mentioned previously, we estimate from our simulations that  $20 \pm 10\%$  of electrons are thermally ionized.

To understand the dynamics of charge carriers during silicon fracture, we compute the electrostatic potential (EP) on grid points, i.e., by summing the individual Gaussian charge density potentials. In Figure 3.8a–c, we provide snapshots of the electrostatic potential at three points during the fracture simulation. Initially, the system has zero potential (white color). As a crack evolves, we observe the production of negative charge carriers in the free space inside the crack (blue color). Figure 3.8c shows the final state of the system after the crack has propagated through the unit cell, with the crack edges outlined in black and the midline highlighted in red. Heterolytic bond cleavage

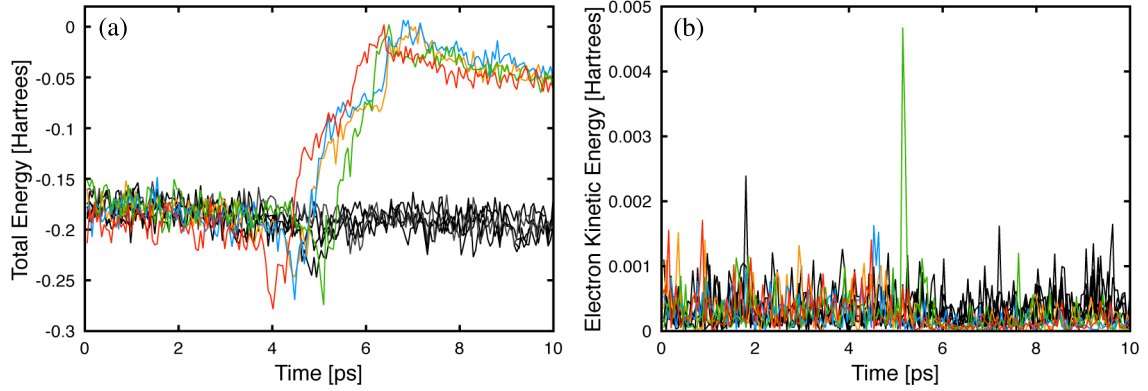


Figure 3.7: (a) The total energy of the same group of electrons as Figure 3.5. (b) The kinetic energy of said group of electrons.

due to thermal fluctuation and hot spot formation causes  $2.6 \times 10^{-2} \pm 1.3 \times 10^{-2}$  more electrons per  $\text{nm}^2$  to remain on one side of the crack than the other, which results in the left crack face having (+2.13 V) potential and the right face having (+1.12V) potential. The potential gradient across the crack corresponds to a voltage of 1.02 V. Li and colleagues reported measuring voltages of tens of mV with some cracks producing voltages up to 0.39 V [22]. The electrostatic potential difference between the crack surfaces reflects the dynamics of charge carriers during silicon fracture.

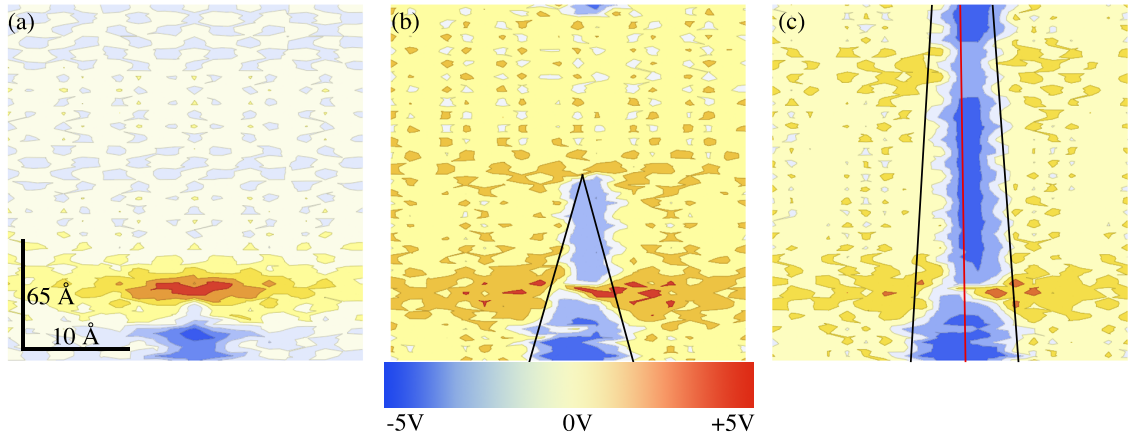


Figure 3.8: The evolution of electrostatic potential calculated on a grid is given at (a) 0 ps, (b) 9 ps, and (c) 15 ps. Warm colors denote positive potential and cool colors signify negative potential. The crack edges are given by solid black lines and the midline of the crack is provided in red.

We computed the number of ionized electrons at each time point in our crack trajectories and the results are presented in Figure 3.9b. Electrons are ionized if the sum of their potential and kinetic

energy exceeds zero:

$$E = E_{ke} + 2 \cdot E_{pe} - \frac{3}{2} \cdot \frac{1}{s^2} > 0. \quad (3.1)$$

In eFF each electron's potential energy is recorded as half the sum of its pairwise interactions with other particles plus its electronic kinetic energy, the second term in the middle expression. To correctly account for the potential energy we must multiply  $E_{pe}$  by two. We subtract the electronic kinetic energy,  $3/2 \cdot 1/s^2$ , because doubling the potential energy doubles the electronic kinetic energy which is implicitly included in each particle's potential energy (see equation (2.4) for further details on the eFF Hamiltonian). Given the size of our {111} cell, these correspond to a total electron yield of  $5.3 \times 10^{11}$  to  $1.6 \times 10^{12} \text{ cm}^{-2}$ . Langford and co-workers detected current transients whose integrated area corresponded to yields of  $10^9$  or  $10^{11}$  carriers/cm<sup>2</sup>, though their {111} crack velocities were around 900 m/s [23]. They stated that faster cracks produced larger carrier yields. Our {111} crack velocity is two times faster, which explains why we observe larger ionized electron yields.

From the equilibrium dynamics of the cracked system, we determined the electrical conductivity using the Green-Kubo integral of the electric current correlation function by computing:

$$\sigma_{GK} = \frac{1}{3k_BTV} \int_0^\infty \langle \mathbf{j}(t) \cdot \mathbf{j}(0) \rangle dt \quad (3.2)$$

where  $\mathbf{j}(t)$  is the electric current flux, and the integral argument corresponds to the electric current velocity correlation that is expressed as

$$J(t) = \langle \mathbf{j}(t) \cdot \mathbf{j}(0) \rangle = \sum_{i=1}^N \sum_{j=1}^N \langle q_i q_j \mathbf{v}_i(t) \cdot \mathbf{v}_j(0) \rangle = Z(t) + \sum_{i=1}^N \sum_{j \neq i}^N \langle q_i q_j \mathbf{v}_i(t) \cdot \mathbf{v}_j(0) \rangle = Z(t) + \Delta(t) \quad (3.3)$$

where  $i$  and  $j$  are different particles.  $Z(t)$  is the current autocorrelation and  $\Delta(t)$  is the cross-correlation term between particles. Figure 3.9a shows the current velocity correlation,  $J(t)$ , for our {111} system at 300 K and after the crack has occurred. The post-crack data trace is initially positive because free charge carriers are moving across the gap; these carriers have strong autocorrelation signals. Integrating these traces and applying the result to 3.2 gives us a measure of the conductivity

of our cells before and after fracture. Before the fracture our cell has an electrical conductivity of  $2.69 \times 10^{-5}$  S/cm; after fracture the cell has a conductivity of  $3.72 \times 10^{-3}$  S/cm. Pure silicon samples (like our simulation cells) have conductivity as low as  $10^{-4}$  S/cm and decreasing the dopant concentration causes silicon to asymptotically approach  $10^{-5}$  S/cm [44]. Our post-crack sample has a calculated conductivity on the order of n-doped silicon samples with dopant concentrations of  $4 \times 10^{12}$   $\text{cm}^{-3}$ . This indicates that the production of mobile charge carriers as a direct result of fracture accounts for the experimentally observed fracture current bursts. It also corroborates the observation of conduction band electrons in Figure 3.7a.

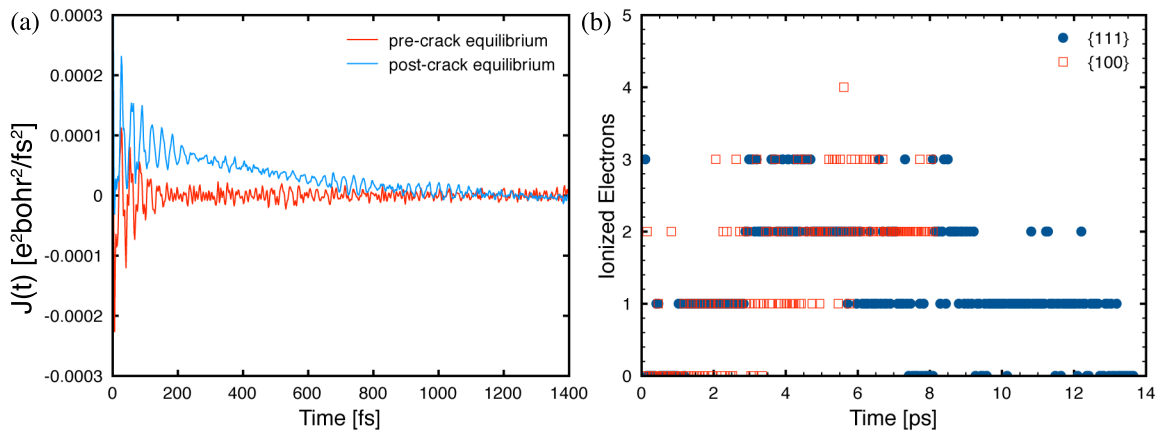


Figure 3.9: (a) The electric current velocity correlation functions for the  $\{111\}$  system at equilibrium (red) and after a crack has occurred (blue). (b) The ionized electron yield along the crack trajectory for the  $\{111\}$  and  $\{100\}$  models.

### 3.5 Conclusions

We show here that our ECP for silicon in the electron force field method (eFF) provides an accurate representation of the dynamics of material failure, including charge transfer, voltage impulses, and electron ionization. In this study we demonstrated that eFF could replicate the physics of brittle fracture of silicon independent of crack orientation. The equilibrium and dynamic mechanical properties computed from our simulations are in excellent agreement with experimental measurements and the predictions of other reactive forcefields. Furthermore, we observed the generation of volt-

ages and the production of charge carriers in good agreement with experiment. We have performed preliminary tests to infer spectral emissions from the ground state and excited electron eigenstates from eFF dynamics, albeit within the limitations of the Gaussian basis set representation and the ECP approximation, by computing the autocorrelation function of the electron wavepackets and Fourier transforming this function to obtain the eigenstates of the system. This technique allows us to roughly estimate the emissions that accompany shock, fracture, or triboluminescence.

The significance of these results stem from the capability of eFF to accurately track the long-term dynamics of electrons under nonadiabatic conditions. This provides new insights into the phenomenon of electron ejection, voltage fluctuations, and charge carrier induction. Since eFF has been demonstrated to predict the transformation of  $\text{H}_2$  and Li from ground state, to intermediate states of warm-dense matter, to highly excited and plasma state regimes and Auger decay, we consider that eFF is suitable for treating electronic effects in materials under a wide range of extreme conditions.

# References

- [1] T. Shiota and K. Yasuda, “Simultaneous measurement of the emission of photons and charged particles during fracture of brittle materials,” *Mat. Sci. and Eng.: B*, vol. 173, no. 1–3, pp. 248–252, 2010.
- [2] K. Yasuda *et al.*, “Some aspects of photon emission of polycrystalline ceramics during fracture,” *Phil. Mag. A*, vol. 82, no. 17–18, pp. 3251–3261, 2002.
- [3] F. Urakaev, “Mechanodestruction of minerals at the crack tip (overview): 2. theory,” *Phys. and Chem. of Min.*, vol. 35, pp. 231–239, 2008.
- [4] J. T. Dickinson, E. E. Donaldson, and M. K. Park, “The emission of electrons and positive ions from fracture of materials,” *J. Mat. Sci.*, vol. 16, pp. 2897–2908, 1981.
- [5] J. R. Kermode, T. Albaret, D. Sherman, N. Bernstein, P. Gumbsch, M. C. Payne, G. Csanyi, and A. De Vita, “Low-speed fracture instabilities in a brittle crystal,” *Nature*, vol. 455, no. 7217, pp. 1224–1227, 2008.
- [6] L. B. Freund, *Dynamic fracture mechanics. Cambridge Monographs on Mechanics and Applied Mathematics.*, Cambridge University Press, 1998.
- [7] A. A. Griffith, “The phenomena of rupture and flow in solids,” *Phil. Trans. R. Soc.*, vol. 221, pp. 163–198, 1921.
- [8] D. H. Warner, W. A. Curtin, and S. Qu, “Rate dependence of crack-tip processes predicts twinning trends in f.c.c. metals,” *Nat. Mater.*, vol. 6, no. 11, pp. 876–881, 2007.
- [9] R. C. Brodie and D. F. Bahr, “Fracture of polycrystalline silicon,” *Mat. Sci. and Eng. A*, vol. 351, no. 1–2, pp. 166–173, 2003.
- [10] M. J. Buehler, F. F. Abraham, and H. Gao, “Hyperelasticity governs dynamic fracture at a critical length scale,” *Nature*, vol. 426, pp. 141–146, 2003.
- [11] M. J. Buehler, A. C. T. van Duin, and W. A. Goddard, III, “Multiparadigm modeling of dynamical crack propagation in silicon using a reactive force field,” *Phys. Rev. Lett.*, vol. 96, no. 9, p. 095505, 2006.
- [12] T. Zhu, J. Li, and S. Yip, “Atomistic study of dislocation loop emission from a crack tip,” *Phys. Rev. Lett.*, vol. 93, p. 025503, Jul 2004.
- [13] C. Scandian, H. Azzouzi, N. Maloufi, G. Michot, and A. George, “Dislocation nucleation and multiplication at crack tips in silicon,” *Physica Status Solidi (a)*, vol. 171, no. 1, pp. 67–82, 1999.
- [14] A. George and G. Michot, “Dislocation loops at crack tips: nucleation and growth — an experimental study in silicon,” *Mat. Sci. and Eng.: A*, vol. 164, no. 1–2, pp. 118–134, 1993.
- [15] V. I. Betekhtin and A. N. Bakhtibaev, “Durability and creep in single crystals of germanium and silicon,” *Sov. Phys. Doklady*, vol. 14, no. 10, pp. 1007–1010, 1970.

- [16] M. M. Myshlyaev, V. I. Nikitenko, and V. I. Nesterenko, “Dislocation structure and macroscopic characteristics of plastic deformation at creep of silicon crystals,” *Phys. Stat. Sol.*, vol. 36, pp. 89–96, 1969.
- [17] J. A. Hauch, D. Holland, M. P. Marder, and H. L. Swinney, “Dynamic fracture in single crystal silicon,” *Phys. Rev. Lett.*, vol. 82, no. 19, p. 3823, 1999.
- [18] T. Cramer, A. Wanner, and P. Gumbsch, “Energy dissipation and path instabilities in dynamic fracture of silicon single crystals,” *Phys. Rev. Lett.*, vol. 85, no. 4, pp. 788–791, 2000.
- [19] R. D. Deegan, S. Chheda, L. Patel, M. Marder, H. L. Swinney, J. Kim, and A. de Lozanne, “Wavy and rough cracks in silicon,” *Phys. Rev. E*, vol. 67, no. 6, p. 066209, 2003.
- [20] S. Nakao, T. Ando, M. Shikida, and K. Sato, “Temperature effects on fracture behavior of notched silicon film specimen,” *J. Micromech. Microeng.*, p. 18, 2008.
- [21] M. Brede, K. J. Hsia, and A. S. Argon, “Brittle crack propagation in silicon single crystals,” *J. of App. Phys.*, vol. 70, no. 2, pp. 758–771, 1991.
- [22] D. G. Li, D. Haneman, N. S. McAlpine, and B. Chen, “Voltage generation on cleavage of silicon,” *Phys. Rev. Lett.*, vol. 73, no. 8, pp. 1170–1173, 1994.
- [23] S. C. Langford, D. L. Doering, and J. T. Dickinson, “Production of free charge carriers during fracture of single-crystal silicon,” *Phys. Rev. Lett.*, vol. 59, no. 24, pp. 2795–2797, 1987.
- [24] C. J. Kaalund and D. Haneman, “Positive ion and electron emission from cleaved Si and Ge,” *Phys. Rev. Lett.*, vol. 80, no. 16, pp. 3642–3645, 1998.
- [25] E. Busch and D. Haneman, “Fracture phenomena in silicon imaged by infrared radiation from ejected small particles,” *App. Phys. Lett.*, vol. 73, no. 4, pp. 484–486, 1998.
- [26] N. Bernstein and D. W. Hess, “Lattice trapping barriers to brittle fracture,” *Phys. Rev. Lett.*, vol. 91, p. 025501, Jul 2003.
- [27] M. de Koning, A. Antonelli, M. Z. Bazant, E. Kaxiras, and J. F. Justo, “Finite-temperature molecular-dynamics study of unstable stacking fault free energies in silicon,” *Phys. Rev. B*, vol. 58, no. 19, pp. 12555–12558, 1998.
- [28] D. Holland and M. Marder, “Ideal brittle fracture of silicon studied with molecular dynamics,” *Phys. Rev. Lett.*, vol. 80, no. 4, pp. 746–749, 1998.
- [29] F. F. Abraham, J. Q. Broughton, N. Bernstein, and E. Kaxiras, “Spanning the continuum to quantum length scales in a dynamic simulation of brittle fracture,” *Europhys. Lett.*, vol. 44, no. 6, p. 783, 1998.
- [30] J. G. Swadener, M. I. Baskes, and M. Nastasi, “Molecular dynamics simulation of brittle fracture in silicon,” *Phys. Rev. Lett.*, vol. 89, no. 8, p. 085503, 2002.
- [31] M. J. Buehler, H. Tang, A. C. T. van Duin, and W. A. Goddard, III, “Threshold crack speed controls dynamical fracture of silicon single crystals,” *Phys. Rev. Lett.*, vol. 99, no. 16, p. 165502, 2007.
- [32] D. Sen, C. Thaulow, S. V. Schieffer, A. Cohen, and M. J. Buehler, “Atomistic study of crack-tip cleavage to dislocation emission transition in silicon single crystals,” *Phys. Rev. Lett.*, vol. 104, no. 23, p. 235502, 2010.
- [33] M. T. Kim, “Influence of substrates on the elastic reaction of films for the microindentation tests,” *Thin Solid Films*, vol. 283, no. 1–2, pp. 12–16, 1996.
- [34] G. T. A. Kovacs, *Micromachined transducers sourcebook*. Boston, MA: McGraw-Hill, 1998.

- [35] A. M. Fitzgerald, R. S. Iyer, R. H. Dauskardt, and T. W. Kenny, "Subcritical crack growth in single-crystal silicon using micromachined specimens," *J. Mater. Res.*, vol. 17, pp. 683–692, 2002.
- [36] A. M. Fitzgerald, R. H. Dauskardt, and T. W. Kenny, "Fracture toughness and crack growth phenomena of plasma-etched single crystal silicon," *Sens. Actuators A, Phys.*, vol. 83, pp. 194–198, 2000.
- [37] B. Bhushan and X. Li, "Micromechanical and tribological characterization of doped single-crystal silicon and polysilicon lms for microelectromechanical systems devices," *J. Mater. Res.*, vol. 12, pp. 54–63, 1997.
- [38] F. Ericson, S. Johansson, and J. Schweitz, "Hardness and fracture toughness of semiconducting materials studied by indentation and erosion techniques," *Mat. Sci. and Eng.: A*, vol. 105, pp. 131–141, 1988.
- [39] J. T. Su and W. A. Goddard, III, "Excited electron dynamics modeling of warm dense matter," *Phys. Rev. Lett.*, vol. 99, p. 185003, 2007.
- [40] R. Pérez and P. Gumbsch, "Directional anisotropy in the cleavage fracture of silicon," *Phys. Rev. Lett.*, vol. 84, pp. 5347–5350, 2000.
- [41] T. Cramer, A. Wanner, and P. Gumbsch, "Crack velocities during dynamic fracture of glass and single crystalline silicon," *Physica Status Solidi (a)*, vol. 164, no. 1, pp. R5–R6, 1997.
- [42] Y. M. Huang, J. C. H. Spence, O. F. Sankey, and G. B. Adams, "The influence of internal surfaces on the  $(2\bar{A}-1)$  shuffle and glide cleavage reconstructions for Si(111)," *Surface Science*, vol. 256, no. 3, pp. 344–353, 1991.
- [43] K. C. Pandey, "Reconstruction of semiconductor surfaces: Buckling, ionicity, and  $\pi$ -bonded chains," *Phys. Rev. Lett.*, vol. 49, pp. 223–226, 1982.
- [44] R. Hull, *Properties of Crystalline Silicon*. Herts, United Kingdom: INSPEC, The Institute of Electrical Engineers, 1999.

## Chapter 4

# The Electron Dynamics of Shocked Polyethylene Crystal

### 4.1 Abstract

Electron force field (eFF) wavepacket molecular dynamics simulations of the single shock Hugoniot are reported for a crystalline polyethylene (PE) model. The eFF results are in good agreement with previous DFT theories and experimental data which is available up to 80 GPa. We predict shock Hugoniots for PE up to 350 GPa. In addition, we analyze the phase transformations that occur due to heating. Our analysis includes ionization fraction, molecular decomposition, and electrical conductivity during isotropic compression. We find that above a compression of  $2.4 \text{ g/cm}^3$  the PE structure transforms into a Lennard-Jones fluid, leading to a sharp increase in electron ionization and a significant increase in system conductivity. eFF accurately reproduces shock pressures and temperatures for PE along the single shock Hugoniot.

### 4.2 Shocked Polyethylene

The material response of polyethylene (PE) to shock and its behavior in the warm dense matter (WDM) regime is important because it is a common ablator material in direct-drive inertial confinement fusion (ICF) experiments [1, 2]. Experiments at the National Ignition Facility (NIF) have demonstrated that the capsule material can have a considerable impact on the ICF burn efficiency

[2, 3]. Macroscopic modeling of capsule materials for these experiments requires accurate constitutive engineering models. Producing quality engineering models requires a detailed microscopic understanding of the equations of state (EOS), electrical conductivity, and optical properties for a given material. Here, we examine the effects of electronic excitations during hydrostatic shock of PE.

Theoretical studies of PE in extreme conditions are abundant. A variety of methods including quantum mechanics (QM), conventional forcefields, and reactive forcefields are able to reproduce a common equation of state gauge: the experimental Rankine-Hugoniot curve [1, 4]. Born-Oppenheimer quantum molecular dynamics (BOQMD) methods and conventional forcefields presume adiabaticity in their approach to simulating the high energy states of PE. This assumption limits the scope of these techniques to temperatures well below the Fermi-temperature, near the electronic ground state of PE [5]. Conventional and reactive forcefields are parameterized based on Born-Oppenheimer potential energy surfaces. The result of using Born-Oppenheimer methods is that the effects of electronic excitations are absent from the system’s EOS, and along the particular EOS path corresponding to the Rankine-Hugoniot. Quantum mechanical finite-temperature density functional theory (DFT) methods, unlike BOQMD approaches, allow for electron excitations, however the Kohn-Sham orbital description precludes these methods from revealing dynamic electron effects like Auger processes [6, 7]. Finite-temperature DFT methods, like those used in [4] and [1], are good points of comparison for eFF because they allow for thermal electron excitations.

### 4.3 Crystalline Polyethylene Model and Computational Methods

A crystalline PE model was created by truncating and hydrogen passivating the chains in a  $2 \times 6 \times 3$  supercell of orthorhombic polyethylene (see Figure 4.1). Truncating the chains in this fashion prevents unnatural stresses from forming along the length of each chain. The final cell contained 12  $C_{12}H_{26}$  molecules: 1,632 particles total (144 carbon, 312 hydrogen, and 1,176 electrons). In real

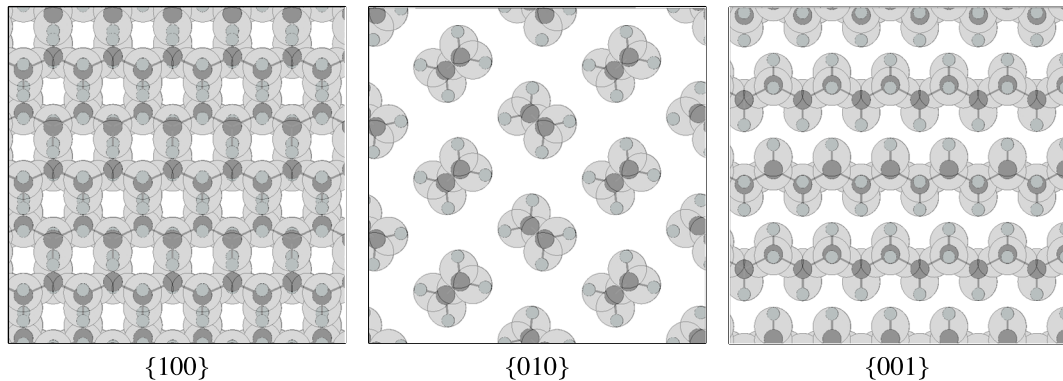


Figure 4.1: Three views of orthorhombic polyethylene with electrons.

samples of crystalline PE the chains are finite in length and the PE is only crystalline in small domains with lamella ranging from 70 to 300 Å in thickness and extending several microns laterally [8, 9]. Because eFF lacks van der Waals forces, the equilibrium volume of crystalline PE is 30% too large in eFF. To counter this, the volume of the PE cell was adjusted so that the ground state reference has a density of 0.95 g/cm<sup>3</sup>; this produced 1.3 GPa of stress which was subtracted from all subsequent pressure computations. To generate points along the Hugoniot path, we prepared samples of increasing density up to 3.0 g/cm<sup>3</sup> by isothermally and isotropically compressing the reference cell at 300 K. Each cell was then ramped to 1,500 K over the course of 500 fs and it was allowed to equilibrate as an NVE ensemble at 1,500 K for another 500 fs. After heating each cell was cooled by decreasing the temperature in 30 K steps during which 200 fs of NVT dynamics was followed by 200 fs of NVE dynamics. The Nosé-Hoover thermostat was used for sample preparation.

In Chapter 2 the various definitions and uses of electron mass were explained. For this study we wanted to accurately model the timescale of electronic excitations so we carefully chose the dynamic electron mass. To do this we computed a few Hugoniot points with 1.0 amu, 0.1 amu, and 0.01 amu electrons and found negligible differences in pressure and temperature at these points. An artificially heavy electron mass enables the use of longer integration time steps. For this study we set the dynamic electron mass to 0.1 amu. To conserve mass in the system we subtracted the mass of each atom’s electrons from the standard atomic mass (e.g., we set carbon atom masses to 11.4107 amu and hydrogen atom masses to 0.90794 amu). Because we used light electrons we used

an integration time step of 0.5 attoseconds (0.0005 fs).

A Hugoniot curve is the locus of thermodynamic states that can be reached by shock compression of an initial state. These states satisfy the Rankine-Hugoniot energy condition [10, 11]

$$U - U_0 = \frac{1}{2}(P + P_0)(V_0 - V) \quad (4.1)$$

where  $U$  is the internal energy,  $P$  is the pressure of the system, and  $V$  is the cell volume. It is assumed that each point on this seam corresponds to a state of thermodynamic equilibrium wherein the stress state is hydrostatic. For solids, this latter condition is only valid when the yield stress is much lower than the mean stress [12]. When the initial state variables  $P_0$ ,  $V_0$ , and  $U_0$  are those of the uncompressed sample at room temperature, the Rankine-Hugoniot curve is called the principal Hugoniot. We generated states on the principal Hugoniot using the following iterative procedure. First the volume of the system is specified, representing a particular degree of compression. How each density point was prepared is described in the preceding paragraph. The temperature of the system is quickly increased by changing the set-point of the thermostat. 100 fs of dynamics are run after the thermostat jump, during which averages of the energy, temperature, and pressure of the new state are obtained. These values are used to evaluate the residual energy of each step  $E_{res,i}$ , given by

$$E_{res,i} = (U - U_0) - \frac{1}{2}(P + P_0)(V_0 - V). \quad (4.2)$$

When  $|E_{res,i}/E_{ke,i}| < 0.05$  the Hugoniot condition is considered satisfied. If this inequality is not satisfied an additional 100 fs iteration is performed. The new thermostat setpoint is calculated from:

$$T_{i+1} = T_i \left( 1 + 0.05 \left| \frac{E_{res,i}}{E_{ke,i}} \right| \right) \quad (4.3)$$

where  $E_{ke,i}$  is the average kinetic energy of the system at step  $i$ . Once this iterative procedure has converged, the thermostat is turned off and the system is allowed to propagate as a microcanonical (NVE) ensemble for an additional 1 ps. This calculation ensures that the Hugoniot condition is

actually met and the properties of the systems were obtained from these dynamics.

## 4.4 Results and Discussion

### 4.4.1 The Principal Hugoniot

Figure 4.2 is the principal Hugoniot projected onto the pressure-density plane. For compressions below  $2.0 \text{ g/cm}^3$  eFF matched the experimental and DFT Hugoniot points quite closely (see Figure 4.2b). At higher densities the eFF simulations overpredicted the shock pressure relative to DFT. Above  $2.0 \text{ g/cm}^3$  the results show that eFF is systematically “stiffer” than the experimental and DFT/AM05 [13] data. However, eFF outperforms several classical MD potentials such as AIREBO [14], OPLS [15], and exp-6 (not shown) [16]; the data for these can be found in [4]. eFF also outperformed the tight-binding QM method above  $2.0 \text{ g/cm}^3$ . These results demonstrate the difficulty in modeling the behavior of materials under shock compression. Figure 4.3 shows the temperature-pressure plane of the Hugoniot calculated by the methods for which temperature data was available. The system temperatures produced by the eFF calculations are in good agreement with conventional forcefields, reactive forcefields, and QM. The raw data presented in this Chapter is available in Appendix C, table C.6.

At high compression interesting material features appear in the principal Hugoniot. In the AM05 data series a shoulder feature appears at  $2.3 \text{ g/cm}^3$ . This feature is not as pronounced in the eFF Hugoniot, however, for both methods inflections in the temperature-density plane of the Hugoniot curve indicate phase transitions (see Figure 4.4). Subtle temperature suppression is evident in the eFF temperature-density curve at  $2.0$  and  $2.6 \text{ g/cm}^3$ . These data features correspond to tangible transitions in the the molecular structure. Mattsson reported that the AM05 shoulder at  $2.3 \text{ g/cm}^3$  corresponded to PE backbone bond breaking [4]. The causes for the eFF data features will be discussed shortly.

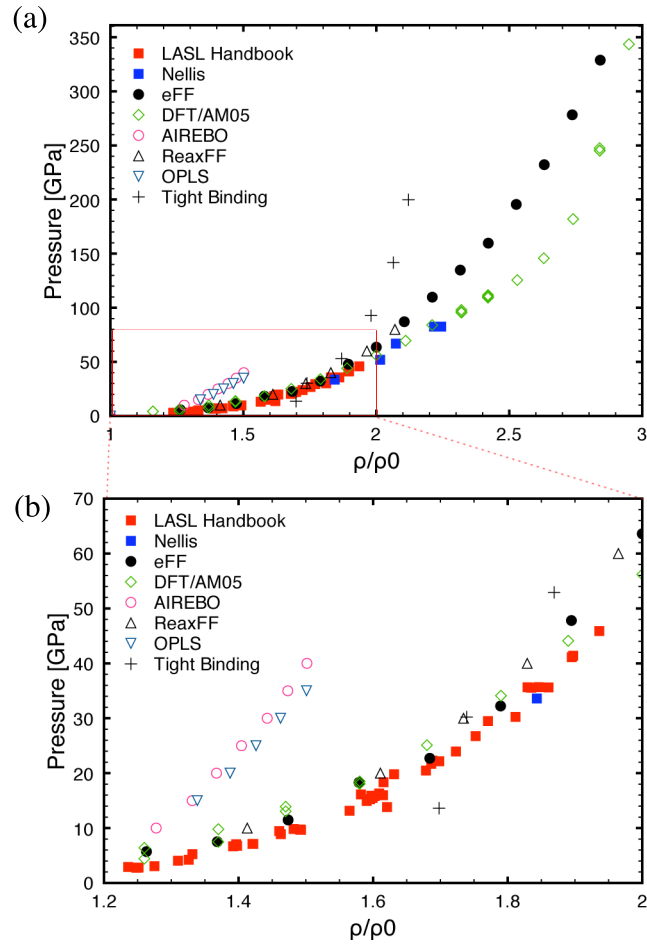


Figure 4.2: (a) The principal Rankine-Hugoniot for PE. Experimental data from the LASL shock compression handbook [17] and Nellis [18] is provided along with data for the classical MD potentials, OPLS [4], and AIREBO [4], a reactive force field, ReaxFF [4], and quantum mechanical approaches, DFT/AM05 and tight binding [19], for comparison. (b) An expansion of the low compression region of the Hugoniot.

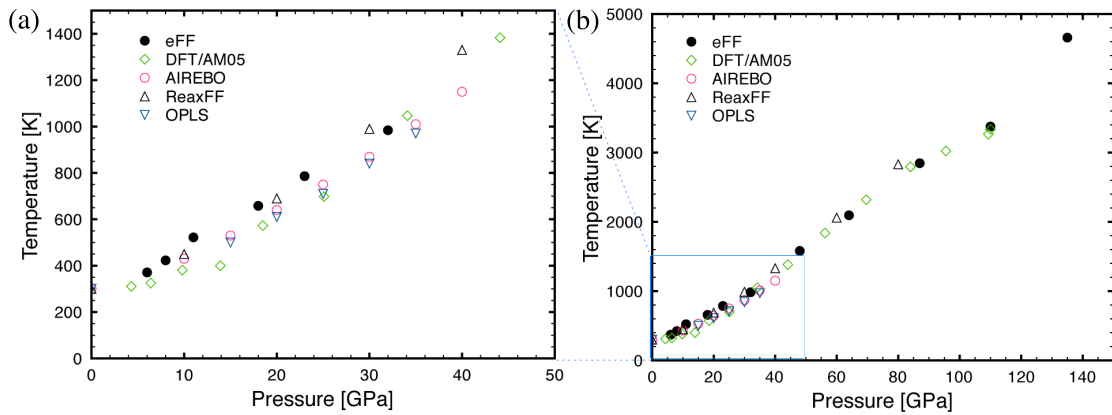


Figure 4.3: (a) The pressure-temperature locus of the Hugoniot curve for the eFF, DFT/AM05, OPLS, AIREBO, and ReaxFF methods. (b) The pressure-temperature seam at greater pressures.

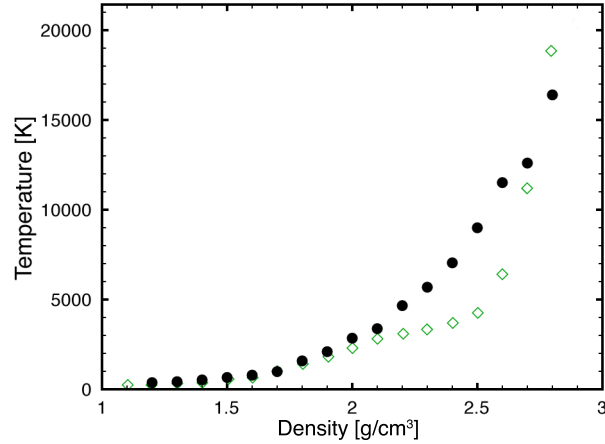


Figure 4.4: The temperature-density plane of the principal Hugoniot for the eFF (black circles) and DFT/AM05 (open green diamonds) methods.

#### 4.4.2 Structural Decomposition

An analysis of the pairwise radial distribution functions (RDFs) for different degrees of compression demonstrates that significant structural decomposition occurs upon shock. Figure 4.5(a) shows that carbon bonds are compressed as the sample is compressed. As the density of the material increases the nearest neighbor C-C pair peak (1.55 Å) broadens and the next nearest neighbor C-C pair distance (2.6 Å) is lost indicating that the carbon backbone is fragmented. The C-H pair distribution function in Figure 4.5b indicates a gradual phase change to an atomic fluid of hydrogens. The 2.9 g/cm<sup>3</sup> series resembles a Lennard-Jones fluid. At this level of shock compression the hydrogens are totally dissociated from the PE chains. The H-H pair distribution function in Figure 4.5c also shows that order is lost. At high compression the H-H RDF also resembles a Lennard Jones fluid. From this data we conclude that the structure is shocked strongly enough to cause a phase transition to a state where the carbon backbones remain partially intact but they are solvated by loosely associated hydrogen atoms. For densities corresponding to temperatures around 3,000 K small peaks in the H-H data in Figure 4.5c near 0.7 Å show that molecular hydrogen is formed. Mattsson and collaborators also found hydrogen formation when their shocked PE reached 2,800–3,100 K [20]. In their simulations and in the eFF simulations this temperature range corresponded to densities of 2.2–2.3 g/cm<sup>3</sup>. For temperatures higher than 3,100 K the molecular hydrogen becomes too energetic

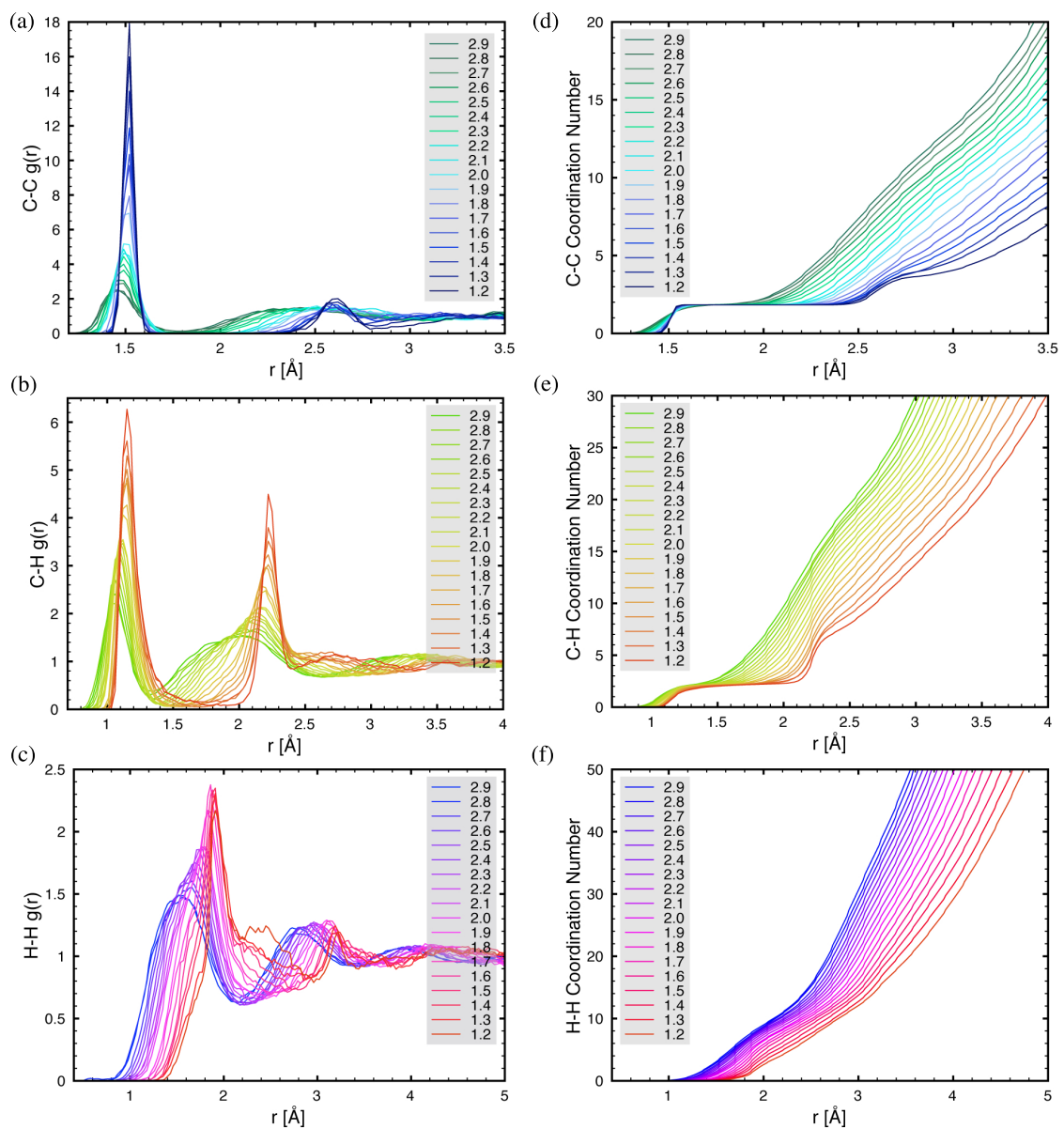


Figure 4.5: Radial distribution functions for (a) C-C atom pairs, (b) C-H pairs, and (c) H-H pairs. The corresponding coordination number functions for (d) C-C pairs, (e) C-H pairs, and (f) H-H pairs.

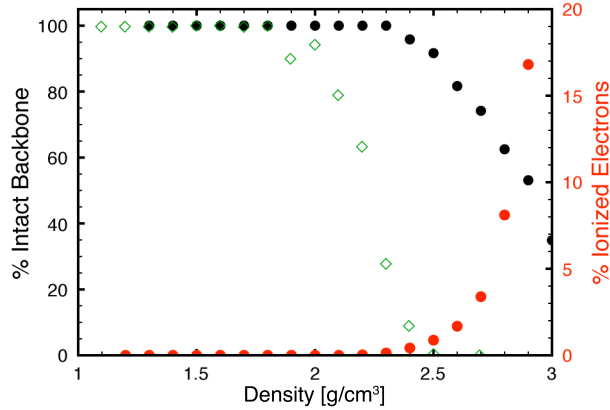


Figure 4.6: Structural decomposition along the PE Hugoniot. The open black circles and open green diamonds correspond to the % intact C-C backbone for the eFF and DFT/AM05 simulations, respectively. The red circles are the average % ionization along the Hugoniot calculated from the eFF simulations.

to stay bound, and at lower temperatures the hydrogen do not have enough energy to dissociate from their polyethylene backbone. The eFF results are consistent with MD and DFT results for equivalent temperatures.

One of eFF's greatest assets is its ability to separate electron degrees of freedom, energies, positions, momentum, and forces from those of the nuclei. This gives us unrivaled ability to measure electronic physical quantities. In our investigation of PE we have used this to measure the ion fraction at each stage of shock. To do this we measure the kinetic and potential energy of each electron at each timestep in our simulations. Figure 4.6 shows the onset of electron ionization at  $2.5 \text{ g/cm}^3$ . Ionization increases exponentially. The rapid increase in ionization fraction above  $2.6 \text{ g/cm}^3$  is evidently the cause of the shoulder in the temperature-density Hugoniot between  $2.6$  and  $2.7 \text{ g/cm}^3$ . Above this threshold electron ionization draws energy from the system and this affects the pressure and temperature of the Hugoniot. The production of carriers in our simulations implies that PE is conductive at high states of compression. The production of ions is precipitated by the breaking of C-C bonds, and this relationship is evident in Figure 4.6. The percentage of intact backbone for the DFT/AM05 study is also presented in Figure 4.6. eFF predicts that the polymer backbone begins to fracture at  $2.4 \text{ g/cm}^3$  and DFT/AM05 predicts that fracture begins at  $2.0 \text{ g/cm}^3$ . This discrepancy is due to the fact that eFF overestimates the strength of carbon-carbon  $\sigma$ -bonds (for

ethane the bond dissociation energy is 140 kcal/mol versus 90 kcal/mol experimental) [21].

### 4.4.3 Conductivity

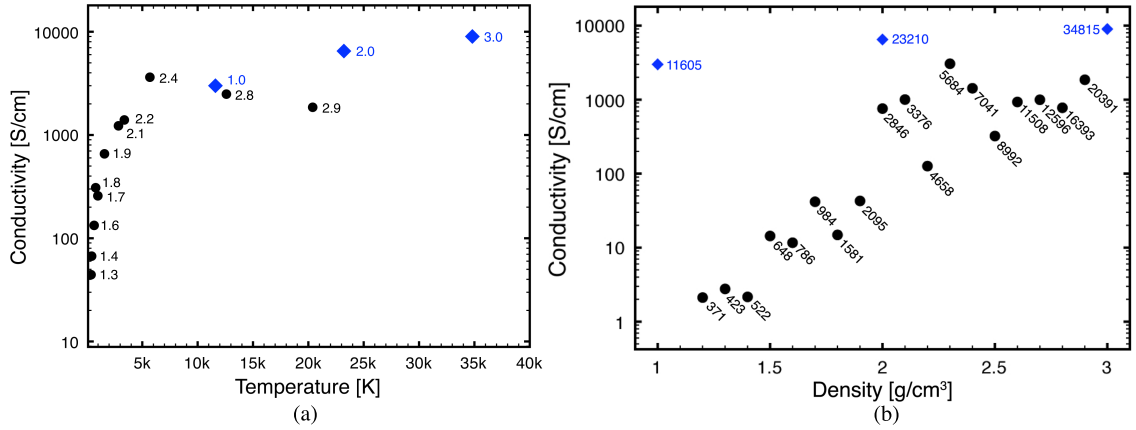


Figure 4.7: (a) The direct current electrical conductivity plotted against temperature and (b) plotted along the eFF Hugoniot curve (black circles). The blue diamonds are finite temperature DFT data points for PE in the warm dense matter regime [1].

In order to quantify the conductivity of the shocked system we determined the direct current conductivity using a classical Green-Kubo analysis [22, 23]. We determined the electrical conductivity in the same manner described in Chapter 3.4.3. Figure 4.7 shows the results of this analysis for eFF Hugoniot points. eFF predicts that conductivity increases exponentially along the Hugoniot curve until the temperature reaches roughly 5000 K at which point it levels off. Indeed, FT-DFT studies of PE in the warm dense matter [1] regime find conductivities between 3,000 and 10,000 S/cm for samples at 1 g/cm<sup>3</sup> and 11,605 K to 3 g/cm<sup>3</sup> and 34,815 K. Figure 4.7a shows the temperature dependence of the conductivity. Comparing the eFF and FT-DFT data as a whole, there is a clear transition to a metallic state in the vicinity of 5000 K. The downward slope connecting the density points 2.4, 2.8, and 2.9 reflects the sensitivity of the classical Green-Kubo method to thorough equilibration. Outliers were omitted from 4.7a, but all the data points are provided in 4.7b. Between 5000 K and 20391 K the sample has a conductivity of 2100 S/cm which is roughly equivalent to the conductivity of shocked fluid hydrogen at 140 GPa [24]. Above 2.5 g/cm<sup>3</sup>, in the semimetallic PE regime, the RDF analysis suggests that hydrogen is fluid. This suggests that our conductivity

analysis might be applicable to hydrogen-rich fluids at high temperatures and pressures.

The quality of our quasi-classical Green-Kubo analysis is a result of the accuracy of the eFF potential. Despite not being formulated in terms of occupied bands near the Fermi level, eFF produces the correct excitations. The eFF potential is rigorously derived from a solution to Schrödinger’s time-dependent equation of motion, which integrates two quantum-derived potential terms and classical electrostatics into its Hamiltonian. In particular, the Pauli function is parametrized based on the orthogonalization of valence bond-type orbitals. When a sample is well described by valence bonding, like polyethylene, eFF will succeed in modeling the potential of each electron. Each electron “feels” the correct potential, thus ionization potentials are accurate for Carbon and Hydrogen. In extreme conditions, the distribution of valence and core electronic states spreads and eventually the highest energy electrons become unbound much like the tail of a Fermi-Dirac distribution above the Fermi level. This behavior explains why we observe the correct carrier mobilities, ionization yields, and conductivities for eFF simulations in extreme conditions.

## 4.5 Conclusions

We have simulated the response of PE to hydrostatic shock compression using the eFF wavepacket molecular dynamics method. eFF accurately reproduces previously published experimental and theoretical findings for high energy shock Hugoniot of PE and provides further insight into the effects of electron excitations and ionization at extreme pressures and temperatures (e.g., above  $2.4 \text{ g/cm}^3$  the polymer backbone begins to break and electrons exponentially ionize). For 300 GPa shocks significant structural deterioration and ionization will occur. eFF also enabled us to study the electronic conductivity of PE as it transitions at high temperatures into a plasma phase; a unique feature that is impossible to obtain via conventional force fields or QM. The fidelity of the eFF Hugoniot indicates that van der Waals interactions are not important under extreme shock conditions. We expect the results presented in this paper will stimulate further work on the applicability of eFF to open problems in high energy-density physics.

# References

- [1] D. A. Horner, J. D. Kress, and L. A. Collins, “Effects of metal impurities on the optical properties of polyethylene in the warm dense-matter regime,” *Phys. Rev. B*, vol. 81, p. 214301, Jun 2010.
- [2] T. C. Sangster, R. Betti, R. S. Craxton, J. A. Delettrez, D. H. Edgell, L. M. Elasky, V. Y. Glebov, V. N. Goncharov, D. R. Harding, D. Jacobs-Perkins, R. Janezic, R. L. Keck, J. P. Knauer, S. J. Loucks, L. D. Lund, F. J. Marshall, R. L. McCrory, P. W. McKenty, D. D. Meyerhofer, P. B. Radha, S. P. Regan, W. Seka, W. T. Shmayda, S. Skupsky, V. A. Smalyuk, J. M. Soures, C. Stoeckl, B. Yaakobi, J. A. Frenje, C. K. Li, R. D. Petrasso, F. H. Sguin, J. D. Moody, J. A. Atherton, B. D. MacGowan, J. D. Kilkenny, T. P. Bernat, and D. S. Montgomery, “Cryogenic DT and D<sub>2</sub> targets for inertial confinement fusion,” *Phys. Plasmas*, vol. 14, no. 5, p. 058101, 2007.
- [3] P. Amendt, C. Cerjan, A. Hamza, D. E. Hinkel, J. L. Milovich, and H. F. Robey, “Assessing the prospects for achieving double-shell ignition on the national ignition facility using vacuum hohlraums,” *Phys. Plasmas*, vol. 14, no. 5, p. 056312, 2007.
- [4] T. R. Mattsson, M. D. Lane, K. R. Cochrane, M. P. Desjarlais, A. P. Thompson, and G. P. Grest., “First-principles and classical molecular dynamics simulation of shocked polymers,” *Phys. Rev. B*, vol. 81, p. 054103, 2010.
- [5] S. Pittalis, C. R. Proetto, A. Floris, A. Sanna, C. Bersier, K. Burke, and E. K. U. Gross, “Exact conditions in finite-temperature density-functional theory,” *Phys. Rev. Lett.*, vol. 107, p. 163001, Oct 2011.
- [6] N. D. Mermin, “Thermal properties of the inhomogeneous electron gas,” *Phys. Rev.*, vol. 137, pp. A1441–A1443, Mar 1965.
- [7] R. Car and M. Parrinello, “Unified approach for molecular dynamics and density-functional theory,” *Phys. Rev. Lett.*, vol. 55, pp. 2471–2474, Nov 1985.
- [8] M. J. Doyle *Polym. Eng. Sci.*, vol. 40, no. 2, pp. 330–335, 2000.
- [9] N. K. Bourne, J. C. F. Millett, and S. G. Goveas, “The shock response of polyoxymethylene and polyethylene,” *J. Phys. D.: Appl. Phys.*, vol. 40, pp. 5714–5718, 2007.
- [10] W. J. M. Rankine *Phil. Trans. Roy. Soc.*, vol. 160, p. 277, 1870.
- [11] H. Hugoniot *J. de l’Ecole Polytechnique*, vol. 57, p. 3, 1887.
- [12] M. B. Boslough and J. R. Asay, *High-Pressure Shock Compression of Solids*. New York, NY: Springer-Verlag, 1993.
- [13] R. Armiento and A. E. Mattsson, “Functional designed to include surface effects in self-consistent density functional theory,” *Phys. Rev. B*, vol. 72, p. 085108, 2005.
- [14] S. J. Stuart, A. B. Tutein, and J. A. Harrison, “A reactive potential for hydrocarbons with intermolecular interactions,” *J. Chem. Phys.*, vol. 112, p. 6472, 2000.

- [15] W. L. Jorgensen, D. S. Maxwell, and J. Tirado-Rives, "Development and testing of the opls all-atom force field on conformational energetics and properties of organic liquids," *J. Am. Chem. Soc.*, vol. 118, p. 11225, 1996.
- [16] O. Borodin, G. D. Smith, and D. Bedrov, "Development of many-body polarizable force fields for li-battery components: 1. ether, alkane, and carbonate-based solvents," *J. Phys. Chem. B.*, vol. 110, p. 6279, 2006.
- [17] S. P. Marsh, *LASL Shock Handbook*. Berkeley, CA: University of California Press, 1980.
- [18] W. Nellis, F. Ree, R. Trainor, A. Mitchell, and M. Boslough, "Equation of state and optical luminosity of benzene, polybutene, and polyethylene shocked to 210 gpa," *J. Chem. Phys.*, vol. 80, p. 2789, 1984.
- [19] J. D. Kress, S. R. Bickham, L. A. Collins, B. L. Holian, and S. Goedecker, "Tight-binding molecular dynamics of shock waves in hydrocarbons," *AIP Conference Proceedings*, vol. 505, no. 1, pp. 381–384, 2000.
- [20] T. R. Mattsson and K. R. Cochrane, "Pair correlations for the hydrostatic shock of polyethylene." Private communication, 2010.
- [21] J. T. Su, *An Electron Force Field for Simulating Large Scale Excited Electron Dynamics*. PhD thesis, California Institute of Technology, Pasadena, CA, 2007.
- [22] Y. Shim and H. J. Kim, "Dielectric relaxation, ion conductivity, solvent rotation, and solvation dynamics in a room-temperature ionic liquid," *J. Phys. Chem. B*, vol. 112, pp. 11028–11038, 2008.
- [23] M. H. Kowsari, S. Alavi, B. Najafi, K. Gholizadeh, E. Dehghanpisheh, and F. Ranjbar, "Molecular dynamics simulations of the structure and transport properties of tetra-butylphosphonium amino acid ionic liquids," *Phys. Chem. Chem. Phys.*, vol. 13, pp. 8826–8837, 2011.
- [24] W. J. Nellis, S. T. Weir, and A. C. Mitchell, "Minimum metallic conductivity of fluid hydrogen at 140 GPa (1.4 Mbar)," *Phys. Rev. B*, vol. 59, pp. 3434–3449, Feb 1999.

## Chapter 5

# Core Pseudoparticles as an Effective Core Potential

### 5.1 Motivation

The motivation for developing an effective core potential (ECP) for eFF is threefold. First, separating electrons into two classes – core and valence – allows us to remove chemically inert core electrons from the calculation. Minimizing the number of electrons required to describe each atom reduces the computational workload and this creates the possibility of performing calculations with hundreds of thousands of *atoms*. Besides reducing the total number of electrons, excluding the core electrons permits the use of longer integration time steps, since the Nyquist rate is typically set by the fast radial breathing modes of core electrons. Lastly, the ECP parameters can be used to improve atomic and molecular properties for which all-electron eFF is deficient. In this chapter the theory and rationale behind the novel ECP form will be explained and the fitting technique will be described. A variety of validation cases are provided and the performance of the ECP is compared to all-electron eFF.

### 5.2 Theoretical Development of Core Pseudoparticles

The first effective core potentials for FSGO methods became available in the early 1970s, and these largely mimicked the function of pseudopotential methods for Hartree-Fock techniques [1, 2]. Frost's

FSGO method was supplemented with a pseudopotential that replaced the core electrons of atoms up to germanium [3] through the use of angular momentum projectors [3–5]. The general form of the effective potential by Topiol and coworkers is

$$V(r_i) = \frac{-n_v}{r_i} + \sum_i \frac{B_l P_l}{r_i^2} \quad (5.1)$$

where  $V(r_i)$  is the potential felt by the  $i^{\text{th}}$  valence electron and  $n_v$  is the number of valence electrons,  $B_l$  is a parameter, and the projector onto the  $l^{\text{th}}$  angular momentum state is

$$P_l = \sum_m |lm\rangle\langle lm|. \quad (5.2)$$

This type of pseudopotential has the advantage of having an analytic form for each  $B_l$  in terms of the Hartree-Fock atomic valence orbital energies. This function is also fast to integrate over the FSGO functions [4]. Interestingly, the authors of these early studies found that more sophisticated pseudopotentials provided *poorer* results [4]. The effective potential has two purposes: to replace the Coulomb and exchange integrals over the core orbitals, and to enforce the Pauli exclusion principle. Being that there are no Coulomb or exchange integrals in eFF, and considering the failure of sophisticated pseudopotentials to yield the best results for similar FSGO methods, we surmised that following the approach of traditional angular-momentum-dependent pseudopotentials might not be the best option for eFF.

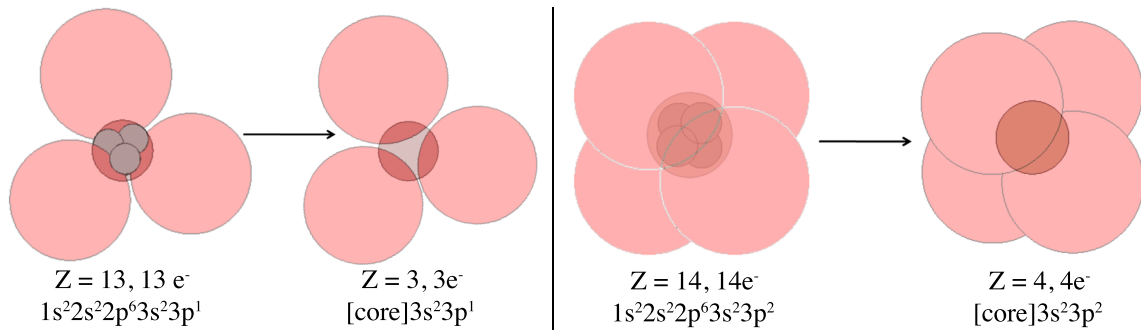


Figure 5.1: The construction of core pseudoparticles from all-electron atoms: aluminum (left) and silicon (right). The  $2sp^3$  core electrons are visible as tan nested tetrahedra.

In the spirit of eFF’s simplicity, we devised a novel form of effective core approximation. Our goal was to create the simplest possible effective core potential that would be fast to evaluate, and that would produce results at least as accurate as DFT calculations. Ultimately we devised a method whereby the nucleus and core electrons are coalesced together to form a “core pseudoparticle”. Figure 5.1 is a conceptualization of this process. The particle’s interactions with other nuclei and valence electrons will be determined by standard electrostatic interaction potentials and a pseudoparticle Pauli function to enforce the Pauli principle. Because both the core pseudoparticle and the valence electrons are spherical, this approach is termed an s-s overlap potential. The s-s overlap potential is expected to work well for  $sp^3$  hybridized electrons, or for bonding where the electron density is centered between the nuclei. There is no effective potential function to be evaluated, rather a simple set of pairwise energy interactions and forces are computed between each pseudoparticle and all other particles. This method is nicknamed “effcore”, since it is not a true pseudopotential method.

Aluminum and silicon were chosen as test cases for the development of effcore because they span two important electron regimes despite being separated by only one period. Aluminum has metallic electrons and silicon has covalent electrons. Besides this, aluminum is an important impactor and target material in hypervelocity impact experiments. Silicon is probably the most important material of the twentieth century. Each element has 10 core electrons, so significant savings are achieved by using a pseudoparticle.

This construction of a core pseudoparticle is conceptually simple but difficult to fit parameters to. Figure 5.1 shows the process for aluminum and silicon. In the case of aluminum, the atom contains 13 protons, 13ish neutrons, and 13 electrons. The core electron configuration is  $1s^2 2s^2 2p^3 3s^2 3p^1$ . Combining the 10 core electrons and 13 protons into a single particle produces a core pseudoparticle with a 3+ charge, a mass of 26.981539 amu, and an unknown radius. The three valence electrons are kept in the description of the atom. The core pseudoparticle has the same mass as the normal atomic mass so its dynamic properties are the same. What is left to be determined is the nature of the pseudoparticle’s electrostatic interactions and how it remains orthogonal to other orbitals (its Pauli potential).

The Hamiltonian for effcore is straightforward:

$$U(R, r, S, s) = E_{NN}(R) + E_{CC}(R) + E_{CN}(R) + E_{Ne}(R, r, s) + E_{Ce} + E_{ee}(r, s) + E_{ke}(s) + E_{Pauli}(\uparrow\downarrow, S) + E_{Pauli,C}(S). \quad (5.3)$$

The meaning of the subscripts is the same as in equation (2.3), except that we've also added the core pseudoparticles with subscript  $C$ . Besides the new electrostatic terms between cores, nuclei, and electrons, there is  $E_{Pauli,C}(S)$ , the Pauli potential between pseudoparticles and other electrons. Because we are making the assumption that cores are chemically inert, we have omitted a core electronic kinetic energy term; this essentially fixes the core radii. As a result, the core radius is a fitting parameter that is meant to reproduce the mean all-electron core radius under a wide variety of chemical environments. In §5.2.1 and §5.2.2 the new potential energy terms will be presented.

### 5.2.1 Core Pseudoparticle Pauli Potential

Consider the eFF wavefunction corresponding to a single silicon atom; it has the form of the wavefunction in equation (2.3). We can rewrite this as a factored product of core and valence electrons:

$$\Psi = \prod \Psi_{core} \prod \Psi_{valence}. \quad (5.4)$$

The electron density corresponding to the core electrons must be removed and replaced with an analytic function describing the Pauli repulsion between the collective core electron density and valence electrons (or other atom's electrons). The core electron wavefunction is just the product of each basis function for the core electrons:

$$\Psi_{core} = \prod_j^{N_{core}} \exp\left[-\frac{(\mathbf{r} - \mathbf{x}_j)^2}{s_j^2}\right]. \quad (5.5)$$

From equations (2.10) and (2.11) it is evident that the Pauli energy is proportional to  $S^2$ , the squared overlap between the floating Gaussian functions. Consider the overlap,  $S$ , between the core electrons

and a single valence electron:

$$S = \int_{-\infty}^{\infty} \Psi_{core} \Psi_{v1}(\mathbf{r} - \mathbf{x}_v) dx = \int_{-\infty}^{\infty} \prod_j^{N_{core}} \exp\left[-\frac{(\mathbf{r} - \mathbf{x}_j)^2}{s_j^2}\right] \Psi_{v1}(\mathbf{r} - \mathbf{x}_v) dx. \quad (5.6)$$

This integral is the convolution of several Gaussian functions, and the convolution of two or more Gaussian functions is merely another Gaussian function [6, 7]. Developing an analytic expression to fit this Gaussian would be unwieldy, and so we give it a simplified form. We define the core-valence Pauli energy term in the following manner:

$$E_{Pauli,Ce}(r, s) = a \cdot \exp\left[-\frac{br^2}{(c + s_{val}^2)}\right] \quad (5.7)$$

where the function is centered on the core-pseudoparticle and  $r$  is the distance between the valence electron and the core pseudoparticle, and  $s$  is the radius of the valence electron. The fitting parameters,  $a$ ,  $b$ , and  $c$ , serve to approximate the effects of the Pauli interactions between the core electrons and the valence electron, and also to parameterize the Pauli interactions between the now absent core electrons.

## 5.2.2 Core Pseudoparticle Electrostatic Potentials

The new electrostatic potentials between core pseudoparticles and other nuclei and electrons are very similar to the interactions between electrons and other particles because of the Gaussian shape of both classes of particles. The Coulomb potentials are defined as:

$$E_{C,N} = \frac{1}{4\pi\epsilon_0} \sum_{i,j} \frac{Z_i Z_j}{R_{ij}} \text{Erf}\left[\frac{\sqrt{2}R_{ij}}{r_{core,j}^2}\right] \quad (5.8)$$

$$E_{C,e} = \frac{1}{4\pi\epsilon_0} \sum_{i,j} \frac{Z_i Z_j}{R_{ij}} \text{Erf}\left[\frac{\sqrt{2}R_{ij}}{\sqrt{r_{core,j}^2 + r_{e,j}^2}}\right] \quad (5.9)$$

$$E_{C,C} = \frac{1}{4\pi\epsilon_0} \sum_{i,j} \frac{Z_i Z_j}{R_{ij}} \text{Erf}\left[\frac{\sqrt{2}R_{ij}}{\sqrt{r_{core,j}^2 + r_{core,j}^2}}\right]. \quad (5.10)$$

In equations (5.8), (5.9), and (5.10),  $Z$  is the particle charge,  $R_{ij}$  is the distance between each particle, and  $r$  refers to the particle radius. The subscripts  $N$ ,  $C$ , and  $e$  refer to nuclei, core pseudoparticles, and electrons, respectively.

### 5.3 Fitting Technique

In effcore the parameters to be fit are in the core Pauli potential and the radius of the core pseudoparticle. Adjusting these parameters influences the structure and energy of the molecule or atom nonlinearly. For example, adjusting the core Pauli potential influences not just the radii of nearby electrons, but also their positions. Adjusting the radius of the core pseudoparticle has the same effect. And naturally, if bonding electrons move, so do the nuclei that they bind. This makes it difficult to fit parameters using linear least-squares fitting schemes, and it makes it nearly impossible to fit them by hand. Contrast this to fitting parameters in conventional forcefields (see Chapter 2.1.2 for more discussion); the fitting parameters have clear physical interpretations, thus fitting is more straightforward. Besides the fact that the fitting parameters in effcore have no clear physical meaning, the range of potential values is unknown for cores as complicated as those of aluminum and silicon. Fitting four parameters for effcore demanded a more sophisticated fitting scheme.

To search for a global minima in a four-dimensional parameter space where the range of values is unknown, stochastic optimization techniques are useful tools. A genetic algorithm is a general stochastic optimization method. Technically the method is a heuristic that seeks an optimal solution by mimicking the natural process of evolution [8]. Sets of system parameters are encoded as strings in a chromosome as a set of “genes”. These genes represent a candidate solution whose performance is measured by a “fitness function”. This function is defined entirely by the user so the GA method can be applied to nearly any type of optimization problem. The size of the population is defined by the user, and it consists of several individuals with randomly assigned alleles. Once the population is initiated, each member is passed through the fitness function and its performance is recorded by the algorithm. At this stage the most fit members of the population are selected for and this is the computational analogue of survival of the fittest. Once ranked, pairs of individuals are mated

in a process similar to reproduction. A crossover operator determines the genetic mixing in the reproduction process and a mutation operator can mutate certain genes. The mutation operator allows for some genetic drift and prevents the algorithm from converging into a local minima. In some GAs only a fraction of the individuals in the following generation are produced by reproduction; the remainder of individuals are introduced randomly to produce entropy in the heuristic. The algorithm continues in this manner until the maximum number of generations has been reached, or an optimal solution meets a convergence criterion. The method is highly flexible but user inputs like the number of generations, the population size, the mutation rate, and the initial distribution of genes can influence the rate of convergence and parameter space coverage. The latter effect may prevent the algorithm from converging to the global optimum.

The genetic algorithm does the hard work and the user is left to design the fitness function and choose the molecules in the fitting library. To find optimal parameters for silicon and aluminum, a balanced library of small molecules and bulk material values was constructed. The libraries contained  $\text{XH}_4$ ,  $\text{X}_2\text{H}_4$ ,  $\text{XH}_3$  radical, anion, and cation, X-H bond stretch intermediates, X-X bond stretch intermediates, Si-diamond bulk, and fcc-Al bulk ( $X = \text{Si}, \text{Al}$ ). From this set of molecules we extracted geometric values, heterolytic and homolytic bond dissociation energies, optimum lattice constants, cohesive curves, and bond curves. We aimed to include 3 to  $4N$  metrics in the fitness function where  $N$  is the number of parameters to be fit. The weighted differences between our fitness metrics and available experimental or QM data were used to compose the final fitness score. The weighting coefficients could be adjusted to favor certain properties (i.e., bond curves versus bond lengths and angles, or cohesive energy curvature). The final values were weighted towards optimal geometries and bond energies; bulk properties were sacrificed. The small basis size of the eFF wavefunction ensures that the final performance of any eFF method will be a compromise. The genetic algorithm was run with the following conditions: a four-gene chromosome (genes:  $a$ ,  $b$ ,  $c$ , and  $r_{\text{core}}$ ) defined the phenotypes of a population of 80 individuals that were allowed to evolve for 1000 generations with a mutation rate of 0.5. The parameters were constrained to  $\{x \in \mathbb{R} \mid 0 \leq x \leq 100\}$ . The results of these optimizations are presented in Table 5.1.

Element	a	b	c	$r_{\text{core}}$
Al	0.486	1.049	0.207	1.660
Si	0.321	2.283	0.815	1.691

Table 5.1: Parameter fits

The results of the genetic algorithm fitting procedure are reassuring. From a large range of potential values, the algorithm converged on a reasonable set of parameters. A striking result of the fit is that the Al and Si core pseudoparticles' radii are nearly the same value as Vanderbilt's ultrasoft pseudopotential radius for these two atoms: 1.6 bohr [9]. It's even reassuring that the algorithm converged on nearly the same value for the Al and Si radius since these atoms share core electron configurations. This occurred despite each atom having very different fitting libraries.

## 5.4 Computational Performance

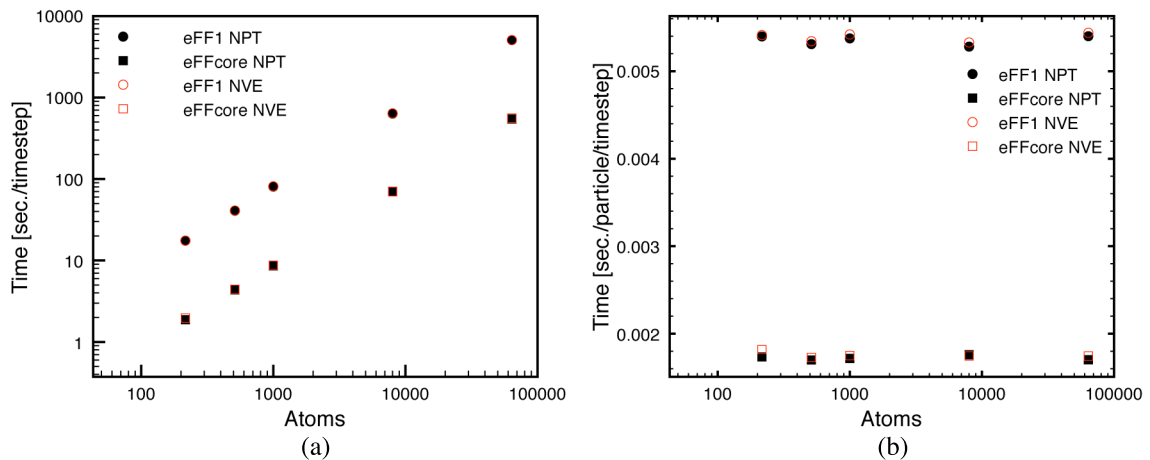


Figure 5.2: Single processor performance for bulk silicon: (a) The cpu time (in seconds) per timestep. (b) The cpu time per timestep per particle (includes nuclei and electrons). Run on a Linux CentOS 4.5/RHEL 4 system with 2.33 GHz Dual Quad Core Intel Xeon processors.

Effcore benefits from three performance advantages over eFF: (1) the total number of particles needed to model each atom is reduced, (2) energy evaluations between core pseudoparticles and electrons are faster than normal electron-electron energy evaluations, and (3) the integration time step that can be used for dynamics is increased significantly. Figure 5.2 shows the computational

performance of eFF and effcore for dynamics calculations on increasingly large bulk silicon supercells. Figure 5.2a demonstrates that effcore is about 10 times faster for any system size, and the computational time for both eFF and effcore scale linearly. The linear scaling is a result of using a spline-cutoff, bins, and neighbor lists (available in the LAMMPS implementation of eFF). Figure 5.2b shows that the speed-up is not a mere consequence of reducing the number of particles per atom. If the number of particles are normalized, effcore is still roughly 3 times faster than eFF because the core Pauli potential is faster to evaluate than an actual core electron-valence electron Pauli potential evaluation.

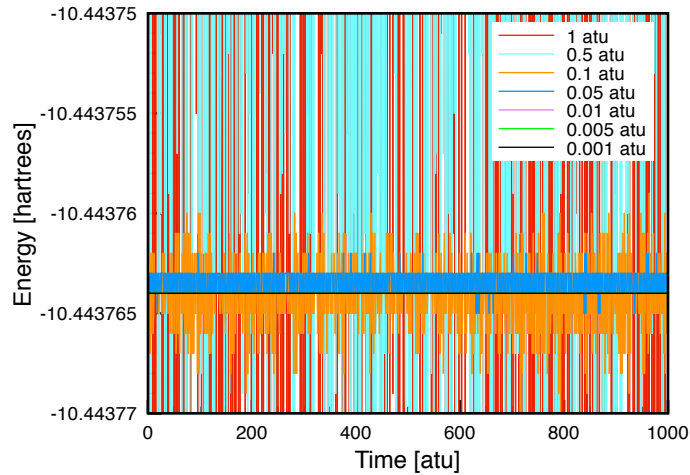


Figure 5.3: Conservation of energy during NVE dynamics.

Figure 5.3 shows the conservation of energy for effcore NVE dynamics (energy is plotted as the mean energy per molecule). In this representative system a gas of disilane particles is equilibrated at 300 K and then allowed to propagate as a microcanonical ensemble for roughly 1 ps (1 atu = 1.03 fs). In a similar eFF calculation an integration time step of 0.005 atu would have to be used. The data shows that 0.05 atu shows perfect energy conservation over 1000 atu; even 0.1 atu time steps did not drift, though the variance is  $\pm 3 \times 10^{-6}$  Hartrees per molecule. This means that 10 to 20 eFF time steps are needed where only 1 effcore time step is used. As stated earlier, this performance advantage can be attributed to removing the fast radial breathing modes of 1s core electrons, and to fixing the core pseudoparticle's radius.

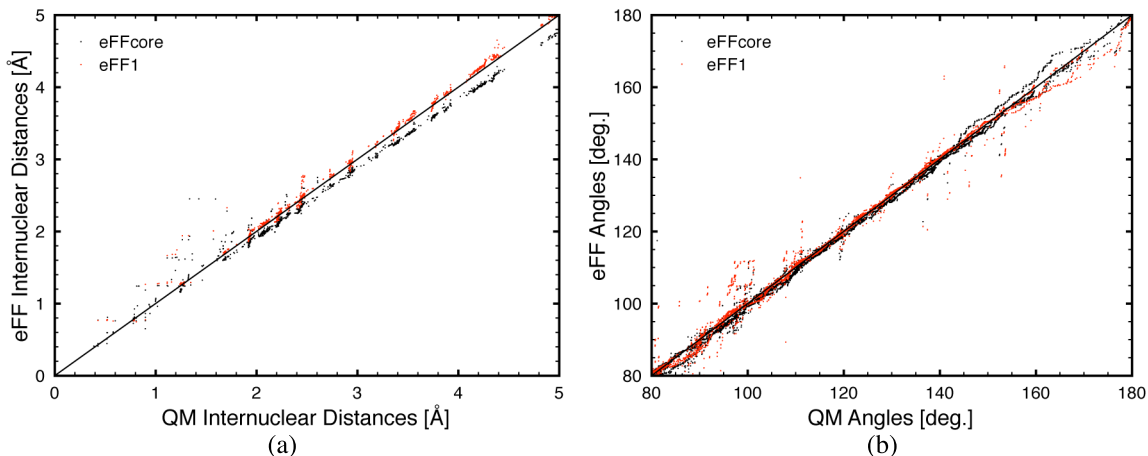


Figure 5.4: Comparisons of (a) internuclear distances and (b) angles between eFF1, eFFcore, and B3LYP/6-31g\*\* reference values for a variety of silicon hydrides and saturated silyl-hydrocarbons.

The net effect of the three performance enhancements is a 100–200 $\times$  speed-up for dynamics simulations depending on the chosen integration time step. This allows the user to perform calculations that are hundreds of times larger, or hundreds of times longer. It is worth mentioning that parallel eFF calculations scale linearly and this means that nearly any system size can be computed if enough processors are available [10].

## 5.5 Validation of the Fit Parameters

### 5.5.1 Silicon

This section will detail a series of validation tests for the fitted ECP. When examining these validation tests remember that many of these properties are emergent. While certain geometric properties and energies were explicitly fit, most were not. We begin with geometries for saturated silicon hydrides. eFF1 produces stable geometries for silicon hydrides and silicon bulk. The eFF1 core structure is an emergent property of the eFF Hamiltonian. 1s electrons are nuclei-centered. 2s and 2p electrons “hybridize” into  $2sp^3$  orbitals that arrange themselves like nested tetrahedra within the tetrahedral valence electrons (see Figure 5.1 for an example of this shell structure). This structure is obviously absent in eFFcore structures, but the nearly perfect  $sp^3$  tetrahedral bonding remains. Figure 5.4

Molecule	Si-H ( $\text{\AA}$ )		Si-Si ( $\text{\AA}$ )	
	eFFcore	qm	eFFcore	qm
SiH <sub>4</sub>	1.44	1.437	-	-
Si <sub>2</sub> H <sub>6</sub>	1.459	1.488	2.187	2.35
Si <sub>3</sub> H <sub>8</sub>	1.464 (1.486)	1.488 (1.491)	2.204	2.357
<i>t</i> -Si <sub>4</sub> H <sub>10</sub>	1.456 (1.518)	1.488 (1.494)	2.224	2.359
<i>q</i> -SiH <sub>5</sub> H <sub>12</sub>	1.466	1.488	2.246	2.361

Table 5.2: Small molecule bond lengths

Molecule	H-Si-H (deg.)		H-Si-Si (deg.)		Si-Si-Si (deg.)	
	eFFcore	qm	eFFcore	qm	eFFcore	qm
SiH <sub>4</sub>	109.5	109.5	-	-	-	-
Si <sub>2</sub> H <sub>6</sub>	107.9	108.4	111	110.5	-	-
Si <sub>3</sub> H <sub>8</sub>	108 (106.4)	108.5 (107.4)	110.8 (108.8)	110.8 (109.1)	115.1	112.8
<i>t</i> -Si <sub>4</sub> H <sub>10</sub>	108	108.5	111.3 (106.6)	110.8 (108.1)	112.2	110.8
<i>q</i> -SiH <sub>5</sub> H <sub>12</sub>	107.4	108.4	111.5	110.6	109.5	109.4

Table 5.3: Small molecule angles

shows the computed internuclear distances and angle of a wide variety of silicon hydrides from eFF1 and effcore compared to DFT. eFF1 produces slightly longer bonds than B3LYP/6-31g\*\* and effcore produces slightly shorter bonds. Both perform well.

Figure 5.5 shows the placement of electrons and structures of primary, secondary, and tertiary substituted silicon hydrides and comparison overlays with DFT B3LYP/6-31g\*\* structures. Specific values for structural parameters are provided in Tables 5.2 and 5.3. In general, effcore slightly underestimates Si-H and Si-Si bond distances. The angles (and dihedral angles) are well represented in effcore. The Lewis bonding and hybridization of these complexes arise as a natural consequence of the proper balance of kinetic energy, electrostatic potential, and Pauli repulsion. These qualities also confer dynamic stability on these molecules, and indeed they are stable during NVT, NPT, and NVE dynamics. Figure 2.1 demonstrates this for low- and high-energy systems.

The solid phases of silicon are reasonably well described by effcore. Figure 5.6a shows the cohesive energy curves of silicon diamond for effcore, eFF1, and DFT PBE with a plane wave basis set. Effcore is a vast improvement over eFF1 with regards to the lattice constant. Both effcore and QM replicate the experimental lattice constant of 10.3 bohr (5.44  $\text{\AA}$ ). From the curvature of the cohesive energy curves the bulk modulus can be calculated. The experimental bulk modulus is

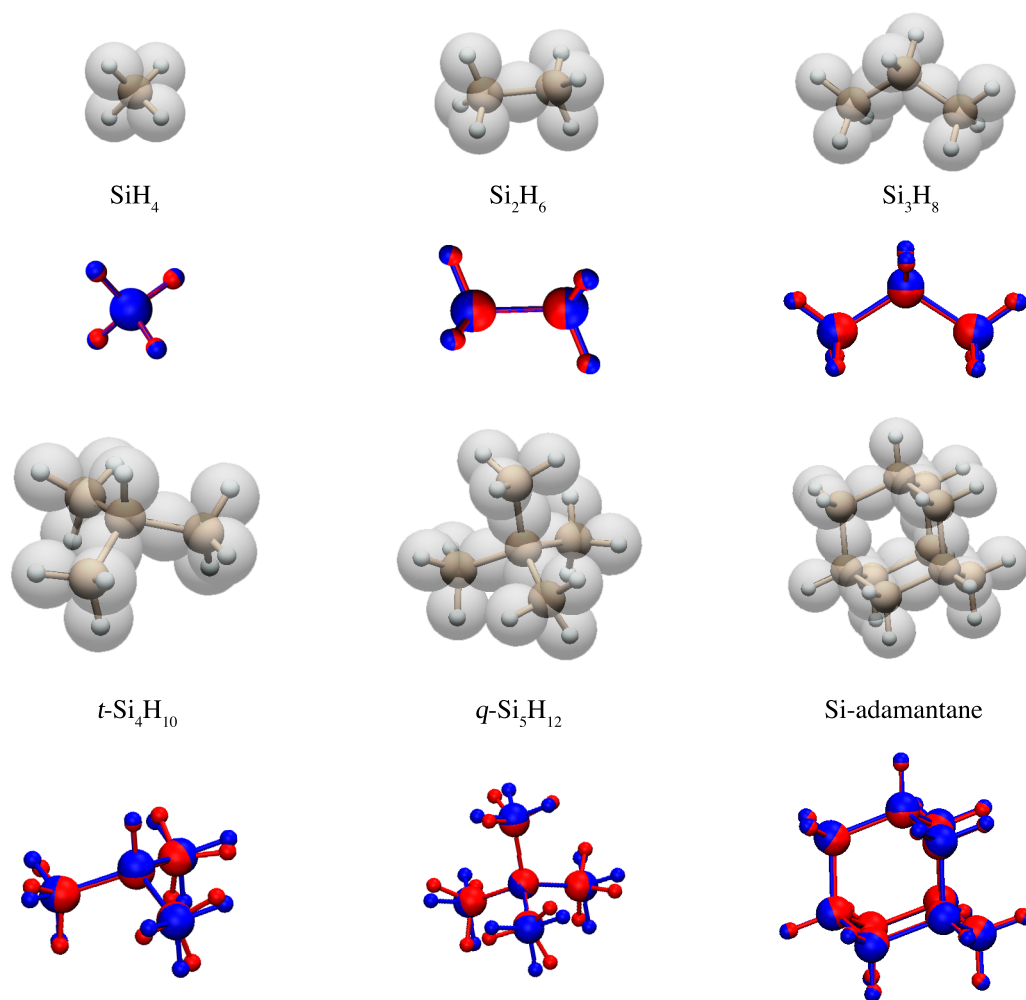


Figure 5.5: A gallery of primary, secondary, tertiary, and quaternary substituted silicon hydrides. Structures from effcore (red) are overlaid with those from B3LYP/6-31g\*\* (blue).

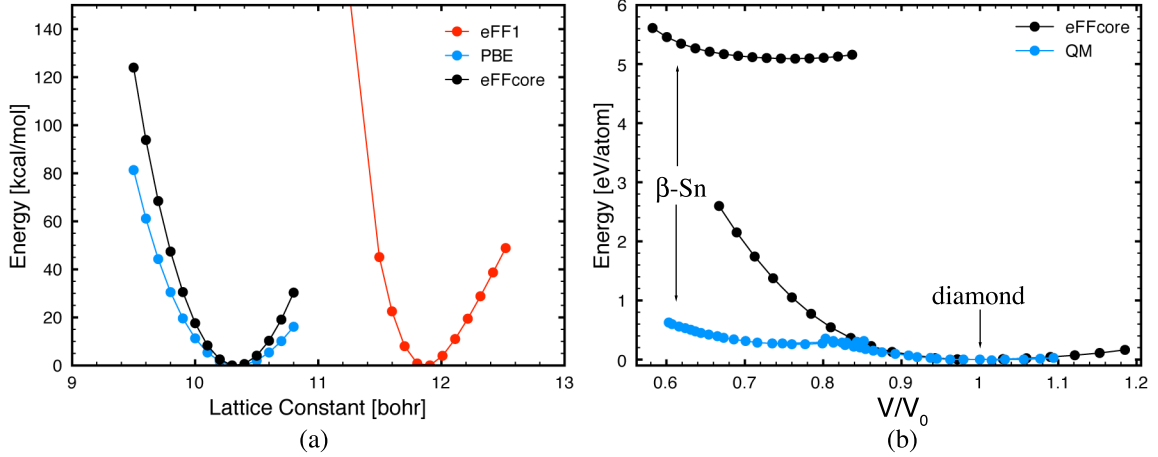


Figure 5.6: (a) Cohesive energy curves for silicon diamond (A4). (b) The energy of  $\beta$ -Sn silicon (A5) relative to the A4-silicon with QM values from [11].

Property	Experiment	eFF1	eFFcore
ionization potential [eV]	8.2	7.9	8.0
work function [eV]	4.6	4.7	3.1
bulk modulus $B_0$ [GPa]	100 <sup>†</sup>	200	200
Young's modulus $E$ [GPa]	160 <sup>†</sup>	-	160
shear modulus $G$ [GPa]	40 <sup>†</sup>	-	20*
yield strength [GPa]	7	-	15

Table 5.4: Emergent material properties. \*Calculated from the linear elastic relationship  $G = 9B_0E/9B_0 - E$ . <sup>†</sup> from reference [13].

100 GPa [12], but effcore produces a bulk modulus of 200 GPa. Table 5.4 compares the values of emergent properties between experiment, eFF1, and effcore. In general, eFF provides moduli that are too stiff; for example the carbon diamond bulk modulus is 440 GPa, but eFF predicts 800 GPa. We were able to find sets of parameters that produced bulk silicon with perfect bulk modulus, shear modulus, and Young's modulus, but these parameters also produced unstable small molecules and poor bond energies. We chose to sacrifice the quality of our bulk properties in order to obtain good bond energies and geometries.

Figure 5.6b shows the volumetric relative energy curves for  $\beta$ -Sn silicon and diamond silicon relative to the experimental volume. The  $\beta$ -Sn structure of silicon is a compressed phase that is distorted from the cubic diamond form by shortening the  $c$  lattice length so that  $c/a = 0.552$  [11, 14, 15]. The transition to the metallic  $\beta$ -Sn phase occurs under 9–12.5 GPa of pressure [11, 14],

and being that this falls within the definition of extreme pressure, being able to describe this phase is desirable. In the metallic  $\beta$ -Sn phase, each silicon is sixfold coordinated. This complicates the placement of  $\sigma$ -bonding electrons since bulk silicon has a filled octet, and a valence of four. The  $\beta$ -Sn structure leads to non-Lewis bonding. In the compressed structure, the radii of the electrons decreases and their electronic kinetic energy increases, thus the potential energy of the system increases. The degree of this response causes a gross overestimation of the potential energy and this is reflected in Figure 5.6b. Attempts to anneal the structure, and possibly find better electron configurations, were only marginally successful. In those cases the energy minima of the  $\beta$ -Sn phase was still 1 eV per atom above the diamond reference energy. Ultimately the localized electron description that eFF is inadequate for studying systems where electron delocalization or p-electron character are important.

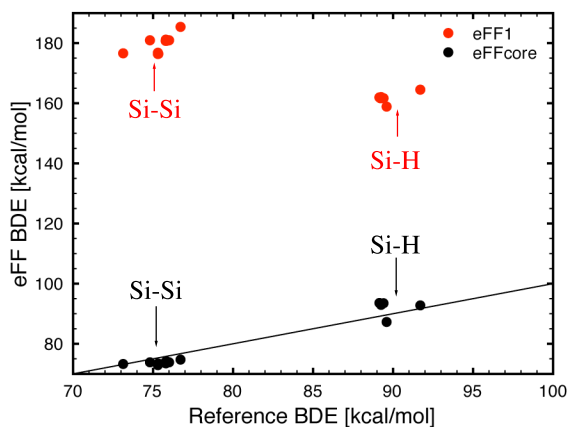


Figure 5.7: eFF homolytic bond dissociation energies versus reference QM or experimental data (values closer to the line are better). See Table 5.5 for the bonds and references.

Where eFFcore truly outperforms eFF is in its description of bond energies. Figure 5.7 shows the computed bond energies for a variety of compounds plotted against reference experimental values or DFT. Poor bond energies were heavily penalized in the GAs fitness function and so it is no surprise that eFFcore fixes eFF1's inability to predict homolytic bond dissociation energies. eFF1 over-predicts the strength of Si-Si bonds in absolute terms and relative to Si-H bonds. Si-H bond strengths are under-predicted in absolute terms and relative to Si-Si bonds. The quality of the eFFcore

bond energies for Si-Si bonds is largely responsible for the success of the simulations in Chapter 3.

Bond or Reaction	Reference	Expt/QM	eFF1	eFFcore
SiH <sub>3</sub> -H	[16, 17]	91.7	164.5	92.8
Si <sub>2</sub> H <sub>5</sub> -H	[16, 17]	89.1	161.9	93.6
SiH <sub>3</sub> -SiH <sub>3</sub>	[16]	76.7	185.3	74.7
Si <sub>2</sub> H <sub>5</sub> -SiH <sub>3</sub>	[16]	74.8	180.9	73.8
Si <sub>2</sub> H <sub>5</sub> -Si <sub>2</sub> H <sub>5</sub>	[16]	73.1	176.6	73.3
Si <sub>3</sub> H <sub>7</sub> -H	[18]	89.4	161.7	93.5
Si <sub>4</sub> H <sub>9</sub> -H	[18]	89.2	161.7	93.4
Si <sub>5</sub> H <sub>11</sub> -H	[18]	89.3	162.0	92.9
Si <sub>6</sub> H <sub>13</sub> -H	[18]	89.2	161.7	93.4
Si <sub>7</sub> H <sub>15</sub> -H	[18]	89.2	161.7	93.5
Si <sub>8</sub> H <sub>17</sub> -H	[18]	89.2	161.6	93.4
SiH <sub>3</sub> + Si <sub>2</sub> H <sub>5</sub> → Si <sub>3</sub> H <sub>8</sub>	[18]	76.0	180.9	73.8
SiH <sub>3</sub> + Si <sub>3</sub> H <sub>7</sub> → Si <sub>4</sub> H <sub>10</sub>	[18]	75.9	180.8	74.1
SiH <sub>3</sub> + Si <sub>4</sub> H <sub>9</sub> → Si <sub>5</sub> H <sub>12</sub>	[18]	75.8	180.8	74.0
SiH <sub>3</sub> + Si <sub>5</sub> H <sub>11</sub> → Si <sub>6</sub> H <sub>14</sub>	[18]	75.8	181.2	73.5
SiH <sub>3</sub> + Si <sub>6</sub> H <sub>13</sub> → Si <sub>7</sub> H <sub>16</sub>	[18]	75.8	180.6	74.0
SiH <sub>3</sub> + Si <sub>7</sub> H <sub>15</sub> → Si <sub>8</sub> H <sub>18</sub>	[18]	75.8	180.8	74.0
Si <sub>2</sub> H <sub>5</sub> + Si <sub>4</sub> H <sub>9</sub> → Si <sub>6</sub> H <sub>14</sub>	[18]	75.6	176.4	73.4
Si <sub>2</sub> H <sub>5</sub> + Si <sub>5</sub> H <sub>11</sub> → Si <sub>7</sub> H <sub>16</sub>	[18]	75.3	176.8	72.9
Si <sub>2</sub> H <sub>5</sub> + Si <sub>6</sub> H <sub>13</sub> → Si <sub>8</sub> H <sub>18</sub>	[18]	75.3	176.4	73.4
MeSiH <sub>3</sub> → CH <sub>3</sub> + SiH <sub>3</sub>	[19]	89.6	158.9	87.3

Table 5.5: Calculated bond dissociation energies (kcal/mol)

Reactive species are stable and well described by eFF. Figure 5.8 shows a series of electronic states of SiH<sub>3</sub>. Charged species and radicals are stable in eFF and effcore, and the energies of these species compare well to experimental and DFT values. One exception is that the electron affinity SiH<sub>3</sub> is incorrect. The planar SiH<sub>3</sub><sup>-</sup> species is unstable in effcore because it is unable to model the electron delocalization that should exist in this species. The geometry of the silyl radical is correctly predicted to be pyramidal instead of planar; high-level CI calculations support this result [20, 21].

Despite not being explicitly parametrized in eFF, properties like barriers to rotation and strain energies of cyclic molecules are well described. Table 5.6 shows the ring strain energies of the different conformers of Si<sub>6</sub>H<sub>12</sub>. Effcore performs slightly better than eFF1 and both compare well to QM. The rotational barrier of Si<sub>2</sub>H<sub>6</sub> is 1.12 kcal/mol, and eFF and effcore both predict 0.5 kcal/mol [22].

The validation tests in this section demonstrate that with only one basis function per electron, effcore provides accurate geometries for small molecules and bulk silicon. It predicts bond dissociation energies, ionization energies, the relative energy of reactive species, and other emergent properties

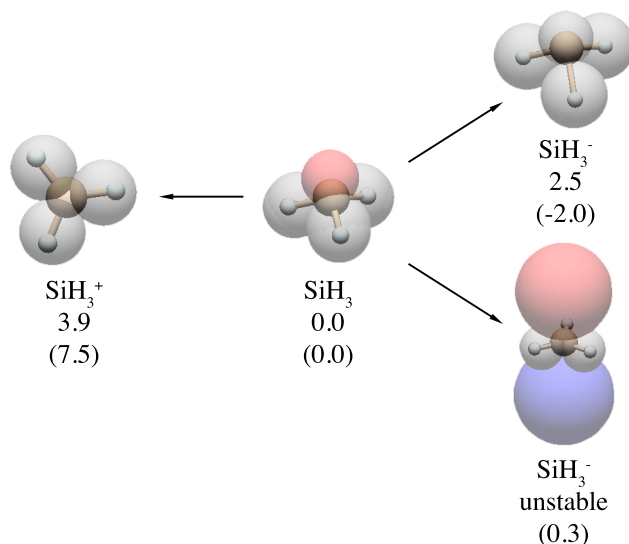


Figure 5.8: The energies (eV) of reactive  $\text{SiH}_3$  species. B3LYP/6-311g\*\*++ values are in parenthesis.

with good fidelity. With the exception of a few properties, the effcore approximation meets the goal that we initially set: it performs at least as well as DFT for a wide variety of systems. Of course, with effcore we can study systems much larger than can be studied with DFT, and we can do this in a broader range of conditions.

Method	chair	sofa	twist	boat	RMSD
B3LYP/6-311G**	0	3.1	1.8	2.1	0
eFF1	0	2.6	0.7	0.8	1.01
eFFcore	0	2.7	1.3	1.4	0.55

Table 5.6: Ring strain of various  $\text{Si}_6\text{H}_{12}$  conformers (kcal/mol)

### 5.5.2 Si(111)- $7\times 7$ Reconstruction

The elucidation of the Si(111)- $7\times 7$  surface reconstruction took some 22 years after its initial discovery [23, 24], and it took the work of theorists and experimentalists to reveal the complicated details of this surface. Though the structure has been resolved, the mechanism behind this transformation is still unclear [25]. We thought this complex rearrangement would be a good test study for the newly vetted effcore approximation for silicon.

The Si(111)- $7\times 7$  surface is produced by cleaving bulk silicon in ultrahigh vacuum along (111)

planes. Heating the surface to at least 650 K and allowing it to cool produces the  $7\times 7$  reconstruction. The currently accepted structure for this reconstruction is the dimer-atom-stacking fault (DAS) model of Takayanagi and coworkers [26]. Before beginning dynamics simulations, the surface energies of the various surface structures that comprise the DAS must be computed.

When this study began, eFF could only handle rectangular periodic boundary conditions, so supercells of the monoclinic structures were created and rectangular projections were extracted from these. Figure 5.9 shows some of the reconstruction intermediates. Slabs were created so that the z-dimension is finite and surrounded by vacuum on either side. The x and y dimensions are fully periodic. The slabs contain 6 bulk layers (3 (111) bilayers) and each slab is passivated by hydrogen on one side. The DAS model posits that adatoms are positioned on the top surface. Adatoms bind to three second-layer atoms and they either sit atop a third-layer atom, as in the  $\sqrt{3}\times\sqrt{3}$ T4 model, or they sit above a hollow in the surface such that the atom beneath is a fifth-layer atom, as in the  $\sqrt{3}\times\sqrt{3}$ H3 model. There are no H3 adatoms in the das $7\times 7$  model. The das $7\times 7$  structure is quite complex and an excellent description can be found in reference [25]. Simply put, the das $7\times 7$  reconstruction sits above  $7\times 7$  unit cells of Si(111). The surface contains 12 T4 adatoms, a 12 member ring hole with a fourth-layer dangling bond in the center, 18 dimer atoms, 6 second-layer dangling bonds in 8 member ring holes, and a stacking fault. To create this structure, the das $3\times 3$  model, and the das $5\times 5$  model, 3 layers that contain these features are added to the 6 layers of bulk silicon. The das $3\times 3$  model contains 2 T4 adatoms, a 12 member ring hole, a fourth-layer dangling bond, and 6 dimer atoms. The das $5\times 5$  model contains 6 T4 adatoms, a 12 member ring hole, 12 dimer atoms, 2 second-layer dangling bonds and a stacking fault. These structures were not trivial to prepare. eFF requires its user to place  $\sigma$ -bonding electrons between bonded atoms and the irregular structures and dangling bonds of the Si(111) reconstruction intermediates make this a challenging task.

The reason that the das $7\times 7$  model is the most stable annealed state of Si(111) surface is that it minimizes the number of dangling surface electrons. The das $7\times 7$  structure eliminates 30 dangling bonds, so 30 times the surface energy of the  $1\times 1$  unrelaxed surface (1.20 eV) is potentially gained, but in reality the das $7\times 7$  model only stabilizes the surface by 7.54 eV (0.26 eV per removed dangling

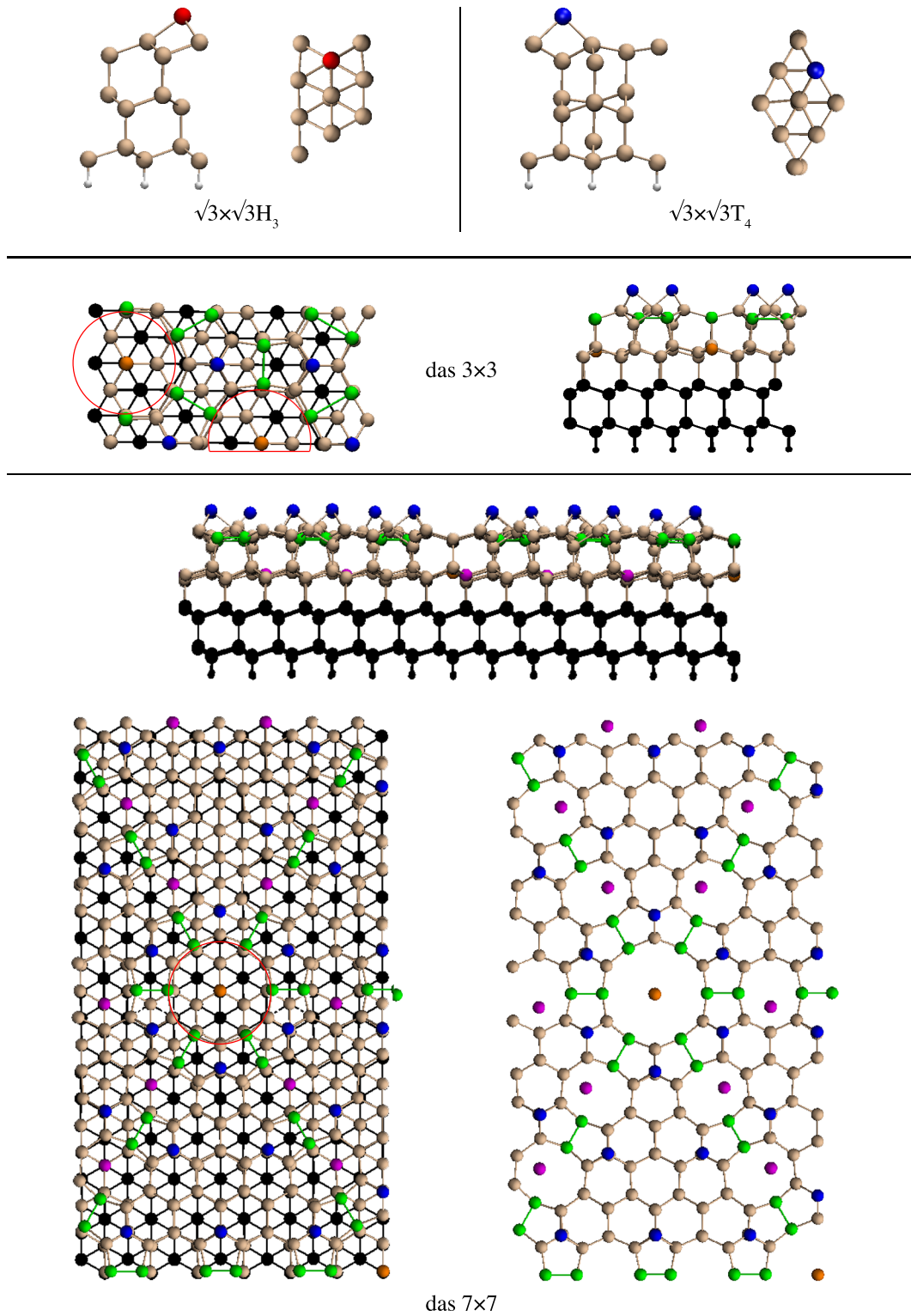


Figure 5.9: Si(111)-7 $\times$ 7 reconstruction intermediates. The das3 $\times$ 3 and das7 $\times$ 7 structures are actually rectangular 2 $\times$ 1 projections extracted from 2 $\times$ 2 supercells of the reconstruction models. T<sub>4</sub> adatoms are colored blue, fourth-layer dangling bond atoms are colored orange, dimer atoms are green, and second layer dangling bond atoms are colored magenta. In the das3 $\times$ 3 structure the 12 member ring hole is highlighted with red circles.

bond) – this is because a significant strain penalty is incurred. To ensure that the dynamics one observes will be correct, the surface energies of various surface states need to be computed to verify that their relative energies are ordered correctly. The surface energy,  $E_s$ , is defined by

$$E_s = \frac{E_m - (b \times E_b) - (m \times n \times E_{H1x1})}{m \times n} \quad (5.11)$$

where  $E_m$  is the minimized energy of the structure in question,  $b$  is the number of silicon atoms in the structure,  $E_b$  is the energy per silicon atom in bulk silicon,  $m \times n$  is the number of  $1 \times 1$  unit cells, and  $E_{H1x1}$  is the energy change per hydrogen atom when passivating an unreconstructed  $1 \times 1$  unit cell. The eFF analogues of the  $1 \times 1$  unrelaxed structure,  $\sqrt{3} \times \sqrt{3}\text{H3}$ ,  $\sqrt{3} \times \sqrt{3}\text{T4}$ , das3 $\times$ 3, das5 $\times$ 5, and das7 $\times$ 7 structures were minimized and their surface energies were computed according to (5.11). The results relative to the  $1 \times 1$  unrelaxed surface are presented in Table 5.7.

Method	unrelaxed slab	$\sqrt{3} \times \sqrt{3}\text{H3}$	$\sqrt{3} \times \sqrt{3}\text{T4}$	das3 $\times$ 3	das5 $\times$ 5	das7 $\times$ 7
DFT/PBE	0	0.13	-0.12	-0.15	-0.18	-0.18
effcore	0	-0.44	-0.06	1.7	1.3	0.81

Table 5.7: The energies of Si(111)-7 $\times$ 7 reconstruction intermediates relative to the unrelaxed surface energy [eV]

The results show that eFF incorrectly predicts that the  $\sqrt{3} \times \sqrt{3}\text{H3}$  and  $\sqrt{3} \times \sqrt{3}\text{T4}$  surfaces are more stable than any of the DAS reconstructions. Effcore incorrectly predicts that the H3 surface has a lower energy than the T4 surface. While effcore predicts the correct trend in the relative surface energies of the 3 $\times$ 3, 5 $\times$ 5, and 7 $\times$ 7 reconstructions, the sign and magnitude of their surface energies are incorrect. All three should be more stable than unreconstructed, unrelaxed Si(111) surface.

A close examination of the das7 $\times$ 7 model reveals the reason for this. DFT/PBE calculations show that the bond length between T4 adatoms and second-layer neighbors is 2.49 Å and the distance to the third-layer atom that it sits atop is 2.5 Å. Effcore predicts 2.48 and 2.9 Å for these two distances. The effcore angle between Si-T4-Si is 84.2°, while DFT/PBE measures 94.2° [25]. Since the nearest neighbor bond distance is correct while the next-nearest neighbor bond is too long, and since the Si-

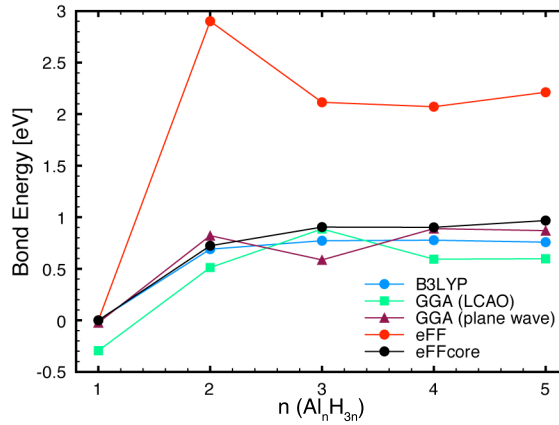
T4-Si angle is so acute, it is clear that the second-layer atoms are too crowded. The cell boundaries were also minimized, so this means that the stacking faults and dimer bonds introduce strain into the second and third layers of the reconstruction. The effcore dimer bonds measure alternating 2.57 Å and 2.47 Å as they radiate outward from the 12 member ring hole. The DFT/PBE dimer bonds measure 2.45 Å, meaning the effcore dimer bonds are too long; perhaps if they were shorter the T4 clusters wouldn't be so crowded. Even the bond between the silicon atom bearing the dangling electron in the center of the 12 member ring and bulk silicon is too short: 2.3 Å versus PBE's 2.39 Å. The cause of the surface strain is likely the dimer bonds which are too long. Without the flexibility to hybridize bonds to include more p-character, the effcore  $\sigma$ -bonds are too s-like, and thus too long. Since the stability of the DAS surface reconstructions is derived from balancing the elimination of dangling surface electrons and the strain introduced by the reconstruction, accurately modeling the energetic costs of each is critical to obtaining the correct surface energy.

### 5.5.3 Aluminum

The fit parameters for aluminum were validated against small aluminum hydride molecules and aluminum bulk.

Table 5.8 shows the geometries of  $\text{AlH}_3$  and  $\text{Al}_2\text{H}_6$ . Effcore and eFF correctly predict the three-center, two-electron bridged bond motif in  $\text{Al}_2\text{H}_6$ . The geometries indicate that both effcore and eFF do a good job of modeling this structure. While eFF bond lengths are generally better, effcore predicts more accurate bridge bond angles and lengths. In addition to these small molecules a series of  $\text{Al}_n\text{H}_{3n}$  ( $n = 1, 2, 3, \dots$ ) clusters were computed and their bond energies relative to the single  $\text{AlH}_3$  were compared to previous QM results and eFF. Effcore predicts the correct bond energies in both magnitude and trend, while eFF fails to reproduce either of these attributes correctly. However, for more complicated all-aluminum clusters (like those in references [27] and [28]), both eFF and effcore failed to produce stable structures. In these structures 90° bonds and unusual coordination numbers were overwhelming for eFF and effcore, which succeed with Lewis or VSEPR type bonding and fail with delocalized or unusually hybridized bonding types.

Bond/Angle	B3LYP	M06	eFF1	eFFcore
<u>AlH<sub>3</sub></u>				
Al-H	1.58	1.58	1.60	1.52
H-Al-H	120	120	120	120
<u>Al<sub>2</sub>H<sub>6</sub></u>				
Al-Al	2.58	2.61	2.20	2.67
Al-H	1.58	1.57	1.60	1.48
Al-bridge H	1.74	1.74	1.62	1.78
Al-Al-bridge H	42.1	41.4	47.1	41.5
H-Al-H	127.5	128.2	116.7	128.6
H-Al-bridge H	109.3	109.0	110.9	108.9
H-bridge H	2.68	2.70	2.65	2.66

Table 5.8: Aluminum hydride geometric values ( $\text{\AA}$  and degrees)Figure 5.10: The bond energies of  $\text{Al}_n\text{H}_{3n}$  clusters [eV]. QM from [28]

The fit values for effcore provide an improved description of bulk silicon. In eFF the lattice constant of fcc-aluminum is overestimated by some 4%. The lattice constant was a metric in the fitness function so naturally effcore matches the experimental value, 4.05  $\text{\AA}$ , perfectly. For reference, DFT/LDA slightly underestimates the lattice constant. These three methods are compared in Figure 5.11. From the curvature of the cohesive energy curves the 0 K bulk modulus values were calculated. eFF predicts a bulk modulus of 44 GPa while effcore predicts a value of 108 GPa while the room temperature experimental value is 76 GPa. Studies have found that the calculation of bulk moduli from quadratic fits to the cohesive energy tend to overestimate the moduli because they neglect temperature and zero-point phonon effects that exist in experimental measurements [29]. Gaudoin and coworkers found that when they removed these effects from the experimental measurement, the

actual bulk modulus was 81 GPa. Nonetheless, effcore is too stiff. We did not compute the higher energy bcc-Al phase, though we anticipate that, like the  $\beta$ -Sn phase in silicon, eFF and effcore will predict cell energies that are too high. This was also an issue in eFF studies on lithium; eFF predicted that the fcc phase is the ground state when actually the bcc phase is [30]. Partially periodic slabs are currently unstable with the Al effcore parameters listed in Table 5.1, and it is unclear why. Al slabs are stable with eFF1, but they become amorphous during minimization with effcore. This will have to be fixed before the effcore description of Al can be used in high velocity impact studies of Al.

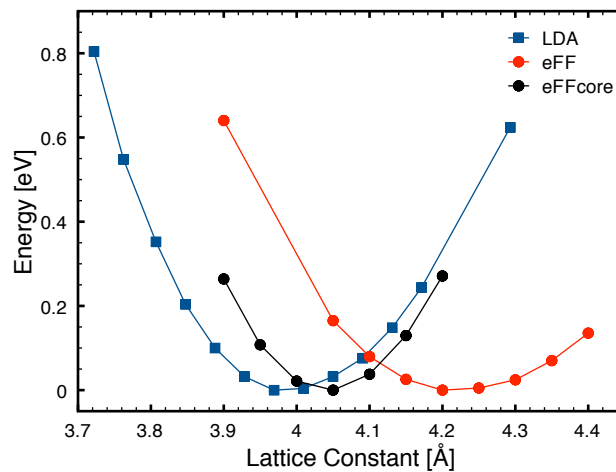


Figure 5.11: fcc-Al bulk cohesive energy curves. DFT/LDA from [29]

## 5.6 Future Directions

As mentioned in §5.2, the ECP presented in this chapter is based on the overlap and interaction of s-electrons. Consequently it works particularly well for systems where bonding is tetrahedral, or where electrons have a high degree of s-character. eFF2 [31] demonstrated that it is possible to model p-like electrons with s-like Gaussian functions if functions are used to describe the nature of the electron based on its position relative to other nuclear coordinates. A similar strategy could be used to extend the ECP to p-like systems. Alternatively, ellipsoidal basis functions could be used, but this would require re-deriving the equations of motion for the electrons. Future efforts to extend

this ECP should place an emphasis on describing double and triple bond energies, and the energies of heteroatom bonds and ionization potentials — eFF2 failed to improve on these features [31]. eFF has enormous potential as a fast method to study the dynamics of large complex systems, but much more work is needed so that elements like oxygen, nitrogen, and heavier atoms can be included in simulations.

# References

- [1] J. C. Barthelat and P. H. Durand, "Pseudopotentials and localized molecular orbitals. application to the methane molecule," *Chem. Phys. Lett.*, vol. 16, pp. 63–67, 1972.
- [2] L. R. Kahn and W. A. Goddard, III, "*Ab initio* effective potentials for use in molecular calculations," *J. Chem. Phys.*, vol. 56, pp. 2685–2701, 1972.
- [3] S. Topiol, J. W. Moskowitz, A. A. Frost, and M. A. Ratner, "Pseudopotential floating spherical Gaussian orbital calculations on group IV hydrides," *J. Chem. Soc., Faraday Trans. 2*, vol. 74, pp. 1521–1527, 1978.
- [4] S. Topiol, A. A. Frost, M. A. Ratner, and J. W. Moskowitz, "Use of pseudopotentials within the floating spherical Gaussian orbital method: Calculations on methane," *J. Chem. Phys.*, vol. 65, p. 4467, 1976.
- [5] S. Topiol, A. A. Frost, J. W. Moskowitz, and M. A. Ratner, "A new, simple *ab initio* pseudopotential for use in floating spherical Gaussian orbital calculations. 2. some results for hydrocarbons," *J. Am. Chem. Soc.*, vol. 99, no. 13, pp. 4276–4278, 1977.
- [6] G. B. Arfken, *Mathematical methods for physicists*. London, UK: Academic Press, 5th ed., 1985.
- [7] P. M. Morse and H. Feshbach, *Methods of Theoretical Physics, Part I*. Boston, MA: McGraw-Hill Science/Engineering/Math, 1953.
- [8] D. E. Goldberg, *Genetic algorithms in search, optimization, and machine learning*. Menlo Park, CA: Addison-Wesley, 1989.
- [9] D. Vanderbilt, "Soft self-consistent pseudopotentials in a generalized eigenvalue formalism," *Phys. Rev. B*, vol. 41, pp. 7892–7895, Apr 1990.
- [10] A. Jaramillo-Botero, J. T. Su, A. Qi, and W. A. Goddard, III, "Large-scale, long-term nonadiabatic electron molecular dynamics for describing material properties and phenomena in extreme environments," *J. Comp. Chem.*, vol. 32, no. 3, pp. 497–512, 2011.
- [11] M. T. Yin and M. L. Cohen, "Theory of static structural properties, crystal stability, and phase transformations: Application to Si and Ge," *Phys. Rev. B*, vol. 26, no. 10, p. 5668, 1982.
- [12] H. J. McSkimin and P. Andreatch, Jr., "Elastic moduli of silicon vs. hydrostatic pressure at 25.0°C and 195.8°C," *J. App. Phys.*, vol. 35, no. 7, pp. 2161–2165, 1964.
- [13] J. J. Wortman and R. A. Evans, "Young's modulus, shear modulus, and Poisson's ratio in silicon and germanium," *J. of App. Phys.*, vol. 36, no. 1, pp. 153–156, 1965.
- [14] M. Durandurdu and D. A. Drabold, "High-pressure phases of amorphous and crystalline silicon," *Phys. Rev. B*, vol. 67, no. 21, pp. 212101–212101, 2003.
- [15] J. S. Kasper and S. M. Richards, "The crystal structures of new forms of silicon and germanium," *Acta Crystallographica*, vol. 17, no. 6, pp. 752–755, 1964.

- [16] Y. R. Luo, *Handbook of bond dissociation energies in organic compounds*. Boca Raton, Florida: CRC Press, 2003.
- [17] Y. Luo and P. D. Pacey, "Methyl substituent effects on the dissociation energies of Si-X bonds," *J. Phys. Org. Chem.*, vol. 4, pp. 562–565, 1991.
- [18] I. Alkorta and J. Elguero, "Theoretical study of the bond energy in *n*-silanes and *n*-germanes: Comparison with *n*-alkanes," *Chem. Phys. Lett.*, vol. 429, pp. 58–61, 2006.
- [19] R. Walsh, "Bond dissociation energies in organosilicon compounds," *Acc. Chem. Res.*, vol. 14, pp. 246–252, 1981.
- [20] G. Olbrich, "MRD CI calculations of excited states of the SiH<sub>3</sub> radical, including potential curves for the inversion mode and the dissociation SiH<sub>3</sub> → SiH<sub>2</sub> + H," *Chem. Phys.*, vol. 101, no. 3, pp. 381–391, 1986.
- [21] C. Chatgililoglu, "Structural and chemical properties of silyl radicals," *Chem. Rev.*, vol. 95, no. 5, pp. 1229–1251, 1995.
- [22] B. Beagley, A. R. Conrad, J. M. Freeman, J. J. Monaghan, B. G. Norton, and G. C. Holywell, "Electron diffraction studies of the hydrides Si<sub>2</sub>H<sub>6</sub> and P<sub>2</sub>H<sub>4</sub>," *J. Mol. Struct.*, vol. 11, no. 3, pp. 371–380, 1972.
- [23] R. E. Schlier and H. E. Farnsworth, "Structure and adsorption characteristics of clean surfaces of germanium and silicon," *J. Chem. Phys.*, vol. 30, p. 917, 1959.
- [24] K. Kajiyama, Y. Tanishiro, and K. Takayanagi, "Reconstructions and phase transitions of Ge on the Si(111)-7×7 surface: II. 7×7 and 5×5 structures stabilized by Ge," *Surface Science*, vol. 222, no. 1, pp. 47–63, 1989.
- [25] S. D. Solares, S. Dasgupta, P. A. Schultz, Y. H. Kim, C. B. Musgrave, and W. A. Goddard III, "Density functional theory study of the geometry, energetics, and reconstruction process of Si (111) surfaces," *Langmuir*, vol. 21, no. 26, pp. 12404–12414, 2005.
- [26] K. Takayanagi, Y. Tanishiro, and S. Takahashi, "Structure analysis of the Si(111)-7x7 reconstructed surface by transmission electron diffraction," *Surf. Sci.*, vol. 164, pp. 367–378, 1985.
- [27] M. Alipour and A. Mohajeri, "Computational insight into the static and dynamic polarizabilities of aluminum nanoclusters," *J. Phys. Chem. A*, vol. 114, pp. 12709–12715, 2010.
- [28] H. Kawamura, V. Kumar, Q. Sun, and Y. Kawazoe, "Cyclic and linear polymeric structures of Al<sub>n</sub>H<sub>3n</sub> (n= 3-7) molecules," *Phys. Rev. A*, vol. 67, no. 6, p. 063205, 2003.
- [29] R. Gaudoin and W. M. C. Foulkes, "Ab initio calculations of bulk moduli and comparison with experiment," *Phys. Rev. B*, vol. 66, no. 5, p. 052104, 2002.
- [30] H. Kim, J. T. Su, and W. A. Goddard, III, "High-temperature high-pressure phases of lithium from electron force field (eFF) quantum electron dynamics simulations," *Proc. Nat. Acad. Sci.*, vol. 108, pp. 15101–15105, 2011.
- [31] J. T. Su, *An electron force field for simulating large scale excited electron dynamics*. PhD thesis, California Institute of Technology, Pasadena, CA, 2007.

## Appendix A

# Ligand Effects in Rhodium Catalyzed Methane Activation

### A.1 Introduction

Developing homogeneous catalysts for the conversion of natural gas products to liquid chemicals is an important industrial and academic goal. Despite the interest in this field, few working systems have been discovered. While many systems succeed at activating the alkyl or arene C-H bond, far fewer are capable of functionalizing the metal alkane bond to yield oxo-functionalized products [1–3]. Thus far the most successful catalytic cycles have relied on electronegative redox-active cations in oxy-acid solvents [4–7]. The high electronegativity of cations such as Pt(II), Hg(II), Pd(II), and Au(III) makes reductive heterolysis or elimination of M-R intermediates of these metals facile. C-H activation is also well established in earlier transition metals. For metals like Re, Os, Ir, and Ru, the relative electron-richness of the metal center makes C-H activation easy, but the electropositivity of these metals renders functionalization difficult [8, 9]. So far early transition metal-based catalysts have not been successfully incorporated into catalytic cycles which activate alkanes without free radicals, carbocations, or carboanions, and which oxo-functionalize the M-R species. In this contribution we wish to present theoretical findings that suggest a suitable catalyst for accomplishing this task in a mildly acidic aerobic solution.

Our work in this area began with studying the C-H activation mechanisms of Periana’s Hg(II)/sulfuric acid system and Shilov’s chloroplatinate/sulfuric acid system [4, 8]. Encouraged by acid protection

of the activated methyl group, we focused our studies on C-H activation by late transition metals in neat base. In studying these systems we developed an electrophilic paradigm for C-H activation in which electron-donating ancillary ligands are used to labilize coordinated solvent molecules [2, 8, 10, 10–15]. While the ancillary ligand allows for coordination of methane, it also decreases the electrophilicity of the metal center, thereby increasing the barrier to C-H activation by insertion. The barrier to substitution in these systems is decreased because the ancillary ligand increases the basicity of the coordinated base’s lone pairs by donating electron density through the metal’s d-orbitals. This paradigm led to the successful engineering of Pt(bpy), Pt(bpym), (NO)Pt, and (NNC)Pt systems for C-H activation [16]. The consequence of increasing electron density at the metal center is that the rate of functionalization may be concomitantly decreased, owing to the fact that this step is likely reductive. This was demonstrated in the Pt(bpym) work. Thus, more electron-rich metals such as Ir, Ru, and Zr are less likely to be incorporated successfully into catalytic cycles that create oxy-functionalized products.

We hypothesized that pairing a relatively electron-rich transition metal like Ir or Rh with a  $\pi$ -acidic ligand would help temper the metal’s electron richness. In fact, oxidative addition of rhodium to carbon-hydrogen bonds is already known [17–19]. With such a system the fine balance of electronics needed for the C-H activation and functionalization steps might be met with compromise. Goldberg’s C-H activation work on (PNP)Rh(I) phenoxide systems demonstrated that Rh with an electron-donating ancillary ligand is capable of activating the arene C-H bond under aqueous conditions [20, 21]. Our own theoretical studies on Ir revealed that Ir prefers the +3 oxidation state because of the accessibility of the vacant 6s orbital. Rh favors the Rh(I) oxidation state over Rh(III) because the 5s orbital is less accessible than the 4d orbitals. We expect C-H activation to be possible from both Rh(I) and Rh(III) because there are ample examples of both [18, 19].

N-heterocyclic carbenes, particularly those in pincer ligand motifs have demonstrated their utility in organometallic chemistry [22, 23]. Arduengo-type pincer carbenes in particular confer remarkably high entropic chelating effects when complexed with transition metals. This stability makes them robust to a variety of conditions, and their strong  $\sigma$ -donating ability confers novel electronic properties

to the complexes they form [24]. Goldberg’s work on Rh-catalyzed arene C-H activation prompted us to examine Rh complexed with 2,6-bis(methylimidazol-2-ylidene)-pyridine (CNC) ligand, which should be robust enough for reaction in aqueous or neat acidic or basic conditions.

Water inhibition is problematic for catalytic cycles carried out in fuming sulfuric acid, thus it is important to consider systems that are tolerant to the presence of water. Trifluoroacetic acid is moderately acidic ( $\text{pK}_a = 0.3$ ) and it is volatile. Trifluoroacetate (TFA) coordinates well to organometallic complexes, and, because it is a competent O-donor, it decreases water affinity by increasing electron density at the metal center [10]. As a solvent, TFA or its acid allow for close control of the reaction pH and the dielectric constant, which varies greatly based on water concentration [25]. Tuning the dielectric constant of the reaction medium presents us with another variable for optimizing barriers at various stages of the catalytic cycle. TFA may also be used as a nucleophile during the functionalization step.  $\text{S}_{\text{N}}2$  attack on the activated methyl group yields a reduced catalyst and methyl trifluoroacetate. Because the methyl ester of TFA has a low boiling point, TFA is an effective functionalizing agent and product protectant. The volatility of this product ensures that industrial separation of the product will be facile.

## A.2 Computational Methods

Quantum mechanical calculations were carried out using the B3LYP density functional. This functional is a combination of the hybrid three-parameter Becke exchange functional (B3) and the Lee-Yang-Parr correlation functional (LYP) as implemented in the Jaguar 7.5 electronic structure program [26, 27]. Geometry optimizations and solvation energy calculations were carried out using the Hay and Wadt effective core potential for Rh, and the Pople-style 6-31G\*\* basis for all other atoms and the valence electrons of Rh [28]. For singlepoint energy calculations the basis set for Rh was adapted from the 6-311G++\*\* basis by adding two f-functions, while the effective core potential was not changed.

Solvation energy calculations were carried out using the Poisson-Boltzmann model (PBF) [29]. For water, the dielectric constant was set to 80.37, and the probe radius was set to 1.40 Å. For neat

trifluoroacetic acid the dielectric constant was set to 20.0 and the probe radius was set to 2.45 Å. The dielectric constant of trifluoroacetic acid has been shown to vary with temperature and water concentration; a dielectric constant of 20.0 was chosen to fit reaction conditions at 300K and 1M H<sub>2</sub>O [30, 31]. We have found the calculated solvation energies of small ions like H<sup>+</sup> and OH<sup>-</sup> to be inaccurate, so instead we use their experimental free energies.

Stationary points and transition states were confirmed with normal-mode analysis. All geometric minima have precisely zero normal modes, while transition states have exactly one imaginary frequency. In cases where methyl rotations led to small negative or positive frequencies, we shifted frequencies below 50 cm<sup>-1</sup> to 50 cm<sup>-1</sup> and we recalculated the entropy of vibration.

The Gibbs free energies reported here are calculated as follows at a temperature of 298 K:

$$G = H - TS \tag{A.1}$$

$$H = E_{ZPVE}^{gp} + E_{SCF}^{gp} + H_{vib}^{gp} + H_{lib} + E_{solv} \tag{A.2}$$

$$S = S_{vib}^{gp}. \tag{A.3}$$

The enthalpy we calculate is based on the gas phase zero point vibrational energy, self-consistent field electronic energy, and vibrational enthalpy, librational enthalpy, and the energy of solvation calculated using PBF. The librational enthalpy accounts for hindered translation-rotations in solution, and we calculate these by summing  $1/2k_B T$  for the potential and kinetic energy of the three molecular translational and rotational modes, for a total of  $6k_B T$  per molecule. We calculate the entropy as the gas phase entropy of vibration with the operating assumption that low frequency modes ( $< 50 \text{ cm}^{-1}$ ) will not exist in solution.

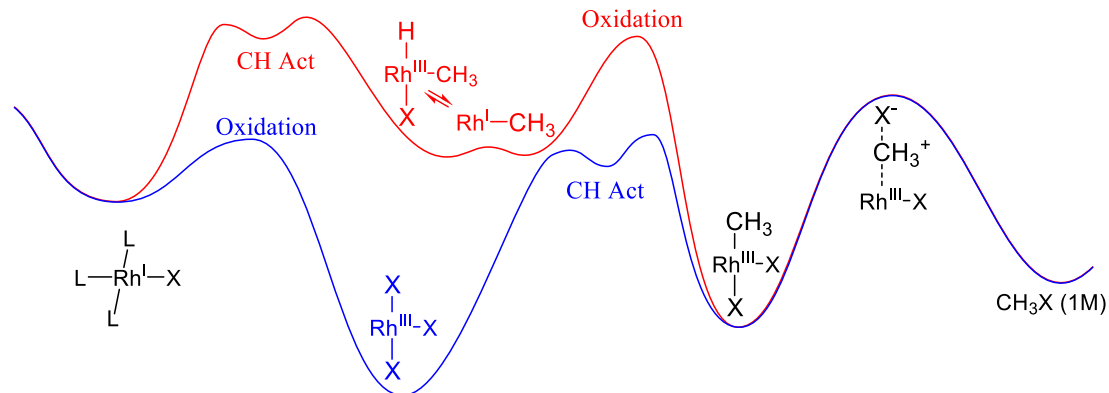


Figure A.1: Pathways for methane C-H activation using Rh(I) (red) and Rh(III) (blue) in solvent, X.

## A.3 Results and Discussion

### A.3.1 Two Pathways to C-H Activation

We hypothesized that C-H activation can occur through either the Rh(I) or Rh(III) oxidation states of Rh(CNC) and Rh(PNP<sup>Me</sup>) species and so we will discuss the full catalytic cycle for both oxidation states in the following sections. The scope of our investigation includes aqueous solvation with varying pH levels and solvation in trifluoroacetic acid (TFAH). Figure A.1 shows the C-H activation mechanisms for the Rh(I) and Rh(III) species. For each pathway a precursor complex undergoes ligand substitution with the solvent to yield a solvent-specific starting state. Coordination of methane is followed by C-H activation. Finally reductive functionalization of the methylrhodium species yields product and the regenerated catalyst. There are benefits and drawbacks to using each oxidation state. If the Rh(I) precursor can be protected from oxidation to Rh(III), then the cycle can take advantage of the comparatively low C-H activation barriers. The downside to the Rh(I) cycle is that the stability of the Rh(III)X<sub>2</sub>CH<sub>3</sub> species might reduce the availability of catalyst precursor. Additionally, one is always fighting oxidation when using Rh(I). This last flaw makes C-H activation from Rh(III) attractive, though the stability of Rh(III)X<sub>3</sub> species can make coordination and C-H activation barriers high. In both cycles the final step from Rh(III)X<sub>2</sub>CH<sub>3</sub> to product is endergonic.

In the following sections we present the free energies of intermediates and transition states for

both of these pathways and discuss the merits and deficiencies of both. We begin with the most promising system, Rh(III) in water, and follow with other calculated pathways that guided our search for a complete and viable pathway to C-H activation and functionalization.

### A.3.2 Rh(III) in Water

Figure A.2 shows the full catalytic cycle for the conversion of methane to methanol in water catalyzed by Rh(III)(CNC), Rh(III)(PNP), and Rh(III)(PNP<sup>CF3</sup>) at pH = 0. This cycle starts from a Rh(I)-OH<sub>2</sub> species like **1.1**, **2.1**<sup>CH3</sup>, or **2.1**<sup>CF3</sup>. For **1.1** oxidation to the various protonation states (**1.2**, **1.3**, **1.4**) are energetically favored, as expected. The same is true for **2.1**<sup>CH3</sup>, however, when the PNP methyl groups are substituted with electron withdrawing -CF<sub>3</sub> groups we find that the oxidation is slightly disfavored. This is because the trifluoromethyl groups decrease the electron density on **2.1**<sup>CF3</sup>, and this results in an increased oxidation potential. Another attractive aspect of the Rh(III) cycle is that in all cases, the oxidation step does not yield species lower in free energy than the overall catalytic cycle free energy of -29.8 kcal/mol. Even after the oxidation step there is still thermodynamic driving force for the reaction to proceed and produce CH<sub>3</sub>OH.

The relative stabilities and in-solution availabilities of species **1.2**, **1.3**, **1.4**, **2.2**<sup>R</sup>, **2.3**<sup>R</sup>, **2.4**<sup>R</sup>, and **2.5**<sup>R</sup> are dependent on the pH of the reaction solution, though we have shown the values for pH = 0. Using a low pH helps reduce the amount of Rh(III)(L)(OH<sup>-</sup>)<sub>3</sub> species, whose Rh(III)-OH bonds are less labile than Rh(III)...OH<sub>2</sub> bonds. At pH 0, **1.4** is the ground state for the Rh(III)(CNC) cycle. From **1.4**, coordinating a methane and displacing an aquo ligand produces [Rh(III)(CNC)(OH)(OH<sub>2</sub>)(CH<sub>4</sub>)<sub>2</sub>]<sup>+</sup> (not shown in scheme 1) which has a ΔG = 3.2 kcal/mol relative to **1.2**. From the methane complex, the internal electrophilic substitution transition state, **TS-IS.1**, is only 6.5 kcal/mol uphill. The overall barrier between **1.4** and **TS-IS.1** is 35.9 kcal/mol. Analogously, the ground state in the Rh(III)(PNP<sup>CH3</sup>) cycle is **2.2**<sup>CH3</sup>, though due to the high degree of positive charge on the complex and the nature of our implicit solvation model, the validity of this species' calculated free energy may be called into question. **2.4**<sup>CH3</sup> is slightly less stable at -26.7 kcal/mol. From **2.2**<sup>CH3</sup>, **TS-IS2**<sup>CH3</sup> is 37.6 kcal/mol uphill. If we account for alternative pH

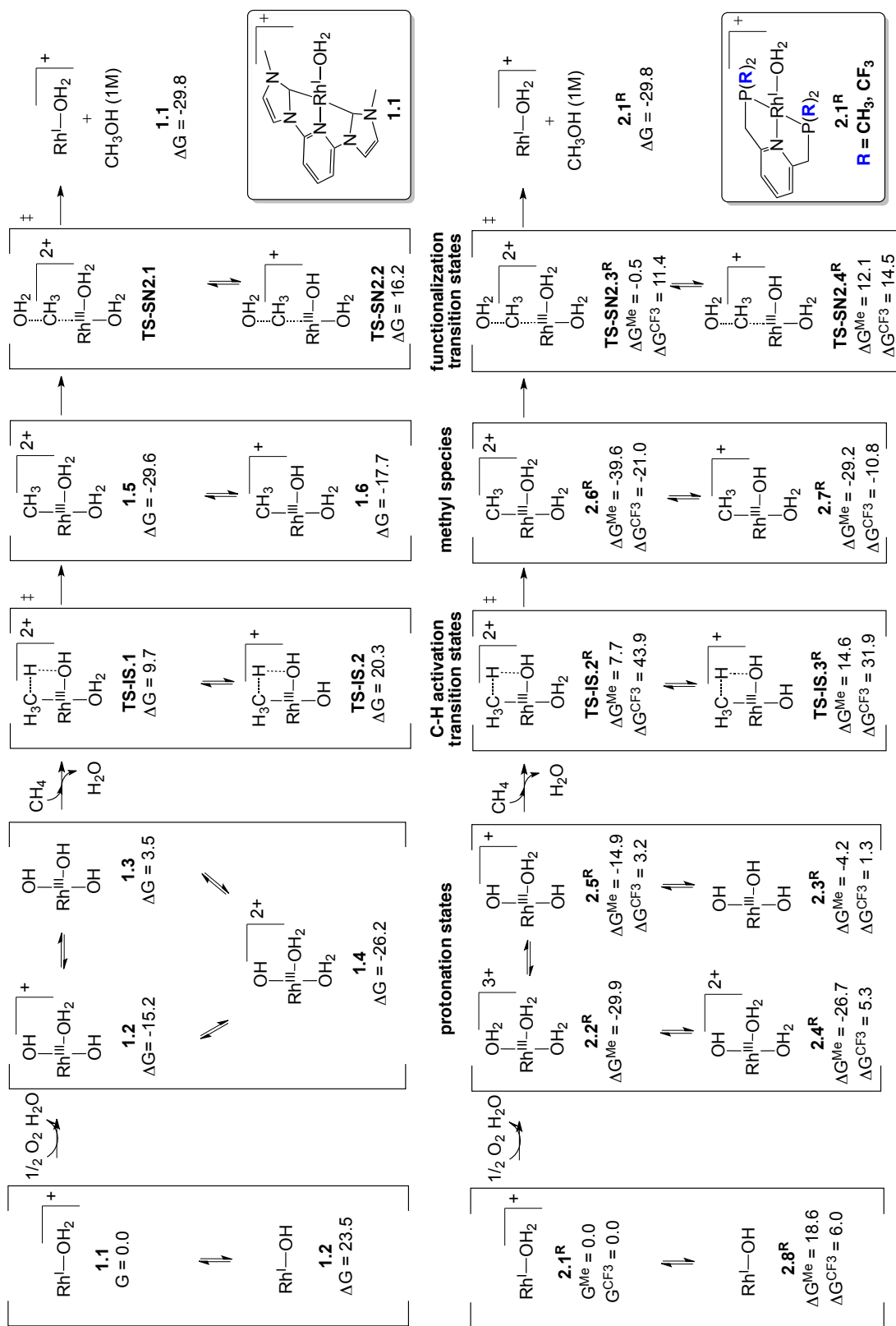
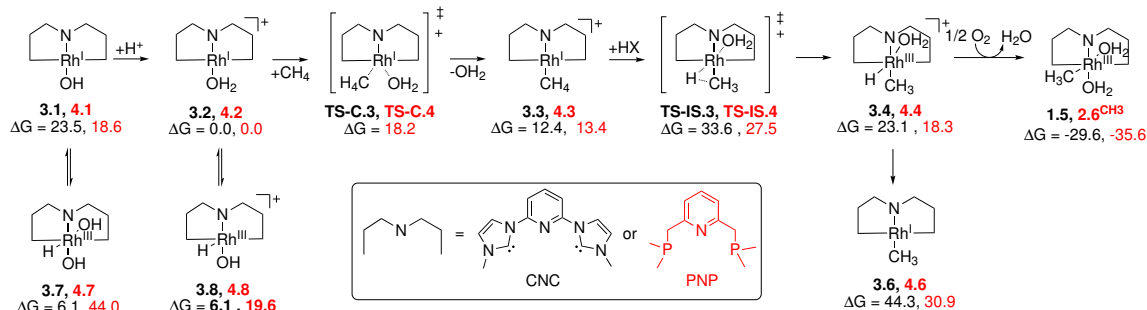


Figure A.2: Methane activation catalytic cycles from Rh(III) in water at pH = 0.

levels the internal substitution barriers can be decreased. Between pH 2 and 5, the barrier between **2.4**<sup>CH<sub>3</sub></sup> and **TS-IS.2**<sup>CH<sub>3</sub></sup> is 34.4 kcal/mol. Increasing the pH to levels between 5 and 8 decreases the barrier between **2.4**<sup>CH<sub>3</sub></sup> and **TS-IS.2**<sup>CH<sub>3</sub></sup> to 32 kcal/mol. From **2.5**<sup>CF<sub>3</sub></sup> the lowest barrier to C-H activation is through **TS-IS.3**<sup>CF<sub>3</sub></sup>. The plausibility of this step is improved by using a moderate pH so that the **2.5**<sup>CF<sub>3</sub></sup> is stabilized relative to other protonation states. The trends in the barriers to internal electrophilic substitution indicate that a more electrophilic, or otherwise electron poor, Rh(III) center helps stabilize the transition state. The barriers to C-H activation are higher for the CNC species because the N-heterocyclic carbene is a good  $\sigma$ -donor, and it is weakly backbonded to Rh(III).

The activated methyl groups are abstracted from the catalyst by reductive functionalization. The C-H activation products, Rh(III)(L)(CH<sub>3</sub>)(X)<sub>2</sub>, are comparatively stable. **1.5** and the final free energy of the reaction are nearly identical, though evaporating MeOH could coax the reaction forward. **2.6**<sup>CH<sub>3</sub></sup> is minima in the reaction cycle by 10 kcal/mol. **2.6**<sup>CF<sub>3</sub></sup> is more stable than any of the **2.x**<sup>CF<sub>3</sub></sup> protonation states, but its free energy is not as low as **2.6**<sup>CH<sub>3</sub></sup> or **1.5**. Most significantly, **2.6**<sup>CF<sub>3</sub></sup> is not the minima in the reaction cycle, and this ensures that there is still thermodynamic driving force for the production of methanol. From the rhodium-methyl species reductive functionalization occurs in the form of binuclear nucleophilic substitution with water acting as the nucleophile. As the most electrophilic species, **TS-SN2.3**<sup>CF<sub>3</sub></sup> enjoys the lowest S<sub>N</sub>2 barrier. The free energy of activation between **2.6**<sup>CF<sub>3</sub></sup> and **TS-SN2.3**<sup>CF<sub>3</sub></sup> is merely 32.4 kcal/mol. The free energies of activation from **1.5** and **2.6**<sup>CH<sub>3</sub></sup> are 33.9 and 39.1 kcal/mol, respectively. Presumably the S<sub>N</sub>2 barrier for **TS-SN2.3**<sup>CF<sub>3</sub></sup> is lower because **2.6**<sup>CF<sub>3</sub></sup> is a better nucleophile than its analogues. These results are significant because we have predicted a complete catalytic cycle for the oxidation of methane to methanol with barriers below 32 kcal/mol. The Rh(III)(PNP<sup>CF<sub>3</sub></sup>)OH<sub>2</sub> catalyst is successful because it destabilizes **2.2-5**<sup>CF<sub>3</sub></sup> and **2.6-7**<sup>CF<sub>3</sub></sup>, thereby decreasing the barriers to coordination, C-H activation, and functionalization. We predict that the electron-poor phosphorus atoms might be targets for nucleophilic attack and this is a concern.

Figure A.3: C-H activation *via* Rh(I) in pH = 0 water.

### A.3.3 Rh(I) in Water

Figure A.3 shows the methane activation cycle of Rh(I)(CNC/PNP) in water. At pH = 0, the precursor complexes, **3.1** and **4.1** are protonated to yield **3.2** and **4.2**, which are 23.5 and 18.6 kcal/mol more stable. Oxidation of the catalyst by water to produce **3.7** and **4.7** is unlikely given the high free energy of this transformation. However, autooxidation of **3.2** and **4.2** by splitting the aquo ligand yields **3.8** and **4.8**, and the free energy of this transformation is only uphill by 6.1 and 19.6 kcal/mol, respectively. Coordination of methane occurs by displacement of the equatorial aquo ligands and produces **3.3** and **4.3**. From **3.3** and **4.3**, C-H activation proceeds by insertion. The barriers to insertion for the CNC and PNP complexes are reasonably low, as expected. The same trend as in the Rh(III) results is observed, the barrier to C-H activation is lower for the more electrophilic Rh(III)PNP complexes. We found that insertion barriers were some 30 kcal/mol lower than internal electrophilic substitution barriers (not shown). Insertion is lower than IES in these Rh(I) complexes because square planar **3.3** and **4.3** have singly occupied  $d_{xy}$  orbitals that help stabilize the transfer of the hydride to the axial site. We hypothesize that either **3.3/4.3** or **3.6/4.6** will be targets for oxidation. With a free energy of -18.3 kcal/mol, **3.4** will be more abundant than the square planar methyl intermediates **3.6** and **4.6**, and we expect that oxidation will occur through this intermediate. It is unclear whether Rh in species **3.4** and **4.4** is closer to Rh(I) or Rh(III), but coupling these complexes to the oxygen reduction half reaction makes Rh formally Rh(III) by the elimination of the hydride. Notice that **1.5** and **2.6<sup>CH3</sup>** are where the Rh(I) and Rh(III) pathways converge. Unfortunately the oxidations of **3.4** and **4.4** are highly exothermic, and the resulting

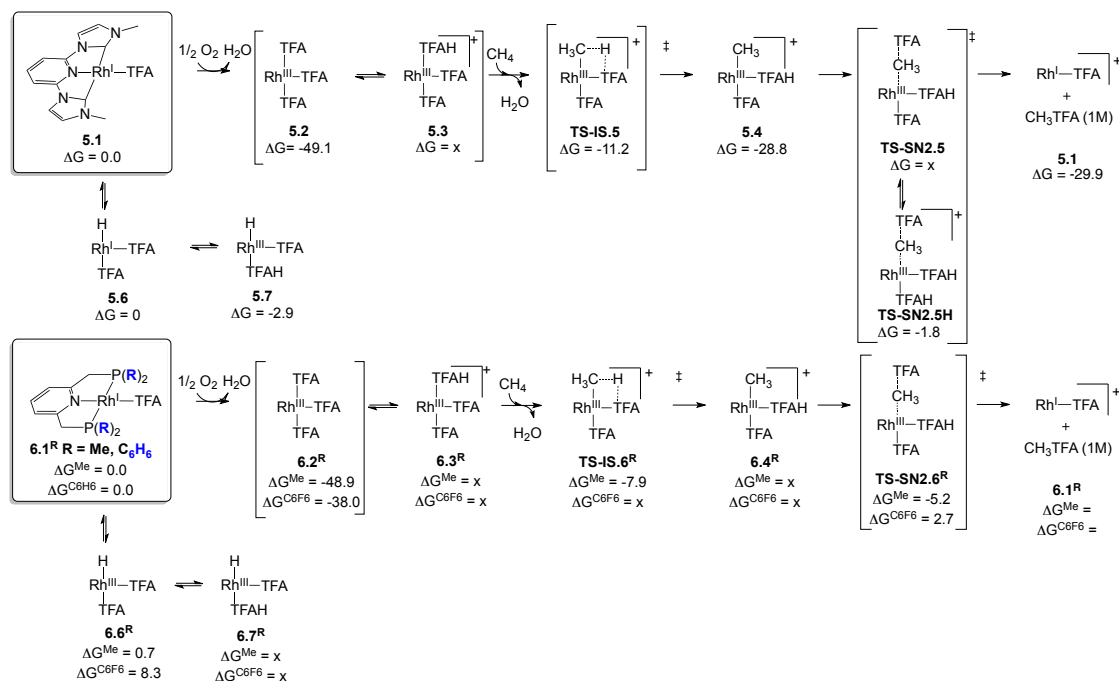


Figure A.4: The Rh(III) C-H activation catalytic cycle in pH = -7 TFAH.

species are lower in free energy than the methanol product. Functionalization of **1.5** and **2.6<sup>R</sup>** was discussed in §A.3.2.

### A.3.4 Rh(III) in TFA

We calculated the Rh(III) pathway in trifluoroacetic acid (pH = -7) because we hypothesized that the volatile  $\text{CH}_3\text{TFA}$  product would be easier to recover in an experimental setting than some of the methylsulfonate products that are formed in the Shilov methane activation chemistry. We also reasoned that TFA might be an effective nucleophile, and that functionalization by nucleophilic attack might be easier with a soft nucleophile (compared to hard nucleophiles like water or hydroxide).

Figure A.4 shows the results of this study. The first and possibly most important observation to draw when contrasting the Rh(III) pathways in water and TFA is in the relative stabilities of the  $\text{Rh(III)X}_3$  species: TFA anions form a very strong bond with Rh(III), and the result is that oxidation products **5.2**, **5.3**, **6.2<sup>R</sup>**, and **6.3<sup>R</sup>** are lower in energy than the various protonation states of the aqueous  $\text{Rh(III)(CNC)}$  and  $\text{Rh(III)(PNP<sup>R</sup>)}$  complexes in Figure A.2. This produces

comparatively lower ground states for the Rh(III) TFA systems, a fact that increases the relative C-H activation barrier heights. Indeed the barrier for C-H activation from **5.2** is 37.9 kcal/mol and from **6.2**<sup>CH<sub>3</sub></sup> is 41 kcal/mol. Compare this to 35.9 kcal/mol for **1.4** and 34.4 for **2.4**<sup>R</sup>. The effect of the perfluorophenyl substituted PNP ligand is similar to the effect of the trifluoromethyl substituted PNP ligand in §A.3.2: the electron withdrawing nature of the organofluorophosphine pincers makes Rh(III) electron poor. Because of this, the coordination bonds that Rh(III) can make to solvent molecules are weak relative to the unmodified Rh(CNC) and Rh(PNP) complexes. Following internal electrophilic substitution (**8.5**, **TS-IS.6R**), the methylrhodium(III) complex can undergo reductive functionalization by S<sub>N</sub>2 attack. A TFA anion attacks the axial methyl group and a two-electron reduction results. From the **5.4** the activation energy of **8.5H** is only 27 kcal/mol. This is a promising finding, and we suggest that stoichiometric experiments on reductive functionalization from **5.4** be carried out as a proof of concept test. Of course the barrier relative to the pathway minima is much higher: 47.3 kcal/mol relative to **5.2**. The free energy of activation for the S<sub>N</sub>2 attack is 43.7 kcal/mol relative for **TS-SN2.6**<sup>CH<sub>3</sub></sup> and 40.7 kcal/mol for **TS-SN2.6**<sup>C<sub>6</sub>F<sub>6</sub></sup> (relative to the pathway groundstate Rh(III)(TFA)<sub>3</sub> complex). The single step reductive functionalization barriers are unexpectedly low, but because the Rh(III)(TFA)<sub>3</sub> precursors are so stable, the catalytic cycle is likely to halt after oxidation. In light of this, C-H activation from Rh(III) in TFA is not promising, though we will reiterate that a stoichiometric test of the S<sub>N</sub>2 functionalization step would be an interesting experiment to conduct.

### A.3.5 Rh(I) in TFA

The final study of the two oxidation state pathways to C-H activation is for Rh(I) species in trifluoroacetic acid. The challenge in executing this chemistry is in avoiding oxidizing Rh(I) to Rh(III). The pathway in Figure A.5 shows that this oxidation is highly exothermic in TFA. From **7.1**, protonation of the equatorial TFA ligand makes it labile to substitution with methane. The activation energy of coordination is 17.2 kcal/mol, and the Rh(I)CNC...CH<sub>4</sub> species is an unstable complex. With a TFAH in one axial site the barrier to insertion is low:  $\Delta G^\ddagger = 17.2$  kcal/mol. Interestingly,

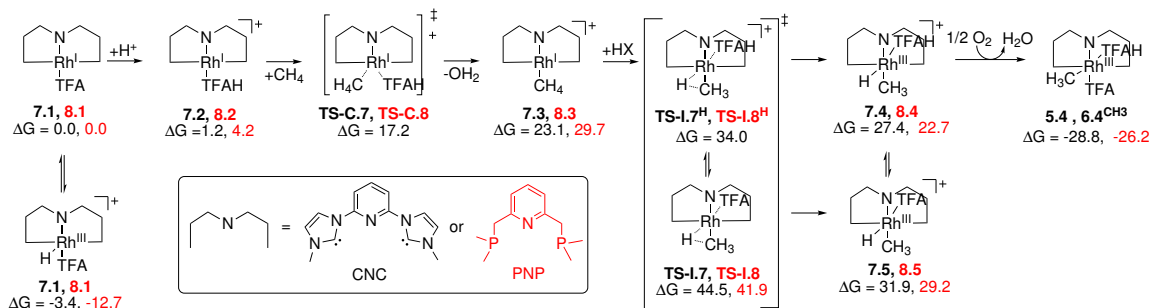


Figure A.5: The Rh(I) C-H activation catalytic cycle in pH = -7 TFAH.

the barrier is much higher when there is an axial TFA ligand. **TS-I.7** and **TS-I.8** have considerably higher activation free energies. The products of C-H activation are also high energy species, and as we discussed in the aqueous Rh(I) pathway, this is problematic. **7.5** and **8.5** will be present in low concentrations so oxidation might be a slow process. This also increases the possibility of oxidizing other intermediates, like **7.1** and **8.1**. The low insertion barriers for this pathway make it an interesting prospect, if oxidation can be avoided.

### A.3.6 Decreasing the Reductive Functionalization Barrier with Bulky Ancillary Ligands

The aqueous, acidic Rh(III)(PNP<sup>CF3</sup>) catalytic cycle in §A.3.2 satisfies the criteria for a good catalytic cycle: the barriers to coordination, C-H activation, and reductive functionalization are reasonably low, none of the intermediates have lower free energy than the product, the starting material is regenerated naturally, and deleterious side reactions should not damage the catalyst (as long as the conditions are acidic enough). Of the three transition states in the cycle, the reductive S<sub>N</sub>2 attack by water or hydroxide is the most questionable. We wondered whether we could change the structure of the ancillary ligand to destabilize the [L]-Rh(III)Me species by elongating the Rh-Me bond so that the S<sub>N</sub>2 barrier would be lower. We achieved this by creating PNP derivatives with bulky phosphine substituents. Figure A.6 shows some of the modified PNP ligands and Table A.1 shows the results of this series of calculations.

The upper half of table one shows the results of our PNP ligand steric study when the solvent

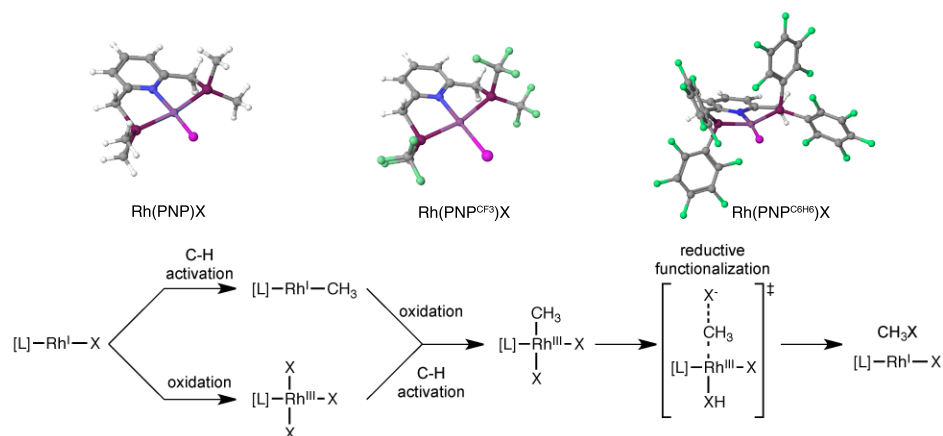


Figure A.6: Three derivatives of PNP (from left to right): PNP, PNP<sup>CF<sub>3</sub></sup>, and PNP<sup>C<sub>6</sub>H<sub>5</sub>6</sup>, and the Rh(I) and Rh(III) C-H activation pathway.

[L]	[L]Rh(I)CH <sub>3</sub>	[L]Rh(III)(X) <sub>3</sub>	[L]Rh(III)(CH <sub>3</sub> )X <sub>2</sub>	TS-S <sub>N</sub> 2	CH <sub>3</sub> X
		X = TFA, pH = -7			
PNP	-/35.6	-48.7	-35.7	-6.5	-29.9
PNP <sup>tBu</sup>	-	-31.7	-16.5	13.3	-29.9
PNP <sup>C<sub>6</sub>H<sub>6</sub></sup>	22.7/29.3	-42.4	-32.2	-3.8	-29.9
Pm+PPm+	44.5/-	-22.1	-	-	-29.9
		X = OH(2), pH = 0			
PNP	18.3/30.9	-26.7	-35.6	-2.0	-30
PNP <sup>tBu</sup>	-	-6.3	-16.7	3.9	-30

Table A.1: Gibbs free energies (kcal/mol) along the reaction coordinate defined in figure A.6.

is pH = -7 TFAH. Interestingly, the barrier between [L]Rh(CH<sub>3</sub>)X<sub>2</sub> and TS-S<sub>N</sub>2 does not change much for PNP, PNP<sup>tBu</sup>, or PNP<sup>C<sub>6</sub>H<sub>6</sub></sup>; each activation free energy is around 29 kcal/mol. What does change is the stability of the [L]Rh(III)(X)<sub>3</sub> species. With PNP<sup>tBu</sup> as an ancillary ligand, the intermediates in Figure A.6 are destabilized by 17 to 20 kcal/mol. PNP<sup>C<sub>6</sub>H<sub>6</sub></sup> has the same effect, but to a smaller extent; intermediates with this ligand are destabilized by 3 to 6 kcal/mol. While not the desired effect, this is a useful finding because one of the issues with the Rh(III)(PNP) cycle is the detrimental stability of Rh(III)PNP(TFA)<sub>3</sub> species. Destabilizing solvent-coordinated intermediates helps shift the equilibrium towards the product.

The lower half of Table A.1 shows the results of our PNP ligand steric study when the solvent is pH = 0 water. In this case the result of substituting the phosphine methyl groups with a more voluminous ligand matched our expectations. Notice that the activation free energy of S<sub>N</sub>2 attack is

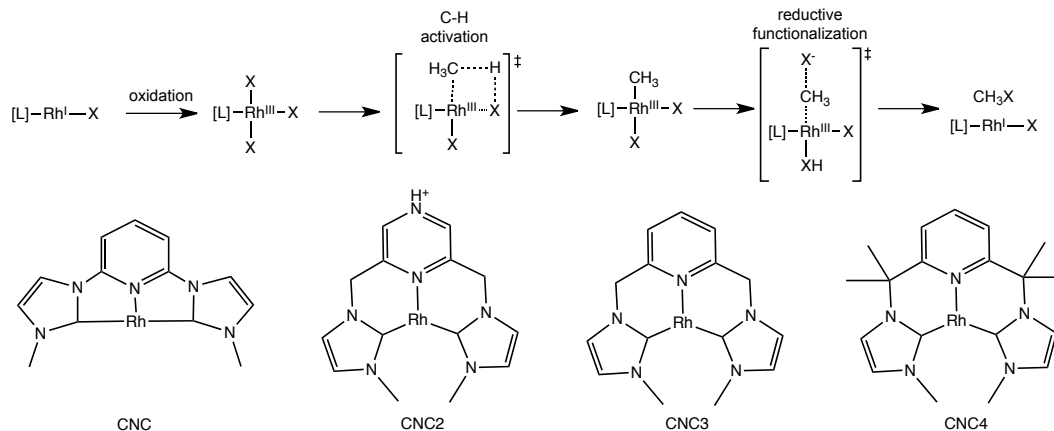


Figure A.7: Derivatives of the CNC ligand and the Rh(III) C-H activation pathway.

Ligand	[L]Rh(I)X	[L]Rh(III)X <sub>3</sub>	TS-I	[L]Rh(III)CH <sub>3</sub> X <sub>2</sub>	TS-S <sub>N</sub> 2	CH <sub>3</sub> X
CNC	0	-49.1	-11.2	-28.8	1.9	-29.9
CNC2	0	-23.9	24.4	-11.8	9.7	-29.9
CNC3	0	-56	-13.8	-39.4	-0.3	-29.9
CNC4	0	-36.7	2.82	-22.2	-3.1	-29.9

Table A.2: Gibbs free energies (kcal/mol) along the reaction coordinate defined in Figure A.7.

reduced to 20.6 kcal/mol from 29.2 kcal/mol relative to  $[L]Rh(CH_3)X_2$  when *tert*-butyl groups are substituted for methyl groups. This favorable outcome is the result of the  $PNP^{tBu}$  ligand's ability to destabilize  $[L]Rh(III)X_3$  and  $[L]Rh(CH_3)X_2$  without also increasing the activation energy. The destabilization energy is on par with the level of destabilization that the  $PNP^{CF_3}$  complex provides. Another advantage of the steric destabilization paradigm is that it protects the phosphine group from nucleophilic attack.

In Figure A.7 we show the modifications we made to the CNC ligand in order to study the effect of sterics on the S<sub>N</sub>2 reductive functionalization step for CNC based catalysts in acidic water. Like the aqueous acidic PNP catalytic cycle, the lowest energy structures in the CNC pathway are the solvent-ligated Rh(III) complexes. Generally methyl substitutions to the methylene linkers between the pyridine moiety of CNC have the effect of interfering with the axial sites. This reduces the binding strength of solvent molecules in  $Rh(III)(CNC^R)X_3$  and fortunately the S<sub>N</sub>2 barrier is not proportionally destabilized. The net result is that for CNC4 the  $Rh(III)(CNC^R)X_3$  complex is increased to -36.7 kcal/mol from -49.1 kcal/mol (for the unaltered CNC ligand) and the S<sub>N</sub>2 barrier

is actually decreased to -3.1 kcal/mol. This decreases the net barrier between these two states to 33.6 kcal/mol from 51 kcal/mol! The protonated para-pyrazine ligand, CNC2, is an interesting case. The proton makes the complex sufficiently electropositive that the oxidation potential is increased and the solvent ligated species are only -23.9 kcal/mol downhill. For this ligand the net barrier to  $S_N2$  attack is 33.6 kcal/mol. The downside of this ligand is that it significantly decreases Rh(III)s ability to mediate the internal electrophilic substitution of the methane hydride to the water ligand, and this barrier is increased by 10.4 kcal/mol. The results of these ligand sterics studies indicate that substituting bulky groups onto planar ligands can help interfere with coordination to the active axial sites in Rh(III) catalysts. For both CNC and PNP we found modified ligands that decreased the barrier to  $S_N2$  reductive functionalization while destabilizing the  $[L]Rh(III)X_3$  species that can be thermodynamic sinks in the catalytic cycle. The only downside to such an approach is the decrease in solubility that we expect for the hydrocarbon-substituted CNC and PNP ligands.

## A.4 Conclusions

The C-H activation mechanism for Rh(I) and Rh(III) CNC and PNP complexes has been identified in two solvents. We found that in general the Rh(III) catalytic cycle was more favorable because increasing the electrophilicity of the metal center decreases the barriers to C-H activation and functionalization. Using a relatively electron-poor metal center also decreases the extent to which oxidation can interfere with the desired transformations. Rh(III)(PNP<sup>CF3</sup>) in acidic water was the most successful catalytic system that we examined, and we suggest experimental studies using this catalyst. We also found that a “soft” nucleophile like TFA<sup>-</sup> could effectively functionalize the Rh(III)Me product of C-H activation, and the barriers to reductive functionalization can be reduced by introducing sterically bulky substituents to the ancillary ligand. Future studies will include the results of coupling mild one-electron oxidants like vanadyl phosphate to the C-H activation cycle. Using one-electron oxidations helps to avoid some of the excessively stable oxidation products that result from O<sub>2</sub> oxidation.

# References

- [1] B. L. Conley, S. K. Ganesh, J. M. Gonzales, W. J. Tenn, K. J. Young, J. Oxgaard, W. A. Goddard, III, and R. A. Periana, "Facile functionalization of a metal carbon bond by O-atom transfer," *J. Am. Chem. Soc.*, vol. 128, no. 28, pp. 9018–9019, 2006.
- [2] G. Bhalla, X. Y. Liu, J. Oxgaard, W. A. Goddard, and R. A. Periana, "Synthesis, structure, and reactivity of O-donor Ir(III) complexes: C-H activation studies with benzene," *J. Am. Chem. Soc.*, vol. 127, no. 32, pp. 11372–11389, 2005.
- [3] R. H. Crabtree, "Organometallic alkane C-H activation," *J. Organometallic Chem.*, vol. 689, no. 24, pp. 4083–4091, 2004.
- [4] R. A. Periana *et al.*, "A mercury-catalyzed, high-yield system for the oxidation of methane to methanol," *Science*, vol. 259, no. 5093, pp. 340–343, 1993.
- [5] R. Periana, D. Taube, S. Gamble, and H. Taube, "Selective methane oxidation by ch activation," *Abstracts of Papers of the American Chemical Society*, vol. 212, no. 2, pp. 37–ORGN, 1996.
- [6] R. A. Periana *et al.*, "A novel, high-yield system for the oxidation of methane to methanol," *Studies Surf. Sci. Catal.*, vol. 81, pp. 533–544, 1994.
- [7] R. Periana, D. Taube, S. Gamble, H. Taube, and H. Fuji, "High yield, low temperature oxidation of methane to methanol," 1998.
- [8] M. Ahlquist, R. A. Periana, and W. A. Goddard, III, "C-H activation in strongly acidic media. the co-catalytic effect of the reaction medium," *Chem. Comm.*, vol. 17, no. 17, pp. 2373–2375, 2009.
- [9] B. A. Arndtsen, R. G. Bergman, T. A. Mobley, and T. H. Peterson, "Selective intermolecular carbon-hydrogen bond activation by synthetic metal complexes in homogeneous solution," *Acc. Chem. Res.*, vol. 28, no. 3, pp. 154–162, 1995.
- [10] B. L. Conley, W. J. Tenn, K. J. H. Young, S. K. Ganesh, S. K. Meier, V. R. Ziatdinov, O. Mironov, J. Oxgaard, J. Gonzales, W. A. Goddard, and R. A. Periana, "Design and study of homogeneous catalysts for the selective, low temperature oxidation of hydrocarbons," *J. Mol. Cat. A*, vol. 251, no. 1–2, pp. 8–23, 2006.
- [11] D. H. Ess, S. M. Bischof, J. Oxgaard, R. A. Periana, and W. A. Goddard, III, "Transition state energy decomposition study of acetate-assisted and internal electrophilic substitution C-H bond activation by (acac-O,O)2Ir(X) complexes (X = CH3COO, OH)," *Organometallics*, vol. 27, no. 24, pp. 6440–6445, 2008.
- [12] D. H. Ess, W. A. Goddard, III, and R. A. Periana, "Electrophilic, ambiphilic, and nucleophilic C-H bond activation: Understanding the electronic continuum of C-H bond activation through transition-state and reaction pathway interaction energy decompositions," *Organometallics*, vol. 29, no. 23, pp. 6459–6472, 2010.

- [13] J. Oxgaard, W. J. Tenn, R. J. Nielsen, R. A. Periana, and W. A. Goddard, "Mechanistic analysis of iridium heteroatom C-H activation: Evidence for an internal electrophilic substitution mechanism," *Organometallics*, vol. 26, no. 7, pp. 1565–1567, 2007.
- [14] W. J. Tenn, K. J. H. Young, J. Oxgaard, R. J. Nielsen, W. A. Goddard, and R. A. Periana, "Heterolytic CH activation and catalysis by an O-donor iridiumhydroxo complex," *Organometallics*, vol. 25, no. 21, pp. 5173–5175, 2006.
- [15] K. J. H. Young, S. K. Meier, J. M. Gonzales, J. Oxgaard, W. A. Goddard, and R. A. Periana, "Heterolytic CH activation with a cyclometalated Platinum(ii) 6-Phenyl-4,4-di-tert-butyl-2,2-Bipyridine complex," *Organometallics*, vol. 25, no. 20, pp. 4734–4737, 2006.
- [16] R. A. Periana, D. J. Taube, S. Gamble, H. Taube, T. Satoh, and H. Fujii, "Platinum catalysts for the high-yield oxidation of methane to a methanol derivative.," *Science*, vol. 280, no. 5363, pp. 560–564, 1998.
- [17] A. H. Janowicz, R. A. Periana, J. M. Suchanan, C. A. Kovac, J. M. Stryker, M. J. Wax, and R. G. Bergman, "Oxidative addition of soluble iridium and rhodium complexes to carbon-hydrogen bonds in methane and higher alkanes.," *Pure Appl. Chem.*, vol. 56, no. 1, pp. 13–23, 1984.
- [18] R. A. Periana and R. G. Bergman, "Oxidative addition of rhodium to alkane C-H bonds — enhancement in selectivity and alkyl group functionalization.," *Organometallics*, vol. 3, no. 3, pp. 508–510, 1984.
- [19] R. A. Periana and R. G. Bergman, "Isomerization of the hydridoalkylrhodium complexes formed on oxidative addition of rhodium to alkane C-H bonds - evidence for the intermediacy of  $\eta$ -2-alkane complexes," *J. Am. Chem. Soc.*, vol. 108, no. 23, pp. 7332–7346, 1986.
- [20] S. K. Hanson, D. M. Heinekey, and K. I. Goldberg, "C-H bond activation by Rhodium(I) phenoxide and acetate complexes: Mechanism of H-D exchange between arenes and water," *Organometallics*, vol. 27, no. 7, pp. 1454–1463, 2008.
- [21] S. M. Klok, D. M. Heinekey, and K. I. Goldberg, "C-H bond activation by Rhodium(i) hydroxide and phenoxide complexes," *Angew. Chem. Int. Ed. Engl.*, vol. 46, no. 25, pp. 4736–4738, 2007.
- [22] C. S. J. Cazin, ed., *Heterocyclic Carbenes in Transition Metal Catalysis and Organocatalysis*. New York: Springer, 2010.
- [23] D. Bourissou, O. Guerret, F. P. Gabba, and G. Bertrand, "Stable carbenes," *Chem. Rev.*, vol. 100, no. 1, pp. 39–92, 2000.
- [24] M. Poyatos, J. A. Mata, E. Falomir, R. H. Crabtree, and E. Peris, "New Ruthenium(II) CNC-pincer bis(carbene) complexes: Synthesis and catalytic activity," *Organometallics*, vol. 22, no. 5, pp. 1110–1114, 2003.
- [25] F. E. Harris and C. T. O'Konski, "The dielectric constant of liquid trifluoroacetic acid," *J. Am. Chem. Soc.*, vol. 76, no. 17, pp. 4317–4318, 1954.
- [26] C. Lee, W. Yang, and R. G. Parr, "Development of the Colle-Salvetti correlation-energy formula into a functional of the electron density," *Phys. Rev. B*, vol. 37, pp. 785–789, 1988.
- [27] A. D. Becke, "Density-functional thermochemistry. III. the role of exact exchange," *J. Chem. Phys.*, vol. 98, no. 7, pp. 5648–5652, 1993.
- [28] P. J. Hay and W. R. Wadt, "*Ab initio* effective core potentials for molecular calculations. potentials for K to Au including the outermost core orbitals," *J. Chem. Phys.*, vol. 82, no. 1, pp. 299–310, 1985.

- [29] B. Marten, K. Kim, C. Cortis, R. A. Friesner, R. B. Murphy, M. N. Ringnalda, D. Sitkoff, and B. Honig, "New model for calculation of solvation free energies: Correction of self-consistent reaction field continuum dielectric theory for short-range hydrogen-bonding effects," *J. Phys. Chem.*, vol. 100, no. 28, pp. 11775–11788, 1996.
- [30] J. H. Simons, "The dielectric constant of trifluoroacetic acid," *J. Am. Chem. Soc.*, vol. 72, pp. 1426–1427, 1950.
- [31] W. Dannhauser and R. H. Cole, "On the dielectric constant of trifluoroacetic acid," *J. Am. Chem. Soc.*, vol. 74, no. 23, pp. 6105–6105, 1952.

## Appendix B

# Estimating Phosphorescence Lifetimes in Cyclometalated Platinum Phosphors

### B.1 Phosphorescent Cyclometalated Platinum Complexes

Coordinatively unsaturated square planar cyclometallated Pt(II) complexes have attracted much attention in recent years because of their potential applications as organic light emitting diodes (OLEDs) [1, 5, 7, 9, 11, 20, 34–37, 39], chemosensors [8], photooxidants [24], liquid crystal optical storage materials [6], photochemical energy converters [24], and non-linear optical materials [23]. These complexes are particularly attractive because of their high phosphorescence quantum yields and short emission lifetimes; both qualities are requisites for effective OLEDs [31]. Besides being strongly emissive, Pt(II) cyclometalated complexes are interesting because their emission characteristics are sensitive to local environments [17, 21, 33], their square planar geometries allow for interesting stacking effects and intermolecular interactions [16, 19], and some complexes have even emitted white and near-infrared light [2, 3, 29, 32].

In a phosphorescent OLED, the excitons created by electron-hole recombination are triplets so emission must come from the triplet manifold [3]. Theoretically this implies that 100% quantum efficiency is attainable, but this also means that radiative relaxation is competing with non-radiative decay processes. Pt(II) complexes are effective because intersystem crossing between the singlet and triplet excited manifolds is promoted by strong spin-orbit coupling from the Pt center [4, 18, 32].

Once the excited wavepacket is in a triplet metal-to-ligand charge transfer state ( $^3\text{MLCT}$ ) or triplet ligand centered ( $^3\text{LC}$ ) state it can borrow transition dipole moment from the  $^1\text{MLCT}$  state via spin-orbit coupling and relax to the singlet ground state. Several groups have documented cyclometalated Pt(II) complexes that exhibit the photophysics just described. Che and co-workers demonstrated that adding electron-donating substituents to the 4-position of the terpyridine ligand in  $[\text{Pt}(\text{tpy})\text{Cl}]^+$  leads to emission at room temperature in fluid with lifetimes in the microsecond range [15]. Thompson and co-workers synthesized a series of Pt(II)-based complexes with  $\text{C}^*\text{N}^-$ -type monoanion cyclometalating ligands that demonstrated emission across the visible spectrum and quantum yields between 0.02 and 0.25 with lifetimes shorter than 30 microseconds [22]. Pt(II) complexes with tridentate coordinated ligands of the form  $\text{N}^-\text{C}^*\text{N}$  were synthesized and are capable of emitting with quantum efficiencies up to 0.6 in degassed solution with lifetimes shorter than 20 microseconds [11]. Swager and coworkers synthesized a variety of new Pt(II) complexes whose emission blue-shifts and upon detection of the cyanogen halides with high quantum efficiency and short lifetimes [11]. Platinum dyads with  $\text{C}^*\text{N}$  ligands synthesized by the Thompson group demonstrated modest improvements over their monomeric analogues [22]. In recent years several studies have attempted to improve luminescence characteristics by tuning the ancillary ligand with varying success [27, 36, 38]. The weakly luminescent complexes in these studies have a common characteristic: the presence of geometrically distorted metal centered (MC)  $d-d^*$  excited states that provide non-radiative decay channels that lead away from the ground state. In fact, for strongly luminescent complexes, a strong induced ligand field in the metal-to-ligand bond raises the energy of the metal centered  $d-d^*$  states above the  $^3\text{MLCT}$  states and this effect is what makes Pt(II) complexes such efficient emitters.

The Thompson group discovered that two isomers based on their  $\text{C}^*\text{N}$  Pt(II)( $\beta$ -diketonato) template (see Figure B.2), (1-naphthylpyridine)Pt(II)(bis-(2,2,6,6-tetramethyl-3,5-heptadionato-O,O)) (1NpPt) and (2-naphthylpyridine)Pt(II)(bis(2,2,6,6-tetramethyl-3,5-heptadionato-O,O)) (2NpPt), exhibited similar absorption patterns but drastically different emission characteristics and emission lifetimes. Both complexes absorb between 350 and 480 nm, corresponding to a  $^1\text{MLCT}$  excitation,

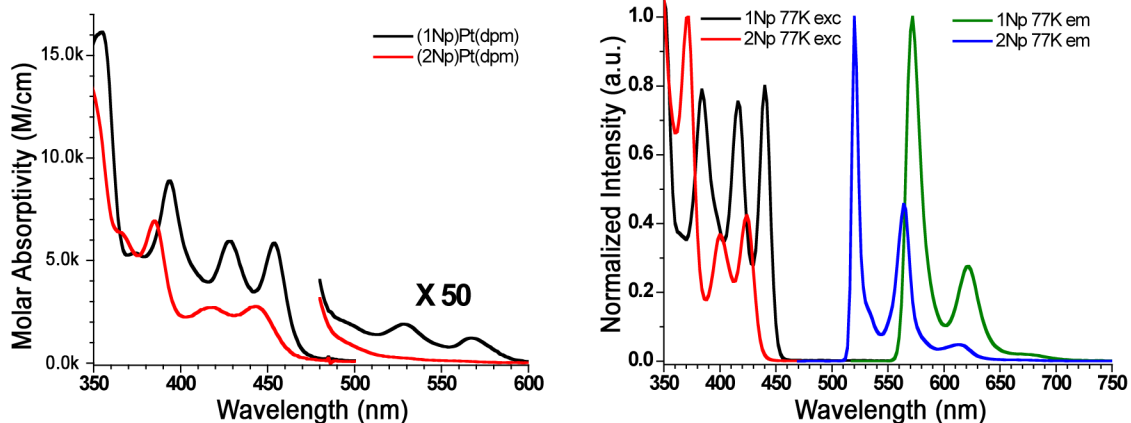


Figure B.1: The experimental absorption spectra (left) and combined absorption-emission spectra (right) of 1NpPt and 2NpPt.

with weaker absorption peaks above 500 nm and below 600 nm, corresponding to  $^3\text{MLCT}$  excitation (Figure B.1). The emission spectra reveal that 1NpPt emits at 572 nm and 2NpPt emits at 520 nm. This is curious given the similarity between these two isomers. In fact, 2NpPt emission is similar to the emission spectra of the free Np ligand. The measured lifetimes for 1NpPt and 2NpPt are 14  $\mu\text{s}$  and 380  $\mu\text{s}$  in 2-MeTHF at 77 K, respectively. 2NpPt has another curious emission characteristic: at room temperature its emission peak red shifts to 572 nm from 520 nm at 77 K. 1NpPt also red shifts at room temperature, but only to 590 nm from 572 nm. The similarity between their absorption spectra indicates that in both isomers the S1 and S2 states are similar in energy. Intersystem crossing occurs but then there must be a difference in the triplet manifold energies for 1NpPt and 2NpPt since their emission wavelengths and lifetimes are so different.

In this study we will explore the electronic factors that cause the NpPt isomers to phosphoresce differently, and we will examine two similar molecules, (7,8-benzoquinoline)Pt(II)(acetylacetonato-O,O), (bzqPt), and (2-phenylpyridine)Pt(II)(acetylacetonato-O,O), (ppyPt), for reference and to verify any trends that may emerge. Using TD-DFT and multi-configuration self-consistent field calculations we compute their excitation energies and explore their excited state manifolds. Besides probing energies and geometries at select points on the ground and excited state manifolds, we will compute the spin-orbit coupling of these states and use the values to estimate photophysical

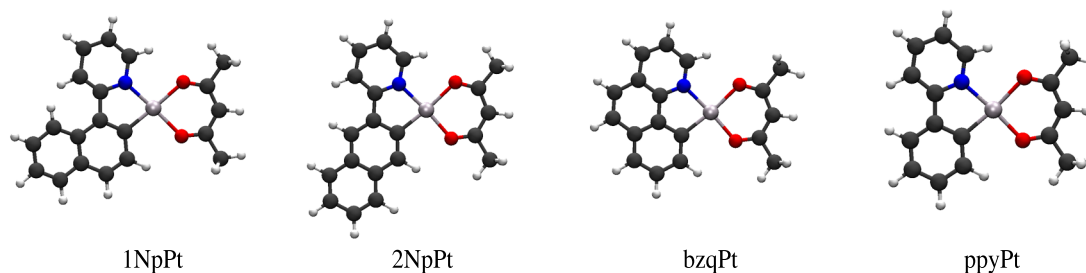


Figure B.2: The subjects of this study:  $(C^{\wedge}N)Pt(II)(acac)$ .  $C^{\wedge}N = 1Np, 2Np, bzq,$  and  $ppy$ .

quantities like the S1-T1 intersystem crossing rates and phosphorescence rates.

## B.2 Computational Methodology

In order to understand the lifetime discrepancy between the two NpPt complexes, their photophysics were investigated using density functional- and wavefunction-based quantum chemical theories. To reduce computation burden we replaced the bis-(2,2,6,6-tetramethyl-3,5-heptadionato-O,O) groups on 1NpPt and 2NpPt with acetylacetonato (acac) groups. This should not affect energies significantly since the removed alkyl groups are inert to excitation in the visible spectrum. Two series of calculations were performed: a TD-DFT investigation of vertical excitation energies, and a complete active space self-consistent field (CASSCF) study of excitation energies, spin-orbit coupling, and non-ground state potential energy surfaces.

Ground state singlet geometries were generated by performing DFT geometric minimizations using the B3LYP, PBE, M06, M06-2X, and M06-HF functionals in the Jaguar 7.5 electronic structure program. From these minimized geometries TD-DFT excitation calculations were performed and the first 10 excitation energies were computed. These results can be found in Table B.1. The geometry optimizations were conducted using the Hay and Wadt (Los Alamos core potential) effective core potential for Pt [14], and the Pople-style 6-31G\*\* basis for all other atoms and the valence electrons of Pt; this basis is commonly referred to as lacvp\*\*. The TD-DFT excitation energies were calculated using the same Hay and Wadt ECP but the Gaussian basis was changed to 6-311G\*\*++.

The CASSCF and CI calculations in this chapter were performed using the GAMESS-US suite of

codes [28]. Since PBE produced the best excitation spectra, its computed ground state geometries were used for CASSCF calculations. The CASSCF gradients of the PBE S0 geometries were below  $3 \times 10^{-3}$  Hartree/bohr so we did not reoptimize the ground state geometries. For these calculations the SBKJC effective core potential and valence basis set were used. The SBKJC ECP removes 60 core electrons from platinum and 2 from nitrogen, carbon, and oxygen [30]. The valence electron basis set for SBKJC is 3-21g\* for H, C, N, and O. The DFT optimized structures were used to generate a set of CASSCF orbitals from which an appropriate active space was chosen. The active space was increased systematically — to help convergence — using the orbitals involved in excitation (as determined by TD-DFT). Finally, an active space of eighteen electrons in twelve orbitals was formed for each complex; the active space includes the highest energy transition-metal-based and ligand-based orbitals, as well as three virtual orbitals. The (18,12) active spaces created the best wavefunctions for the complexes given the amount of computer memory and time available. After the configuration interaction coefficients are optimized in the CASSCF routine, the density matrix for a specified root (i.e., S1) can be optimized to produce the wavefunction for an excited state. The wavefunctions from CASSCF(18,12) were then subjected to second-order Möller-Plesset (MP2) energy corrections to recover the correlation energies. The results of the excitation calculations are given in Table B.3.

Excited state potential energy surfaces were explored by optimizing the geometries of excited states and searching for minimum energy crossing points using CASSCF to compute energies and gradients. In a minimum energy crossing point (MEXP) search, two starting wavefunctions and a starting geometry are provided. The Newton-Raphson optimizer operates with a Lagrangian multiplier imposing the constraint that the energy of both wavefunctions be the same [10]. The spin orbit coupling constants and transition dipole moments at minimum energy crossing points and stationary states were computed using the spin-orbit configuration interaction technique in GAMESS with the full Pauli-Breit spin-orbit operator [12].

The XYZ coordinates of the S0, T1, and MEXP geometries for the four molecules are provided in Appendix C.

## B.3 Computing Radiative and Non-Radiative Decay Rates

### B.3.1 Radiative Transitions

Computing the rates of spin-allowed and spin-forbidden radiative processes is relatively straightforward. The phosphorescence rate can be computed using the energy gap between the T1 minima and the S0 manifold lying underneath. Since phosphorescence is spin-forbidden to the zeroth-order approximation, first-order corrections to the Hamiltonian must be made: spin-orbit coupling constants between the S1 and T1 states are needed. The phosphorescence rate,  $k_r(T_m \rightarrow S_0)$ , is expressed as follows [26, 32]:

$$k_r(T_m \rightarrow S_0) = \frac{16 \times 10^6 \pi^3 E(T_m) \eta^2}{3h\epsilon_0} \left( \sum_n \frac{\langle T_m | \hat{H}_{so} | S_n \rangle \langle S_n | \mu_{el} | S_0 \rangle}{E(S_n) - E(T_m)} \right)^2 \quad (\text{B.1})$$

where  $E(T_m)$  is the energy of the  $T_m \rightarrow S_0$  transition,  $\langle T_m | \hat{H}_{so} | S_n \rangle$  is the spin-orbit coupling matrix element between the  $S_n$  excited singlet state and the  $T_m$  emissive state,  $\langle S_n | \mu_{el} | S_0 \rangle$  is the transition dipole moment between the excited and ground singlet states, and  $\eta$  is the refractive index of the medium. This equation accounts for the transition dipole borrowing that is enabled by the strong spin-orbit interaction between the excited  $T_m$  and  $S_n$  states. The fluorescence rate can be computed similarly using the Einstein spontaneous emission coefficient, since fluorescence is spin-allowed:

$$k_r(S_n \rightarrow S_0) = \frac{4e^2}{3c^3 \hbar^4} (E_{S_n} - E_{S_0})^3 (\langle S_n | \mu_{el} | S_0 \rangle)^2 \quad (\text{B.2})$$

where  $c$  is the speed of light, and  $e$  is the fundamental charge.

### B.3.2 Non-Radiative Transitions

Calculating non-radiative unimolecular transition rates is trickier. Examples of such transitions include intersystem crossing and internal conversion. Most quantum mechanical calculations are made within the Born-Oppenheimer approximation using zeroth-order approximations to the Hamiltonian. That is, they exclude scalar relativistic and spin-orbit coupling terms. As a result the computed

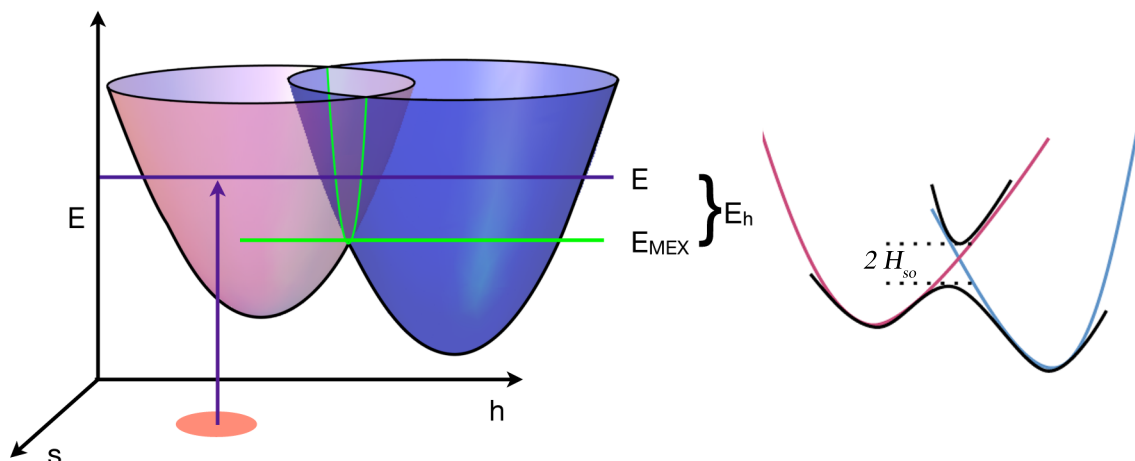


Figure B.3: A conceptualization of two intersecting excited state manifolds and the seam,  $s$  (green curve), orthogonal to the crossing coordinate,  $h$ .

potential energy surfaces are diabatic. Figure B.3 shows two diabatic surfaces in red and blue. Diabatic surfaces may intersect one another, but there is no way for a wavepacket to cross from one to the other since the eigenfunctions of diabatic Hamiltonians are pure spin-states. A Hamiltonian that includes spin-orbit coupling terms, however, produces adiabatic surfaces that do not cross. To be clear, that means that spin-orbit coupling near the crossing point produces adiabatic upper and lower surfaces. An example of an adiabatic surface is the lower black outline of the diabatic surfaces in Figure B.3 that shows a double well connected by a transition state at the minimum energy crossing point. The corresponding upper surface would be the cone formed by the intersection of the red and blue diabatic surfaces, and the space in between the upper and lower surfaces in the crossing seam is split by spin-orbit coupling. When spin-orbit coupling operators are included in the Hamiltonian, the eigenfunctions are mixtures of different spin states, thus a wavepacket may traverse the minimum energy crossing point by switching from one electronic spin state to another *nonadiabatically*. Computing the rates for these transitions requires nonadiabatic transition state theory.

Imagine the red surface in Figure B.3 is the S1 manifold, and the blue surface is the T1 manifold. Then the minimum energy crossing point between these is the point where intersystem crossing will occur. Spin-orbit coupling in the vicinity of this point allows a wavepacket to cross between the

S1 manifold by switching spin states. To compute the rate of this process we need to calculate the nonadiabatic unimolecular reaction rate using RRKM theory [13]. The rate of the spin forbidden reaction is given by

$$k(E) = \frac{N_{cr}(E)}{h\rho(E)} \quad (\text{B.3})$$

where  $\rho(E)$  is the density of rovibrational states of the reactant and the effective integrated density of states in the crossing seam,  $N_{cr}(E)$ , is defined by:

$$N_{cr}(E) = \int \rho_{cr}(E - E_h)p_{sh}(E_h)dE_h. \quad (\text{B.4})$$

The integrated density of states is derived by assuming that the motions in the system can be divided into two classes. The first is motion in the hopping coordinate,  $h$ , which is orthogonal to the crossing seam (the seam is the green parabola in Figure B.3). The second class is comprised of the spectator degrees of freedom that are parallel to the crossing seam. The integral in (B.4) is the convolution of the hopping probability,  $p_{sh}(E_h)$  and the density of spectator degrees of freedom corresponding to the remaining energy in the system,  $\rho_{cr}(E - E_h)$ . The hopping probability is determined from Landau-Zener theory [25]

$$p_{sh}(E) = (1 - P_{LZ})(1 + P_{LZ}) \quad (\text{B.5})$$

where  $P_{LZ}$  is defined as

$$P_{LZ} = \exp\left(\frac{-2\pi H_{so}^2}{h\Delta F} \sqrt{\frac{\mu}{2E}}\right). \quad (\text{B.6})$$

Here  $H_{so}$  is the spin-orbit coupling between the two states at the crossing point,  $\Delta F$  is the difference between the gradients of both surfaces at the crossing point,  $\mu$  is the reduced mass, and  $E$  should be  $E_h$ , which is the difference between the initial excitation energy (the vertical excitation energy from  $S_0$  to  $S_1$ ) and the energy at the crossing point,  $E_{mex}$ .  $E_h$  is the energy available to the spectator degrees of freedom. The form of (B.6) ensures that the hopping probability will be zero at energies below the minimum energy crossing point energy. Calculating the intersystem crossing rate using this nonadiabatic-RRKM (NARRKM) method requires locating the minimum energy crossing point

between two manifolds, calculating the spin-orbit coupling at that point, determining the gradient of each manifold at that point, identifying the crossing coordinate, and then computing the densities of states of the reactant and transition state. This is not a trivial task.

## B.4 Results and Discussion

### B.4.1 Excitation Energies

Table B.1 shows the TD-DFT excitation spectra for several popular DFT functionals and compares the values of the first five excited states to peaks extracted from the experimental absorption spectra. The states are not explicitly assigned but they are ordered T1, T2, T3, S1, T4 for the experimental spectra. The oscillator strengths indicate the nature of excitation for the TD-DFT calculations. Oscillator strengths  $> 0.01$  typically indicate S0-Sn transitions since these are spin-allowed. The RMSD values represent the deviation from the experimental spectra. An examination of the experimental absorption spectrum, Figure B.1, shows that both compounds have absorption peaks between 350 and 480 nm, or 50 to 80 kcal/mol, which supports the results in Table B.1. The oscillator strength magnitudes calculated from TD-DFT correlate well with the experimental molar absorptivities. Both experiment and theory show that the S1 and S2 states of 1NpPt and 2NpPt are preferentially populated over the lower energy T1 and T2 states. This is not unexpected as excitation from the singlet ground state to the triplet manifold is classically considered spin-forbidden. Of the five density functionals, PBE performs the best. Among the Minnesota family of functionals, M06 performed the best. This is somewhat surprising because M06-HF is purported to work well for excitation energy calculations [40]. B3LYP, PBE, and M06 were on par with one another, though PBE was the most accurate. Table B.3 shows the CASSCF(18,12) T1 and S1 vertical excitation energies as well as the energy of the S1-T1 minimum energy crossing point (MEXP) above the S0 minima. The DFT and CASSCF calculations provide reasonably good agreement with one another.

A rudimentary examination of the orbitals reveals the nature of each type of excitation. The orbitals of each complexes S0 state are plotted in Figure B.4. The lowest unoccupied molecular

State	Expt (eV)	Expt (nm)	B3LYP		PBE		M06		M06-HF		M06-2X	
			E (nm)	<i>f</i>								
1NpPt												
1	2.19	567	424	0.0581	496	0.0254	411	0.0538	340	0.1772	356	0.1353
2	2.35	528	378	0.0048	459	0.0032	369	0.0045	309	0.0599	304	0.0116
3	2.74	453	369	0.056	454	0.0081	357	0.0714	285	0.0133	296	0.1684
4	2.90	428	352	0.1298	433	0.1496	338	0.0962	282	0.0105	293	0.0014
5	3.16	393	338	0.0844	416	0.0011	324	0.1324	281	0.0397	282	0.1004
2NpPt												
1	2.80	442	443	0.0282	557	0.0163	422	0.0271	317	0.0046	341	0.0484
2	2.97	417	382	0.0021	482	0.0008	367	0.0021	305	0.192	306	0.1285
3	3.23	384	372	0.0247	479	0.0102	357	0.0693	299	0.0693	293	0.1314
4	3.41	363	369	0.0736	462	0.0339	353	0.0261	285	0.0002	284	0.0045
5	3.55	350	346	0.0726	429	0.0199	331	0.0826	284	0.0032	281	0.0013
RMSD			77		73		87		144		139	
bzqPt												
1			426	0.0367	528	0.0201	410	0.0346	322	0.0036	337	0.0664
2			385	0.0021	488	0.0008	369	0.0021	305	0.0378	303	0.0161
3			370	0.031	460	0.0318	355	0.0372	294	0.0387	296	0.0003
4			343	0.1459	421	0.0824	329	0.1323	288	0.0043	285	0.0049
5			332	0.0094	405	0.0335	316	0.0001	287	0.0007	281	0.0011
ppyPt												
1			406	0.0277	490	0.0107	392	0.0266	317	0.0178	327	0.0756
2			373	0.004	456	0.002	360	0.0038	301	0.1682	294	0.0256
3			355	0.0482	436	0.0041	342	0.0648	284	0.0001	285	0.0079
4			341	0.1049	423	0.0905	328	0.0731	283	0.007	279	0.0911
5			327	0.0127	405	0.0393	311	0.0001	280	0	278	0.0006

Table B.1: The experimental and computed absorption spectra and oscillator strengths, *f*, of 1NpPt, 2NpPt, ppyPt, and bzqPt

	B3LYP	PBE	M06	M06-HF	M06-2X
State	1NpPt				
1	2.2899	1.6369	2.1683	3.5804	3.1991
2	0.6206	0.5603	0.5959	1.9857	0.8657
3	2.0965	0.8861	2.3285	0.8974	3.2573
4	3.1173	3.7131	2.6313	0.7922	0.2964
5	2.4632	0.3098	3.0208	1.5393	2.4539
State	2NpPt				
1	1.6299	1.3899	1.5599	0.5581	1.8749
2	0.4134	0.2948	0.4016	3.5292	2.8902
3	1.3975	1.0177	2.2928	2.1009	2.8625
4	2.4026	1.8247	1.3986	0.0965	0.5211
5	2.3112	1.346	2.4113	0.4421	0.2767
State	bzqPt				
1	1.8251	1.5033	1.7366	0.4995	2.1803
2	0.4126	0.2821	0.4065	1.5646	1.0201
3	1.5614	1.7629	1.6764	1.5564	0.1392
4	3.2608	2.7162	3.044	0.5128	0.5458
5	0.8161	1.7002	0.0671	0.2101	0.2567
State	ppyPt				
1	1.5456	1.0543	1.4888	1.0973	2.293
2	0.5609	0.4439	0.5427	3.2797	1.2649
3	1.9064	0.6198	2.1712	0.0883	0.6927
4	2.7566	2.852	2.2575	0.6501	2.324
5	0.9411	1.8382	0.0639	0.0167	0.187

Table B.2: Transition dipole moments (Debye) from the TD-DFT calculations

Molecule	T1	S1	S1-T1	MEXP
1NpPt	565	415	451	
2NpPt	380	365	386	
bzqPt	355	376	362	
ppyPt	382	373	335	

Table B.3: CASSCF(18,12) vertical excitation energies (nm)

orbital (LUMO) in the S0 manifold is occupied in the S0  $\rightarrow$  T1 vertical excitation, so the S0 LUMO is actually the T1 highest occupied molecular orbital (HOMO). In the 1NpPt S0 LUMO, we find both d-orbital and ligand centered  $\pi$ -orbital character. This indicates that the T1 state is a  $^3\text{MLCT}$  state. Like 1NpPt, ppyPt has  $^3\text{MLCT}$  character in the T1 HOMO, and ppyPt is also fast emitter. The presence of electron probability density on each Pt center indicates that each complex undergoes  $^1\text{MLCT}$ -to- $^3\text{MLCT}$  excitation. But why are 2NpPt and bzqPt slow emitters? Their S0 HOMO orbitals are similar to the 1NpPt and ppyPt HOMO orbitals. There is a noTable difference between the fast and slow emitters and that is the absence of electron probability density on 2'-C that binds

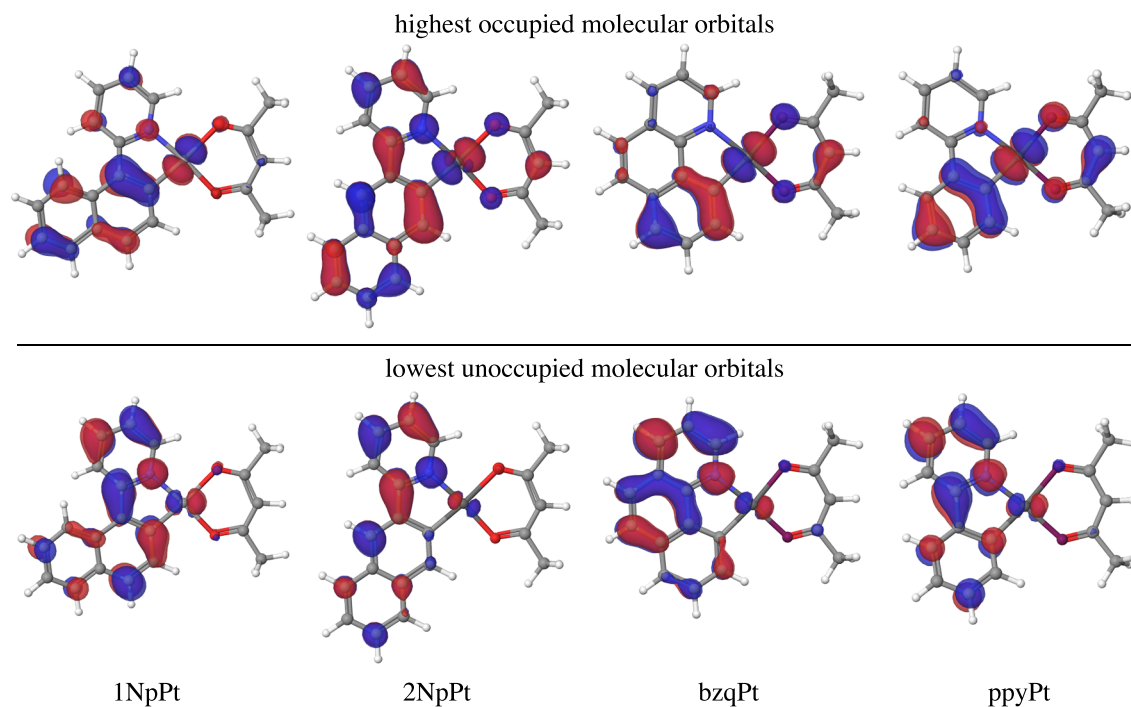


Figure B.4: The highest occupied and lowest unoccupied orbitals of the S0 optimized geometries for 1NpPt, 2NpPt, bzqPt, and ppyPt.

covalently to Pt. The S0 LUMO orbitals of the slow emitters exhibit this absence while the fast emitters do not. Somehow this makes these states more  $^3\text{LC}$ -like in their emission spectra despite having density on the Pt center.

With the excitation spectra accurately modeled, the excited state potential energy surfaces were explored. To truly understand the photophysics of systems as complicated as organometallic complexes, the details of the higher potential energy surfaces must be calculated.

#### B.4.2 Radiative Decay Rates

Table B.4 shows the energies of the S0, T1, S1, and S1-T1 MEXP manifolds relative to the T1 relaxed geometry (the local minima of the T1 manifold). Notice that the 2NpPt T1 and S1 surfaces are both quantitatively higher than their 1NpPt counterparts. This explains emission from the T1 minima where 2NpPt emits at a shorter wavelength than 1NpPt. 1NpPt's phosphorescence is typical of normal Pt cyclometallates; it occurs near 570 nm, and it has a lifetime of 14  $\mu\text{s}$ . 2NpPt, on the

other hand, has a 380  $\mu\text{s}$  lifetime, and its emission is similar to the free ligand at 520 nm. This indicates that the 2NpPt T1 state is strongly ligand centered, and coupling to a  $^1\text{MLCT}$  state must be weak. Like 2NpPt, bzqPt has a relatively long lifetime of 122  $\mu\text{s}$ . ppyPt has the shortest lifetime of the four complexes: 8  $\mu\text{s}$ . Notice that the lifetimes of these complexes are inversely proportional to the energy gap between the T1 minima and the S0 manifold at this geometry.

Molecule	S0	T1	S1	S1-T1MEXP
1NpPt	-1.92	0.00	0.64	0.55
2NpPt	-2.45	0.00	0.33	0.39
bzqPt	-2.59	0.00	0.35	0.83
ppyPt	-1.80	0.00	0.14	1.41

Table B.4: CASSCF state energies (eV) relative to the T1 state at the T1 minima

Molecule	T1 minima				S1-T1 mexp	
	$\langle \hat{H}_{so}^{S0-T1} \rangle$	$\langle \hat{H}_{so}^{S1-T1} \rangle$	$\langle \mu_{el}^{S0-T1} \rangle$	$\langle \mu_{el}^{S0-S1} \rangle$	$\langle \hat{H}_{so}^{S0-T1} \rangle$	$\langle \hat{H}_{so}^{S1-T1} \rangle$
1NpPt	25.6	18.4	0.0009	6.513	25.3	53.6
2NpPt	4.6	19.1	0.0008	0.896	30.9	27.4
bzqPt	5.1	32.1	0.0067	3.767	34.3	540.0
ppyPt	16.3	25.8	0.0038	1.944	42.9	485.1

Table B.5: CASSCF spin orbit coupling constants  $\hat{H}_{so}$  ( $\text{cm}^{-1}$ ) and transition moments  $\mu_{el}$  (Debye) for states at the T1 minima and S1-T1 minimum energy crossing point

For efficient phosphorescence to occur, singlet character must be mixed into excited triplet states. To quantify the extent of this mixing, previous experimental studies estimated the spin-orbit coupling matrix element from the oscillator strengths and absorption frequencies of the  $^3\text{LC}$  and  $^1\text{MLCT}$  states. Previous studies quantified the mixing by calculating the spin-orbit coupling under the one-center approximation from TD-DFT wavefunctions. However, the one-center approximation only allows for mixing between states of similar character like  $^1\text{MLCT}$  and  $^3\text{MLCT}$ , not  $^3,^1\text{MLCT}$  and  $^1,^3\text{LC}$  mixing. The approximation is therefore not useful for our purposes. Instead, the spin-orbit coupling matrix elements and spin-mixed transition dipole moments were calculated using complete active space-configuration interaction (CAS-CI) wavefunctions. The wavefunctions are used as a basis that forms matrix elements over the full two-electron Breit-Pauli operator, and the resulting matrix is diagonalized to obtain the spin-orbit coupled wavefunctions and spin-orbit eigenvalues.

		Rates ( $s^{-1}$ )			
		S1 $\rightarrow$ S0		T1 $\rightarrow$ S0	
Molecule	Expt.	CASSCF	DFT/PBE	CASSCF	DFT/PBE
1NpPt	$7.14 \times 10^4$	$1.86 \times 10^8$	$5.31 \times 10^7$	$6.30 \times 10^2$	$6.87 \times 10^6$
2NpPt	$2.63 \times 10^3$	$5.17 \times 10^6$	$1.06 \times 10^7$	$1.03 \times 10^2$	$3.50 \times 10^6$
bzqPt	$8.20 \times 10^3$	$8.32 \times 10^7$	$3.11 \times 10^7$	$5.09 \times 10^3$	$4.83 \times 10^6$
ppyPt	$1.25 \times 10^5$	$2.28 \times 10^7$	$3.38 \times 10^7$	$2.65 \times 10^2$	$2.97 \times 10^6$

		Lifetimes ( $\mu s$ )			
		S1 $\rightarrow$ S0		T1 $\rightarrow$ S0	
Molecule	Expt.	CASSCF	DFT/PBE	CASSCF	DFT/PBE
1NpPt	14	0.005	0.019	1588	0.146
2NpPt	380	0.194	0.094	9737	0.286
bzqPt	122	0.012	0.032	196	0.207
ppyPt	8	0.044	0.030	3779	0.337

Table B.6: The calculated rates and lifetimes for fluorescence and phosphorescence and the experimental phosphorescence rates and lifetimes

This method includes all the nuclei (it is not a one-center approximation), and it includes all the two-electron terms, so it correctly accounts for the  $^1\text{MLCT}/^3\text{LC}$  mixing. The results of these calculations are shown in Table B.5.

Equations (B.1) and (B.2) were used to compute radiative rates and lifetimes and the results of these calculations are listed in Table B.6. From these calculations we find that, as expected, the fluorescence rate is an order of magnitude faster than phosphorescence. The CASSCF calculations seriously underestimate the rate of phosphorescence by four orders of magnitude. PBE and CASSCF agree on the fluorescence rate, so the errors in the phosphorescence rate do not likely stem from the transition dipole moments. Unfortunately neither TD-DFT nor CASSCF are able to predict the trend in the phosphorescence lifetimes of the four complexes correctly. Either these methods are not advanced enough to accurately compute photophysical properties for organometallic complexes, or there are other dynamics going on which complicate the calculation of these properties.

### B.4.3 Intersystem Crossing

Figure B.5 shows the S0 groundstates overlaid with the MEXP geometries for each molecule. The structural differences are subtle; for 2NpPt, bzqPt, and ppyPt the differences are in the ligand bond lengths reflecting the  $d \rightarrow \pi^*$  transitions. 1NpPt is the only non-planar of the four molecules in

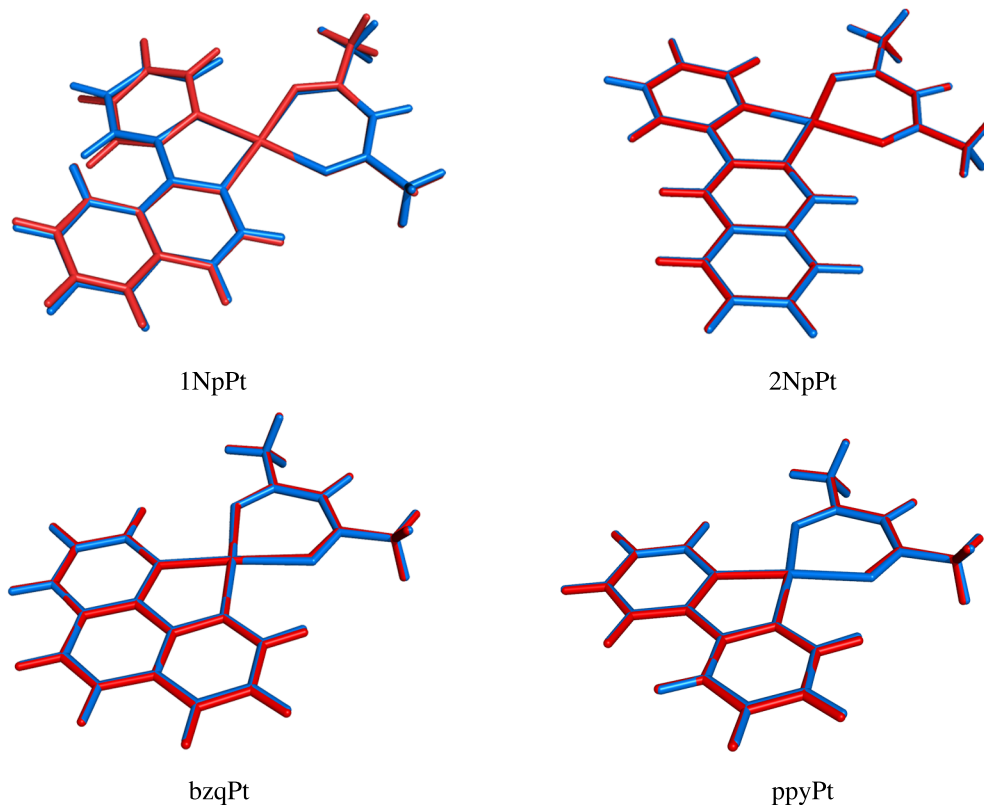


Figure B.5: Overlays of groundstate S0 stationary points (blue) and the S1-T1 minimum energy crossing point geometries (red) for 1NpPt, 2NpPt, bzqPt, and ppyPt.

its ground state and this is because of the steric bumping between 3-H and 3'-H. In its MEXP, 1NpPt's rings flex even further out of the plane. It is easy to understand why intersystem crossing is so fast considering the similarity between the MEXP and S0 minima for these four molecules. The slightest wavepacket motion in an excited manifold could place the packet on the S0 or T1 geometries (which like the MEXP geometries, are nearly identical to the S0 geometry). In fact, The Pt-C,N,O bond lengths are within a hundredth of an Å no matter what the geometry of each molecule. The structural deformations take place in the Np, bzq, ppy, and acac ligands. This of course indicates that the predominant excitations are MLCT states, and this is reflected in the orbitals presented in Figure B.4.

While the triplet excited states are populated to a small degree after excitation, most of the excitation is driven into the singlet excited states, as evidenced by the oscillator strengths of these transitions. The fact that these complexes phosphoresce implies that the excited wavepacket must

Molecule	$p_{sh}$	$k_{ISC}$	$\tau_{ISC}$
1NpPt	$5.74 \times 10^{-4}$	$3.28 \times 10^{10}$	$3.05 \times 10^{-11}$
2NpPt	$1.54 \times 10^{-4}$	$0.56 \times 10^{10}$	$1.78 \times 10^{-10}$
bzqPt	$4.24 \times 10^{-2}$	$7.64 \times 10^{12}$	$1.31 \times 10^{-13}$
ppyPt	$6.19 \times 10^{-2}$	$9.28 \times 10^{12}$	$1.08 \times 10^{-13}$

Table B.7: Landau-Zener hopping probabilities, intersystem crossing rates ( $s^{-1}$ ), and lifetimes (s)

intersystem cross. It is possible that the rate of ISC might determine the lifetime discrepancy between 1NpPt and 2NpPt. To test this hypothesis, the NARRKM ISC rates were computed from the ground state vibrational density of states, and the integrated density of states at the minimum energy crossing point using equations (B.3), (B.4), and (B.5). Table B.7 shows the results of these calculations. The computed intersystem crossing rates are directly proportional to the hopping probabilities calculated based on the spin-orbit coupling at the MEXP. Because the spin-orbit coupling between the S1 and T1 states of 1NpPt and 2NpPt is relatively weak, their hopping probabilities are two orders of magnitude smaller than those of ppyPt and bzqPt. This is reflected in the intersystem crossing rates, which are also smaller. Intersystem crossing is quite fast in these complexes, with the slowest rate being 5.6 per nanosecond. bzqPt and ppyPt were the fastest to intersystem cross because of their strong spin-orbit coupling, and the lifetime of the S1 state is expected to be shorter than picoseconds for each of these. Nonetheless, these complexes intersystem cross at a much faster rate than fluorescence is predicted to occur, and this accounts for the prevalence of radiative decay through phosphorescence.

Unfortunately the results of the NARRKM calculations only reinforce what is already known about these complexes: that the initial excitation from the S0 state drives the wavepacket onto the S1 manifold where ultrafast intersystem crossing is enabled due to the high density of states near the MEXP, and due to the structural similarities between the MEXP and S0 minima. Following intersystem crossing, spin-orbit coupling between the T1 and S1 states allows for transition dipole borrowing and this allows for efficient phosphorescence. The NARRKM calculations do not explain the lifetime discrepancy between 1NpPt and 2NpPt, nor can they be used to describe the lifetime trend between the four test molecules, because the rate of ISC is much faster than the

phosphorescence rate.

## B.5 Conclusions

In this study TD-DFT and CASSCF calculations were able to crudely reproduce the excitation spectra of 1NpPt, 2NpPt, bzqPt, and ppyPt. TD-DFT performed reasonably well given how much faster it is than CASSCF/MP2. The spin-orbit coupling constants between the S0 and T1 states of these complexes were used to compute their phosphorescence lifetimes, and while DFT overestimated the rates by two to three orders of magnitude, CASSCF underestimated the rates by the same margin. Evidently the transition dipole moments, spin-orbit coupling constants, and energy levels predicted by these methods are too crude to be used for radiative rate calculations. Errors for the spin-orbit coupling constants of 3<sup>rd</sup>-row metals are known to be as large as 120% [12]. Neither method was sensitive enough to qualitatively describe the rate or lifetime trends among this set of four complexes. Nonadiabatic RRKM calculations were used to estimate the intersystem crossing rates and the results supported the experimentally inferred rate.

The phosphorescence rate calculations are not satisfying, so work is underway to address the limitations of the SBKJC basis set. Using a larger number of basis functions might be too expensive during MP2 calculations, but it might be possible to use a large basis during spin-orbit coupling calculations. With higher precision values for spin-orbit coupling and better transition dipole moments, it might be possible to replicate the experimental trend. More work is needed to understand why 2NpPt and bzqPt are slower emitters than 1NpPt and ppyPt.

# References

- [1] C. Adachi, M. A. Baldo, S. R. Forrest, S. Lamansky, M. E. Thompson, and R. C. Kwong. *Appl. Phys. Lett.*, 78:1622, 2001.
- [2] V. Adamovich, J. Brooks, A. Tamayo, A. M. Alexander, P. I. Djurovich, B. W. D'Andrade, C. Adachi, S. R. Forrest, and M. E. Thompson. High efficiency single dopant white electrophosphorescent light emitting diodes. *New J. Chem.*, 26(9):1171–1178, 2002.
- [3] M. A. Baldo, D. F. O'Brien, M. E. Thompson, and S. R. Forrest. *Phys. Rev. B.*, 60:14422, 1999.
- [4] M. A. Baldo, M. E. Thompson, and S. R. Forrest. *Nature (London)*, 403:750, 2000.
- [5] J. Brooks, Y. Babayan, S. Lamansky, P. I. Djurovich, I. Tsyba, R. Bau, and M. E. Thompson. Synthesis and characterization of phosphorescent cyclometalated platinum complexes. *Inorganic Chemistry*, 41(12):3055–3066, 2002.
- [6] J. Buey, L. Diez, P. Espinet, H. S. Kitzerow, and J. A. Miguel. *Chem. Mater.*, 8:2375, 1996.
- [7] S. C. Chan, M. C. W. Chan, Y. Wang, C. M. Che, K. K. Cheung, and N. Zhu. *Chem. Eur. J.*, 7:4180, 2001.
- [8] W. B. Connick and H. B. Gray. *J. Am. Chem. Soc.*, 119:11620, 1997.
- [9] I. Eryazici, C. N. Moorefield, and G. R. Newkome. *Chem. Rev.*, 108:1834, 2008.
- [10] A. Farazdel and M. Dupuis. On the determination of the minimum on the crossing seam of two potential energy surfaces. *Journal of Computational Chemistry*, 12(2):276–282, 1991.
- [11] S. J. Farley, D. L. Rochester, A. L. Thompson, J. A. Howard, and J. G. Williams. Controlling emission energy, self-quenching, and excimer formation in highly luminescent N<sup>+</sup>C<sup>-</sup>N-coordinated Platinum(II) complexes. *Inorg. Chem.*, 44:9690–9703, 2005.
- [12] D. G. Fedorov, S. Koseki, M. W. Schmidt, and M. S. Gordon. Spin-orbit coupling in molecules: chemistry beyond the adiabatic approximation. *Int. Rev. Phys. Chem.*, 22:551–592, 2003.
- [13] J. Harvey. Understanding the kinetics of spin-forbidden chemical reactions. *Phys. Chem. Chem. Phys.*, 9:331–343, 2007.
- [14] P. J. Hay and W. R. Wadt. *Ab initio* effective core potentials for molecular calculations. potentials for K to Au including the outermost core orbitals. *J. Chem. Phys.*, 82(1):299–310, 1985.
- [15] H. K. Kip, L. K. Cheng, K. K. Cheung, and C. M. Che. *J. Chem. Soc., Dalton Trans.*, pages 2933–2938, 1993.
- [16] S. C. F. Kui, S. S. Y. Chui, C. M. Che, and N. Zhu. *J. Am. Chem. Soc.*, 128:8297, 2006.
- [17] S. W. Lai, C. W. Chan, K. K. Cheung, and C. M. Che. *Organometallics*, 18:3327, 1999.

- [18] X.-N. Li, Z.-J. Wu, and H.-J. Zhang. Comparative study of electronic structure and optical properties of a series of Pt(II) complexes containing different electron-donating and -withdrawing groups: a DFT study. *J. Phys. Org. Chem.*, 23:181–189, 2010.
- [19] W. Lu, M. C.-W. Chan, T. C. Cheung, S. M. Peng, and C. Che. *Organometallics*, 38:4046, 2001.
- [20] W. Lu, B. X. Mi, M. C. W. Chan, Z. Hui, C. M. Che, N. Zhu, and S. T. Lee. *J. Am. Chem. Soc.*, 126:4958, 2004.
- [21] W. Lu, B. X. Mi, M. C. W. Chan, Z. Hui, N. Zhu, S. T. Lee, and C. M. Che. *Chem. Commun.*, page 206, 2002.
- [22] B. Ma, P. I. Djurovich, M. Yousufuddin, R. Bau, and M. E. Thompson. *J. Phys. Chem. C*, 112:8022–8031, 2008.
- [23] C. Makedonas, C. A. Mistopoulou, F. J. Lahoz, and A. I. Balana. Synthesis, characterization, and crystal structure of the Pd(phen)(bdt) complex. a DFT and TDDFT study of its ground electronic and excited states compared to those of analogous complexes. *Inorganic Chemistry*, 42(26):8853–8865, 2003.
- [24] J. E. McGarrah, Y. J. Kim, M. Hissler, and R. Eisenberg. *Inorg. Chem.*, 40:4510, 2001.
- [25] E. E. Nikitin. *Annu. Rev. Phys. Chem.*, 50:1–20, 1999.
- [26] K. Nozaki. Theoretical studies on photophysical properties and mechanism of phosphorescence in fac-Ir(2-phenylpyridine)<sub>3</sub>. *J. Chin. Chem. Soc.*, 53:101–112, 2006.
- [27] D. Ravindranathan, D. A. Vezzu, L. Bartolotti, P. D. Boyle, and S. Huo. Improvement in phosphorescence efficiency through tuning of coordination geometry of tridentate cyclometalated Platinum(II) complexes. *Inorg. Chem.*, 49:8922–8928, 2010.
- [28] M. W. Schmidt, K. K. Baldrige, J. A. Boatz, S. T. Elbert, M. S. Gordon, J. H. Jensen, S. Koseki, N. Matsunaga, K. A. Nguyen, S. J. Su, T. L. Windus, M. Dupuis, and J. A. Montgomery. General atomic and molecular electronic structure system. *J. Comp. Chem.*, 14:1347–1363, 1993.
- [29] J. R. Sommer, R. T. Farley, K. R. Graham, Y. Yang, J. R. Reynolds, J. Xue, and K. S. Schanze. Efficient near-infrared polymer and organic light-emitting diodes based on electrophosphorescence from (Tetraphenyltetranaphtho[2,3]porphyrin)platinum(II). *Applied Materials and Interfaces*, 1(2):274–278, 2009.
- [30] W. J. Stevens, M. Krauss, H. Basch, and P. G. Jasiens. Relativistic compact effective potentials for efficient, shared-exponent basis sets for the third-, fourth-, and fifth-row atoms. *Can. J. Chem.*, 70:612–630, 1992.
- [31] S. W. Thomas, K. Venkatesan, P. Mller, and T. M. Swager. Dark-field oxidative addition-based chemosensing: New bis-cyclometalated Pt(II) complexes and phosphorescent detection of cyanogen halides. *J. Am. Chem. Soc.*, 128(51):16641–16648, 2006.
- [32] G. S.-M. Tong and C.-M. Che. Emissive or nonemissive? a theoretical analysis of the phosphorescence efficiencies of cyclometalated Platinum(II) Complexes. *Chem. Eur. J.*, 2009(15):7225–7237, 2009.
- [33] K. H. Wong, C. W. Chan, and C. M. Che. *Chem. Eur. J.*, 5:2845, 1999.
- [34] K. M. C. Wong, W. S. Tang, B. W. K. Chu, N. Zhu, and V. W. W. Yam. *Organometallics*, 23:3459, 2004.
- [35] W. Y. Wong, Z. He, S. K. So, K. L. Tong, and Z. Lin. *Organometallics*, 24:4079, 2005.

- [36] W. Wu, W. Wu, S. Ji, H. Guo, P. Song, K. Han, L. Chi, J. Shao, and J. Zhao. Tuning the emission properties of cyclometalated platinum(II) complexes by intramolecular electron-sink arylethynylated ligands and its application for enhanced luminescent oxygen sensing. *J. Mater. Chem.*, 20(43):9775–9786, 2010.
- [37] H. Yesin, D. Donges, W. Humbs, J. Strasser, R. Sitters, and M. Glasbeek. *Inorg. Chem.*, 41:4915, 2002.
- [38] J. Yi, B. Zhang, P. Shao, Y. Li, and W. Sun. Synthesis and photophysics of Platinum(II) 6-Phenyl-4-(9,9-dihexylfluoren-2-yl)-2,2-bipyridine complexes with phenothiazinyl acetylide ligand. *J. Phys. Chem. A*, 114(26):7055–7062, 2010.
- [39] H. Zhang, B. Zhang, Y. Li, and W. Sun. *Inorg. Chem.*, 48:3617, 2009.
- [40] Y. Zhao and D. G. Truhlar. The M06 suite of density functionals for main group thermochemistry, thermochemical kinetics, noncovalent interactions, excited states, and transition elements: two new functionals and systematic testing of four M06-class functionals and 12 other functionals. *Theor. Chem. Account*, 120:215–241, 2008.

## Appendix C

# Supplemental Material

Table C.1: Experimental crack tip velocities versus reduced critical energy release rates for  $\{111\}\langle 112\rangle$  fracture. The references for this data are provided in Chapter 3

$G/G_c$	Tip Velocity (m/s)	$G/G_c$ Error	Velocity Error (m/s)
1.00	1948	0.4	194
1.75	2060	0.6	207
1.83	2450	0.6	246
2.04	2199	0.7	216
2.13	2545	0.8	77
2.15	2372	0.8	90
2.36	2346	0.9	255
2.95	2493	1.1	246
3.69	2398	1.4	242
4.09	2900	1.5	290
5.38	2424	2.1	238
5.52	2926	2.1	290
5.87	3194	2.2	324
7.29	3445	2.8	346

Table C.2: Computed eFF crack tip velocities versus reduced critical energy release rates

eFF periodic	
$G/G_c$	Tip Velocity (m/s)
0.92	0
0.92	0
0.92	0
0.97	0
1.07	1276
1.12	1134
1.15	1122
1.15	2250
1.24	2390
1.49	2321
1.56	2432
1.62	2184
1.65	2154
1.69	2217
1.73	2465
1.94	3219
1.94	2022
1.78	2518
2.05	2339
2.08	2069

eFF slab	
$G/G_c$	Tip Velocity (m/s)
1.00	823
1.10	1672
1.23	2392
1.38	2492
1.43	2292
1.62	2529
1.97	2520

Table C.3: Computed ReaxFF crack tip velocities versus reduced critical energy release rates

$G/G_c$	Tip Velocity (m/s)
0.35	64
0.42	127
0.50	63
0.58	57
0.68	56
0.78	68
0.89	63
1.00	2177
1.38	2536
3.11	3010
5.54	2948
8.65	3132
12.46	3273
16.96	3493
22.15	3445

Table C.4: Computed Stilling-Weber crack tip velocities versus reduced critical energy release rates

$G/G_c$	Tip Velocity (m/s)
1.00	97
1.28	156
1.57	875
2.27	1964

Table C.5: Computed multi scale-method crack tip velocities versus reduced critical energy release rates

DCET	
$G/G_c$	Tip Velocity (m/s)
0.56	0
0.85	0
0.96	1478
1.07	2003
1.19	2508
1.44	2625
1.67	2975
1.70	2683
1.81	2781
1.96	2644
2.63	2606

EDIP	
$G/G_c$	Tip Velocity (m/s)
1.00	136
1.30	350
2.04	1108
2.36	992

Table C.6: eFF Hugoniot equation of state data for polyethylene

$\rho/\rho_0$	P (GPa)	$U_p$ (km/s)	$U_s$ (km/s)	T (K)	% ionized electrons	$\sigma$ (Siemens)
1.26	6	1.2	4.9	371	0.0	44
1.37	8	1.6	5.1	423	0.0	67
1.47	11	2.1	5.8	522	0.0	10
1.58	18	2.8	7.0	658	0.0	133
1.68	23	3.2	7.4	786	0.0	309
1.79	32	4.0	8.5	984	0.0	258
1.89	48	5.0	10.0	1581	0.0	657
2.00	64	5.9	11.3	2095	0.0	95
2.11	87	7.1	12.9	2846	0.0	1227
2.21	110	8.1	14.2	3376	0.0	1398
2.32	135	9.1	15.5	4659	0.0	154
2.42	160	10.1	16.6	5684	0.1	3627
2.53	196	11.3	18.2	7041	0.4	570
2.63	232	12.5	19.6	8992	0.9	88
2.74	278	13.8	21.2	11508	1.7	355
2.84	329	15.2	22.8	12596	3.4	2487
2.95	376	16.4	24.2	16393	8.1	186
3.05	470	18.5	26.8	20391	16.8	1855

The S0 and T1 coordinates are from DFT PBE/lacvp\*\* optimizations and the S1-T1 minimum energy crossing point coordinates come from CASSCF(18,12)/SBKJC MEXP searches.

1NpPt  
41

PT 0.875 0.014 0.002  
N -0.154 -1.694 -0.091  
C -1.700 -4.096 0.425  
C 0.459 -2.982 -0.063  
C -1.547 -1.641 0.076  
C -2.324 -2.722 0.343  
C -0.296 -4.157 0.197  
H 1.536 -2.986 -0.188  
H -3.387 -2.632 0.528  
H 0.227 -5.117 0.218  
H -2.331 -4.982 0.477  
C -0.931 0.743 0.127  
C -3.634 1.676 0.101  
C -2.015 -0.197 0.015  
C -1.225 2.158 0.300  
C -2.519 2.589 0.317  
C -3.389 0.282 -0.111  
H -0.385 2.836 0.412  
H -2.745 3.646 0.460  
O 1.866 1.872 0.080  
O 2.784 -0.827 -0.150  
C 3.939 -0.255 -0.180  
C 3.127 2.126 0.010  
C 4.155 1.145 -0.112  
H 5.182 1.499 -0.155  
C 5.135 -1.189 -0.304  
C 3.497 3.602 0.066  
C -5.794 -0.018 -0.516  
C -4.502 -0.543 -0.467  
C -4.956 2.189 0.066  
C -6.032 1.349 -0.224  
H -6.626 -0.664 -0.795  
H -4.345 -1.580 -0.728  
H -5.118 3.250 0.252  
H -7.046 1.745 -0.249  
H 4.783 -2.225 -0.323  
H 5.820 -1.052 0.543  
H 5.691 -0.978 -1.228  
H 4.581 3.751 0.015  
H 3.117 4.045 0.997  
H 3.024 4.133 -0.773

1NpPt\_S1T1mexp  
41

PT 0.863 0.047 -0.054  
N -0.190 -1.649 -0.221  
C -1.604 -3.988 0.708  
C 0.385 -2.942 -0.332  
C -1.541 -1.584 0.158  
C -2.256 -2.638 0.633  
C -0.294 -4.088 0.163  
H 1.401 -2.978 -0.709  
H -3.287 -2.531 0.959  
H 0.209 -5.057 0.109  
H -2.162 -4.854 1.062  
C -0.943 0.797 0.166  
C -3.673 1.676 0.047  
C -2.020 -0.160 0.066  
C -1.275 2.200 0.355  
C -2.581 2.607 0.319  
C -3.398 0.281 -0.113  
H -0.459 2.902 0.505  
H -2.835 3.661 0.459  
O 1.886 1.876 0.138  
O 2.746 -0.824 -0.329  
C 3.914 -0.278 -0.267  
C 3.153 2.098 0.116  
C 4.160 1.100 -0.055  
H 5.195 1.434 -0.035  
C 5.094 -1.217 -0.466  
C 3.567 3.555 0.274  
C -5.769 -0.090 -0.624  
C -4.473 -0.589 -0.475  
C -4.998 2.162 -0.091  
C -6.039 1.288 -0.417  
H -6.578 -0.765 -0.904  
H -4.273 -1.639 -0.646  
H -5.197 3.225 0.050  
H -7.055 1.663 -0.530  
H 4.770 -2.249 -0.297  
H 5.919 -0.970 0.213  
H 5.465 -1.132 -1.498  
H 4.657 3.665 0.279  
H 3.159 3.959 1.212  
H 3.150 4.140 -0.559

1NpPt\_t1geom  
41

Pt 2.333 0.880 -5.659  
N 4.250 1.439 -5.569  
C 6.954 2.049 -5.176  
C 4.656 2.725 -5.520  
C 5.191 0.387 -5.496  
C 6.551 0.725 -5.243  
C 5.993 3.078 -5.353

H 3.853 3.463 -5.605  
 H 7.263 -0.078 -5.053  
 H 6.270 4.134 -5.323  
 H 7.998 2.296 -4.964  
 C 3.120 -0.901 -5.531  
 C 4.556 -3.381 -5.561  
 C 4.601 -0.902 -5.624  
 C 2.446 -2.106 -5.337  
 C 3.146 -3.321 -5.286  
 C 5.294 -2.165 -5.817  
 H 1.357 -2.090 -5.234  
 H 2.612 -4.262 -5.116  
 O 0.412 0.153 -5.708  
 O 1.637 2.913 -5.749  
 C 0.390 3.218 -5.793  
 C -0.641 0.905 -5.754  
 C -0.695 2.310 -5.793  
 H -1.693 2.754 -5.833  
 C 0.078 4.704 -5.851  
 C -1.935 0.114 -5.767  
 C 7.277 -3.518 -6.372  
 C 6.628 -2.274 -6.275  
 C 5.237 -4.615 -5.643  
 C 6.586 -4.686 -6.030  
 H 8.310 -3.566 -6.727  
 H 7.155 -1.377 -6.607  
 H 4.684 -5.533 -5.416  
 H 7.083 -5.659 -6.091  
 H 1.010 5.284 -5.830  
 H -0.555 5.003 -4.999  
 H -0.479 4.948 -6.771  
 H -2.821 0.763 -5.799  
 H -1.987 -0.523 -4.869  
 H -1.949 -0.558 -6.641

2NpPt  
 41

PT -0.840 -0.058 -0.001  
 N -0.467 1.913 -0.000  
 C 0.194 4.617 -0.005  
 C -1.443 2.851 0.000  
 C 0.863 2.281 -0.003  
 C 1.197 3.646 -0.005  
 C -1.151 4.213 -0.002  
 H -2.462 2.454 0.002  
 H 2.250 3.935 -0.007  
 H -1.967 4.939 -0.002  
 H 0.456 5.678 -0.007  
 C 1.135 -0.144 -0.003  
 C 3.985 0.090 0.002  
 C 1.783 1.147 -0.002  
 C 1.923 -1.285 -0.001

C 3.345 -1.207 0.001  
 C 3.171 1.253 -0.000  
 H 1.445 -2.271 -0.002  
 H 3.665 2.232 0.000  
 O -1.026 -2.086 -0.008  
 O -2.969 0.220 0.007  
 C -3.792 -0.766 0.010  
 C -2.164 -2.706 -0.007  
 C -3.451 -2.138 0.002  
 H -4.285 -2.846 0.004  
 C -5.265 -0.395 0.021  
 C -2.037 -4.219 -0.015  
 C 5.408 0.160 0.005  
 C 4.167 -2.370 0.004  
 C 5.549 -2.267 0.007  
 C 6.176 -0.992 0.008  
 H 5.886 1.146 0.005  
 H 3.683 -3.353 0.004  
 H 6.164 -3.172 0.010  
 H 7.268 -0.925 0.010  
 H -5.376 0.698 0.045  
 H -5.773 -0.829 0.899  
 H -5.774 -0.788 -0.876  
 H -0.977 -4.505 -0.041  
 H -2.549 -4.649 -0.892  
 H -2.506 -4.654 0.883

2NpPt\_S1T1mexp  
 41

PT -0.833 -0.036 -0.001  
 N -0.469 1.915 -0.000  
 C 0.202 4.639 -0.005  
 C -1.467 2.880 0.000  
 C 0.851 2.306 -0.003  
 C 1.197 3.660 -0.005  
 C -1.173 4.218 -0.002  
 H -2.475 2.478 0.002  
 H 2.250 3.944 -0.007  
 H -1.980 4.948 -0.002  
 H 0.465 5.695 -0.007  
 C 1.115 -0.117 -0.003  
 C 3.996 0.069 0.002  
 C 1.783 1.186 -0.002  
 C 1.943 -1.309 -0.001  
 C 3.382 -1.225 0.001  
 C 3.154 1.263 -0.000  
 H 1.445 -2.278 -0.002  
 H 3.656 2.229 0.000  
 O -1.045 -2.090 -0.007  
 O -2.937 0.191 0.007  
 C -3.792 -0.774 0.010  
 C -2.165 -2.726 -0.007

C -3.462 -2.150 0.002  
 H -4.292 -2.851 0.004  
 C -5.267 -0.391 0.021  
 C -2.041 -4.237 -0.015  
 C 5.398 0.161 0.005  
 C 4.175 -2.385 0.004  
 C 5.576 -2.282 0.007  
 C 6.181 -1.012 0.008  
 H 5.878 1.141 0.005  
 H 3.686 -3.359 0.004  
 H 6.181 -3.184 0.010  
 H 7.268 -0.930 0.010  
 H -5.375 0.699 0.045  
 H -5.767 -0.826 0.898  
 H -5.768 -0.785 -0.875  
 H -0.980 -4.512 -0.041  
 H -2.549 -4.654 -0.894  
 H -2.506 -4.659 0.885

2NpPt\_t1geom  
 41

Pt -1.938 0.736 -6.671  
 N -0.008 1.298 -6.676  
 C 2.717 1.883 -6.687  
 C 0.406 2.582 -6.681  
 C 0.913 0.243 -6.677  
 C 2.297 0.561 -6.682  
 C 1.756 2.925 -6.687  
 H -0.395 3.326 -6.679  
 H 3.025 -0.254 -6.683  
 H 2.048 3.976 -6.690  
 H 3.786 2.119 -6.692  
 C -1.113 -1.046 -6.669  
 C 0.308 -3.547 -6.660  
 C 0.314 -1.053 -6.672  
 C -1.816 -2.269 -6.663  
 C -1.139 -3.537 -6.658  
 C 1.010 -2.312 -6.668  
 H -2.911 -2.249 -6.662  
 H 2.105 -2.337 -6.669  
 O -3.846 -0.008 -6.672  
 O -2.653 2.742 -6.666  
 C -3.904 3.048 -6.661  
 C -4.914 0.727 -6.671  
 C -4.981 2.133 -6.665  
 H -5.985 2.566 -6.662  
 C -4.216 4.534 -6.652  
 C -6.209 -0.062 -6.676  
 C 0.960 -4.807 -6.654  
 C -1.845 -4.753 -6.650  
 C -1.167 -6.005 -6.644  
 C 0.224 -6.019 -6.646

H 2.054 -4.837 -6.656  
 H -2.940 -4.725 -6.648  
 H -1.737 -6.937 -6.637  
 H 0.765 -6.971 -6.642  
 H -3.282 5.111 -6.630  
 H -4.826 4.801 -5.772  
 H -4.795 4.817 -7.547  
 H -5.994 -1.138 -6.698  
 H -6.822 0.201 -7.555  
 H -6.809 0.168 -5.779

bzqPt  
 37

PT -0.598 0.032 0.001  
 O -2.004 1.501 -0.003  
 O -2.061 -1.524 0.004  
 C -3.324 -1.274 0.004  
 C -3.920 0.006 -0.001  
 C -3.278 1.260 -0.005  
 C -4.214 -2.503 0.009  
 C -4.135 2.512 -0.013  
 H -5.013 0.035 -0.002  
 H -3.494 3.403 0.006  
 H -4.769 2.542 -0.915  
 H -4.807 2.529 0.860  
 H -5.284 -2.251 0.015  
 H -3.996 -3.120 -0.879  
 H -3.986 -3.120 0.894  
 C 3.363 2.811 0.004  
 C 3.416 1.395 0.001  
 C 2.176 0.696 -0.001  
 C 0.902 1.336 0.001  
 C 0.899 2.734 0.005  
 C 2.122 3.452 0.007  
 H -0.051 3.276 0.007  
 H 2.089 4.547 0.010  
 C 0.808 -2.642 -0.001  
 N 0.919 -1.302 -0.001  
 C 2.168 -0.724 -0.002  
 C 3.361 -1.493 -0.003  
 C 3.223 -2.902 -0.004  
 C 1.948 -3.467 -0.003  
 H 1.812 -4.551 -0.003  
 H 4.114 -3.538 -0.005  
 H -0.214 -3.029 0.000  
 C 4.625 0.611 -0.001  
 C 4.604 -0.766 -0.003  
 H 5.541 -1.334 -0.005  
 H 5.587 1.137 0.000  
 H 4.291 3.393 0.006

bzqPt\_S1T1mexp  
 37  
 PT -0.571 0.035 0.000  
 O -2.069 1.484 -0.002  
 O -2.098 -1.405 0.003  
 C -3.367 -1.227 0.004  
 C -4.011 0.052 0.000  
 C -3.354 1.301 -0.004  
 C -4.203 -2.497 0.008  
 C -4.198 2.568 -0.013  
 H -5.099 0.060 -0.000  
 H -3.546 3.448 0.008  
 H -4.822 2.602 -0.916  
 H -4.865 2.589 0.859  
 H -5.278 -2.282 0.014  
 H -3.957 -3.096 -0.879  
 H -3.947 -3.096 0.893  
 C 3.338 2.810 0.004  
 C 3.451 1.345 0.001  
 C 2.242 0.647 0.000  
 C 0.918 1.298 0.001  
 C 0.884 2.770 0.005  
 C 2.067 3.483 0.006  
 H -0.087 3.258 0.006  
 H 2.056 4.573 0.009  
 C 0.833 -2.690 -0.001  
 N 0.931 -1.324 -0.000  
 C 2.192 -0.780 -0.001  
 C 3.400 -1.507 -0.003  
 C 3.291 -2.982 -0.004  
 C 2.016 -3.523 -0.003  
 H 1.872 -4.605 -0.003  
 H 4.186 -3.605 -0.006  
 H -0.165 -3.116 -0.000  
 C 4.694 0.624 -0.001  
 C 4.629 -0.769 -0.003  
 H 5.561 -1.339 -0.004  
 H 5.647 1.151 -0.001  
 H 4.252 3.407 0.005

bzqPt\_t1geom  
 37  
 Pt 0.300 0.608 0.034  
 O 2.327 0.833 0.050  
 O -0.023 2.691 0.041  
 C 0.939 3.554 0.054  
 C 2.317 3.257 0.061  
 C 2.925 1.982 0.057  
 C 0.484 4.998 0.061  
 C 4.437 1.894 0.058  
 H 3.001 4.110 0.070

H 4.751 0.842 0.100  
 H 4.855 2.357 -0.852  
 H 4.860 2.433 0.922  
 H 1.324 5.708 0.075  
 H -0.137 5.193 -0.829  
 H -0.154 5.179 0.942  
 C 0.165 -4.201 0.017  
 C -1.036 -3.406 0.007  
 C -0.858 -1.987 0.014  
 C 0.410 -1.356 0.029  
 C 1.567 -2.187 0.038  
 C 1.423 -3.592 0.032  
 H 2.560 -1.729 0.050  
 H 2.319 -4.222 0.040  
 C -2.711 1.145 0.007  
 N -1.686 0.215 0.014  
 C -1.982 -1.114 0.006  
 C -3.319 -1.619 -0.011  
 C -4.378 -0.638 -0.019  
 C -4.041 0.724 -0.010  
 H -4.826 1.485 -0.016  
 H -5.422 -0.962 -0.032  
 H -2.399 2.190 0.015  
 C -2.349 -3.911 -0.009  
 C -3.471 -3.021 -0.018  
 H -4.482 -3.441 -0.031  
 H -2.520 -4.992 -0.016  
 H 0.083 -5.293 0.012

ppyPt  
 35  
 PT -0.321 0.029 -0.000  
 O -1.721 1.511 -0.005  
 O -1.823 -1.500 0.006  
 C -3.083 -1.236 0.006  
 C -3.662 0.052 -0.001  
 C -2.998 1.295 -0.006  
 C -3.986 -2.454 0.016  
 C -3.835 2.560 -0.015  
 H -4.754 0.097 -0.002  
 H -3.180 3.442 -0.013  
 H -4.482 2.592 -0.907  
 H -4.494 2.597 0.869  
 H -5.054 -2.192 0.002  
 H -3.761 -3.087 -0.858  
 H -3.779 -3.060 0.914  
 C 3.570 2.853 0.008  
 C 3.661 1.458 0.006  
 C 2.485 0.680 0.002  
 C 1.197 1.298 0.000  
 C 1.131 2.702 0.002  
 C 2.304 3.469 0.006

H 4.479 3.462 0.011  
 H 4.646 0.979 0.008  
 H 0.150 3.189 0.001  
 H 2.236 4.563 0.008  
 C 0.981 -2.642 -0.004  
 N 1.180 -1.304 -0.000  
 C 2.456 -0.778 -0.001  
 C 3.555 -1.654 -0.004  
 C 3.356 -3.035 -0.008  
 C 2.046 -3.541 -0.008  
 H 1.845 -4.614 -0.011  
 H 4.213 -3.714 -0.011  
 H 4.566 -1.239 -0.005  
 H -0.068 -2.950 -0.003

ppyPt\_S1T1mexp  
 35

PT -0.309 0.027 0.000  
 O -1.810 1.504 -0.003  
 O -1.853 -1.369 0.005  
 C -3.136 -1.173 0.005  
 C -3.764 0.088 -0.001  
 C -3.083 1.350 -0.005  
 C -3.968 -2.442 0.014  
 C -3.917 2.623 -0.014  
 H -4.851 0.119 -0.001  
 H -3.262 3.502 -0.012  
 H -4.556 2.651 -0.907  
 H -4.569 2.656 0.869  
 H -5.044 -2.236 0.002  
 H -3.698 -3.051 -0.859  
 H -3.714 -3.026 0.910  
 C 3.581 2.800 0.007  
 C 3.703 1.421 0.005  
 C 2.522 0.626 0.002  
 C 1.172 1.276 0.001  
 C 1.120 2.738 0.002  
 C 2.275 3.472 0.005  
 H 4.479 3.419 0.010  
 H 4.682 0.954 0.007  
 H 0.140 3.206 0.000  
 H 2.252 4.561 0.007  
 C 1.007 -2.696 -0.003  
 N 1.180 -1.320 -0.000  
 C 2.469 -0.851 -0.001  
 C 3.602 -1.642 -0.004  
 C 3.442 -3.100 -0.007  
 C 2.137 -3.585 -0.007  
 H 1.940 -4.660 -0.009  
 H 4.310 -3.758 -0.011  
 H 4.595 -1.197 -0.004  
 H -0.014 -3.062 -0.002

ppyPt\_t1geom  
 35

Pt 0.312 0.952 -0.003  
 O 2.329 0.941 0.004  
 O 0.203 2.978 -0.007  
 C 1.213 3.220 -0.005  
 C 2.371 2.791 -0.000  
 C 2.656 1.722 0.003  
 C 1.095 4.535 -0.007  
 C 3.915 1.380 0.008  
 H 3.191 3.509 0.001  
 H 4.051 0.297 0.011  
 H 4.391 1.798 -0.881  
 H 4.385 1.802 0.897  
 H 2.094 4.975 -0.005  
 H 0.555 4.853 -0.900  
 H 0.557 4.871 0.880  
 C 0.316 -3.926 0.003  
 C -0.897 -3.221 0.001  
 C -0.897 -1.814 -0.000  
 C 0.323 -1.116 0.002  
 C 1.537 -1.824 0.004  
 C 1.534 -3.228 0.004  
 H 0.313 -5.029 0.004  
 H -1.852 -3.773 0.001  
 H 2.495 -1.279 0.003  
 H 2.488 -3.782 0.006  
 C -3.281 0.949 0.129  
 N -2.103 0.288 0.135  
 C -2.152 -1.057 0.003  
 C -3.340 -1.765 -0.135  
 C -4.539 -1.058 -0.137  
 C -4.513 0.328 -0.002  
 H -5.429 0.910 0.000  
 H -5.485 -1.581 -0.243  
 H -3.334 -2.844 -0.241  
 H -3.207 2.028 0.237

## Appendix D

### Published Research

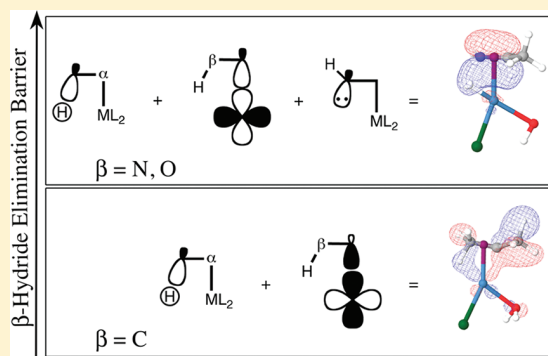
# Understanding $\beta$ -Hydride Eliminations from Heteroatom Functional Groups

Patrick L. Theofanis\* and William A. Goddard, III

Materials and Process Simulation Center, Beckman Institute (139-74), California Institute of Technology, Pasadena, California 91125, United States

**S** Supporting Information

**ABSTRACT:** Using density functional theory, we investigated detailed aspects of the quintessential organometallic process,  $\beta$ -hydride elimination (BHE). In general, we find that most BHE processes from alkyl functional group  $\beta$ -atoms are facile, while BHE processes from heteroatom functional groups (N and O) are prohibitively high in energy. We present calculated molecular orbitals and atomic NBO charges obtained from snapshots along reaction profiles to present a qualitative overview for how heteroatoms adversely affect these processes. We discuss these results to provide an illustration for how these processes proceed, clarifying a sometimes oversimplified model for these reactions.



## I. INTRODUCTION

$\beta$ -hydride elimination (BHE), the [2 + 2] pericyclic hydride rearrangement, is a well-established process frequently encountered in organometallic reaction mechanisms. BHE is an extraordinarily prevalent reaction mechanism, and it is commonly presented in reports,<sup>1–8</sup> reviews,<sup>9–11</sup> and textbooks.<sup>12–16</sup>

Despite its literature precedence, more can be learned about BHE, especially when heteroatoms are involved in the process. This became apparent to us while we examined the details of the Wacker process. Early reports on the Wacker process erroneously labeled the final oxidation step as a BHE from a [(1-hydroxyethane-1-yl)PdCl] complex to form an  $\eta^2$ -coordinated aldehyde, [(acetaldehyde)PdCl]: Pd-CH(CH<sub>3</sub>)-O-H\*  $\rightarrow$  H\*-Pd(CH(CH<sub>3</sub>)=O).<sup>12,17–22</sup> Our report on Wacker oxidation<sup>23</sup> and that of others<sup>24</sup> investigated if BHE is a generally facile process for coordinatively saturated ligands. We found this false. For BHE from coordinated alkanes, we found expectedly low barriers. For BHE from ligands with an alcohol functional group at the  $\beta$ -position, we discovered prohibitive barriers insurmountable in most chemical environments. A theoretical study on Wacker-like side reactions in a palladium polymerization catalyst also observed high barriers for this type of BHE; instead, they attributed their oxidative side reaction to water-mediated deprotonation of a (2-hydroxyethane-1-yl)Pd complex, which also yielded an aldehyde.<sup>25</sup> This result surprised us, and we became interested in the factors that lead to the increased barrier height for  $\beta$ -hydride elimination from heteroatoms.

We have found another catalytic cycle in which  $\beta$ -hydride elimination from a  $\beta$ -heteroatom is proposed to be involved. In the “Hieber base reaction”, a process to create metal carbonyl

hydrides, a  $\beta$ -hydride elimination from an iron–carboxyl complex is proposed: [(CO)<sub>4</sub>Fe-C(O)-O-H\*]<sup>-</sup>  $\rightarrow$  [H\*-Fe(CO)<sub>4</sub>]<sup>-</sup> + CO<sub>2</sub>.<sup>26,27</sup> We state the existence of this mechanism to illustrate that authors will propose BHE from a  $\beta$ -heteroatom without regard to its feasibility. Our hope is that our study will prompt chemists to re-examine the likelihood of  $\beta$ -hydride elimination from  $\beta$ -heteroatoms.

To begin, we should state that BHE from alkyl ligands on d<sup>8</sup> metals such as Ni, Pd, and Pt is a well-understood process. The necessary conditions for BHE are self-evident: a vacant coordination site on the H-accepting metal, a hydrogen atom bound to a  $\beta$ -atom, and a near-planar geometry of the metal,  $\alpha$ -atom,  $\beta$ -atom, and the hydrogen which maximizes orbital overlap.<sup>13</sup> Thorn and Hoffmann, who studied the microscopic reverse of BHE, olefin insertion into a metal–hydride bond, and subsequently Morokuma and co-workers were the first groups to present orbital symmetry descriptions of the BHE mechanism for  $\beta$ -alkyl fragments based on ab initio calculations.<sup>28,29</sup> These studies do an excellent job of describing, in a qualitative sense, the molecular orbitals (MOs) that contribute to and facilitate  $\beta$ -hydride transfer. Figure 1 is a reproduction of the orbitals identified by Morokuma and co-workers. Morokuma identifies the orbitals that define the agostic metal–hydride interaction, and he accurately describes the flow of orbital density throughout the reaction coordinate. The  $\sigma_{CH}$  and  $\sigma_{M\alpha}$  orbitals, their antibonding counterparts, and their linear combination,  $\Psi_3^{TS}$ , are especially important because they define the active bonds during the BHE.

Received: June 23, 2011

Published: August 25, 2011

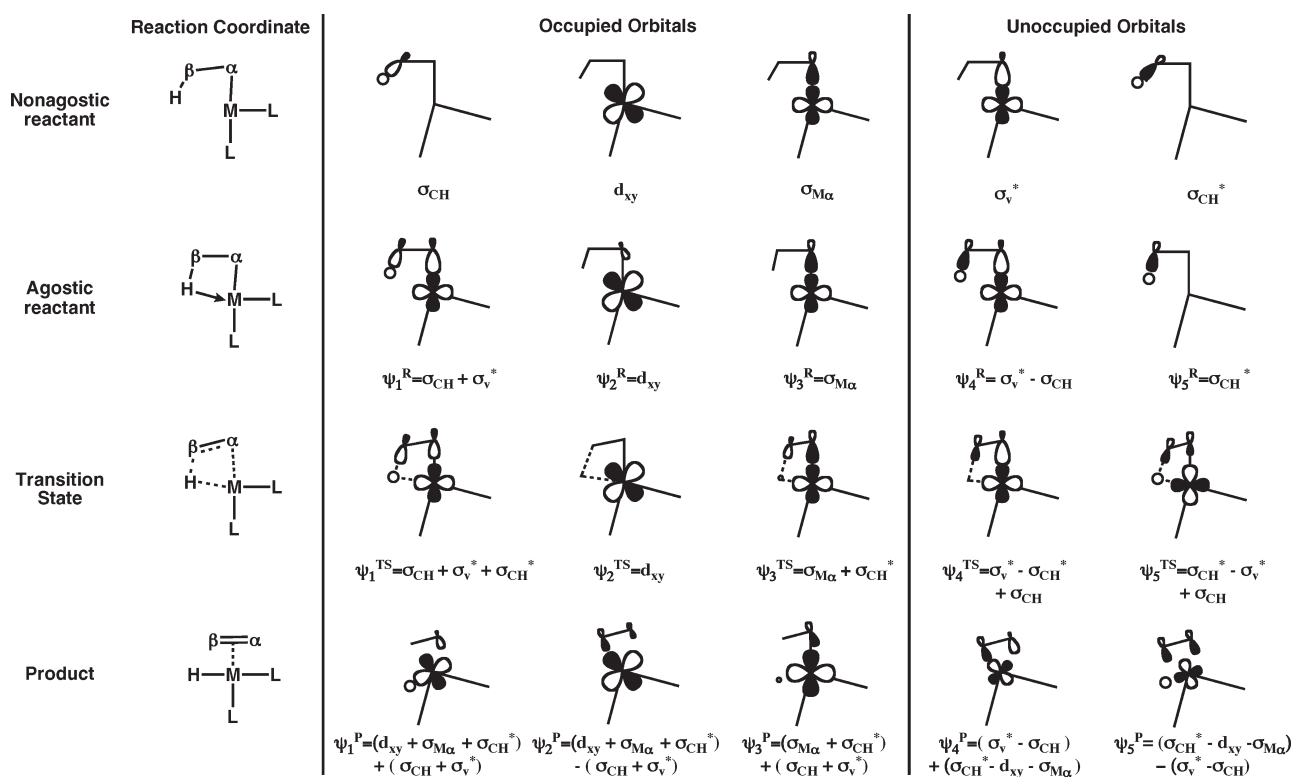


Figure 1. Reproduction of the orbitals presented by Koga, Obara, Kitaura, and Morokuma.<sup>28</sup>

When a heteroatom is introduced into the reactive portion of the molecule, its lone pairs are introduced into the active set of MOs. It is the role of these MOs that has not been investigated to date. This is not to say that  $\beta$ -heteroatom elimination has not been studied. An important distinction must be made here. What other groups call a  $\beta$ -heteroatom is actually the atom or functional group at the  $\gamma$ -position. In conventional  $\beta$ -hydride elimination, the  $\gamma$ -hydrogen is being shifted, not the  $\beta$ -carbon to which it is initially bonded. We are interested in studying BHE when the  $\beta$ -atom itself is a heteroatom. Several studies have examined the energetic differences between  $\gamma$ -heteroatom elimination and BHE on Pd(II) complexes with heteroatom functional groups attached to the  $\beta$ -position of an alkyl ligand.<sup>30–32</sup> They found that  $\gamma$ -elimination was kinetically favorable when the heteroatom group was a halide, but elimination of the  $\gamma$ -heteroatom group was favorable when it was an alcohol, imine, or alkoxide.<sup>33</sup> The position of the heteroatom is critical to its affect on BHE. BHE's from square-planar alkoxy and amido transition-metal complexes wherein the  $\alpha$ -atom is O or N are well-known, and they occur readily.<sup>34–36</sup> We aim to study the affect of a  $\beta$ -heteroatom on BHE processes, something that has not been examined to date.

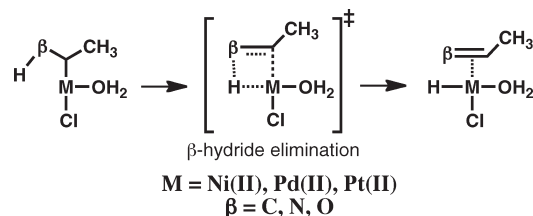
Other studies examined the role of the  $M \cdots H$  agostic interaction in Pd(CH<sub>2</sub>–CF<sub>2</sub>–H\*) complexes: calculations have been carried out on (2,2-difluoroethan-1-yl)Pd to measure the importance of electron donation from the CH  $\sigma$ -bond into the metal vacant site. These calculations revealed that the electron-withdrawing fluorine atoms were able to decrease the agostic Pd $\cdots$ H interaction and thereby raise the barrier to BHE.<sup>28</sup> In a similar manner the electronegativity of  $\beta$ -heteroatoms such as nitrogen and oxygen might also weaken the agostic interaction. Furthermore, it is possible that a lone pair on the  $\beta$ -atom might be able to stabilize the vacant coordination site on the metal more so than the  $\beta$ -H  $\sigma$ -bond.

Because our collective understanding of BHE failed to predict that BHE from  $\beta$ -heteroatoms is more energetically costly than BHE from alkyl groups, and because an MO treatment of BHE from groups other than alkyl groups is largely missing from the theoretical literature, we decided to study these systems in depth. In particular, we want to examine the importance of the  $\beta$ -lone-pair–metal interaction. Unfortunately, basic orbital symmetry illustrations only go so far to elucidate BHE processes. Quantum mechanics (QM) calculations are a valuable tool to extend these illustrations and further illuminate key points; therefore, we have used density functional theory to provide insight into BHE.

We present data showing that BHE from nitrogen and oxygen heteroatoms is rarely energetically feasible. We report the enthalpies of several BHE processes (in the gas phase and solvated in water), tracing molecular orbitals and atom-centered NBO charges along the [2 + 2] cyclization. From these data we present a straightforward summary of events to explain the nature of BHE processes.

## II. CALCULATION DETAILS

We used the B3LYP flavor of density functional theory (DFT) as implemented in the Jaguar 7.0 software package for all calculations. To optimize geometries and calculate vibrational frequencies, we used the popular B3LYP density functional with the Los Alamos electronic core potential (ECP) basis set on metals, LACVP\*\*, while using the 6-31G\*\* basis set on all other atoms. Subsequent single-point energies were calculated with the more robust ECP LACV3P\*\* and the 6-311G\*\*++ basis set. We also used the PBF Poisson–Boltzmann continuum solvation method to simulate an aqueous environment (with  $\epsilon = 80.37$  and the probe radius set to 1.40 Å). Solvation energy corrections were added to our normal enthalpies. This approach has been shown to be useful in investigations on organometallic mechanisms.<sup>6,37–41</sup>

Scheme 1. Investigated  $\beta$ -Hydride Elimination Processes<sup>a</sup>

<sup>a</sup> Note that in each case the  $\beta$ -atom is totally saturated with hydrogen atoms so that its valence is filled.

Stationary points and transition states were found using the energy gradient and density gradient converger algorithms available in Jaguar 7.0. We verified the authenticity of these states by ensuring that stationary points and transition states had zero and exactly one calculated imaginary vibrational frequency, respectively. Occasionally, we encountered small imaginary frequencies corresponding to localized rotational mode contamination originating from the water ligand's low rotational barrier. We calculated energy profiles along this rotational mode to ensure that the energy of this structure was not critically dependent on this mode. That is, we verified that the rotation of the water ligand never caused major changes in the structure of the molecule.

We investigated key characteristics of points along the reaction profiles for BHE from three  $d^8$  transition metals: Ni, Pd, and Pt. The structure template for this study is depicted in Scheme 1. We coordinated three different saturated ligands to each metal: 1-methylethan-1-yl, 1-aminoethan-1-yl, and 1-hydroxyethan-1-yl. Note that in the last two ligands a nitrogen or oxygen atom occupies the  $\beta$ -position, respectively. In addition to the aforementioned ligands, our metals are coordinated to ancillary aquo and chloride ligands. In this paper we provide information for the isomer in which the chloride ligand is trans to the saturated primary ligand. Water is coordinated to the metals in the cis position, and the remaining cis site is left vacant in the reactants. This structure template is depicted in Scheme 1. In the products the formerly vacant site is occupied by the transferred hydride. We provide data for the *cis*-chloro isomers in the Supporting Information. We effectively studied variants on the reaction shown in Scheme 1.

We also carried out intrinsic reaction coordinate (IRC) calculations to verify that the starting, transition state (TS), and ending structures were the lowest energy path along the BHE reaction coordinate. At points along these paths, we identified key orbitals involved in bond-making and bond-breaking processes. Finally, we calculated NBO atomic charges to provide a general picture of the electronic density around each atom involved in BHE processes.

### III. RESULTS AND DISCUSSION

**BHE Theory.** An empirical description of the BHE mechanism already exists. From the experimental data, one finds that BHE occurs most readily when a  $\beta$ -hydrogen is available on a transition-metal ligand and an empty coordination site on the metal exists. Experiments have shown that BHE is most facile when the system can adopt a planar conformation with respect to the  $M-\alpha-\beta-H$  dihedral angle.<sup>34,42,43</sup> Presumably, this is true because such a conformation maximizes orbital overlap between the nascent  $M-H$  and  $\pi$ -bonds.

Molecular orbitals from our Pd-based Wacker oxidation system and its 1-aminoethan-1-yl and 1-hydroxyethan-1-yl analogues are prime examples of facile and prohibitive BHE processes. From an inspection of each case's MOs, and from MOs presented in other reports, we developed a template to identify the most

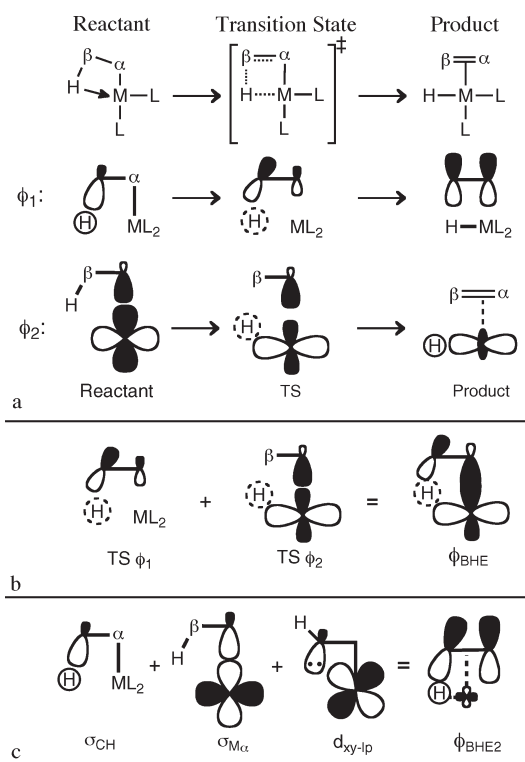


**Figure 2.** (a) Correlation diagram for the active orbitals in a conventional BHE. (b) Linear combination of transition state molecular orbitals encountered when the " $\beta$ " is an alkyl fragment. (c) Linear combination of transition state molecular orbitals encountered for BHE when the " $\beta$ " is a nitrogen or oxygen atom.

relevant symmetry allowed MOs for BHE.<sup>44</sup> These MOs are represented schematically in Figure 2.

$[2 + 2]$  pericyclic rearrangements involve two key bonding MOs: specifically, those corresponding to  $M-H$ ,  $M-\alpha$ ,  $\alpha-\beta$ , or  $\beta-H$  bonds, depending on what point of the reaction coordinate is being inspected. Figure 2a shows the progression of these canonical orbitals as the reaction proceeds. In the reactant, the two MOs of interest are the  $\beta-H$  and  $M-\alpha$   $\sigma$ -bonds. The two product MOs that complete the  $[2 + 2]$  rearrangement are the  $M-H$   $\sigma$ -bonding orbital and the  $\alpha-\beta$   $\pi$ -bonding orbital. A linear combination of the reactant and product MOs comprise the MOs in the TS of this rearrangement. In Figure 2b we show a linear combination of the two transition state orbitals, the sum of which we call  $\phi_{\text{BHE}}$ . In addition to these four canonical orbitals, we considered a linear combination of transition state MOs that would participate in BHE when a heteroatom is present: in Figure 2c, orbitals corresponding to oxygen and nitrogen lone pairs directed toward the metal compete for the vacant site with the  $\beta$ -hydride, and we call this combination  $\phi_{\text{BHE}2}$ .

With this template of reactive orbitals, we describe BHE in qualitative terms. Calculated DFT data for specific examples of BHE will now be interpreted in terms of this MO model.

**BHE from Pd(II) Centers.** We begin with the reactant complexes that serve as starting points for  $\beta$ -hydride elimination (Figure 3). Already, we find some distinguishable characteristics. First, **1a** has a well-defined agostic  $C-H$  bond ( $r_{\text{Pd}\cdots\text{H}} = 1.78 \text{ \AA}$ ) into the Pd vacant site.

In contrast, the agostic bond between the  $\beta$ -H and Pd is not present in either **2a** or **3a** ground state complexes ( $r_{\text{Pd}\cdots\text{H}} = 2.7$

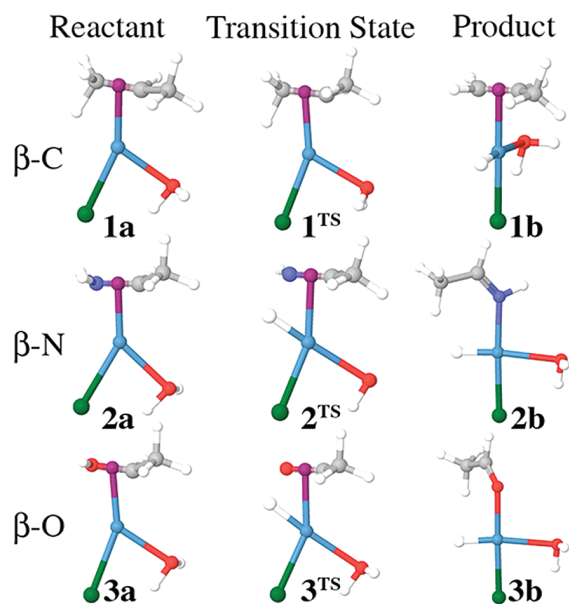


Figure 3. Calculated reactant, transition state, and product structures for the Pd-based compounds.

Table 1. Enthalpies for the  $\beta$ -Hydride Elimination in Scheme 1<sup>a</sup>

species	enthalpy (kcal/mol)			
	reactant	planar reactant	TS	product
1	0		1 (3.8)	-5.7 (0.9)
2	0	15.5	26.6 (34.1)	-0.5 (6.9)
3	0	8.4	21.6 (28.2)	-2.6 (-0.7)
4	0	31.1	26.5 (33.0)	2.2 (-9.0)
5	0	16.6	37.4 (38.6)	-18.7 (-10.8)
6	0		5.8 (7.9)	3.5 (6.1)
7	0	25.5	35.3 (40.0)	5.3 (8.4)
8	0	6	28.3 (35.8)	-3 (0.3)

<sup>a</sup> The values in parentheses are solvation-corrected enthalpies. Where planar reactant energies are provided, the  $\alpha$ - $\beta$  bond is rotated so that the  $\beta$ -H is forced into the  $M$ - $\alpha$ - $\beta$  plane.

and 2.71 Å, respectively). Rather, there is a well-defined dative bond from the lone pair of the  $\beta$ -heteroatom to the metal. Since the lone pair is coordinated to the vacant site, the hydride is rotated out of the plane of the Pd- $\alpha$ - $\beta$  atoms.

To estimate the relative strength of these lone-pair interactions, we calculated the energies of the 2a and 3a systems where the Pd- $\alpha$ - $\beta$ -H dihedral angles were fixed to be 0°. The  $\Delta H$  values for these structures are given in Table 1, as well as the relative enthalpies of the transition states and products of BHE. For 2a the planar structure is 15.5 kcal/mol higher than the fully relaxed structure with the lone-pair dative bond. For 3a, the planar structure is 8.4 kcal/mol higher. It is interesting that the 3a planar reactant is lower in energy than the 2a planar reactant. This is probably due to additional back-bonding to the Pd from the second oxygen lone pair. The preference for lone pair interaction versus the agostic H-bond means that each structure will have to undergo an  $\alpha$ - $\beta$  bond rotation for BHE to occur.

Each product structure involves a Pd coordinated to an unsaturated  $\alpha$ - $\beta$  fragment. Given that the barrier to BHE from 1a to 1b is

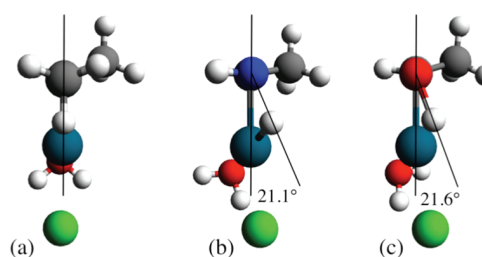


Figure 4. Transition state geometries for Pd complexes: (a) 1<sup>TS</sup>; (b) 2<sup>TS</sup>; (c) 3<sup>TS</sup>. The angles given are the dihedral angles Pd- $\alpha$ - $\beta$ -H\*.

so low, we would expect to observe this experimentally. Indeed, there are multiple examples in the literature of these processes occurring.<sup>5,10</sup> The  $\Delta H$  values for 2b and 3b are also favorable, but in both cases the BHE barrier is high. The most stable products for BHE from the 2a and 3a analogues are the  $\eta^1$ -coordinated species (iminoethyl- $\kappa$ N)Pd(H<sub>2</sub>O)Cl (2b) and (acetaldehyde- $\kappa$ O)Pd(H<sub>2</sub>O)Cl (3b), rather than  $\eta^2$ -coordinated compounds.

Our TS calculations are consistent with our previous Wacker oxidation results on alkyl systems. BHE from an alkane  $\beta$ -fragment has a very low barrier: 1 kcal/mol for 1<sup>TS</sup>. This is consistent with the results of previous studies on similar systems.<sup>23,33</sup> These barriers contrast dramatically with BHE barriers from amine and alcohol  $\beta$ -fragments. The BHE TS enthalpy for 2<sup>TS</sup> is 26.6 kcal/mol. For 3<sup>TS</sup> the barrier is 21.6 kcal/mol. Including the effects of water solvation only slightly changed the barriers to 3.8 kcal/mol for 1<sup>TS</sup>, 34.1 kcal/mol for 2<sup>TS</sup>, and 28.2 kcal/mol for 3<sup>TS</sup>, showing that these barriers will not be substantially affected by solvent effects. This is expected, because these molecules do not have large changes in charge density distribution or net charge throughout the BHE reaction coordinate. The transition state geometries for 1<sup>TS</sup>, 2<sup>TS</sup>, and 3<sup>TS</sup> are given in Figure 4.

TS geometries linking the reactant and product structures reveal a distinct peculiarity in BHE mechanisms. For 1<sup>TS</sup>, the Pd,  $\alpha$ -C,  $\beta$ -C, and H atoms all lie nearly syn-coplanar ( $\theta = 1.3^\circ$ ), in accordance with the conventional BHE geometric requirements outlined above. For 2<sup>TS</sup>, however, the Pd,  $\alpha$ -C,  $\beta$ -N, and H atoms do not lie in a plane. Rather, they orient themselves with a dihedral angle of 21.1°. A similar dihedral angle is present in 3<sup>TS</sup>, where the Pd, C, O, and H atoms form a dihedral angle of 21.6°. On the basis of the large dihedral angles found in the reactant and TS structures of 2<sup>TS</sup> and 3<sup>TS</sup>, there must be lone-pair interactions between the  $\beta$ -N and  $\beta$ -O heteroatoms into the metal's vacant coordination site in the transition structure.

The MOs for these processes reveal the nature of both the energetic barriers and geometries along the BHE reaction coordinate. When " $\beta$ " is CH<sub>2</sub>,  $\phi_{\text{BHE}}$  values are nearly identical in the starting and transition state structures. Energetically,  $\phi_{\text{BHE}}$  in 1<sup>TS</sup> is only 1.0 kcal/mol greater than that of its corresponding reactant orbital, and this energy difference in striking proximity to the actual calculated barrier of 1.3 kcal/mol indicates that very little electronic rearrangement needs to occur for BHE to take place. The orientation of the orbital allows a planar geometry, and good overlap between the hydride and Pd's empty coordination site is maintained.

When the  $\beta$ -atom is N, as in 2, the most stable of the canonical orbitals,  $\phi_{\text{BHE}2}$ , is a linear combination of  $\sigma_{M-\alpha}$ ,  $\sigma_{CH}$ , and  $d_{xy-lp}$  (see Figure 2c). No orbital in this case directly resembles the  $\phi_{\text{BHE}}$  orbital found in the alkane case. However, if the geometry of the Pd- $\alpha$ - $\beta$ -H dihedral angle in the reactant is forced to be

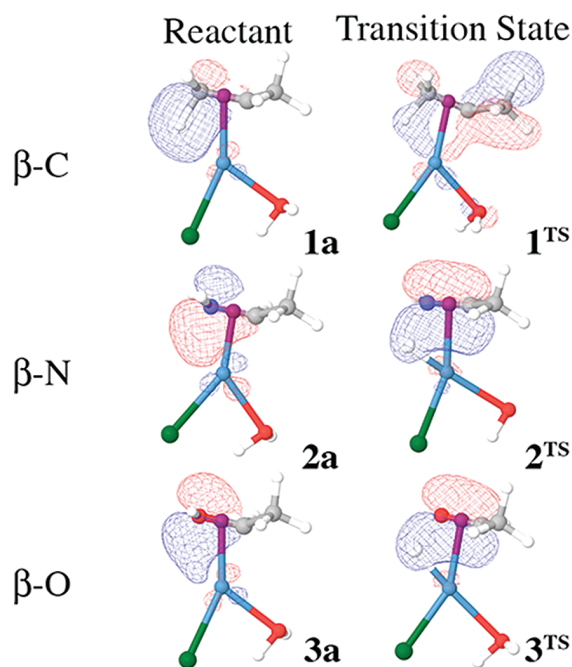


**Figure 5.** Selected molecular orbitals of the Pd reactants and transition states. The agostic interaction is plainly visible in **1a** and **1<sup>TS</sup>**, whereas the lone pairs interact with the metal center in **2a** and **2b**. Compare the molecular orbitals in **2<sup>TS</sup>** and **3<sup>TS</sup>** with the orbital in Figure 2c.

**Table 2.** Enthalpies for Ground State Structures Deformed To Have the Same Pd– $\alpha$ – $\beta$ –H Dihedral Angle as Each Transition-State Structure

species	M– $\alpha$ – $\beta$ –H angle (deg)	enthalpy (kcal/mol)
2	21.1	26.5
3	21.6	7.9
4	28.6	36.0
5	42.4	14.9
7	16	30.3
8	36	13.0

planar as in an ideal BHE, the  $\phi_{\text{BHE}}$  orbital emerges, though the artificially planar species is energetically destabilized by 15.5 kcal/mol. In this artificial geometry (artificial in the sense that it does not lie along the intrinsic reaction coordinate), the overlap between the hydride and metal d orbital is visibly weaker than that for the alkane ( $r_{\text{Pd}\cdots\text{H}} = 2.21 \text{ \AA}$ )  $\phi_{\text{BHE}}$  orbital. In **2<sup>TS</sup>**, we find no orbital corresponding to  $\phi_{\text{BHE}}$ . Instead, we find an orbital with strong  $\pi$ -character orthogonal to the plane of the hydrogen transfer (see Figure 5). This localized orbital resembles  $\phi_{\text{BHE}2}$  in Figure 2c, wherein most of the density belongs to the forming  $\pi$ -bond. These results imply that the energetic barrier to BHE from nitrogen is due to the cost of breaking nitrogen's lone pair stabilization of the empty metal coordination site. We verified this by taking **2a** and **3a** and rotating the  $\alpha$ – $\beta$  bond until the Pd– $\alpha$ – $\beta$ –H angle matches this angle in **2<sup>TS</sup>** and **3<sup>TS</sup>**. In Table 2 we give the results of these calculations. For the Pd complexes the cost of rotating the  $\beta$ -H into the TS geometry is a significant fraction of the overall barrier to BHE in each case. Additionally, the importance of the lone pair interaction is reflected in a

“twisting” motion of the imaginary mode in the TS. This character arises from rotating the hydride into the Pd– $\alpha$ – $\beta$  plane.

The alcohol  $\beta$ -group behaves much like the amine  $\beta$ -group. In fact, the lone pair of oxygen forms a stronger bond to the metal center, as is evident by the lack of any orbital containing significant Pd– $\alpha$  bonding character in **3a**. Again, we artificially created a reactant compound where H is aligned with the Pd– $\alpha$ – $\beta$  plane to find the BHE orbital. This orbital has even weaker Pd–H overlap than that in the case of nitrogen ( $r_{\text{Pd}\cdots\text{H}} = 2.37 \text{ \AA}$ ), and it is destabilized by 51.4 kcal/mol relative to the  $\phi_{\text{BHE}2}$  orbital. This artificially planar structure for **3a** is 8.4 kcal/mol above the true ground state. The energy to rotate the hydride into the TS geometry on the ground state potential energy surface is a significant fraction of the TS barrier at 7.9 kcal/mol. These results indicate to us that breaking the lone-pair–metal interaction is a major contributor to the overall  $\Delta H^\ddagger$  value of BHE. The imaginary vibrational mode of **3<sup>TS</sup>** also has an O–H bond stretching component and a component that represents rotation about the  $\alpha$ – $\beta$  bond, and this is dissimilar to the linear bond stretching found in ideal BHE imaginary modes.

An analysis of NBO charges along this reaction coordinate provides more information about the nature of the hydride transfer. BHE is traditionally thought of as a [2,2] pericyclic rearrangement. By virtue of this category of rearrangement, charge should be relatively conserved and should remain synchronous throughout the rearrangement. That is, there should be minimal rearrangement of intranuclear charge. Table 3 contains information about the atomic NBO charges for the reactant, TS, and product complexes for the two different isomers of each variant. For **1**, the NBO charge on the hydride remains within 0.15e between **1a**, **1<sup>TS</sup>**, and **1b**. Surprisingly, the “hydride” in **1a** is actually partially positive. Even in **1<sup>TS</sup>**, the “hydride” retains its positive charge at 0.2e. In **1b**, the “hydride” is nearly neutral, which indicates that the charge from the rest of the complex has been rearranged to repopulate electron density on the hydride. From the charge on the  $\beta$ -C in **1b**, it is evident that this atom donated negative charge to the hydride and Pd. The charge on Pd decreases by 0.1e, and the charge on  $\beta$ -C increases by 0.15e. In the reactant and TS of **2** and **3**, the  $\beta$ -hydride is highly electropositive, as is expected for an atom bonded to electronegative atoms such as nitrogen and oxygen. In **2a** and **3a** the charge on H is 0.4e and 0.49e, respectively. In the products, **2b** and **3b**, the hydride's charge is nearly neutral. Coincidentally, this agrees quite well with a simple model of reactivity based on the relative electronegativities of carbon, nitrogen, and oxygen. In **2a,b** both heteroatoms have drawn electron density away from the hydrogen, yielding an electropositive H. Consequently, the hydrogen will then have less electron density to provide an agostic bond to the metal center. For **2** and **3**, there is an energetic cost to transfer the hydride to the metal, since the H absorbs negative charge during bonding to palladium. The degree of charge on the H in the **2<sup>TS</sup>** and **3<sup>TS</sup>** transition states suggests that these reactions are more akin to proton transfers than hydride transfers. Just as in **1b**, in **2b** and **3b** the Pd center experiences a charge decrease and  $\beta$ -N and  $\beta$ -O donate their negative charge to the hydride with the remainder being drawn from the rest of the complex. The timing of the charge redistribution is interesting: for **1**, we see that the  $\beta$ -H maintains its charge through the transition state. Only in the product does charge redistribution occur. In **2** and **3**, the charge redistribution is gradual and we see that the  $\beta$ -H has lost positive charge in the TS. This indicates that charge reorganization is a prerequisite for BHE to occur in  $\beta$ -heteroatom species and that

Table 3. NBO Charges (in Terms of  $e$ ) for Selected Atoms along the Reaction Path<sup>a</sup>

species	M	X	reactant			transition state			product		
			M	H	X	M	H	X	M	H	X
1	Pd	C	0.50	0.20	-0.58	0.49	0.20	-0.58	0.40	0.05	-0.42
2	Pd	N	0.47	0.40	-0.74	0.36	0.24	-0.65	0.35	0.01	-0.62
3	Pd	O	0.57	0.49	-0.66	0.42	0.30	-0.55	0.47	0.04	-0.57
4	Pt	N	0.43	0.40	-0.72	0.33	0.27	-0.66	0.44	0.06	-0.67
5	Pt	O	0.52	0.50	-0.65	0.33	0.33	-0.61	0.51	0.04	-0.58
6	Ni	C	0.66	0.20	-0.60	0.53	0.02	-0.42	0.55	-0.05	-0.44
7	Ni	N	0.63	0.40	-0.76	0.51	0.17	-0.66	0.55	-0.13	-0.64
8	Ni	O	0.72	0.49	-0.67	0.57	0.27	-0.57	0.62	-0.15	-0.56

<sup>a</sup> X is the  $\beta$ -atom, H is the transferring "hydride", and M is the metal. Note that for the systems in which X = N, O the transferring hydrogen loses a larger amount of positive charge along the reaction coordinate. This is indicative of proton transfer rather than hydride transfer behavior.

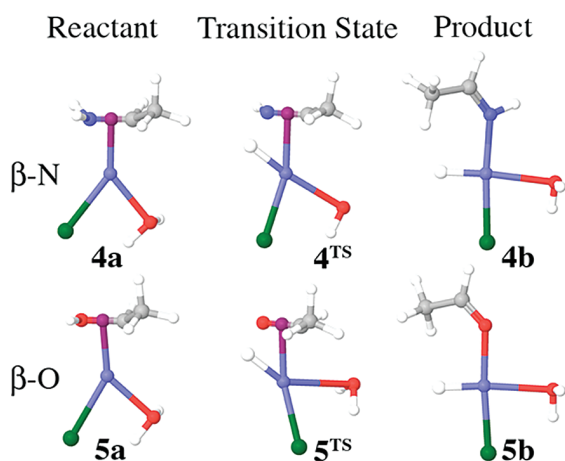


Figure 6. Calculated reactant, transition state, and product structures for the Pt-based compounds.

the preorganization occurs on the upslope of the reaction coordinate. This charge asynchronicity is a significant contributing factor to the high barrier to BHE for ligands bearing  $\beta$ -heteroatoms.

**Pt(II) Results.** Our investigation continued with a study of BHE to platinum(II), another  $d^8$  metal (Figure 6). The results are consistent with those of palladium.

We did not find a "reactant" state for (1-methylethan-1-yl)-Pt(H<sub>2</sub>O)Cl. This species minimized to a product structure analogous to **1b**, which indicates that there is no barrier to BHE.

The primary differences between BHE in platinum and palladium are in the barriers to reaction. The barriers to reaction are generally smaller for platinum, while the reaction is exothermic. The barrier to BHE for **4a** is 26.5 kcal/mol. The barriers are higher for the alcohol analogue: BHE from **5a** is 37.4 kcal/mol uphill with a product, **5b**, energy of -18.7 kcal/mol. The barrier heights for the alcohol and amine analogues indicate that, like the palladium example, lone pair interactions stabilize the reactants.

The importance of the lone-pair-metal coordination is verified by the geometry of the transition states in **4<sup>TS</sup>** and **5<sup>TS</sup>**. In **5<sup>TS</sup>**, the Pt- $\alpha$ - $\beta$ -H dihedral angle is 42.4° in the transition state. In **4<sup>TS</sup>**, the Pt- $\alpha$ - $\beta$ -H dihedral angle is 28.6°. As before, this suggests that there is a strong stabilizing interaction between the lone pairs of the heteroatoms and the vacant coordination site on the metal. To test the strength of this, we again fixed the dihedral angle is at 0° in the reactants. The cost of rotating the lone pair

out of the coordination site for **4a** and **5a** is 33.9 and 14.3 kcal/mol, respectively.

The significance of the lone-pair-metal interaction is also reflected in the MOs. In **4<sup>TS</sup>**, we find an MO that resembles  $\phi_{\text{BHE2}}$ , as described in Figure 2c. There is strong overlap between the lone pair and the metal's vacant coordination site. In the artificially planar reactant structure, this overlap is lost, and the reactant is destabilized by 31.1 kcal/mol. A  $\phi_{\text{BHE}}$  orbital is created, although the overlap between the hydride and vacant site is weak. The energy of this orbital is 29.4 kcal/mol higher than that of the  $d_{xy-lp}$  orbital in the fully relaxed reactant. This increase in energy reflects the importance of the lone-pair stabilization. Just as we did for our palladium complexes, we measured the energy of each Pt reactant when the  $\alpha$ - $\beta$  bond is rotated so that the Pt- $\alpha$ - $\beta$ -H dihedral angle matches the TS angle. For **4a** this cost 36 kcal/mol. The high cost of performing this rotation demonstrates the strength of the lone-pair to metal coordination energy.

The orbitals for **5a** and **5<sup>TS</sup>** are similar to those of **4a** and **4<sup>TS</sup>**. An important difference is the strength of the oxygen lone-pair-metal interaction. In the fully relaxed reactant, the lone pair is strongly coordinated to platinum. This is verified by the high cost of rotating the hydrogen into the Pt- $\alpha$ - $\beta$  plane: fixing the Pt- $\alpha$ - $\beta$ -H dihedral angle at 0° leads to the formation of a  $\phi_{\text{BHE}}$  orbital that is 51.4 kcal/mol higher in energy than the  $d_{xy-lp}$  orbital. This may seem to conflict with the fact that the planar reactant is only 16.6 kcal/mol above **5a**, but it does not. Because oxygen has two lone pairs, there is partial lone-pair stabilization even when the hydrogen is fixed in the planar reactant structure. This fact also partially explains why the barriers to BHE from oxygen are lower than that of nitrogen. The TS  $\phi_{\text{BHE2}}$  orbital is significantly different than the ideal BHE case that is found in **1<sup>TS</sup>**. Like **2<sup>TS</sup>**, **3<sup>TS</sup>**, and **4<sup>TS</sup>**, in **5<sup>TS</sup>** there is significant twisting character in the imaginary mode of the transition state so we can conclude that rotation of the terminal alcohol is largely responsible for the barrier to BHE.

In all cases, the transition states are late and productlike. In **4<sup>TS</sup>**  $r_{\text{Pt}\cdots\text{H}}$  is 1.65 versus 1.52 Å in **5b**, while  $r_{\text{C-N}}$  is 1.38 versus 1.35 Å in the transition state and products, respectively. In **5<sup>TS</sup>**  $r_{\text{Pt}\cdots\text{H}}$  is 1.67 Å versus 1.52 Å in **5b**, while  $r_{\text{C-O}}$  is 1.36 versus 1.28 Å in the transition states and products, respectively.

In the Pt complexes we observe significant charge redistribution when the  $\beta$ -atom is N or O. The difference in charge on the  $\beta$ -H between **4b** and **4a** is -0.34e, and that between **5b** and **5a** is

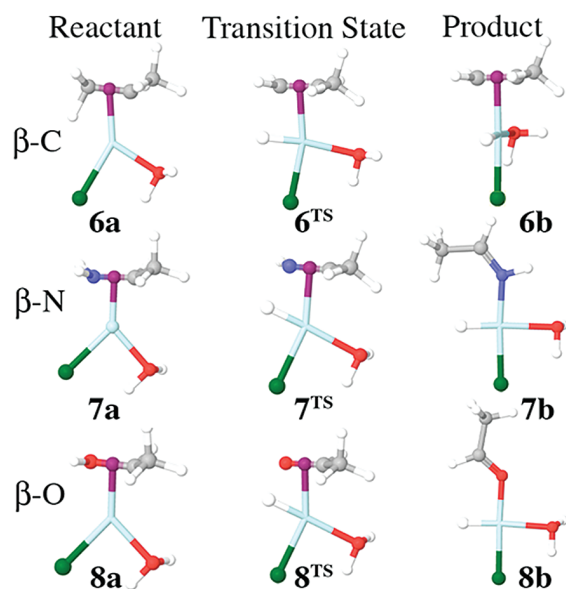


Figure 7. The calculated reactant, transition state and product structures for the Ni based compounds.

−0.46e. For both heteroatoms,  $\beta$ -hydride elimination of an electropositive hydrogen atom occurs, with charge being drawn away from the  $\beta$ -atoms. Interestingly, Pt retains its charge throughout the course of the BHE. Contrast this with Pd, which loses positive charge. This is likely due to the fact that platinum has a lower electron affinity than Ni or Pd. Between **4a** and **4b** the  $\beta$ -N only increases by 0.05e, despite the fact that the hydride decreases its charge by 0.36e. Similarly, between **5a** and **5b**, the  $\beta$ -O only increases by 0.07e while the hydride decreases by 0.46e. This cannot be related to the geometry of the products, since **2b** and **4b** and **3b** and **5b** all have similar product geometries.

**Nickel(II) Results.** Our study concludes with an analysis of BHE from Ni(II). Like platinum, the results presented here agree with the results presented in the palladium section of this report (Figure 7).

As expected, the barriers to BHE from Ni are generally higher than that of Pd and Pt. The activation energy for BHE is 5.8 kcal/mol for **6<sup>TS</sup>**. Like **1a**, **6a** has an agostic Ni...H interaction ( $r_{\text{Ni}\cdots\text{H}} = 1.67 \text{ \AA}$ ). This agostic interaction helps to decrease the barrier height for BHE by allowing partial Ni...H bond formation prior to BHE. For **7<sup>TS</sup>** the barrier is at a prohibitively high 35.3 kcal/mol. As for the Pd cases, the **8<sup>TS</sup>** activation energy is higher than that for the alkyl analogue but lower than that for the  $\beta$ -nitrogen example: **8<sup>TS</sup>** is 28.3 kcal/mol above the ground state.

The Ni–C–N–H dihedral angle for **7<sup>TS</sup>** is  $16^\circ$ , and for **8<sup>TS</sup>** the analogous dihedral angle is  $36^\circ$ . As for the Pd and Pt cases, this implies the importance of a stabilizing lone pair coordination into the metal's empty coordination site.

The importance of this interaction is reflected in the MOs of the reactants and transition states. The saturated alkyl reactant, **6a** contains a clear  $\Psi_1^{\text{R}}$  orbital with the unique  $\beta$ -agostic interaction that makes BHE facile. In the TS, we find a  $\phi_{\text{BHE}}$  orbital with strong Ni...H bonding character.

When we fix the Ni– $\alpha$ – $\beta$ –H dihedral in **7a** angle to  $0^\circ$ , a  $\phi_{\text{BHE}}$  MO is produced and the overall energy of the structure is 25.5 kcal/mol higher in energy than the fully relaxed reactant.

The importance of the lone pair stabilization is also demonstrated in **8a** as well. In this case, it costs 6 kcal/mol to rotate the

lone pair out of the vacant site. Again, the  $d_{xy-1p}$  orbital in the reactant is the most stable of the canonical orbitals. When the Ni– $\alpha$ – $\beta$ –H dihedral angle is fixed at  $0^\circ$ , the  $\phi_{\text{BHE}}$  orbital is 70.8 kcal/mol greater in energy than the  $d_{xy-1p}$  orbital. Again, we stress that the only way to prepare a BHE orbital is by twisting the hydrogen into the proximity of the empty coordination site, and this twisting motion is present in the imaginary mode of the transition state.

The product structures are all similar. Furthermore, **6<sup>TS</sup>**, **7<sup>TS</sup>**, and **8<sup>TS</sup>** all have productlike transition states, as indicated by the similarity between the Ni–H and  $\alpha$ – $\beta$  bond lengths (see the Supporting Information for structures).

We found that the Ni complexes behaved like the Pd complexes with regard to charge redistribution when we examined the NBO charges for the Ni BHE reaction coordinate. For the NBO charge population details, see Table 3. In **6a**, **6<sup>TS</sup>**, and **6b** we observe that the hydride retains its 0.2e charge through the transition state but it then decreases to −0.05e in the product **6b**. In the Ni complexes the product H is truly a hydride. Between **6a** and **6b**, Ni decreases by 0.11e, while  $\beta$ -C increases by 0.16e. For BHE starting from **7a** and **8a**, we find that the hydrogen loses significantly more positive charge while the heteroatoms accumulate positive charge. Over the course of BHE,  $\beta$ -N and  $\beta$ -O gain 0.12e in **7b** and **8b**, respectively. As for BHE from **6a**, Ni in **7** and **8** loses 0.8e and 0.1e, respectively. As stated earlier, the necessary redistribution of charge to the heteroatoms is unfavorable and energetically costly. This fact, in conjunction with the geometric changes that are also necessary, leads to the high barriers to BHE from heteroatom functional groups.

The barrier heights for both the  $\beta$ -nitrogen and  $\beta$ -oxygen analogues indicate that traditional BHE is not energetically feasible for heteroatom functional groups of Ni(II) square planar complexes.

Comparing the results of Pd, Pt, and Ni shows that all three of these group 10 metals behave similarly. While the barrier heights decrease as one moves down this group, the trends among their BHE reactivity and chemical character are consistent.

#### IV. CONCLUSIONS

For all three transition metals, the calculated energies indicate that the barrier to BHE from  $\beta$ -heteroatoms is significantly higher than the barrier when the  $\beta$ -atom is carbon. These energies correspond to true BHE's, and they represent the energetic cost of transferring a hydride in the manner traditionally depicted by organometallic chemists. This is not to say that transferring a hydride from a heteroatom functional group is impossible. Instead, we wish to suggest that the chloride-mediated reductive elimination mechanism presented in our previous work is a more likely candidate.<sup>23</sup> Another possible route might involve deprotonation of a precursor amine- or alcohol-bearing ligand to form an anionic imino-, aldehyde-, or keto–metal complex such as  $[(\text{NH}_2\text{CR}_2)\text{M}] + \text{B}^- \rightarrow \text{BH} + [(\text{NH}=\text{CR}_2)\text{M}]^-$  or  $[(\text{HOCR}_2)\text{M}] + \text{B}^- \rightarrow \text{BH} + [(\text{O}=\text{CR}_2)\text{M}]^-$ . The work presented here indicates that the scope of BHE's should be limited to  $\beta$ -atoms that do not contain lone pairs.

We found that the cost of breaking the lone pair to metal interaction for cases where the  $\beta$ -atom contains a lone pair is largely responsible for the increased activation energy for BHE from these compounds. Furthermore, in these cases the “hydride” is more electropositive in the reactant than in cases where the  $\beta$ -atom is carbon. After BHE, the transferred H is nearly

charge neutral. In all cases the  $\beta$ -atom donates charge to the transferring H atom. Ni and Pd lose positive charge density after BHE while Pt retains its charge throughout the course of the BHE. Electronegative  $\beta$ -atoms decrease the strength of any agostic interaction that might exist in the TS, and the presence of lone pairs in these atoms assures that a lone-pair–metal dative interaction will exist in the reactant. The results presented herein suggest that the organometallic mechanism we commonly refer to as  $\beta$ -hydride elimination ought to be called  $\beta$ -proton elimination.

We also note that we attempted to calculate the barriers to BHE from the second-period main-group elements Si, P, and S. In all cases there was no barrier to BHE, owing to the fact that the BHE reactant is not a stationary point for these molecules. In each case the geometry optimization of the reactant converged to the BHE product.

Given the molecular orbital picture for BHE, we can rule out the possibility of facile BHE from  $\beta$ -heteroatoms, and this effectively sets the scope of reagents that are susceptible to BHE. Of course, the lack of experimental evidence for BHE from  $\beta$ -heteroatoms is indirect evidence of this fact, but without a detailed theoretical treatment, there was no way to be sure of this.

## ■ ASSOCIATED CONTENT

**S Supporting Information.** A scheme giving xyz structures for the complexes in Table 1 and tables giving enthalpies for the *trans*-aquo isomers and bond lengths and M– $\alpha$ – $\beta$ –H dihedral angles for complexes **1**–**8** and the *trans*-aquo isomers. This material is available free of charge via the Internet at <http://pubs.acs.org>.

## ■ AUTHOR INFORMATION

### Corresponding Author

\*E-mail: [ptheofan@caltech.edu](mailto:ptheofan@caltech.edu).

## ■ ACKNOWLEDGMENT

We thank John Keith for piquing our interest in this topic and for his helpful recommendations. We gratefully acknowledge financial support of this research by the Chevron Texaco Energy Research and Technology Co.

## ■ REFERENCES

- (1) Mueller, J. A.; Goller, C. P.; Sigman, M. S. *J. Am. Chem. Soc.* **2004**, *126*, 9724.
- (2) Vela, J.; Vaddadi, S.; Cundari, T. R.; Smith, J. M.; Gregory, E. A.; Lachicotte, R. J.; Flaschenriem, C. J.; Holland, P. L. *Organometallics* **2004**, *23*, 5226.
- (3) Lautens, M.; Fang, Y.-Q. *Org. Lett.* **2003**, *5*, 3679.
- (4) Shultz, L. H.; Brookhart, M. *Organometallics* **2001**, *20*, 3975.
- (5) Campbell, A. N.; Gagne, M. R. *Organometallics* **2007**, *26*, 2788.
- (6) Nielsen, R. J. G.; William, A. *J. Am. Chem. Soc.* **2006**, *128*, 9651.
- (7) Schultz, M. J.; Adler, R. S.; Zierkiewicz, W.; Privalov, T.; Sigman, M. S. *J. Am. Chem. Soc.* **2005**, *127*, 8499.
- (8) Huang, X.; Zhu, J.; Lin, Z. *Organometallics* **2004**, *23*, 4154.
- (9) Gellman, A. J. *Acc. Chem. Res.* **1999**, *33*, 19.
- (10) Bryndza, H. E. T.; Wilson *Chem. Rev.* **1988**, *88*, 1163.
- (11) Pearson, R. G. *Chem. Rev.* **1985**, *85*, 41.
- (12) Crabtree, R. H. *The Organometallic Chemistry of the Transition Metals*, 3rd ed.; Wiley: New York, 2001.
- (13) Elschenbroich, C. *Organometallics*, 3rd ed.; Wiley-VCH: Weinheim, Germany, 2006.

(14) Huheey, J. E. K.; Ellen, A.; Keiter, R. L. *Inorganic Chemistry: Principles of Structure and Reactivity*, 4th ed.; HarperCollins College: New York, 1993.

(15) Collman, J. P. H.; Norton, J. R.; Finke, R. G. *Principles and Applications of Organometallic Chemistry*, 1st ed.; University Science Books: Mill Valley, CA, 1987.

(16) Cross, R. J. *Transition Metal-Carbon Bond Cleavage through Beta-Hydrogen Elimination*; Wiley: New York, 1985; Vol. 2.

(17) Heck, R. F. *Hercules Chem.* **1968**, *57*, 12.

(18) Backvall, J. E.; Akermark, B.; Ljunggren, S. O. *J. Am. Chem. Soc.* **1979**, *101*, 2411.

(19) Akermark, B.; Soederberg, B. C.; Hall, S. S. *Organometallics* **1987**, *6*, 2608.

(20) Grushin, V. V. *Chem. Rev.* **1996**, *96*, 2011.

(21) Parshall, G. W.; Ittel, S. D. *Homogeneous Catalysis: The Applications and Chemistry of Catalysis by Soluble Transition Metal Complexes*; Wiley-Interscience: New York, 1992.

(22) Spessard, G. O.; Miessler, G. L. *Organometallic Chemistry*; Prentice Hall: Upper Saddle River, NJ, 2000.

(23) Keith, J. A.; Oxgaard, J.; Goddard, W. A. *J. Am. Chem. Soc.* **2006**, *128*, 3132.

(24) Hosseini, H. E.; Beyramabadi, S. A.; Morsali, A.; Housaindokht, M. R. *J. Mol. Struct. (THEOCHEM)* **2010**, *941*, 138.

(25) DeKock, R. L.; Hristov, I. H.; Anderson, G. D. W.; Gottker-Schnetmann, I.; Mecking, S.; Ziegler, T. *Organometallics* **2005**, *24*, 2679.

(26) Casey, C. P.; Neumann, S. M. *J. Am. Chem. Soc.* **1976**, *98*, 5395.

(27) Hieber, W.; Scharfenberg, C. *Chem. Ber* **1940**, *73*, 1012.

(28) Koga, N.; Obara, S.; Kitaura, K.; Morokuma, K. *J. Am. Chem. Soc.* **1985**, *107*, 7109.

(29) Thorn, D. L.; Hoffmann, R. *J. Am. Chem. Soc.* **1978**, *100*, 2079.

(30) Lin, J. L.; Bent, B. E. *Chem. Phys. Lett.* **1992**, *194*, 208.

(31) Wu, B.; Zhang, J.; Yun, L.; Fu, X. *Dalton Trans.* **2011**, *40*, 2213.

(32) Ryan, C.; de K. Lewis, A.; Caddick, S.; Kaltsoyannis, N. *Theor. Chim. Acta* **2011**, *129*, 303.

(33) Zhao, H.; Ariaferd, A.; Lin, Z. *Organometallics* **2006**, *25*, 812.

(34) Zhao, J.; Hesslink, H.; Hartwig, J. F. *J. Am. Chem. Soc.* **2001**, *123*, 7220.

(35) Bryndza, H. E.; Calabrese, J. C.; Marsi, M.; Roe, D. C.; Tam, W.; Bercau, J. E. *J. Am. Chem. Soc.* **1986**, *108*, 4805.

(36) Sieffert, N.; BuAahl, M. *J. Am. Chem. Soc.* **2010**, *132*, 8056.

(37) Keith, J. A.; Nielsen, R. J.; Oxgaard, J.; Goddard, W. A. *J. Am. Chem. Soc.* **2007**, *129*, 12342.

(38) Keith, J. A.; Behenna, D. C.; Mohr, J. T.; Ma, S.; Marinescu, S. C.; Oxgaard, J.; Stoltz, B. M.; Goddard, W. A. *J. Am. Chem. Soc.* **2007**, *129*, 11876.

(39) Oxgaard, J.; Goddard, W. A. *J. Am. Chem. Soc.* **2004**, *126*, 442.

(40) Su, J. T.; Sarpong, R.; Stoltz, B. M.; Goddard, W. A. *J. Am. Chem. Soc.* **2004**, *126*, 24.

(41) Keith, J. M.; Muller, R. P.; Kemp, R. A.; Goldberg, K. I.; Goddard, W. A.; Oxgaard, J. *Inorg. Chem.* **2006**, *45*, 9631.

(42) McDermott, J. X.; White, J. F.; Whitesides, G. M. *J. Am. Chem. Soc.* **1976**, *98*, 6521.

(43) McDermott, J. X.; White, J. F.; Whitesides, G. M. *J. Am. Chem. Soc.* **1973**, *95*, 4451.

(44) Woodward, R. B.; Hoffmann, R. *The Conservation of Orbital Symmetry*; Verlag Chemie International: Deerfield Beach, FL, 1970.

## Nonadiabatic Study of Dynamic Electronic Effects during Brittle Fracture of Silicon

Patrick L. Theofanis, Andres Jaramillo-Botero,\* William A. Goddard III,† and Hai Xiao

*Division of Chemistry and Chemical Engineering, California Institute of Technology,  
1200 East California Boulevard, Pasadena, California 91125, USA*

(Received 6 July 2011; published 23 January 2012)

It has long been observed that brittle fracture of materials can lead to emission of high energy electrons and UV photons, but an atomistic description of the origin of such processes has lacked. We report here on simulations using a first-principles-based electron force field methodology with effective core potentials to describe the nonadiabatic quantum dynamics during brittle fracture in silicon crystal. Our simulations replicate the correct response of the crack tip velocity to the threshold critical energy release rate, a feat that is inaccessible to quantum mechanics methods or conventional force-field-based molecular dynamics. We also describe the crack induced voltages, current bursts, and charge carrier production observed experimentally during fracture but not previously captured in simulations. We find that strain-induced surface rearrangements and local heating cause ionization of electrons at the fracture surfaces.

DOI: [10.1103/PhysRevLett.108.045501](https://doi.org/10.1103/PhysRevLett.108.045501)

PACS numbers: 62.20.mj, 31.15.xg, 46.50.+a

The observation that brittle fracture of materials can lead to the emission of high energy electrons and UV photons is well documented for materials ranging from polymer thermoplastics, glasses, minerals, and semiconductor crystals [1–4]. There has been no previous atomistic description of the origin of such processes. Although fracture in solids involves breaking of chemical bonds, which can be well described with modern quantum mechanics (QM) methods, the observation of exoelectrons and photon emissions indicates that the processes are not purely adiabatic, complicating the application of QM—in particular for model systems that require more than a few hundred atoms. We show here that the recently developed first-principles-based electron force field (eFF) method for nonadiabatic dynamics accounts for electron emission and large potential differences consistent with the experiments, providing the first atomistic description of the origin of these effects. In this Letter we consider the fracture of silicon crystals producing {100} and {111} fracture planes which have been studied quite thoroughly. The effects that we explain are (1) loading of a crack leads to a sudden onset of crack propagation at 7 GPa followed by uniform velocity of the crack at 2500 km/sec after initiation and (2) voltage fluctuations in the 10–400 mV range, charge creation (up to  $10^{11}$  carriers/cm<sup>2</sup>), and current production (up to 1.3 mA).

It was not possible to explain the sudden onset of crack propagation and constant velocity response to increasing loads observed in the brittle fracture of silicon with earlier force-fields-based methods (e.g., Tersoff, Stillinger-Weber) [5–8]. However, Buehler and co-workers demonstrated that the reactive force field, ReaxFF, correctly describes the experimentally observed crack dynamics in silicon [9–11]. Left unexplained, however, is the generation of voltages and currents during fracture [12,13]. More recent experimental studies have observed the ejection of electrons [14] and other charged particles [15] during

silicon fracture dynamics. No previous attempts were made to model the voltage fluctuations, electron emission, and charge creation phenomena. Current time-dependent QM methods are incapable of describing the dynamics of electron ejection excitation of highly excited states from deformation of the crystal. Quantum mechanical methods are unable to attain the length and time scales ( $> 1000$  atoms over  $> 1$  ps time scales) required to describe the dynamics of fracture. On the other hand, conventional force fields in conjunction with molecular dynamics methods can handle the relevant length and time scales, but they do not describe ejected electrons and excited electronics states. The eFF method allows us to capture the appropriate length and time scales, and most importantly, the electron dynamics during fracture.

The eFF method provides an approximate description of quantum dynamics by describing every electron as a floating spherical Gaussian orbital [16] whose position and size varies dynamically while the nuclei are treated as classical point charge particles. Here the total  $N$ -electron wave function is written as a Hartree product of one-electron orbitals (rather than as an antisymmetrized product). Orthogonality resulting from the Pauli principle is enforced with a spin-dependent Pauli repulsion Hamiltonian which is a function of the sizes and separations of these Gaussian orbitals. The Pauli potential accounts for the kinetic energy change due to orthogonalization, arising from the Pauli principle (antisymmetrization) [17,18]. An additional quantum-derived term in the eFF Hamiltonian is the kinetic energy for each orbital, which accounts for the Heisenberg principle. The full Hamiltonian in eFF also incorporates classical electrostatic terms between nuclei or electrons. eFF has been validated on challenging electronic phenomena arising in materials subjected to extreme conditions including Auger processes [19], hypervelocity impact, and plasma formation [20].

Previously eFF treated all electrons of an atom, including the core electrons [21]. Describing the very short time scales of the high energy core orbitals makes simulating picoseconds of fracture computationally intractable on systems large enough to describe crack propagation in Si crystal. Instead of describing all electrons explicitly, here we replace the core electrons with an effective core pseudopotential while retaining the accuracy in describing the valence electrons. This allows us to study the dynamics of electronic excitations and ejection simultaneous with nucleation and propagation of crack fracture in silicon. This approximation is described in detail in the Supplemental Material [22].

For this study we developed two simulation cells. Figure 1 depicts our “{100}” crack model. In this model the  $x$ - $y$ - $z$  directions are  $(100) \times (011) \times (01\bar{1})$  direction, creating a  $(100)$  fracture plane with a  $[011]$  fracture direction with dimensions of  $3.8 \times 25 \times 3.8 \text{ nm}^3$ . In our “{111}” model, the  $x$ - $y$ - $z$  directions are  $(111) \times (\frac{1}{2}\frac{1}{2}\bar{1}) \times (\frac{1}{2}\frac{1}{2}0)$  which produces 111 crack surfaces with a  $[112]$  crack propagation direction with dimensions of  $2.7 \times 47 \times 4.0 \text{ nm}^3$ . We performed crack simulations on fully periodic replicas and on slabs with hydrogen-passivated surfaces of the previously described geometries. The results presented here correspond to our fully periodic system, though we found negligible differences between the results we obtain in our fully periodic and partially periodic slab models (see Fig. 2). Both systems were prepared in an isothermal-isobaric ensemble using a Nosé-Hoover thermostat and barostat, at 300 K and 1 atm, respectively. In both samples a seed crack of length  $\frac{1}{5}L_y$  is created before a load is applied. A continuous uniaxial strain load is applied to

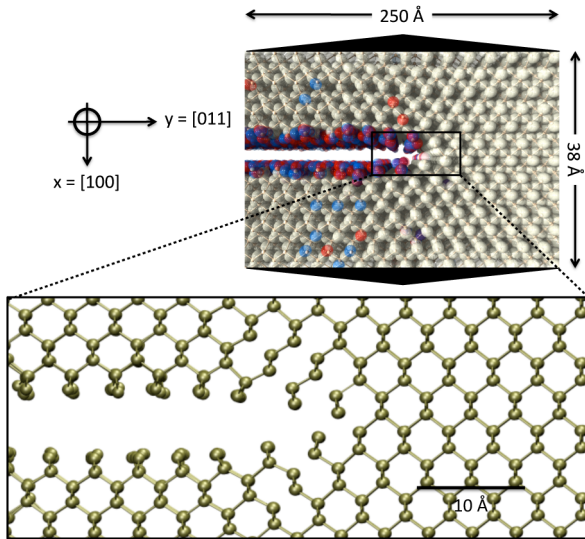


FIG. 1 (color online). A snapshot of a crack propagating in a silicon single crystal with mode I loading in the  $x$  direction producing a  $\{100\}\{011\}$  edge crack. The transparent spheres are paired electrons. Unpaired spin-up and spin-down electrons are shaded.

the cells in the  $x$  dimension at a rate of 1.2% per ps and the sample is allowed to crack naturally, which allows us to test the failure modes of the system. No barostat pressure is imposed in the strain direction.

Figure 2 shows the relationship between the crack tip velocity and the energy release rate normalized by the critical energy release rate determined at the onset of fracture. We computed  $G$  from the uniaxial stress ahead of the crack, the crack length, and Young’s modulus that we compute from our model:  $G = 1.12^2 \pi P_{xx}^2 a / E^2$ .  $K_{ic}$  is computed similarly. Both the  $\{100\}$  and  $\{111\}$  models exhibit brittle fracture and both match the experimental observation that upon reaching a critical load, the crack velocity rapidly jumps to 4 and 2 km/s, respectively, and plateaus thereafter (data for the eFF  $\{100\}$  model are in the Supplemental Material [22]). Table I compares computed mechanical properties to those of experiments. The calculated Griffith critical load for the  $\{111\}$  is 3.16 J/m<sup>2</sup>, which is higher than the experimental value but in agreement with the QM value of 3.1 J/m<sup>2</sup> [29]. This indicates that our model leads to a small amount of lattice trapping. In general, our simulations of the dynamics of fracture in silicon using the eFF pseudopotential reproduce experimental measurements and results produced with other reactive force fields [10].

From our simulations we ascertain that there are two prevalent modes of electron ionization: local field-induced ionization and thermal ionization. The simulations show that ionization occurs as a direct result of fracture. Figure 3 shows the evolution of a representative group of electrons as the fracture progresses. We find that electron ionization is precipitated by the passing of the crack front. Figure 3(c) shows that ionized electrons are excited by 5 eV, making

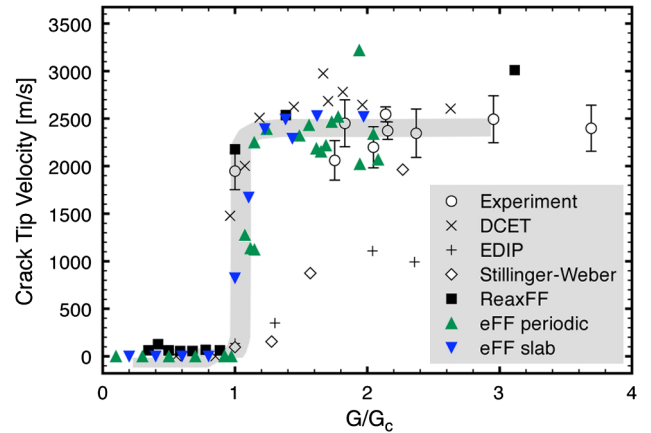


FIG. 2 (color online). Crack tip velocity versus reduced load for  $\{111\}$  fracture with experimental data from [5], ReaxFF-Tersoff and Stillinger-Weber data from [10], environmental dependent interatomic potential (EDIP) and the results of a multiscale method that couples empirical potentials and quantum mechanical tight-binding approaches (DCET) from [31]. The gray line is a visual guide.

TABLE I. Comparison of experimental and computed mechanical values: Young's modulus  $E$  (GPa), yield strength (GPa), Griffith critical load  $G_c$  (J/m<sup>2</sup>), and the stress intensity factor  $K_{ic}$  (MPa). References are in square brackets.

Method	$E$	Yield strength	$G_c$	$K_{ic}$
{111} expt.	163–188 [23]	7 [24]	2.3 [5]	0.76 [25,26]
{111} eFF	166	15	3.16	0.752
{100} expt.	125–202 [27]	...	...	0.91 [28]
{100} eFF	157	15	2.57	0.96

them sufficiently energetic to escape the Si-surface barrier. The initial excitation promotes the electrons to unbound states (total electron energy  $>0$ ), but they subsequently relax to 4.1 eV above the ground state, well into the Si conduction band. A close examination of the energy contributions leading to ionization reveals that in most cases an increase in potential energy causes ionization. The cause of this is heterolytic bond cleavage across the crack. In rare instances a heterolytic cleavage creates an anion on one crack face and a cation on the other crack face. As dangling bonds form  $2 \times 1$  surface dimers, the excess electron causes Pauli exclusion clashes with adjacent surface pairs. As a result, the ionized electron's radius decreases to reduce its overlap with nearby same-spin electrons. The spin clashing forces the electron further from the surface and the electron delocalizes (its radius increases in the eFF description). Ultimately it relaxes and settles into the conduction band.  $80 \pm 10\%$  of ionized electrons are ionized because of local field effects.

In rare circumstances an increase in an electron's kinetic energy after fracture causes it to ionize. Kinetic excitation is caused by local heating so we conclude that while possible, thermal ionization is not the predominant mechanism. In Fig. 2 of the Supplemental Material [22] the kinetic energy of the same group of electrons depicted in Fig. 3 are presented. In that figure only one electron is excited thermally—the fingerprint of thermal excitation in increased kinetic energy. We observe that elastic energy in the stress field ahead of the crack is converted to kinetic energy in the recoil of the new surfaces causing local heating. As mentioned previously, we estimate that  $20 \pm 10\%$  of the electrons are thermally ionized.

To understand the dynamics of charge carriers during silicon fracture, we compute the electrostatic potential on grid points, i.e., by summing the individual Gaussian charge density potentials. In Figs. 4(a) and 4(b), we provide snapshots of the electrostatic potential at two points during the fracture simulation. Initially, the system has zero potential (light shading). As a crack evolves, we observe the production of negative charge carriers in the free space inside the crack. Figure 4(b) shows the final state of the system after the crack has propagated through the unit cell, with the crack edges outlined in black. Heterolytic bond cleavage due to thermal fluctuation and

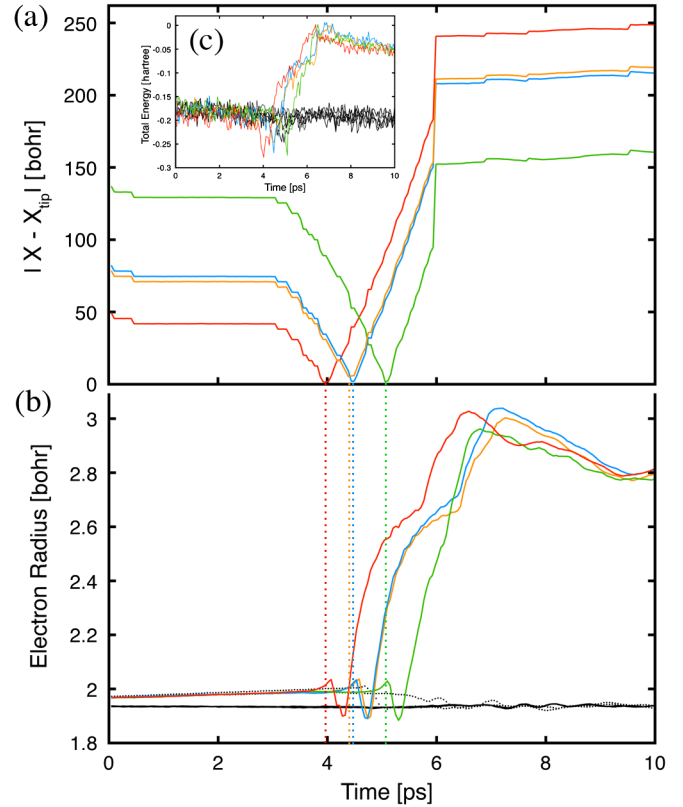


FIG. 3 (color online). (a) The absolute distance between the crack tip and electrons that will ionize. (b) The radii of ionized electrons (shaded), ground state surface electrons (black dotted lines), and bulk electrons (solid black lines). (c) The total energy of the electrons.

hot spot formation causes  $2.6 \times 10^{-2} \pm 1.3 \times 10^{-2}$  more electrons per nm<sup>2</sup> to remain on one side of the crack than the other, which results in the left crack face having (+ 2.13 V) potential and the right face having (+ 1.12 V) potential. The potential gradient across the crack corresponds to a voltage of 1.02 V. Li and colleagues reported measuring voltages of tens of mV with some cracks producing voltages up to 0.39 V [12]. The electrostatic potential difference between the crack surfaces reflects the dynamics of charge carriers during silicon fracture.

We computed the number of ionized electrons at each time point in our crack trajectories (see the Supplemental Material for details and a plot [22]). Given the size of our {111} cell, these correspond to a total electron yield of  $5.3 \times 10^{11}$  to  $1.6 \times 10^{12}$  cm<sup>-2</sup>. Langford and co-workers detected current transients whose integrated area corresponded to yields of  $10^9$  or  $10^{11}$  carriers/cm<sup>2</sup>, though their {111} crack velocities were around 900 m/s [13]. They stated that faster cracks produced larger carrier yields. Our {111} crack velocity is 2 times faster, which explains why we observe larger ionized electron yields.

From the equilibrium dynamics of the cracked system, we determined the electrical conductivity using the Green-Kubo integral of the electric current correlation function as

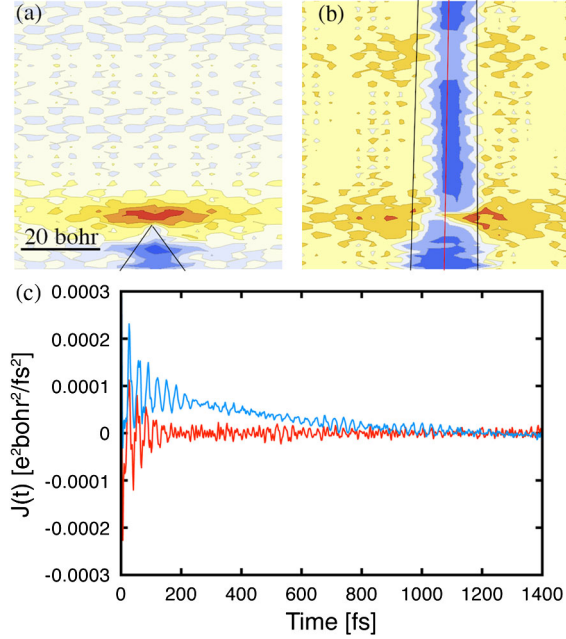


FIG. 4 (color online). The evolution of electrostatic potential is given at (a) 0 ps and (b) 15 ps. After fracture negative potential is distributed asymmetrically between the crack faces (solid black lines). (c) The electric current velocity correlation functions for the  $\{111\}$  system at equilibrium (lower curve) and after the crack has occurred (upper curve).

$$\sigma_{\text{GK}} = \frac{1}{3k_B T V} \int_0^\infty \langle \mathbf{j}(t) \cdot \mathbf{j}(0) \rangle dt, \quad (1)$$

where  $\mathbf{j}(t)$  is the electric current flux, and the integral argument corresponds to the electric current velocity correlation that is expressed as

$$J(t) = \langle \mathbf{j}(t) \cdot \mathbf{j}(0) \rangle = \sum_{i=1}^N \sum_{j=1}^N \langle q_i q_j \mathbf{v}_i(t) \cdot \mathbf{v}_j(0) \rangle, \quad (2)$$

where  $i$  and  $j$  are different particles. Figure 4(c) shows the current velocity correlation,  $J(t)$ , for our  $\{111\}$  system at 300 K and after the crack has occurred. The postcrack data trace is initially positive because free charge carriers are moving across the gap; these carriers have strong autocorrelation signals. Integrating these traces and applying the result to (1) gives us a measure of the conductivity of our cells before and after fracture. Before the fracture our cell has an electrical conductivity of  $2.69 \times 10^{-5}$  S/cm; after fracture the cell has a conductivity of  $3.72 \times 10^{-3}$  S/cm. Pure silicon samples (like our simulation cells) have conductivity as low as  $10^{-4}$  S/cm and decreasing the dopant concentration causes silicon to asymptotically approach  $10^{-5}$  S/cm [30]. Our post crack sample has a calculated conductivity on the order of  $n$ -doped silicon samples with dopant concentrations of  $4 \times 10^{12}$   $\text{cm}^{-3}$ . This indicates that the production of mobile charge carriers as a direct result of fracture accounts for the experimentally observed

fracture current bursts. It also corroborates the observation of conduction band electrons in Fig. 3(c).

We show here that our effective core potential (ECP) for silicon in the electron force field method provides an accurate representation of the dynamics of material failure, including charge transfer, voltage impulses, and electron ionization. In this study we demonstrated that eFF could replicate the physics of brittle fracture of silicon independent of crack orientation. The equilibrium and dynamic mechanical properties computed from our simulations are in excellent agreement with experimental measurements and the predictions of other reactive force fields. Furthermore, we observed the generation of voltages and the production of charge carriers in good agreement with experiment. We have performed preliminary tests to infer spectral emissions from the ground state and excited electron eigenstates from eFF dynamics, albeit within the limitations of the Gaussian basis set representation and the ECP approximation, by computing the autocorrelation function of the electron wave packets and Fourier transforming this function to obtain the eigenstates of the system. This technique allows us to roughly estimate the emissions that accompany shock, fracture, or triboluminescence.

The significance of these results stems from the capability of eFF to accurately track the long-term dynamics of electrons under nonadiabatic conditions. This provides new insights into the phenomenon of electron ejection, voltage fluctuations, and charge carrier induction. Since eFF has been demonstrated to predict the transformation of  $\text{H}_2$  and Li from ground state to intermediate states of warm-dense matter to highly excited and plasma state regimes and Auger decay, we consider that eFF is suitable for treating electronic effects in materials under a wide range of extreme conditions.

The authors would like to thank Julius Su for useful discussions on the original eFF methodology and Markus Buehler for providing his ReaxFF results for the  $\{111\}$  crack simulations. This material is based upon work supported by the Department of Energy National Nuclear Security Administration under Award No. DE-FC52-08NA28613.

\*ajaramil@caltech.edu

†wag@wag.caltech.edu

- [1] T. Shiota and K. Yasuda, *Mater. Sci. Eng. B* **173**, 248 (2010).
- [2] K. Yasuda *et al.*, *Philos. Mag. A* **82**, 3251 (2002).
- [3] F. Urakaev, *Phys. Chem. Miner.* **35**, 231 (2008).
- [4] J. T. Dickinson, E. E. Donaldson, and M. K. Park, *J. Mater. Sci.* **16**, 2897 (1981).
- [5] J. A. Hauch *et al.*, *Phys. Rev. Lett.* **82**, 3823 (1999).
- [6] D. Holland and M. Marder, *Phys. Rev. Lett.* **80**, 746 (1998).
- [7] F. F. Abraham *et al.*, *Europhys. Lett.* **44**, 783 (1998).

- [8] J. G. Swadener, M. I. Baskes, and M. Nastasi, *Phys. Rev. Lett.* **89**, 085503 (2002).
- [9] M. J. Buehler, A. C. T. van Duin, and W. A. Goddard, *Phys. Rev. Lett.* **96**, 095505 (2006).
- [10] M. J. Buehler *et al.*, *Phys. Rev. Lett.* **99**, 165502 (2007).
- [11] D. Sen *et al.*, *Phys. Rev. Lett.* **104**, 235502 (2010).
- [12] D. G. Li *et al.*, *Phys. Rev. Lett.* **73**, 1170 (1994).
- [13] S. C. Langford, D. L. Doering, and J. T. Dickinson, *Phys. Rev. Lett.* **59**, 2795 (1987).
- [14] C. J. Kaalund and D. Haneman, *Phys. Rev. Lett.* **80**, 3642 (1998).
- [15] E. Busch *et al.*, *Appl. Phys. Lett.* **73**, 484 (1998).
- [16] A. Frost, *J. Chem. Phys.* **47**, 3707 (1967).
- [17] C. Wilson and W. Goddard, *Chem. Phys. Lett.* **5**, 45 (1970).
- [18] J. Su, Ph.D. thesis, California Institute of Technology, 2007.
- [19] J. T. Su and W. A. Goddard, III, *J. Chem. Phys.* **131**, 244501 (2009).
- [20] A. Jaramillo-Botero *et al.*, *J. Comput. Chem.* **32**, 497 (2011).
- [21] J. T. Su and W. A. Goddard, III, *Phys. Rev. Lett.* **99**, 185003 (2007).
- [22] See Supplemental Material at <http://link.aps.org/supplemental/10.1103/PhysRevLett.108.045501> for a detailed explanation of the eFF method, additional electron dynamics data, ionization yields, stress energy release rate calculation details, and validation of the effective core potential. Animated trajectories can be found at <http://www.its.caltech.edu/~ptheofan>.
- [23] M. T. Kim, *Thin Solid Films* **283**, 12 (1996).
- [24] G. T. A. Kovacs, *Micromachined Transducers Sourcebook* (McGraw-Hill, Boston, 1998).
- [25] A. M. Fitzgerald *et al.*, *J. Mater. Res.* **17**, 683 (2002).
- [26] A. M. Fitzgerald *et al.*, *Sens. Actuators A, Phys.* **83**, 194 (2000).
- [27] B. Bhushan *et al.*, *J. Mater. Res.* **12**, 54 (1997).
- [28] F. Ericson *et al.*, *Mater. Sci. Eng. A* **105–106**, 131 (1988).
- [29] J. R. Kermode *et al.*, *Nature (London)* **455**, 1224 (2008).
- [30] R. Hull, *Properties of Crystalline Silicon* (Institute of Electrical Engineers, Herts, England, 1999), pp. 413–414.
- [31] N. Bernstein and D. W. Hess, *Phys. Rev. Lett.* **91**, 025501 (2003).

**Electron dynamics of shocked polyethylene crystal**Patrick L. Theofanis, Andres Jaramillo-Botero,<sup>\*</sup> and William A. Goddard III<sup>†</sup>*California Institute of Technology, Division of Chemistry and Chemical Engineering, 1200 E. California Boulevard, Pasadena, California 91125, USA*

Thomas R. Mattsson and Aidan P. Thompson

*Sandia National Laboratories, Albuquerque, New Mexico 87185, USA*

(Received 12 January 2012; published 22 March 2012)

Electron force field (eFF) wave-packet molecular-dynamics simulations of the single shock Hugoniot are reported for a crystalline polyethylene (PE) model. The eFF results are in good agreement with previous density-functional theories and experimental data, which are available up to 80 GPa. We predict shock Hugoniot for PE up to 350 GPa. In addition, we analyze the structural transformations that occur due to heating. Our analysis includes ionization fraction, molecular decomposition, and electrical conductivity during isotropic compression. We find that above a compression of  $2.4 \text{ g/cm}^3$ , the PE structure transforms into an atomic fluid, leading to a sharp increase in electron ionization and a significant increase in system conductivity. eFF accurately reproduces shock pressures and temperatures for PE along the single shock Hugoniot.

DOI: [10.1103/PhysRevB.85.094109](https://doi.org/10.1103/PhysRevB.85.094109)

PACS number(s): 82.35.Lr

**I. INTRODUCTION**

The material response of polyethylene (PE) to shock and its behavior in the warm dense matter (WDM) regime is important because it is a common ablator material in direct-drive inertial confinement fusion (ICF) experiments.<sup>1,2</sup> Experiments at the National Ignition Facility (NIF) have demonstrated that the ICF burn efficiency can be non-negligibly impacted by the capsule material, so it is crucial to understand the properties of this material.<sup>2,3</sup> Macroscopic modeling of capsule materials for these experiments requires accurate constitutive engineering material models. Producing quality engineering models requires a detailed microscopic understanding of the equations of state (EOS), electrical conductivity, and optical properties for a given material. Here, we examine the effects of electronic excitations during hydrostatic shock of PE.

Theoretical studies of PE in extreme conditions are abundant. A variety of methods including quantum mechanics (QM), conventional force fields, and reactive force fields are able to reproduce a common equation of state gauge: the experimental Rankine-Hugoniot curve.<sup>1,4</sup> Born-Oppenheimer quantum molecular-dynamics (BOQMD) methods and conventional force fields presume adiabaticity in their approach to simulating the high-energy states of PE. This assumption limits the scope of these techniques to temperatures well below the Fermi temperature, near the electronic ground state of PE.<sup>5</sup> Conventional and reactive force fields are parametrized based on Born-Oppenheimer potential energy surfaces. The result of using Born-Oppenheimer methods is that the effects of electronic excitations are absent from the system's EOS, and along the particular EOS path corresponding to the Rankine-Hugoniot. Quantum-mechanical finite-temperature density-functional theory (DFT) methods, unlike BOQMD approaches, allow for electron excitations, however the Kohn-Sham orbital description precludes these methods from revealing dynamic electron effects such as Auger processes.<sup>6,7</sup> Finite-temperature DFT methods, like those used in Refs. 4 and 1, are good points of comparison for the electron force field (eFF) because they allow for thermal electron excitations.

**II. THE ELECTRON FORCE FIELD**

The first-principles-based electron force field is a mixed quantum-classical approach for studying nonadiabatic reactive dynamics based on floating spherical Gaussian wave packets.<sup>8</sup> In the past, eFF was successfully applied to nonadiabatic processes such as Auger decay,<sup>9</sup>  $\text{H}_2$  in the WDM regime,<sup>10</sup> the hydrostatic<sup>11</sup> and dynamic<sup>12</sup> shock Hugoniot, and exoelectron emission due to fracture in silicon.<sup>13</sup> eFF is unique in that electronic and nuclear degrees of freedom are separate, which allows for nonadiabatic motion to occur naturally. eFF is many orders of magnitude faster than QM, which allows us to perform large-scale and long-time-scale dynamics simulations.<sup>12</sup>

The eFF method provides an approximate description of quantum dynamics by describing every electron as a floating spherical Gaussian orbital whose position and size vary dynamically while the nuclei are treated as classical point-charge particles.<sup>14</sup> Here the total  $N$ -electron wave function is written as a Hartree product of one-electron orbitals (rather than as an antisymmetrized product). Orthogonality resulting from the Pauli principle is enforced with a spin-dependent Pauli repulsion Hamiltonian that is a function of the sizes and separations of these Gaussian orbitals. The Pauli potential accounts for the kinetic energy change due to orthogonalization, arising from the Pauli principle (antisymmetrization).<sup>8,15</sup> An additional quantum-derived term in the eFF Hamiltonian is the kinetic energy for each orbital, which accounts for the Heisenberg principle. The full Hamiltonian in eFF also incorporates classical electrostatic terms between nuclei or electrons.

eFF energies and forces are used to propagate the nuclei and electron wave function in time using semiclassical wave-packet molecular dynamics.<sup>16</sup> The Gaussian wave packets are subject to the potential produced by neighboring nuclei and electrons; this potential is anharmonic, so the size of each Gaussian is stable at low and intermediate energies. The fact that the wave packets are stable is vindication of the harmonic assumption made during the derivation of the wave-packet

translational and radial equations of motion.<sup>8,12,16</sup> If an electron is excited sufficiently, it may escape its local potential and its radius may expand, causing the collapse of the wave function; this is the eFF analog of electron delocalization. A radial restraint is used to prevent excited electrons from expanding infinitely (which would lead to infinite kinetic energy):  $E_{\text{res}} = 1/2k_s(s - L_{\text{min}}/2)^2$  for  $s > L_{\text{min}}/2$ , where  $L_{\text{min}}$  is the smallest box bound and  $s$  is the Gaussian radius.  $k_s$  is arbitrarily set to 1 hartree per bohr, and the resulting force is  $F_{\text{res}} = -k_s(s - L_{\text{min}}/2)$ . The conditions that invoke this restraint were not encountered in our simulations, though had they been, the effect on the validity of the simulation would be minimal. A large electron imparts a force on those electrons and nuclei that it overlaps with, which is manifested in an increase in pressure. Invoking the radial restraint limits the increase in pressure and kinetic energy.

For this study we used a parallel version of eFF which is included in the LAMMPS software package.<sup>12,17</sup> The LAMMPS website provides performance comparisons of eFF and other conventional and reactive force fields.<sup>18</sup> eFF is roughly 300 times slower (cpu time per time step per particle) than a conventional Lennard-Jones potential, yet it has been demonstrated to have linear strong and weak scaling over a broad range of system sizes and number of processors in LAMMPS. It is important to note that electrons are explicitly described in eFF, i.e., it takes one carbon, two hydrogen, and eight electrons to describe a single  $\text{CH}_2$  unit. Consequently, using the true electron mass in eFF requires the use of much shorter integration time steps, on the order of attoseconds.

### III. COMPUTATIONAL DETAILS

A crystalline PE model was created by truncating and hydrogen passivating the chains in a  $2 \times 6 \times 3$  supercell of orthorhombic polyethylene. Truncating the chains in this fashion prevents unnatural stresses from forming along the length of each chain. The final cell contained 12  $\text{C}_{12}\text{H}_{26}$  molecules: 1632 particles total, 144 carbon, 312 hydrogen, and 1176 electrons. In real samples of crystalline PE, the chains are finite in length and the PE is only crystalline in small domains with lamella ranging from 70 to 300 Å in thickness and extending several microns laterally.<sup>19,20</sup> Because eFF lacks van der Waals forces, the equilibrium volume of crystalline PE is 30% too large in eFF. To counter this, the volume of the PE cell was adjusted so that the ground-state reference has a density of  $0.95 \text{ g/cm}^3$ ; this produced 1.3 GPa of stress, which was subtracted from all subsequent pressure computations. To generate points along the Hugoniot path, we prepared samples of increasing density up to  $3.0 \text{ g/cm}^3$  by isothermally and isotropically compressing the reference cell at 300 K. The temperature was controlled with a Nosé-Hoover thermostat so that the temperature, number of particles, and volume ( $NVT$ ) were defined. Each cell was then ramped to 1500 K over the course of 500 fs and it was allowed to equilibrate as a microcanonical ensemble with a fixed energy, volume, and number of particles ( $NVE$ ) at 1500 K for another 500 fs. After heating, each cell was cooled by decreasing the temperature in 30 K steps during which 200 fs of  $NVT$  dynamics was followed by 200 fs of  $NVE$  dynamics.

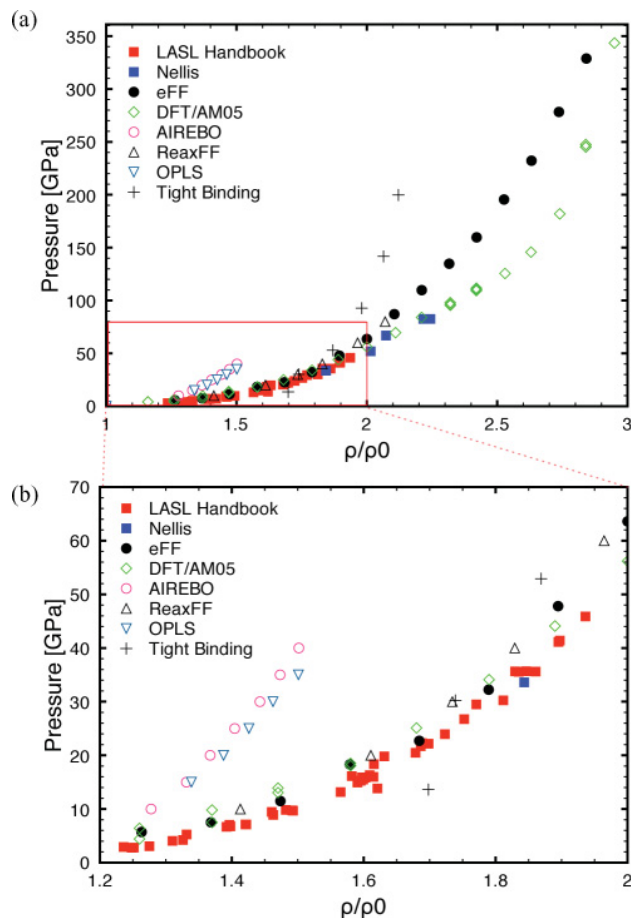


FIG. 1. (Color online) (a) The principal Rankine-Hugoniot for PE. Experimental data from the LASL shock compression handbook<sup>24</sup> and Nellis<sup>25</sup> are provided along with data for the classical MD potentials (OPLS and AIREBO).<sup>4</sup> A reactive force field (ReaxFF<sup>4</sup>) and quantum-mechanical approaches (DFT/AM05 and tight binding<sup>26</sup>) are included for comparison. (b) An expansion of the low compression region of the Hugoniot.

In the eFF method, the electron mass is defined in three separate locations: (i) in the electronic kinetic energy (i.e., wave function), (ii) in the spin-dependent Pauli energy, and (iii) in the equations of motion.<sup>8,12</sup> The effect of modifying the electron mass in (i) and (ii) affects the sizes of electrons in atoms and the lengths of bonds in molecules, therefore we keep these fixed to avoid disrupting the chemistry of the system. In all potential energy terms, the electron mass is set to the true electron mass ( $5.486 \times 10^{-4}$  amu). However, the user may define a different *dynamic electron mass* to evolve the kinetic equations of motion.<sup>8,12</sup> Changing the mass in the equations of motion varies the overall time scale of excited electron motions, with the time scale of excitation relaxations and energy transfer proportional to  $\sqrt{m_e}$ . We refer to this as changing the dynamic masses. This does not affect the net partitioning of energy in the system nor the magnitude of the thermodynamic parameters we are interested in measuring. This does not alter the system's chemistry, just its evolution in time. We verified this by computing a few Hugoniot points with 1.0, 0.1, and 0.01 amu dynamic mass and found negligible differences in pressure and temperature at these points. An

artificially heavy electron mass enables the use of longer integration time steps. For this study, we set the dynamic electron mass to 0.1 amu. To conserve mass in the system, we subtracted the mass of each atom's electrons from the standard atomic mass (e.g., we set carbon atom masses to 11.4107 amu and hydrogen atom masses to 0.907 94 amu). With this dynamic electron mass, we used an integration time step of 0.5 attoseconds (0.0005 fs).

The temperature in eFF (like pressure) is extracted from the dynamics simulation using classical virial expressions summing the kinetic energies of all the nuclear and electronic degrees of freedom:

$$E_{ke} = \frac{3}{2} N k_B T. \quad (1)$$

The kinetic contribution to the heat capacity is set to  $\frac{3}{2} k_B$  by setting  $N$  to the number of nuclei, which is valid for temperatures well below the Fermi temperature. The temperatures presented in this paper were computed using Eq. (1).

A Hugoniot curve is the locus of thermodynamic states that can be reached by shock compression of a specific initial state. These states satisfy the Rankine-Hugoniot energy condition<sup>21,22</sup>

$$U - U_0 = \frac{1}{2}(P + P_0)(V_0 - V), \quad (2)$$

where  $U$  is the internal energy,  $P$  is the pressure of the system, and  $V$  is the cell volume. It is assumed that each point along this curve corresponds to a state of thermodynamic equilibrium wherein the stress state is hydrostatic. For solids, this latter condition is only valid when the yield stress is much lower than the mean stress.<sup>23</sup> When the initial-state variables  $P_0$ ,  $V_0$ , and  $U_0$  are those of the uncompressed sample at room temperature, the Rankine-Hugoniot curve is called the principal Hugoniot. We generated states on the principal Hugoniot using the following iterative procedure. First the volume of the system is specified, representing a particular degree of compression. How each density point was prepared is described in the preceding paragraph. The temperature of the system is quickly increased by changing the set point of

the thermostat. A total of 100 fs of dynamics are run after the thermostat jump, during which averages of the energy, temperature, and pressure of the new state are obtained. These values are used to evaluate the residual energy for a time step  $i$ ,  $E_{res,i}$ , given by

$$E_{res,i} = (U - U_0) - \frac{1}{2}(P + P_0)(V_0 - V). \quad (3)$$

When  $|E_{res,i}|/E_{ke,i} < 0.05$ , the Hugoniot condition is considered satisfied. If this inequality is not satisfied, an additional 100 fs iteration is performed. The new thermostat set point is calculated from

$$T_{i+1} = T_i \left( 1 - 0.05 \frac{E_{res,i}}{E_{ke,i}} \right), \quad (4)$$

where  $E_{ke,i}$  is the average kinetic energy of the system at step  $i$ . Once this iterative procedure has converged, the thermostat is turned off and the system is allowed to evolve for an additional 3 ps. This calculation ensures that the Hugoniot condition is actually met and the properties of the systems were obtained from these dynamics.

## IV. RESULTS AND DISCUSSION

### A. The principal Hugoniot

Figure 1 is the principal Hugoniot projected onto the pressure-density plane. For densities below 2.0 g/cm<sup>3</sup>, eFF matched the experimental and DFT Hugoniot points quite closely [see Fig. 1(b)]. At higher densities, the eFF simulations overpredicted the shock pressure relative to DFT. Above 2.0 g/cm<sup>3</sup>, the results show that eFF is systematically “stiffer” than the experimental and DFT/AM05 (Ref. 27) data. However, eFF provides better agreement with the experimental Hugoniot points than typical classical MD potentials such as AIREBO,<sup>28</sup> OPLS,<sup>29</sup> and exp-6 (not shown);<sup>30</sup> the data for these can be found in Ref. 4. eFF also outperformed the tight-binding QM method above 2.0 g/cm<sup>3</sup>. These results demonstrate the difficulty in modeling the behavior of materials under shock compression. Figure 2 shows the temperature-pressure plane

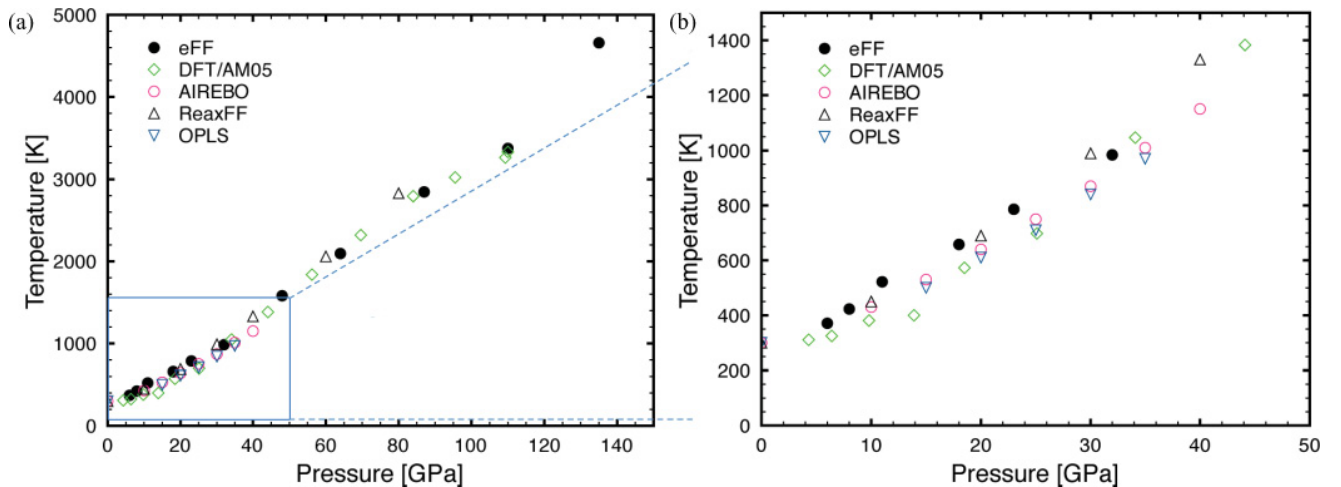


FIG. 2. (Color online) (a) The pressure-temperature locus of the Hugoniot curve for the eFF, DFT/AM05, OPLS, AIREBO, and ReaxFF methods. (b) An expansion of the pressure-temperature seam for lower pressures.

of the Hugoniot calculated by the methods in Fig. 1 for which temperature data were available. The system temperatures produced by the eFF calculations are in good agreement with conventional force fields, reactive force fields, and QM.

At high compression, interesting material features appear in the principal Hugoniot. In the AM05 data series, a shoulder feature appears at  $2.3 \text{ g/cm}^3$ . This feature is not as pronounced in the eFF Hugoniot; however, for both methods, inflections in the temperature-density plane of the Hugoniot curve indicate structural transitions (see figure 1 of the supplemental material). Subtle temperature suppression is evident in the eFF temperature-density curve at  $2.0$  and  $2.6 \text{ g/cm}^3$ . These data features correspond to tangible transitions in the molecular structure. Mattsson reported that the AM05 shoulder at  $2.3 \text{ g/cm}^3$  corresponded to PE backbone bond breaking.<sup>4</sup> The causes for the eFF data features will be discussed shortly.

### B. Structural decomposition

An analysis of the pairwise radial distribution functions (RDFs) for different degrees of compression demonstrates that significant structural decomposition occurs upon shock.<sup>31</sup> Figure 3(a) shows that carbon bonds are compressed as the sample is compressed. As the density of the material increases, the nearest-neighbor C-C pair peak ( $1.55 \text{ \AA}$ ) broadens and the next-nearest-neighbor C-C pair distance ( $2.6 \text{ \AA}$ ) is lost, indicating that the carbon backbone is fragmented. The C-H pair distribution function in Fig. 3(b) also demonstrates that tetrahedral order is lost due to shock compression. The H-H pair distribution function in Fig. 3(c) also shows that geminal (normally  $1.95 \text{ \AA}$ ), synclinal ( $2.4 \text{ \AA}$ ), and antiperiplanar ( $3.2 \text{ \AA}$ ) nearest-neighbor hydrogen peaks are lost at high compression. The  $2.9 \text{ g/cm}^3$  series resembles a classical Lennard-Jones fluid. For densities between  $2.0$  and  $2.1 \text{ g/cm}^3$  corresponding to temperatures around  $3000 \text{ K}$ , small peaks in the H-H data in Fig. 3(c) near  $0.7 \text{ \AA}$  reveal the formation of molecular hydrogen. Mattsson and collaborators also found  $\text{H}_2$  formation when their shocked PE reached  $2800\text{--}3100 \text{ K}$ .<sup>32</sup> In their simulations and in the eFF simulations, this temperature range corresponded to densities of  $2.2\text{--}2.3 \text{ g/cm}^3$ . Select pair correlation functions near DFT/AM05 Hugoniot points are available in the supplemental material. For temperatures higher than  $3100 \text{ K}$ , the molecular hydrogen dissociates, while at lower temperatures the hydrogen atoms do not have enough energy to dissociate from the polyethylene backbones. At high degrees of compression ( $>2.2 \text{ g/cm}^3$ ), the RDFs collectively reveal a fluid phase. The eFF results are consistent with MD and DFT results for equivalent temperatures.

One of eFF's greatest assets is its ability to separate electron degrees of freedom, energies, positions, momentum, and forces from those of the nuclei. This gives us an unrivaled ability to measure electronic physical quantities. In our investigation of PE, we have used this to measure the ion fraction at each stage of shock. To do this, we measure the kinetic and potential energy of each electron at each time step in our simulations.

Figure 4 shows the onset of electron ionization at  $2.5 \text{ g/cm}^3$ . Ionization increases exponentially for higher densities. The rapid increase in the ionization fraction above  $2.6 \text{ g/cm}^3$  is evidently the cause of the shoulder in the temperature-density

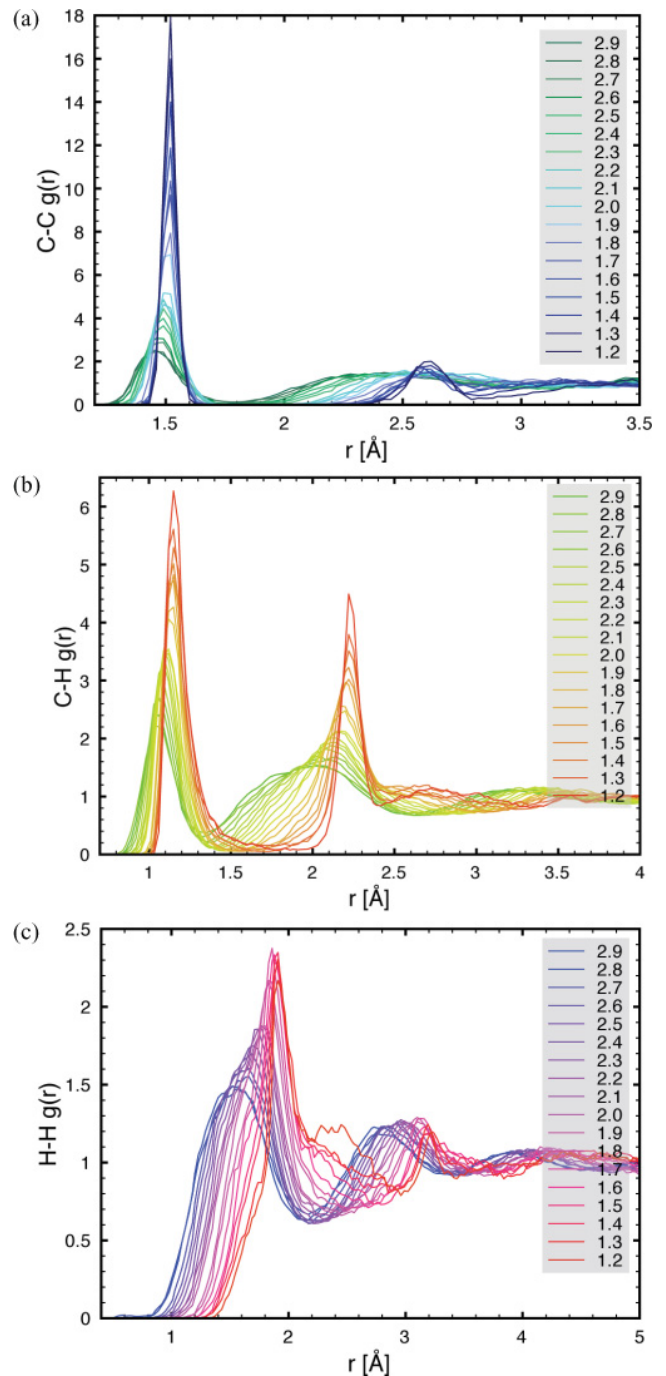


FIG. 3. (Color online) Radial distribution functions for (a) C-C atom pairs, (b) C-H pairs, and (c) H-H pairs. Each curve corresponds to a different density point ( $\text{g/cm}^3$ ) defined by the colors in the legend.

Hugoniot between  $2.6$  and  $2.7 \text{ g/cm}^3$ . Above this threshold, electron ionization draws energy from the system and this affects the pressure and temperature of the Hugoniot. The production of carriers in our simulations implies that PE is conductive at high states of compression. The production of ions is precipitated by the breaking of C-C bonds, and this relationship is evident in Fig. 4. The percentage of intact backbone for the DFT/AM05 study is also presented in Fig. 4. eFF predicts that the polymer backbone begins to fracture at

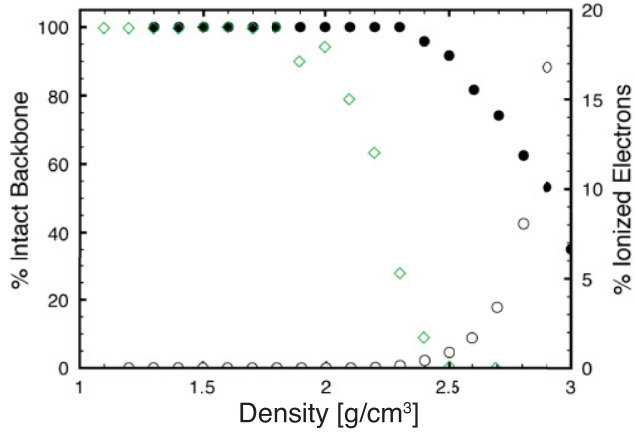


FIG. 4. (Color online) Structural decomposition along the PE Hugoniot. The circles correspond to the % intact C-C backbone for the eFF simulations. The open diamonds show the results from DFT/AM05. The secondary axis shows the % ionization along the Hugoniot calculated from the eFF simulations in open circles.

2.4 g/cm<sup>3</sup> and DFT/AM05 predicts that fracture begins at 2.0 g/cm<sup>3</sup>.

Curiously, both the DFT/AM05 and eFF structural analyses show that the hydrogen modes are excited concurrently with the carbon modes. From bond dissociation energies alone, one would expect C-C bonds ( $D_{0,\text{expt}} = 83$  kcal/mol) to break more readily than C-H bonds ( $D_{0,\text{expt}} = 98$  kcal/mol). eFF overestimates the strength of carbon-carbon  $\sigma$  bonds (for ethane, the bond dissociation energy is 140 kcal/mol versus 110 kcal/mol zero-point energy-corrected snap bond energy).<sup>8</sup> The loss of order in the C-H and H-H RDF functions indicates significant excitation in the hydrogen modes. Likewise, the C-C RDF functions are excited, but for DFT/AM05 and eFF the nearest-neighbor peaks are well defined up to 2.6 g/cm<sup>3</sup>. We believe that an entropic effect is the cause of this phenomenon. Carbon atoms are constrained to the polymer backbone by two heavy atoms while hydrogen atoms are only bound to a single heavy atom. This effectively reduces the vibrational flexibility of carbon atoms to pseudo-one-dimensional phonon modes while hydrogen atoms are free to pivot and vibrate in any direction. With a larger phase space, the hydrogen atoms have greater entropy, which might decrease the free energy of dissociation. Additionally, hydrogen atoms may be excited by collisions with neighboring polyethylene chains since they are more likely to collide before their carbon backbone.

### C. Conductivity

In order to quantify the conductivity of the shocked system, we determined the direct current conductivity using a classical Green-Kubo analysis.<sup>33,34</sup> We determined the electrical conductivity from our  $NVE$  Hugoniot states using the Green-Kubo integral of the electric current correlation function:

$$\sigma_{\text{GK}} = \frac{1}{3k_B T V} \int_0^\infty \langle \mathbf{j}(t) \cdot \mathbf{j}(0) \rangle dt, \quad (5)$$

where  $\mathbf{j}(t)$  is the electric current flux, and the integral argument corresponds to the electric current velocity correlation, which

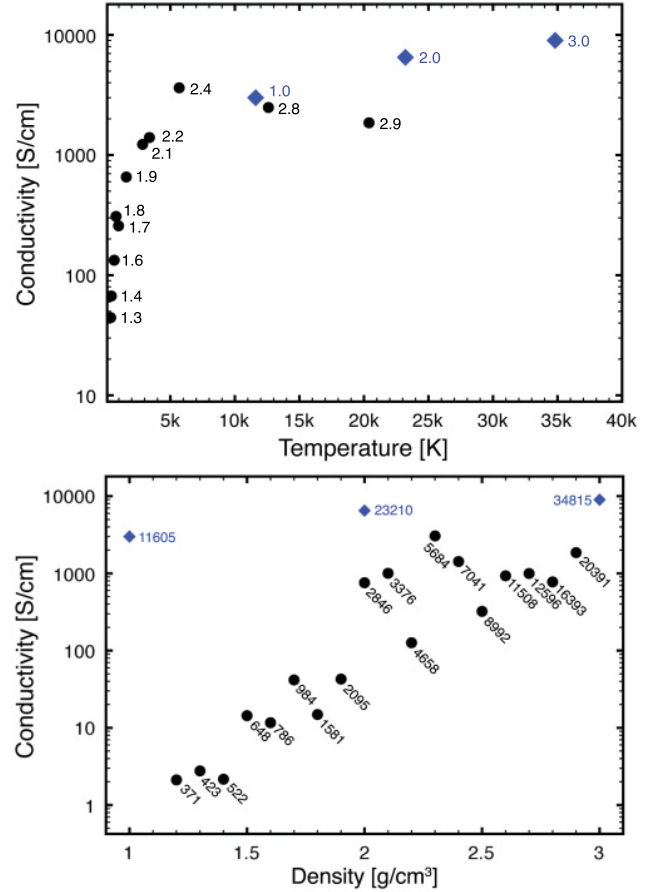


FIG. 5. (Color online) The direct current electrical conductivity of points along the eFF Hugoniot curve (circles) and finite-temperature DFT (diamonds) from Horner.<sup>1</sup> (a) Conductivity plotted against temperature with densities (g/cm<sup>3</sup>) provided. (b) Conductivity plotted against density with temperatures (K) provided.

is expressed as

$$J(t) = \langle \mathbf{j}(t) \cdot \mathbf{j}(0) \rangle = \sum_{i=1}^N \sum_{j=1}^N \langle q_i q_j \mathbf{v}_i(t) \cdot \mathbf{v}_j(0) \rangle, \quad (6)$$

where  $i$  and  $j$  are different particles,  $q$  is the charge on each particle, and  $\mathbf{v}(t)$  is the velocity of each particle. Figure 5 shows the results of this analysis for eFF Hugoniot points. eFF predicts that conductivity increases exponentially along the Hugoniot curve until the temperature reaches roughly 5000 K, at which point it levels off. Indeed, FT-DFT studies of PE in the warm dense matter<sup>1</sup> regime find conductivities between 3000 and 10 000 S/cm for samples at 1 g/cm<sup>3</sup> and 11 605 K to 3 g/cm<sup>3</sup> and 34 815 K. Figure 5(a) shows the temperature dependence of the conductivity. Comparing the eFF and FT-DFT data as a whole, there is a clear transition to a metallic state in the vicinity of 5000 K. The downward slope connecting the density points 2.4, 2.8, and 2.9 reflects the sensitivity of the classical Green-Kubo method to thorough equilibration. Outliers were omitted from Fig. 5(a), but all the data points are provided in Fig. 5(b). Between 5000 and 20 391 K, the sample has a conductivity of 2100 S/cm, which is roughly

equivalent to the conductivity of shocked fluid hydrogen at 140 GPa.<sup>35</sup> Above 2.5 g/cm<sup>3</sup>, in the metallic PE regime, the RDF analysis suggests that hydrogen is fluid. This suggests that our conductivity analysis might be applicable to hydrogen-rich fluids at high temperatures and pressures.

The quality of our quasiclassical Green-Kubo analysis is a result of the accuracy of the eFF potential. Despite not being formulated in terms of occupied bands near the Fermi level, eFF produces the correct excitations. The eFF potential is rigorously derived from a solution to Schrödinger's time-dependent equation of motion, which integrates two quantum-derived potential terms and classical electrostatics into its Hamiltonian. In particular, the Pauli function is parametrized based on the orthogonalization of valence bond-type orbitals. When a sample is well described by valence bonding, like polyethylene, eFF will succeed in modeling the potential of each electron. Each electron "feels" the correct potential, thus ionization potentials are accurate for carbon and hydrogen. In extreme conditions, the distribution of valence and core electronic states spreads and eventually the highest energy electrons become unbound much like the tail of a Fermi-Dirac distribution above the Fermi level. This behavior explains why we observe the correct carrier mobilities, ionization yields, and conductivities for eFF simulations in extreme conditions.

## V. CONCLUSIONS

We have simulated the response of PE to hydrostatic shock compression using the eFF wave-packet molecular-dynamics method. eFF accurately reproduces previously published

experimental and theoretical findings for high-energy shock Hugoniot of PE and provides further insight into the effects of electron excitations and ionization at extreme pressures and temperatures (e.g., above 2.4 g/cm<sup>3</sup> the polymer backbone begins to break and electrons begin to ionize, which increases with temperature along the Hugoniot). We find that by 300 GPa, significant structural deterioration and ionization occur. eFF also enabled us to study the electronic conductivity of PE as it transitions at high temperatures into a plasma phase, a unique feature that is impossible to obtain via conventional force fields or BOQMD. The fidelity of the eFF Hugoniot indicates that van der Waals interactions are not important under extreme shock conditions. We expect that the results presented in this paper will stimulate further work on the applicability of eFF to open problems in high-energy-density physics.

## ACKNOWLEDGMENTS

This material is based upon work supported by the Department of Energy National Nuclear Security Administration under Award Number DE-FC52-08NA28613 (Caltech PSAAP). P.T. would like to thank John Aidun, Aidan Thompson, and Thomas Mattsson for hosting him at Sandia National Laboratories, where part of this work was initiated. Sandia National Laboratories is a multiprogram laboratory managed and operated by Sandia Corporation, a wholly owned subsidiary of Lockheed Martin Corporation, for the US Department of Energy's National Nuclear Security Administration under Contract No. DE-AC04-94AL85000.

\*ajaramil@caltech.edu

†wag@wag.caltech.edu

<sup>1</sup>D. A. Horner, J. D. Kress, and L. A. Collins, *Phys. Rev. B* **81**, 214301 (2010).

<sup>2</sup>T. C. Sangster, R. Betti, R. S. Craxton, J. A. Delettrez, D. H. Edgell, L. M. Elasky, V. Y. Glebov, V. N. Goncharov, D. R. Harding, D. Jacobs-Perkins, R. Janezic, R. L. Keck, J. P. Knauer, S. J. Loucks, L. D. Lund, F. J. Marshall, R. L. McCrory, P. W. McKenty, D. D. Meyerhofer, P. B. Radha, S. P. Regan, W. Seka, W. T. Shmayda, S. Skupsky, V. A. Smalyuk, J. M. Soures, C. Stoeckl, B. Yaakobi, J. A. Frenje, C. K. Li, R. D. Petrasso, F. H. Sguin, J. D. Moody, J. A. Atherton, B. D. MacGowan, J. D. Kilkenny, T. P. Bernat, and D. S. Montgomery, *Phys. Plasmas* **14**, 058101 (2007).

<sup>3</sup>P. Amendt, C. Cerjan, A. Hamza, D. E. Hinkel, J. L. Milovich, and H. F. Robey, *Phys. Plasmas* **14**, 056312 (2007).

<sup>4</sup>T. R. Mattsson, J. M. Lane, K. R. Cochrane, M. P. Desjarlais, A. P. Thompson, F. Pierce, and G. S. Grest, *Phys. Rev. B* **81**, 054103 (2010).

<sup>5</sup>S. Pittalis, C. R. Proetto, A. Floris, A. Sanna, C. Bersier, K. Burke, and E. K. U. Gross, *Phys. Rev. Lett.* **107**, 163001 (2011).

<sup>6</sup>N. D. Mermin, *Phys. Rev.* **137**, A1441 (1965).

<sup>7</sup>R. Car and M. Parrinello, *Phys. Rev. Lett.* **55**, 2471 (1985).

<sup>8</sup>J. T. Su, Ph.D. thesis, California Institute of Technology, Pasadena, CA (2007).

<sup>9</sup>J. T. Su and W. Goddard III, *Proc. Natl. Acad. Sci. USA* **106**, 1001 (2009).

<sup>10</sup>J. T. Su and W. A. Goddard III, *Phys. Rev. Lett.* **99**, 185003 (2007).

<sup>11</sup>H. Kim, J. T. Su, and W. A. Goddard III, *Proc. Natl. Acad. Sci. USA* **108**, 15101 (2011).

<sup>12</sup>A. Jaramillo-Botero, J. T. Su, A. Qi, and W. A. Goddard III, *J. Comp. Chem.* **32**, 497 (2010).

<sup>13</sup>P. L. Theofanis, A. Jaramillo-Botero, W. A. Goddard, III, and H. Xiao, *Phys. Rev. Lett.* **108**, 045501 (2012).

<sup>14</sup>A. A. Frost, *J. Chem. Phys.* **47**, 3707 (1967).

<sup>15</sup>C. W. Wilson and W. A. Goddard III, *Chem. Phys. Lett.* **5**, 45 (1970).

<sup>16</sup>E. J. Heller, *J. Chem. Phys.* **62**, 1544 (1975).

<sup>17</sup>S. J. Plimpton, *J. Comp. Phys.* **117**, 1 (1995).

<sup>18</sup>S. J. Plimpton, [<http://lammps.sandia.gov/bench.html>].

<sup>19</sup>M. J. Doyle, *Polym. Eng. Sci.* **40**, 330 (2000).

<sup>20</sup>N. K. Bourne, J. C. F. Millett, and S. G. Goveas, *J. Phys. D* **40**, 5714 (2007).

<sup>21</sup>W. J. M. Rankine, *Philos. Trans. R. Soc.* **160**, 277 (1870).

<sup>22</sup>H. Hugoniot, *J. de l'Ecole Polytech.* **57**, 3 (1887).

<sup>23</sup>M. B. Boslough and J. R. Asay, in *High-Pressure Shock Compression of Solids*, edited by J. R. Asay and M. Shahinpoor (Springer-Verlag, New York, 1993), p. 7.

- <sup>24</sup>LASL *Shock Handbook*, edited by S.P. March (University of California Press, Berkeley, CA, 1980).
- <sup>25</sup>W. Nellis, F. Ree, R. Trainor, A. Mitchell, and M. Boslough, *J. Chem. Phys.* **80**, 2789 (1984).
- <sup>26</sup>J. D. Kress, S. R. Bickham, L. A. Collins, B. L. Holian, and S. Goedecker, in *Shock Compression of Condensed Matter*, edited by M. D. Furnish, L. Chhabildas, and R. A. Graham, *AIP Conf. Proc. No. 505* (AIP, New York, 2000), p. 381.
- <sup>27</sup>R. Armiento and A. E. Mattsson, *Phys. Rev. B* **72**, 085108 (2005).
- <sup>28</sup>S. J. Stuart, A. B. Tutein, and J. A. Harrison, *J. Chem. Phys.* **112**, 6472 (2000).
- <sup>29</sup>W. L. Jorgensen, D. S. Maxwell, and J. Tirado-Rives, *J. Am. Chem. Soc.* **118**, 11225 (1996).
- <sup>30</sup>O. Borodin, G. D. Smith, and D. Bedrov, *J. Phys. Chem. B* **110**, 6279 (2006).
- <sup>31</sup>See Supplemental Material at <http://link.aps.org/supplemental/10.1103/PhysRevB.85.094109> for coordination number plots corresponding to the radial distribution functions provided in this paper.
- <sup>32</sup>T. R. Mattsson and K. R. Cochrane (private communication).
- <sup>33</sup>Y. Shim and H. J. Kim, *J. Phys. Chem. B* **112**, 11028 (2008).
- <sup>34</sup>M. H. Kowsari, S. Alavi, B. Najafi, K. Gholizadeh, E. Dehghanpisheh, and F. Ranjbar, *Phys. Chem. Chem. Phys.* **13**, 8826 (2011).
- <sup>35</sup>W. J. Nellis, S. T. Weir, and A. C. Mitchell, *Phys. Rev. B* **59**, 3434 (1999).

## Appendix E

# Final Thoughts

When I heard the learn'd astronomer;  
When the proofs, the figures, were ranged in columns before me;  
When I was shown the charts and diagrams, to add, divide, and measure them;  
When I, sitting, heard the astronomer where he lectured with much  
    applause in the lecture-room,  
How soon, unaccountable, I became tired and sick;  
Till rising and gliding out, I wander'd off by myself,  
In the mystical moist night-air, and from time to time,  
Look'd up in perfect silence at the stars.

- Walt Whitman, Leaves of Grass, 1892